SCUOLA DI DOTTORATO

UNIVERSITÀ DEGLI STUDI DI MILANO-BICOCCA

Department of Materials Science

PhD program in Materials Science and Nanotechnology

Cycle XXXII

Quantum chemical modelling of physical and chemical properties of hybrid interfaces between semiconducting oxide surfaces and carbon-based layers

Martina Datteo

Registration number 737017

Supervisor: Prof. Cristiana Di Valentin

Coordinator: Prof. Marco Bernasconi

ACADEMIC YEAR 2018/2019

To my Grandfather

Abstract

Composite materials have attracted the attention of the scientific community due to their outstanding properties and promising applications. Materials interfaces play a crucial role in many of these applications. In the present work of thesis, different types of oxide/C-based layer interfaces have been considered for a quantum chemical investigation. The titanium dioxide surface has been interfaced with both inorganic bidimensional (graphene) and densely packed organic (enediols and silanes) C-based monolayers.

The work aims at revealing the peculiar phenomena that occur at the interface, due to the complementary properties of the two components, that might be relevant for catalysis and bio-functionalization.

The theoretical investigation is based on two levels of theory: self-consistent charge density-functional tight-binding (SCC-DFTB) and density functional theory (DFT) The approximate SCC-DFTB method allows to investigate the dynamical and structural properties of the complex systems, while the most accurate DFT calculations enable to refine the models and study their electronic properties.

The first part of the work is devoted to the modelling of the interface between TiO_2 anatase (101) surface and graphene with defects, since they are often observed in real samples. Furthermore, we have considered the presence of water molecules and their reactivity at the interface to propose possible reaction paths and to investigate the undercover effects due to the reaction confinement.

The second part of the work presents the study on a model of spherical TiO_2 nanoparticle decorated with a densely packed monolayer of two organic molecules: the enediol DOPAC and the organosilane TETT, that are excellent linkers.

DOPAC is a catechol derivative bearing an extra carboxylic group. An extensive set of adsorption modes on the TiO_2 curved surface have been investigated. Molecular dynamics (MD) simulations have also been performed to elucidate the affinity of the carboxylic groups toward the TiO_2 surface and to investigate the thermal effect on the structural conformation of the hybrid inorganic/organic system. Since TiO_2 is an excellent UV light absorbant, we have studied the TiO_2/DOPAC system photoexcitation.

TETT is an organosilane molecule with a propyl chain bearing an ethylenediamine group, further functionalized with three carboxylic groups. Due to the size and complexity of TETT fully-decorated TiO_2 nanoparticle, we have sampled the configurational space through several MD runs.

To conclude, the investigation of different hybrid (metal oxide/C-based layer) systems performed in this works has allowed, on one side, to rationalize the reactivity at the TiO_2/graphene interface, and, on the other side, to perform a comparative analysis between two different types of organic monolayers (by enediols or silanes) on TiO_2 and to assess their potential as linkers for biomolecules attachment and transport.

Contents

Chapter 1 Introduction

Titanium dioxide (TiO_2) has been widely studied as one of the most promising photocatalysts due to its excellent activity, chemical stability and low cost. However, TiO_2 presents some limitations such as a poor absorption of visible light and a rapid recombination of photogenerated electron/hole pairs. For these reasons, many studies have been devoted to TiO_2 modifications. The new properties that arise in TiO_2 hybrid materials can be exploited for technological applications. For example, to name a few, doped or sensitized TiO_2 materials absorb solar energy and increase the quantum efficiency of photocatalytic process.

In this context, three types of composite materials obtained by interfacing titanium dioxide, in the anatase phase, with carbon-based monolayers will be presented in this work of thesis. The carbon-based component is either an inorganic or an organic system: in the first case it is a single layer of carbon atoms, i.e. graphene, whereas in the other cases it is a dense monolayer of organic molecules, i.e. enediols or silanes.

First, we are interested in the mechanism of interaction between the two components at the interface. Therefore, we have studied, at the atomic scale, the structural and electronic properties of these hybrid materials through quantum mechanical calculations.

Then, the hybrid systems (TiO_2/graphene, TiO_2/DOPAC, TiO_2/TETT) may present a different behaviour with respect to the single component system. For example, the composites present modified optical properties, conductivity and biological stability as compared with pristine TiO_2. Moreover, the C-based component can be used to tether bioactive molecules for biomedical applications.

Since titanium dioxide is used in different fields, we start by presenting the fundamental properties of TiO_2 and its modifications (section 1.1), that make it versatile for different applications, such as photocatalysis (section 1.2.1), catalysis (section 1.2.2), photovoltaics (section 1.2.3) and biomedicine (section 1.2.4). The state-of-the-art of the models and of the computational approaches to study TiO_2 is presented in section 1.3. The last section 1.4 clarifies the aim and illustrates the structure of this work of thesis

Fundamental properties of TiO_2

TiO_2 exists in three natural polymorphs: rutile, anatase and brookite (**Figure 1-1**). All three crystals have different adsorption and photo responses properties due to different electronic structure.[1] Rutile is the most thermodynamically stable form in bulk phase, while anatase is very common and stable in nanomaterials.[2, 3] These two crystalline structures can be described in terms of chains of TiO_6 octahedra, where each Ti^{4+} ion is surrounded by an octahedron of six O^{2-} ions. The two crystal structures differ in the distortion of each octahedron and in the assembly pattern of the octahedra chains. In the rutile structure, each octahedron is in contact with 10 neighbour octahedrons (two sharing edge oxygen pairs and eight sharing corner oxygen atoms), while, in the anatase structure, each octahedron is in contact with eight neighbours (four sharing an edge and four sharing a corner). These differences in lattice structures cause different mass densities and electronic band structures between the two forms of TiO_2.[4]

The unique physicochemical properties of TiO_2 crystals are affected not only by the crystal structures but also by their size and shape. In particular, intensive research attention has been paid to the design and synthesis of TiO_2 with highly-reactive facets. For a long period, tailored synthesis of faceted anatase TiO_2 single crystals has been a great challenge. Recently, on the basis of theoretical predictions, Yang et al.[5] successfully synthesized for the first time uniform anatase TiO_2 single crystals with 47% of the highly reactive facets.

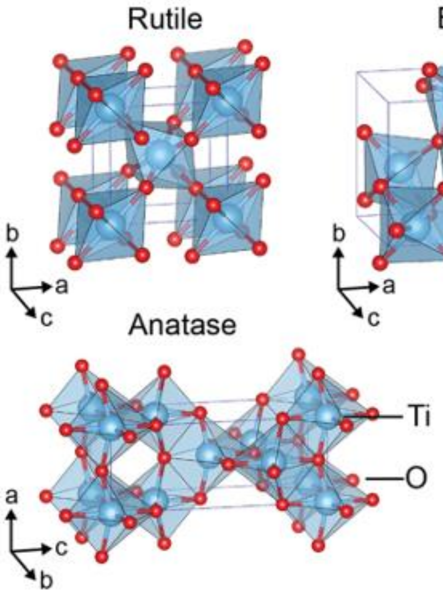

Figure 1-1 Crystal structures of TiO_2 rutile (tetragonal, $P4_2/mmm$), brookite (orthorhombic, Pbca) and anatase (tetragonal, $I4_1/amd$) polymorphs. Reprinted with permission from ref. 6.

However, for practical applications, the band gap of TiO_2 (3.2 eV for anatase and brookite, 3.0 eV for rutile) is so large that it can be only activated under ultraviolet (UV) irradiation, which is only a small fraction of the solar spectrum (<10%).

Photon-induced electron and hole in TiO_2

When TiO_2 nanoparticles absorb a photon with energy larger than the band gap value, electrons are excited from the valence band into the unoccupied conduction band, leading to excited electrons in the conduction band and positive holes in the valence band. After the excitations, these charge carriers can recombine, dissipating, non-radiatively or radiatively, the absorbed energy as heat (as shown in **Figure 1-2**), or they can migrate to the surface of the photocatalyst. All these steps can be drastically affected by the crystal structure, crystallinity and particle size. Lastly, the electrons and the holes can get trapped at the surface and react with electron donors (D) or acceptors (A) adsorbed on the surface of the photocatalyst, as shown in **Figure 1-2**. The competition between these processes determines the overall efficiency for various reactions following the photon absorption process.[7]

Nevertheless, many modification strategies have been proposed to overcome the weaknesses of low separation probability of the photoinduced electron–hole pairs and the narrow light-response range of pristine TiO_2.

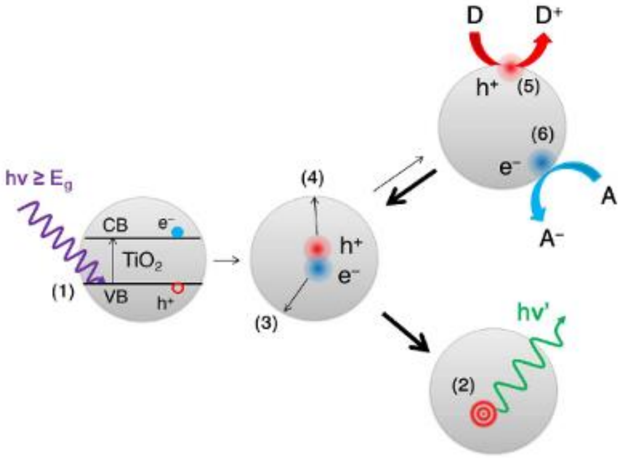

Figure 1-2 Schematic representation of the photo-induced electron and hole in TiO_2 materials: (1) generation of charge carriers by photon absorption; (2) thermal or irradiative recombination of the electron–hole pair; (3) migration and trapping of conduction band electrons to and in titanium sites and (4) of valence band holes to oxygen sites on the surface; (5) oxidative ($D \rightarrow D^+$) and (6) reductive ($A \rightarrow A^-$) reactions initiated by trapped holes and electrons, respectively.

1.1 Modification of the TiO_2 nanomaterials

The existing and promising applications of TiO_2 nanomaterials include paint, toothpaste, UV protection, photocatalysis,[8] photovoltaics,[9] catalysis, sensing[10] and nanomedicine.[11] Although applications as a pigment and photocatalyst are possible using pure TiO_2, it is clear that this is less feasible for photovoltaic and biological applications. Consequently, a lot of effort has been devoted to the construction of nanoscaled TiO_2 composite materials.

To improve the performance of TiO_2 nanomaterials, we should increase their optical activity by shifting the onset of the response from the UV to the visible region. There are several ways to achieve this goal. First, doping TiO_2 nanomaterials (section 1.1.1) with other elements, metal or non-metals, can modify the electronic properties and, thus, alter the optical properties of TiO_2 nanomaterials. Second, sensitizing TiO_2 (section 1.1.2) with colourful inorganic or organic compounds can improve its optical activity in the visible light region. Third, interfacing TiO_2 (section 1.1.2) with carbon based materials, like nanotubes, graphene etc. highly enhances the photo-activity of TiO_2 under visible light irradiation.[12] Fourth, the biofunctionalization of TiO_2 (section 1.1.3) with a self-assembled organic monolayer is an approach to extend the optical absorption to the visible region in biological/medical fields.

1.1.1 Bulk chemical modification: doping

The chemical composition and the properties of TiO_2 can be altered by doping. Specifically, the metal (titanium) or the non-metal (oxygen) component can be replaced and new energy levels are introduced into the band gap of TiO_2.

The presence of these new states induces the red-shift of the lowest electron transition and the visible light absorption. In the case of a transition metal dopant this is due to a charge transfer between the d electrons of the dopant and the conduction band of TiO_2.

Choi et al.[13] performed a systematic study of TiO_2 nanoparticles doped with 21 metal ions and found out that the presence of metal ion dopants influenced the photoreactivity, charge carrier recombination rates, and interfacial electron transfer rates. The dopants should act as both electron traps and hole traps to be photoactive. Trapping either an electron or a hole alone is ineffective because the immobilized charge species quickly recombines with its mobile counterpart. Mo^{6+} and Mo^{5+} coexist in the TiO_2 lattice where they act as an electron trap and a hole trap, respectively. This is consistent with the high photoactivity of Mo-doped TiO_2.

Nagaveni et al.[14] prepared W, V, Ce, Zr, Fe, and Cu ion-doped anatase TiO_2 nanoparticles and found out that the transition metal ions doping negatively influences the photoactivity because it increases the recombination rate of hole/electron pairs, as confirmed by the photoluminescence studies. Thus, these results suggest that substituted metal ions may act as recombination centres instead of suppressing electron-hole recombination.

Since, transition-metal-doped TiO_2 showed thermal instability, various non-metal elements, such as B, C, N, F, S, Cl, and Br, were successfully doped into TiO_2 nanomaterials. Non-metal atoms form strong covalent chemical bonding and form a localized state in the gap. Theoretical and experimental studies have shown that the desired band gap narrowing of TiO_2 can be achieved.

Carbon doping of TiO_2, substitutional to O or interstitial, induces a series of localized occupied states in the band gap, which can explain the absorption edge shift (up to 2 eV) observed experimentally.[15, 16]

The substitutional doping of N was the most effective because its p states contribute to the band-gap narrowing by mixing with O 2p states, just above the top of the valence band. Although doping with S shows a similar band-gap narrowing, it would be difficult to incorporate it into the TiO_2 crystal because of its large ionic radius, as evidenced by a much larger formation energy required for the substitution of S than that required for the substitution of N.[17] In anatase, these dopant states caused a red shift of the absorption band edge towards the visible region, thus favouring the formation of oxygen vacancies. The concomitant presence of C or N species and O vacancies was observed experimentally by X-ray photoelectron spectroscopy and electron paramagnetic resonance.[18, 19] The presence of defects was shown to be responsible for the improved photocatalytic activity in the visible region. However, the increased photoactivity of doped TiO_2 may be associated with more-complex phenomena than the simple presence of the impurity atoms, such as, the changes in the stoichiometry of the sample.

1.1.2 Surface chemical modification: sensitization of TiO_2

The great success of TiO_2 based materials mostly relies on the possibility of surface chemical modification that allows to finely tune the electronic, optical, and charge transport properties of the material.

The sensitization process is referred to the generation of a photocurrent with light energy less than the band gap of semiconductor and the sensitizer is the light adsorbing dyes. Any materials with a narrower band gap or adsorption in the visible or infrared regime can be used as a sensitizer for TiO_2 materials. These materials include inorganic semiconductors with a narrow band gap, metals, organic dyes and carbon base materials like graphene. How efficiently the sensitized TiO_2 can interact with the light depends on how efficiently the sensitizer interacts with the light. The key step in the photosensitization of TiO_2 is the efficient charge transfer from the excited sensitizer to TiO_2, and the resulting charge separation. The match between the electronic structures of the sensitizer and TiO_2 plays a role in this process, and so does the structure of the interface between the sensitizer and TiO_2. Careful design is needed to avoid the charge trapping and recombination, which eventually damage the performance of sensitized TiO_2.

Quantum dot semiconductors

The small band gap semiconductors can photosensitize large band gap semiconductors with no absorption in the visible, due to the band alignment between the two materials.

Sant and Kamat[20] found out that quantum size effects played an important role in the interparticle electron transfer in the CdS-TiO_2 hybrid systems: the electron transfer from photoexcited CdS to TiO_2 was found to depend on the size of TiO_2 nanoparticles. Charge transfer were observed when TiO_2 nanoparticles were sufficiently large (>1.2 nm) and the conduction band of the nanoparticles was located below that of CdS nanoparticles.

Hoyer et al.[21] reported the sensitization of TiO_2 by small PbS nanoparticle (< 2.5 nm). The PbS size is chosen so that photogenerated excess electrons are directly injected from the PbS to the TiO_2 and they found out a strong photoconductance in the visible region.

Metal nanoparticles

Metal nanoparticles such as Ag or Au can efficiently sensitize TiO_2. Tian and Tatsuma[22] found out that nanoporous TiO_2 films loaded with Ag and Au nanoparticles exhibited an effective charge transfer in response to visible light irradiation.

Therefore, metal particles deposited on TiO_2 enhance the photocatalytic activity because they enhance the separation of the electron-hole pairs in the semiconductor.

Organic dyes

Organic dyes have been widely employed to improve optical properties of TiO_2 in dye-sensitized solar cells (DSSCs). Organic dyes are usually transition metal complexes, such as polypyridine complexes, phthalocyanine, and metalloporphyrins. The metal centres for the dyes include Ru(II), Zn(II), Mg(II), Fe(II), and Al(III), while the ligands include nitrogen heterocycles molecules with delocalized π or aromatic ring systems. The complex is coloured because the valence π electrons can be excited by visible light.[23]

These organic dyes are linked to TiO_2 nanoparticle surface via functional groups. There are various interactions between the dyes and the TiO_2 nanoparticle substrate: (a) covalent attachment by directly linking groups of interest, (b) electrostatic interactions via ion exchange, ion-pairing, or donor-acceptor interactions, (c) hydrogen bonding, (d) and van der Waals forces, etc. Most dyes of interest link in the first way. Groups such as silanyl (-O-Si-), amide (-NH-(C=O)-), carboxyl (-O-(C=O)-), and phosphonato (-O-(HPO_2)-) have been shown to from stable linkages. Both carboxylic and phosphonic acid react spontaneously with the surface hydroxyl groups on TiO_2 substrates to form esters and phosphonate ester, respectively. However, the most successful functionalization processes are based on carboxylic acids.

The most common mechanism of the dye sensitization of TiO_2 nanoparticles involves the excitation of the dye and the charge transfer from the dye to TiO_2 nanoparticles, which ultimately reduces the semiconductor. The metal to ligand charge transfer and the ligand-centered (π-π^*) excited states of these complexes are quite long-lived, allowing them to participate in electron-transfer processes. As an efficient photosensitizer, the dye has to meet several requirements. First, the dye should have high absorption efficiency and light absorption in the visible, near-IR, or IR regions. Second, the excited states of the dye should have a long lifetime and a high quantum yield. Third, the dye should match the electronic structures of the TiO_2 nanoparticles to ensure the efficient charge transfer between them; the energy level of the excited state of the dye should be lower than the conduction band of TiO_2.[24]

Carbon base sensitizer

The light harvesting efficiency of conventional DSSC can be improved with other sensitizer. Carbon-based systems like graphene, C-nanotubes, graphene quantum dots, graphene oxide are used as a photosensitizer, because of their large optical absorptivity.

Pristine graphene is known to have a broad and strong absorption profile, absorbing about 2.3% of light.[25] Thus, carbon base materials can replace the traditionally used ruthenium complexes as visible light absorbers for high-efficiency solar energy conversion.

The carbon base material can be interfaced with large band gap semiconductor, such as TiO_2 or ZnS, to obtain, as fast as possible, charge injection processes, due to the band alignment when the two materials are interfaced.[26]

Kenrick J. Williams et. al concluded that photoinduced electron transfer from the graphene quantum dot to the TiO_2 conduction band occurs on the ultra-short time scale of <15 fs (**Figure**

1-3). They ascribed the ultrafast electron injection to strong electronic coupling between the graphene quantum dot and the TiO_2 conduction band through the carboxylate linker.[27]

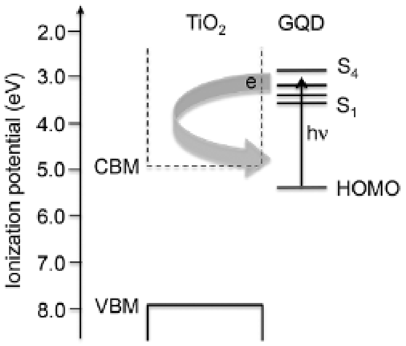

Figure 1-3 Energy level diagram of the graphene quantum dot (GQD) on the TiO_2 surface. VBM: valence band maximum; CBM: conduction band minimum. The thick arrow illustrates hot electron injection into TiO_2 conduction band. Reprinted with permission from ref. 27.

1.1.3 Surface chemical modification: biofunctionalization of TiO_2

TiO_2 nanoparticle can be used in bio-nanotechnology due to the strong oxidizing power after illumination, which can kill bacteria, as observed for Escherichia coli suspensions. However, in contrast to biologically inert bulk TiO_2, nanoparticles are cytotoxic[28, 29] and have to be pre-treated to be safely used in a clinical context.

The recent trends in bio-nanotechnology are to nanostructure and functionalize the inorganic nanoparticles to create a nanoconjugate, by joining the nanomaterials science and the biomedical research fields: the unique properties available in nanoparticles are combined with the inherent structural, specific recognition, or functional properties of biomolecules.[30]

Through chemical modifications of the nanoparticle surface it is possible to regulate chemical reactivity and introduce functionalities for specific biological activities.[31] An efficient biofunctionalization strategy involves covering the nanoparticle with densely packed monolayers of small organic molecules,[32, 33] surfactants, or incapsulating the nanoparticle with dendrimers and polymers.[34, 35]

Similarly to the sensitization of TiO_2 with dye, presented in section 1.1.2, where dyes are linked to TiO_2 nanoparticle surfaces via functional groups, in bioconjugation the bioactive molecule can be anchored to the inorganic nanoparticle by means of small organic molecules.

The organic molecule (linker) acts as a “spacer” between the inorganic and organic components in order to preserve the biological activity of the biomolecules, such as carbohydrates, proteins, DNA and antibodies. The linkers are usually bifunctional so that, one group is bound to the nanoparticle surface, and the other can be used to tether the bioactive molecules (**Figure 1-4**).[35, 36, 37]

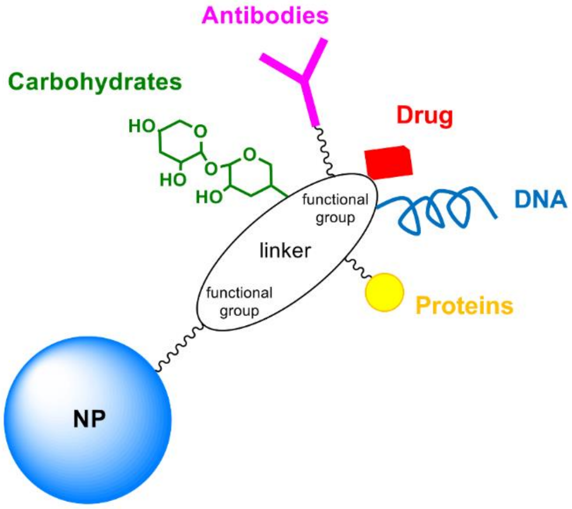

Figure 1-4 Nanoparticle functionalization scheme with different biomolecules through covalent conjugation of bifunctional linker.

Catechol derivatives

The ortho-dihydroxyaryl compounds, named catechols, represent a biomimetic approach for surface functionalization. Initially found in mussel adhesive proteins, dihydroxyphenylalanine (DOPA) or dopamine-derived catechols were successfully used in surface modifications, since cathecols strongly bind to the metal oxides in aqueous media. Furthermore, the presence of additional, electron-withdrawing substituents in the catechol derivatives allows to tune the binding strength.[38]

Well-defined catechol-based monolayers with specific functionalities, like stabilization of nanoparticles, light absorption, and reversible redox chemistry are essential for biomedical applications (**Figure 1-5**).[39, 40]

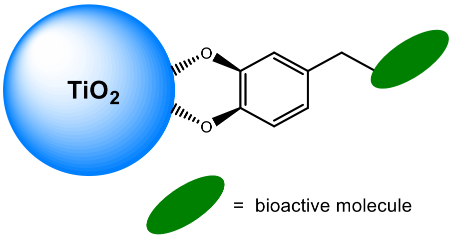

Figure 1-5 Schematic illustration of the ortho-dihydroxyaryl compounds (catechols) on the TiO_2 nanoparticle surface.

Silanes

Surface modification with alkylsilanes is one of the most commonly used methods to assemble monolayers on oxides. The general formula of organosilanes is $RSiX_3$, R_2SiX_2, or R_3SiX, where R is an alkyl group and X is a leaving group, such as chloride, alkoxy, or hydride which can be hydrolysable, follow by the condensation of the organosilanes with the OH-bearing surfaces. After the formation of covalent linkage between the substrate and the anchoring group, it is possible to further functionalize the monolayer without altering its stability.

Commonly, silanes have terminal group at the end of the alkyl chain, which can be used for further biofunctionalization. For example, 3-aminopropyltriethoxysilane (APTES) is commonly used to obtain amine-terminated surfaces, which are applied to promote protein adhesion and cell growth on biological implants.[41] Other terminal functional groups in silanes, such as alkenes or carboxylic acids, have been used to tether a wide range of other biomolecules.[42]

Phosphonates

Phosphonic acids ($R\text{-}PO_3H_2$) and their phosphonate ester derivatives (RPO_3R_2) (R = alkyl, aryl) are attractive anchoring group, due to their ability to self-assemble and react with inorganic substrates, in wide variety of solvents including water.[43] The mechanism of chemisorption of phosphonic acids on metal oxide substrates is greatly affected by reaction conditions, such as temperature, pH value, concentration and solvent. Phosphonic acids and phosphonate esters possess excellent binding properties, in particular on metals and metals oxides of high oxidation state. Owing to the stability of the PO–metal linkages these monolayers are more resistant to hydrolysis than silane or carboxylic acid-derived monolayers,[44, 45] and almost comparable to catechol based or alkene/alkyne-based monolayers.

The three oxygen atoms on the phosphonates can either bind to the surface in mono-, bi-, and tri-dentate modes or with hydrogen bonds. An overview of the resulting complexity in binding modes is depicted in **Figure 1-6**.

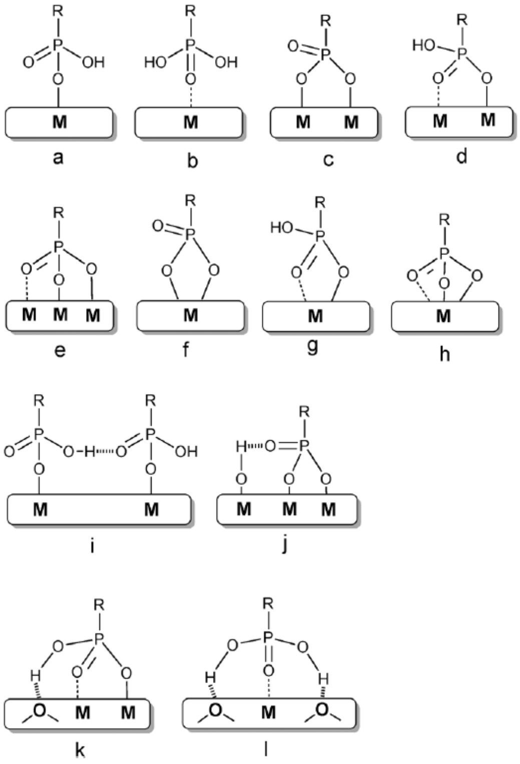

Figure 1-6 Binding modes of phosphonic acids on a metal oxide (M) surface: monodentate (a and b), bridging bidentate (c and d), bridging tridentate (e), chelating bidentate (f and g), chelating tridentate (h), and additional hydrogen-bonding interactions (i–l). Reprinted with permission from ref 36.

To better understand the binding modes of phosphonic acids, Mutin et al. made use of high-field ^{17}O magic-angle spinning NMR to study the binding of ^{17}O-enriched phosphonic acids deposited on a titania anatase support.[46] The resonance signal provides direct evidence for the formation of the PO-Ti linkage, suggesting the existence of multiple binding modes.

Carboxylates

Carboxylic acids have been widely studied to anchor dyes, therefore the binding modes of carboxylic acids on oxide surfaces have been systematically investigated, as reported in (**Figure 1-7**).

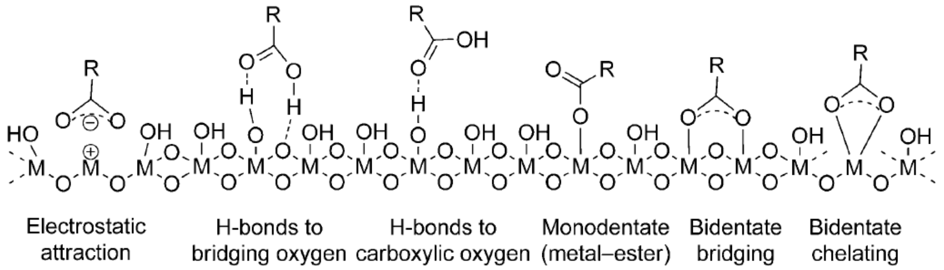

Figure 1-7 Possible binding modes of COOH or COO^- groups to metal oxide surfaces. Reprinted with permission from ref. 36.

Carboxylic acid groups are capable of binding to the oxide surface through H-bond interactions or through coordinative bonds between the carboxylate oxygen and the metal ions. The binding mode observed depends on the substrate, the carboxylic acid and the preparation conditions.

Regarding TiO_2, the binding of carboxylates to the oxide surface[47] is typically weaker and less hydrolytically stable than silanes, phosphonates and alkenes, due to the protonation of the carboxylate group at low pH and hydrolysis at $pH > 9$.

Alkenes/alkynes

The photochemical grafting of alkenes is an alternative method of anchoring organic molecules to -OH terminated surfaces when illuminated with ultraviolet (UV) light at 254 nm. The photochemical reactions produce a well defined monolayer. The Hamers group demonstrated the reaction mechanism on TiO_2.[48] This reaction is quite surprising, because TiO_2 is a widely employed photocatalyst to degrade organic molecules. The mechanism for grafting is depicted in **Figure 1-8**, in which photoexcitation of electron-hole pairs leads to charged Ti-OH groups. These groups interact with the terminal (R) carbon of the molecule, transferring a hydrogen from the -OH group to the β carbon. The finite number of Ti-OH sites on the surface can limit the reactions.

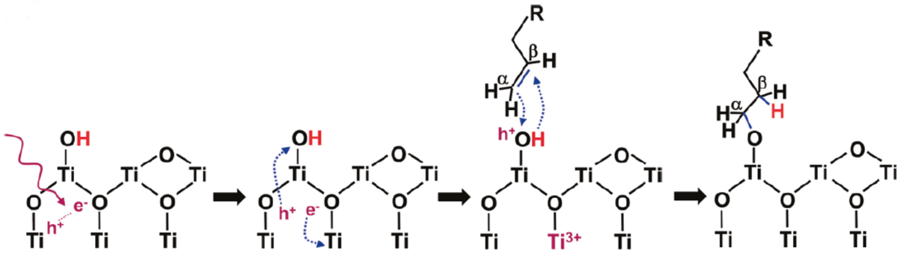

Figure 1-8 Reaction mechanism for the UV grafting of the terminal alkenes to the anatase surface. The absorption of a photon creates an electron and hole, with the electron trapped on Ti^{4+} to create Ti^{3+}, and the hole trapped on a surface hydroxyl group. The charged hydroxyl group interact with the vinyl group, binding to the R carbon and transferring a H atom to β carbon. Reprinted with permission from ref. 36.

By using alkenes with a protected amino group at the distal end, the resulting layers of alkenes provide a starting point for the preparation of DNA-modified TiO_2 thin films exhibiting excellent stability and good biomolecular recognition properties.[49]

1.2 Applications of modified titanium dioxide materials

The modification of the TiO_2 nanomaterials surface with another semiconductor, metal, organic/inorganic molecules or carbon-based material may lead to new properties in the composite material, properties which are not normally present in the single component.[50] Such advantages include the ability to tune the surface properties, i.e., acidity/basicity of the resultant materials, which is important for the adsorption of molecules, a critical factor relevant to catalysis, photovoltaic, biofunctionalization and further modification. The following section, shows the fields in which the composite TiO_2 materials can be used, based on the modifications illustrated in the section 1.1 and within.

1.2.1 Photocatalytic applications

The role of photocatalyst is to initiate or accelerate specific reduction and oxidation (redox) reactions. When the semiconductor catalyst is illuminated with photons whose energy is equal to or greater than their band-gap energy, firstly, an electron is promoted from the valence band

(VB) into the conduction band (CB), leaving a hole behind. Secondly, the excited electrons and holes migrate to the surface. Thirdly, the electrons in the CB should have a chemical potential of +0.5 to -1.5 V versus the normal hydrogen electrode (NHE) and exhibit a strong reduction capacity, while holes in the VB should have a chemical potential of +1.0 to +3.5 V versus the NHE and exhibit a strong oxidative potential. Electrons and holes can act as reductants and oxidants to react with electron donors (D), and electron acceptors (A) adsorbed on the semiconductor surface. Besides, they can get trapped in metastable surface states. It should be noted that, the excited state conduction-band electrons and valence-band holes can recombine and dissipate the input energy in the form of heat or emitted light (**Figure 1-2**). The recombination is often facilitated by a scavenger or crystalline defects, which can trap the electron or the hole. Therefore, a better crystallinity with few defects can usually minimize the trapping states and recombination sites, resulting in an increased efficiency in the use of the photogenerated carriers for desired photoreactions. Based on the fundamental principles of semiconductor photo-catalysis, the recombination between the electron and the hole is detrimental to the efficiency of a semiconductor photocatalyst. For higher photocatalytic efficiency, the electron–hole pairs should be efficiently separated, and charges should be rapidly transferred across the surface/interface to slow down the recombination. It is shown that particle size is a crucial factor in the dynamics of the electron/hole recombination process.[51]

The heterogeneous photocatalysts with multiple integrated functional components could combine the advantages of different components to overcome the drawbacks of single component photocatalysts. A wide range of heterostructures, including metal/semiconductor, semiconductor/semiconductor and molecule/semiconductor, have been explored for improved photocatalysts by increasing the light absorption, promoting the charge separation and transportation and enhancing the redox catalytic activity.[52]

Additionally, composites, which combine carbon-based materials (graphene) and semi-conductor photocatalysts (TiO_2), could potentially offer desirable efficiency for separating electron–hole pairs.

Recently, Zhouet al.[53] demonstrated that uniform dispersion of anatase TiO_2 nanoparticles with narrow particle size distribution on the surface of graphene sheets enhance the photocatalytic activity in the degradation of methylene blue in water under irradiation. The aforementioned results revealed that graphene sheets in the composites can promote charge separation and enhance photocatalytic activity. For the TiO_2–graphene composite, electron–hole pairs are generated within TiO_2 upon excitation under UV light irradiation.[54] These photogenerated electrons transfer to graphene sheets, and then they are scavenged by dissolved oxygen, facilitating the hole–electron separation. Meanwhile, the holes can either react with adsorbed water (or surface hydroxyl) to form hydroxyl radicals or directly oxidize various organic compounds. The major reaction steps in this photocatalytic degradation mechanism under UV-light irradiation are summarized by the following equations:

$$TiO_2 + h\nu \rightarrow TiO_2\ (e^- + h^+) \tag{1.1}$$

$$TiO_2\ (e^-) + \text{graphene} \rightarrow TiO_2 + \text{graphene}\ (e^-) \tag{1.2}$$

$$\text{graphene}\ (e^-) + O_2 \rightarrow \text{graphene} + O_2^- \tag{1.3}$$

$$TiO_2\ (h^+) + {}^-OH \rightarrow TiO_2 + \cdot OH \tag{1.4}$$

$$\cdot OH + \text{pollutants} \rightarrow \text{degradation products} \tag{1.5}$$

It is known that the TiO_2 photocatalyst possesses excellent activity and stability but requires UV irradiation for effective photocatalysis because of its wide band gap. The design of visible-light responsive photocatalysts is desirable but challenging, however it is a chance to optimize the morphology of TiO_2–graphene composites.

Recently, Lee et al.[12] found out the synthesis of graphene-wrapped anatase TiO_2 nanoparticles which highly enhance the photocatalytic activity of TiO_2 under visible light irradiation. They prepared graphene-anatase TiO_2 hybrid NPs by wrapping amorphous TiO_2 NPs with graphene oxide (GO), followed by a one-step GO reduction and TiO_2 crystallization via hydrothermal treatment. The TiO_2 NPs with an average diameter of 500 nm were obtained through a sol-gel process. Then the NP surface was modified with 3-aminopropyltriethoxysilane (APTMS) to have positively charge amine functional groups available on the nanoparticle. As next step they co-assembled the positively charged TiO_2 NPs with negatively charged GO nanosheets. The SEM images, after hydrothermal treatment for the reduction of GO and the crystallization of amorphous TiO_2 NPs, show the hierarchical structure in which nanocrystals are interconnected with intact graphene nanosheets (**Figure 1-9**).

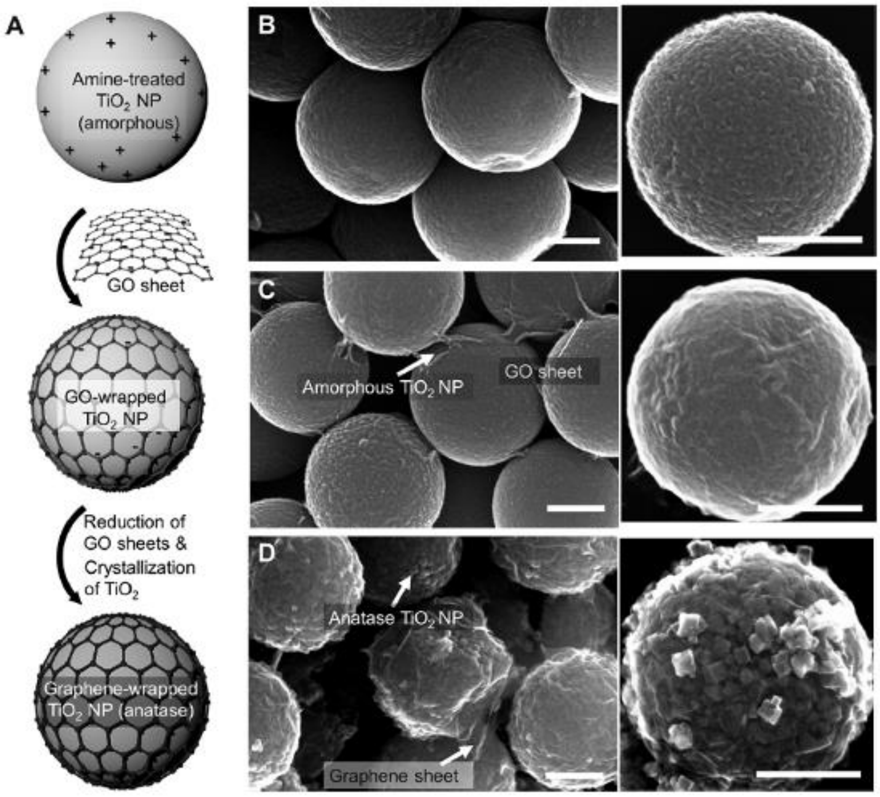

Figure 1-9 Schematic illustration of synthesis steps for graphene-wrapped anatase TiO_2 NPs and corresponding SEM images. (A) Synthesis steps of graphene-wrapped TiO_2 NPs; the surface of amorphous TiO_2 NPs was modified by APTMS and then wrapped by graphene oxide (GO) nanosheets via electrostatic interaction. Graphene-wrapped anatase TiO_2 NPs were synthesized through one-step hydrothermal GO reduction and TiO_2 crystallization. (B) SEM images of bare amorphous TiO_2 NPs prepared by sol-gel method. (C) SEM images of GO-wrapped amorphous TiO_2 NPs. (D) SEM images of graphene-wrapped anatase TiO_2 NPs. Scale bar: 200 nm. Reprinted with permission from ref. 12.

They observed a red-shift in the absorption edge and a strong absorption in the visible light. As compared with the band gap of bare anatase TiO_2 NPs (3.27 eV), the band gap in graphene-TiO_2 NPs was significantly reduced to 2.80 eV.

During the hydrothermal treatment of GO-TiO_2 NPs Ti atoms interact with GO, which provides good contact between the two materials. The resulting Ti−O−C bonds are responsible for the shift of the band-edge that facilitates visible light absorption.[55]

Under a visible irradiation, strong photocurrent response was observed, which confirms high photo-activity of the graphene-TiO_2 NPs. They tested the photocatalytic activity of composite with the photodegradation of methylene blue (MB) under visible light. While MB was slightly degraded in the presence of bare anatase TiO_2 NPs, the degradation was remarkably accelerated with graphene-TiO_2 NPs. The kinetic constants for the degradation of MB with the bare anatase TiO_2 NPs and graphene-TiO_2 NPs are $k = 3.28 \times 10^{-3}$ min^{-1} and $k = 3.41 \times 10^{-2}$ min^{-1}, respectively.

The band gap narrowing (3.2 eV → 2.8 eV) of TiO_2 in the graphene-TiO_2 NPs should change the energy level difference between graphene and TiO_2 enough to allow electrons from the excited MB to flow to the conduction band of TiO_2 NPs via graphene (Path 1 in **Figure 1-10**). Valence electrons of TiO_2 can be also excited to the conduction band state by absorbing visible light due to the sufficiently narrow band gap of graphene-TiO_2 NPs (Path 2 in **Figure 1-10**).

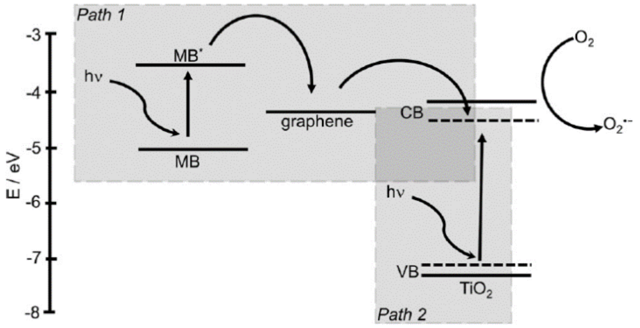

Figure 1-10 Suggested mechanism for the photocatalytic degradation of MB by graphene-wrapped anatase TiO_2 nanoparticles under visible-light. Electrons from MB* flow to the conduction band of TiO_2 nanoparticles via graphene (Path 1). Valence electrons of TiO_2 are excited to the conduction band state by absorbing visible light, which can convert oxygen molecules in the solution to singlet oxygen, the reactive oxygen species (ROSs) (Path 2). MB can be decomposed either by ROSs or by self-degradation under visible light irradiation. CB: conduction band, VB: valence band, MB*: excited state of MB, dotted line: intra-band gap energy level of TiO_2 narrowed (3.2 eV →2.8 eV) by direct interaction with Ti atoms and C atoms during the synthesis of graphene-TiO_2 nanoparticles. Reprinted with permission from ref. 55.

1.2.1.1 Water splitting

In their pioneering work Fujishima and Honda discovered the photocatalytic splitting of water on a TiO_2 electrode under ultraviolet (UV) light with the production of hydrogen.[56, 57] When TiO_2 absorbs UV light, electrons and holes are generated in the conduction and valence bands, respectively. The photogenerated electrons and holes cause redox reactions. Water molecules are reduced by the electrons to form H_2 and oxidized by the holes to form O_2, leading to overall water splitting, as shown in the following reactions:

Water oxidation $2\ H_2O \rightarrow 4\ H^+ + 4e^- + O_2$ (1.6)

Water reduction $4\ H^+ + 4e^- \rightarrow 2\ H_2$ (1.7)

Water splitting $2\ H_2O \rightarrow 2H_2 + 2\ O_2$ (1.8)

The bottom level of the conduction band has to be more negative than the reduction potential of H^+/H_2 (0 V vs NHE), while the top level of the valence band has to be more positive than the oxidation potential of O_2/H_2O (1.23 V), as shown in **Figure 1-11**.

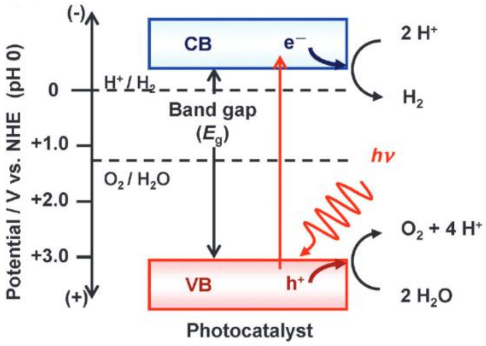

Figure 1-11 Energy diagram for the water splitting. Reprinted with permission from ref. 8.

The potential of the band structure of TiO_2 fulfil the thermodynamically requirement for the water splitting. Other factors such as charge separation, mobility, and lifetime of photogenerated electrons and holes also affect the photocatalytic properties of TiO_2. These factors are strongly affected by the bulk properties of the material such as crystallinity, but surface properties like surface states, surface chemical groups, surface area, and active reaction sites are also important.

It has been reported that pure TiO_2 could not easily split water into H_2 and O_2 in the simple aqueous suspension system. The main problem is the fast undesired electron-hole recombination reaction. Therefore, it is important to prevent the electron-hole recombination process. The Pt-TiO_2 system could be illustrated as a “short-circuited” photoelectrochemical cell, where a TiO_2 semiconductor electrode and a platinum-metal counter electrode are brought into contact. Well-dispersed metal particles trap the electrons, which reduce water.

New photocatalysts are necessary in order to develop materials for splitting water into H_2 and O_2 under visible light. The substitutional doping created a new energy levels in the gap of the TiO_2, as explained in section 1.1.1. These levels have to possess the thermodynamical potential for oxidation of H_2O but also the catalytic properties for the four-electron oxidation reaction.

Borgarello et al. found that water cleavage could be induced with visible light in colloidal solutions of Cr-doped TiO_2 nanoparticles deposited with ultrafine Pt or RuO_2. A pronounced synergistic effect in catalytic activity was noted when both RuO_2 and Pt were co-deposited onto the particle.[58]

1.2.2 Catalytic applications

In the fields of catalysis, the main research aimed at developing catalysts with high activity and stability. Recently, it was observed that reactions, which occur in restricted space between a substrate (metal or metal oxide) and 2D overlayer (graphene, h-BN, or MoS_2), enhance the performance of conventional catalysts. This observed phenomenon is called “catalysis under cover”.[59] In this respect, exciting results were achieved for different reactions in small molecules, like H_2, O_2, CO, and H_2O. For example, intercalated CO at the G/Pt (111) interface shows weaker interactions with metal as well as lower desorption temperatures and a lower reaction barrier for oxidation compared to bare Pt (111).[60] This finding provides a way to design novel catalysts.[61]

The G/TiO_2 can also be conceived as a two-dimensional confined catalysis, where reactions are catalytically promoted under graphene due to the confinement effects, as seen for other substrates. Moreover, the metal oxide can replace the precious Pt, Pd substrate that have inimitable performance in heterocatalysis but are not available for large scale industrial applications due to the high cost and the limited availability on earth.[62]

Up to now the mechanism and the factors which determine the enhanced reactivity are still not entirely clear at the G/TiO_2 interface (**Figure 1-12**). Since it is not a general phenomenon, but it is only observed for specific reactions at specific hybrid interfaces, there are only few computational studies of the reactions at graphene TiO_2 interface.[63]

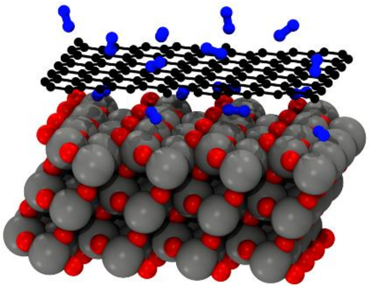

Figure 1-12 Confined space due to the interface of TiO_2 anatase (101) surface with graphene, where a new and peculiar reactivity is observed for a small molecule.

Doping the graphenic component of this type of composites has been little investigated so far, despite the evidence that the presence of dopants leads to enhanced interfacial contacts, thus improving the catalytic efficiency.

1.2.3 Photovoltaic applications

Titanium dioxide nanoparticles are used in dye-sensitized solar cells (DSSC), which mimic the way of plants to convert sunlight into energy, although in this case sunlight is transformed into electrical current.

The general model of a DSSC, initially proposed and developed by Grätzel in 1991,[9] is a liquid junction device that consists of a nanocrystalline TiO_2 photoanode, an iodine redox (I^{-3}/I^{-}) pair electrolyte, and a counter electrode, the cathode, typically made of a thin film of Pt.

In DSSC a photon enters the solar cell through a transparent electrode, usually a fluoride-doped tin dioxide glass named FTO, and can be absorbed by a sensitizer, exciting an electron, as shown in **Figure 1-13**. Then, this electron can be injected into the conduction band of a neighbouring semiconductor and diffuse to the current collector. The electron can be conducted to the outer circuit generating current and flow to the cathode where it is transferred to an electrolyte or a hole conductor. The original state of the dye is restored by electron donation from the electrolyte, usually an organic solvent containing a redox system, such iodide/triiodide couple, and completing the circuit. The voltage (V_{oc}) generated under illumination corresponds to the difference between the Fermi level of TiO_2 and the redox potential of the electrolyte.

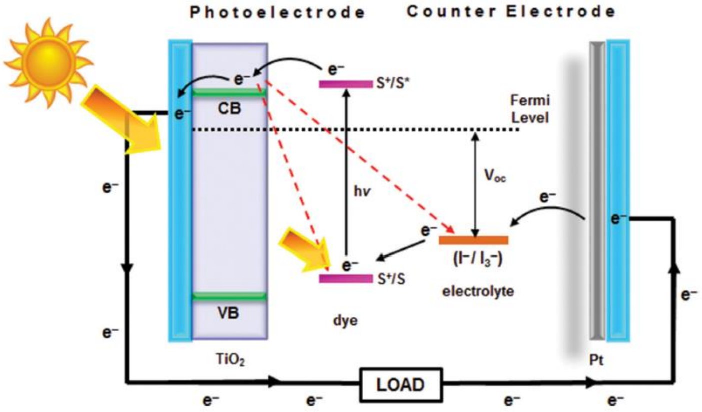

Figure 1-13 Schematic representation and principle of a typical DSSC with nanocrystalline TiO_2 photoelectrode. Reprinted with permission from ref. 69.

To optimize these devices and achieve respectable power conversion efficiencies researchers have looked at ways to maximize light harvesting and minimize losses due to parasitic electron transfer pathways. One limitation of the DSSC is the direct recombination of electrons from the conduction band of TiO_2 to the oxidized dyes or to the electrolyte. Both recombinations take place at TiO_2/dye or TiO_2/electrolyte interface. It has been established that these recombinations can be suppressed by integrating carbon nanotube or graphene into the photoanode of DSSC.[64]

Carbon nanotubes (CNTs) notably possess high charge mobilities, which could be useful to increase the performance of the DSSC. The injected electrons from the excited dye molecules into the conduction band of TiO_2 can be transferred quickly through the CNTs conduit. The right content, the distribution and the dispersibility of CNTs structures in TiO_2 films are essential requirements to optimize conductivity and light harvesting efficiency of the electrode, since the high concentration of CNT decrease the efficiency of the electrodes.[65, 66]

Graphene has remarkable properties including excellent conductivity, superior strength to any material ever isolated, good flexibility, high transparency and chemical resistivity. Graphene improves the performance of the DSCC much more than other carbon-based materials. There are several reasons to explain this observation. Although CNTs can improve the efficiency of DSSCs, their poorer interconnection with the spherical TiO_2 nanoparticles, as compared to graphene, would limit the overall performance of DSSCs due to some charge transfer barrier and possibility of recombination. On the contrary, graphene is a large single sheet that can significantly contact TiO_2 nanocrystals, thus it would significantly suppress the charge recombination. The work function of graphene (–4.42 eV)[67] lies between the conduction band of TiO_2 (–4.4 eV)[68] and FTO substrate (–4.7 eV).[68] Owing to this suitable energy level alignment, photo-generated electrons transfer stepwise from the TiO_2 to FTO substrate without an energy barrier (**Figure 1-14**). Here, graphene can act as a bridge between TiO_2 and FTO substrate. The very high conductivity of graphene can accelerate the electron transporting process and reduce the rate of charge recombination. Because of these advantages, graphene materials have been found to be perfect candidates for the photoelectrode of DSSCs.[69]

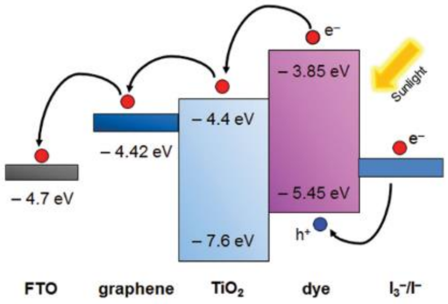

Figure 1-14 Schematic diagram of the energy level for graphene/TiO_2 film based DSSC. Reprinted with permission from ref 69.

1.2.4 Biomedical applications

Light has been used as therapy for more than three thousand years.[70] Ancient Egyptian, Indian and Chinese civilizations used light to treat various diseases, including rickets, vitiligo and skin cancer.[71] Even nowadays the light is used in oncology as an alternative to invasive treatments (surgery, chemotherapy or radiotherapy) employing the modern photodynamic therapy (PDT).

The main component of PDT is the photosensitiser; once in a target cell and/or tissue, as illustrated in the scheme (**Figure 1-15**), the photosensitiser is activated due to the absorption of light with a specific wavelength, and excited from a ground to an excited state. As it returns to the ground state it releases energy, which is transferred to molecular oxygen present in the cell/tissue. The energy transfer to oxygen generates reactive oxygen species (ROS), such as singlet oxygen and free radicals.[72] Such oxidative reactions affect cell structures, leading to cell toxicity that inhibit cancer cells.

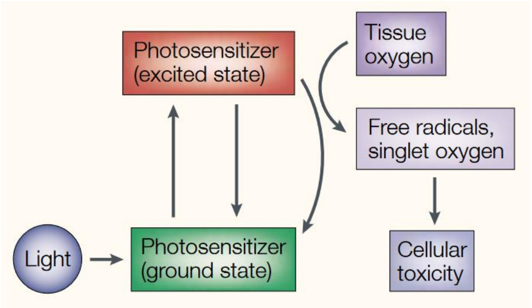

Figure 1-15 Mechanism of action of photodynamic therapy. Reprinted with permission from ref. 72.

Titanium dioxide is a potential photosensitizer due to its excellent ultraviolet light triggered cytotoxicity. However, the UV light has limited tissue penetration and it is harmful for the human body. **Figure 1-16** shows that in the UV region, where pristine TiO_2 absorbs ultraviolet light, a significant part of the incoming light is also absorbed by proteins, melanin, and hemoglobin. On the other hand, water and fat tissue start absorbing at 1000 nm, leaving the optical window in the range of 600−1000 nm as the only region where photoactive species can be efficiently activated for photodynamic therapy. Therefore, also for biomedical applications it is necessary to sensitize TiO_2 to the visible light in the optical window.

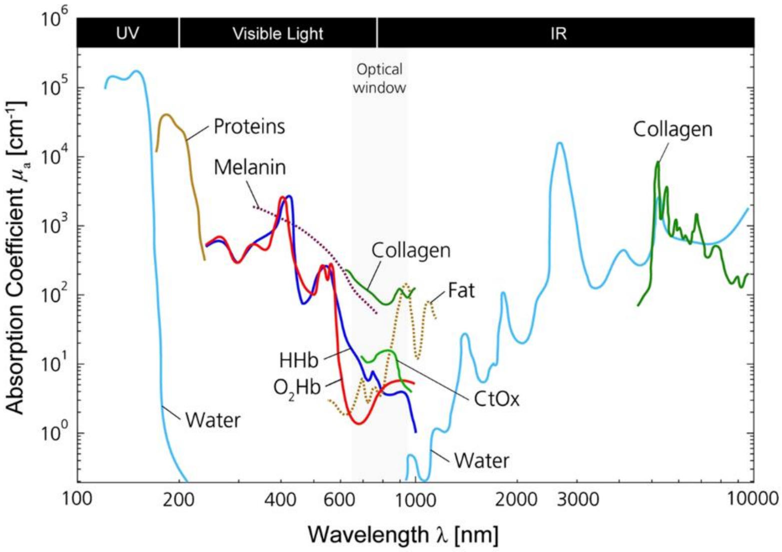

Figure 1-16 Absorption spectra for different chromophores present in human tissue. The spectra for hemoglobin, proteins, water, collagen, fat, and cytochrome oxidase (CtOx) are shown. Optical window through the tissue is in the region from 600 to 1000 nm. Reprinted with permission from ref 73.

The modifications of TiO_2 introduced in the section 1.1 are also used in nanomedicine. As regards the doping methods (section 1.1.1), several metal elements (Pt, Fe)[74, 75] and non-metals elements (C, N)[76] have been used. The sensitizers for the TiO_2 (section 1.1.2) in PDT are organic dyes, like the natural pigment hypcrellin B,[77] the porphyrin chlorine e6 [78] or the large aromatic macrocyclic zinc phthalocyanine.[79] Catechols molecules (section 1.1.3) were the first approach that held promise for extending the optical absorption to the visible region for biological/medical applications.[80, 81]

A successful anticancer effect of TiO_2 requires selective killing of cancer cells while not damaging healthy cells. A good target for the specific localization of the TiO_2 nanoconjugates are the receptors overexpressed on the surface of tumour cells. Once the TiO_2 nanoparticles are functionalized with proteins, the TiO_2 nanoconjugates binds the target on the cell surface, and the subsequent light activation can be used to induce redox reactions to alter cell metabolism or induce cell death.

Recently, monoclonal antibody proteins CEA[82] and pre-S1/S2[83] have been immobilized on the surface of TiO_2 nanoparticles. In the work of Rozhkova et al.[84] the antibody IL13a2R was linked to TiO_2 through a carboxyl group-terminated catechol moiety (DOPAC). The bivalent linker DOPAC simultaneously serves two principal functions. First, chemisorption of DOPAC enhancing and optimizing the nanocrystal exterior charge-transfer dynamics, enabling absorption of a visible part of solar spectrum. Second, chemisorption modifies the particle surface with carboxylic functional groups, which are useful for further covalent tethering to a biomolecule. The resulting carboxylic groups of the TiO_2-DOPAC particles were preactivated using 3-sulfo-1-hydroxy-succinimide/1-ethyl-3-[3-dimethylaminopropyl]carbodiimi-de hydrochloride (sulfo-NHS/EDAC), and then coupled to amino groups of the antibody via carbodiimide chemistry. In this work, they overcame the passive transport of TiO_2 nanoparticles by integrating the hard inorganic nanomaterial with a soft biological material, moreover the integrated nanosized TiO_2/antibody complex retains both its biorecognition ability and its photoreactivity. The TiO_2 nanoconjugate binds exclusively the brain tumours cells and, under exposure of visible light, initiates the production of ROS, which damages the cell membrane and induces programmed death of the cancer cell (**Figure 1-17**).

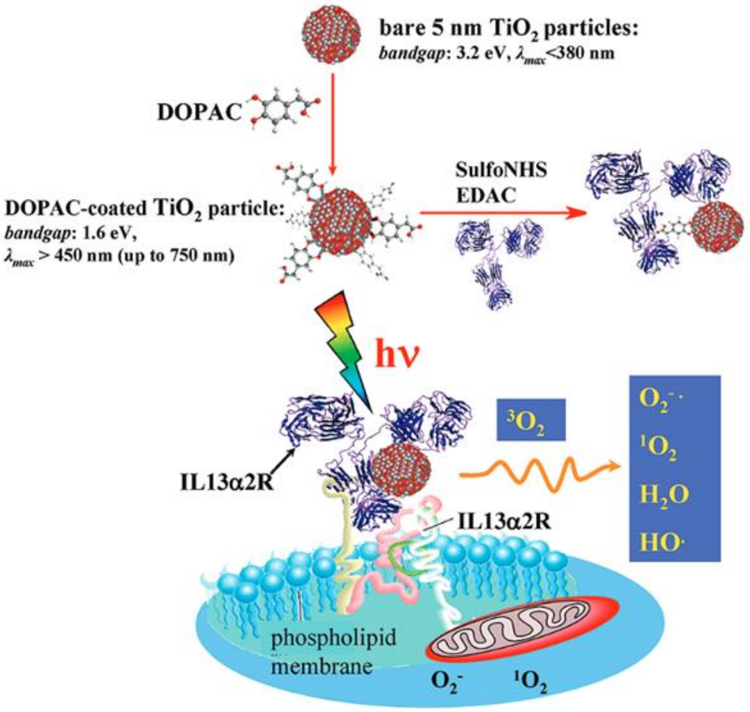

Figure 1-17 Scheme of the TiO_2 nanoparticle bioconjugation with IL13R antibody via DOPAC linker to recognize and bind exclusively to brain cancer cell. The visible light photo-excitation of the nano-biohybrid in an

aqueous solution results in the formation of various ROS, which cause cell membrane damage and cell death. Reprinted with permission from ref 84.

The site selectivity of TiO_2 nanoconjugates can be exploit in drug delivery. For maximizing the therapeutic activity while minimizing the side effects, an ideal drug distribution system should deliver the drug when and where it is required.[85] Up to now, TiO_2 has been studied as a carrier material for various drugs, such as valproic acid widely used in pediatric epilepsy,[86] or daunorubicin [87] one of the most extensively used chemotherapy agents. The drug load depends on the shape of the TiO_2 system, such as whiskers, capsules, and porous shapes. Li et al.[88] confirmed that one-dimensional titanium dioxide whiskers could enhance the potential anti-tumor intracellular efficiency of daunorubicin by increasing the concentration of drug inside the cancer cell, while alleviating the toxic side-effects by efficiently making full use of daunorubicin. Furthermore, it was found that the loading mode between the drug and TiO_2 can significantly affect therapeutic efficacy. Y. Qin et al.[89] loaded doxorubicin on the highly water-dispersible TiO_2 nanoparticles by non-covalent complexation (TiO_2/DOX) or covalent conjugation (TiO_2-DOX) (**Figure 1-18**). In the case of non-covalent complexation, the main fraction of DOX was found inside the nuclei, which was probably due to the pH-responsive release of DOX from TiO_2/DOX in tumour cell, while mostly covalent was distributed in the cytoplasm, and little TiO_2-DOX penetrated the nuclei (**Figure 1-18**). Consequently, TiO_2/DOX exhibited a significantly higher cytotoxicity towards tumour cells than free DOX because of enhanced cellular uptake.

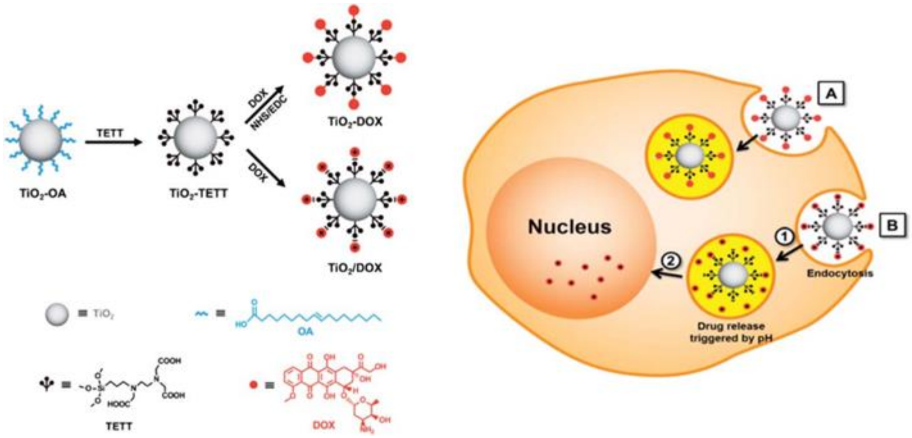

Figure 1-18 On the left, a schematic representation of synthesis of the highly water-dispersible TiO_2 nanoparticles by exchanging the oleic acid coating (OA) with the TETT linker and the loading of DOX via non-

covalent complexation (TiO_2/ DOX) or covalent conjugation (TiO_2-DOX). On the right, illustration of the effect of loading mode on the intracellular location of DOX. Most TiO_2-DOX was distributed in the cytoplasm (A), while in the case of TiO_2/DOX, the main fraction of released DOX was found inside the nuclei (B). Reprinted with permission from ref 89.

The binding of a protein or peptide to TiO_2 can also be exploited to develop a sensitive electrochemical biosensors relevant for diagnostics. These new approaches for sensing would increase the understanding of biotransformations during metabolic events giving insight into intracellular redox analysis and enzyme kinetics that determine cellular metabolic functioning.[90] Moreover, after functionalization with fluorescent dyes, TiO_2 nanoparticle allows the direct imaging of the nanoconjugate using fluorescent microscopy.[91] Therefore, the use of titanium dioxide for biomedical application is evident and promising.[92, 93]

1.3 State-of-the-art of the computational studies of anatase TiO_2

Quantum chemical simulations are a precious tool for the investigation and rationalization of the observed properties of titanium dioxide. Being a widely used material in different fields, it is not surprising that an enormous number of theoretical and computational studies on its physical and chemical properties can be found in literature.

In this section, a brief overview of computational studies on TiO_2 is reported, focusing mainly on stoichiometric anatase TiO_2.[94]

1.3.1 Bulk anatase TiO_2

The primitive unit cell of TiO_2 in the anatase structure is shown in **Figure 1-19** and has a tetragonal unit cell containing four TiO_2 units. The space group of anatase is 4_1/amd, and the local symmetry is D_{2d}. The structure is defined by the crystallographic lattice parameters a = b = 7.782 Å and c = 9.502 Å. Each Ti atom is coordinated to the six neighboring oxygens via two (long) apical and four (short) equatorial bonds, of lengths 1.976 and 1.946 Å, respectively, at 15 K. [95, 96] Each O atom is coordinated to three Ti atoms via one long bond and two short bonds, lying in the same plane. The bonding character of this crystalline solid is found to be largely ionic, with some covalent contribution.[97]

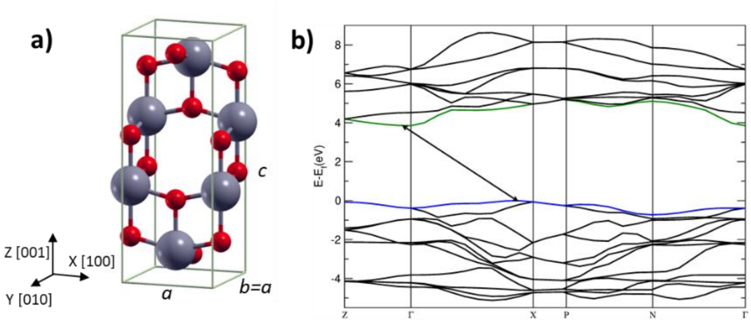

Figure 1-19 a) bulk anatase unit cell. Oxygen atoms and titanium atoms are shown in red and grey, respectively. b) band structure of bulk anatase along with the high symmetry directions of the first Brillouin zone, calculated with DFT(B3LYP-D*).

The electronic structure of semiconductor oxides is challenging to describe even for the most advanced computational methods. One of the critical quantities to be accurately reproduced is the band gap. In anatase, the minimum fundamental band gap is indirect, with the bottom of the conduction band (CB) at Γ and the top of the valence band (VB) close to the X point, as show in **Figure 1-19**. It is important to consider the fundamental (or electronic) band gap and the optical band gap. Experimentally, the fundamental band gap was determined to be 3.2 eV with electrochemical measurements at room temperature (RT),[98] while for the optical band gap a value of ∼3.4 eV was obtained with optical absorption measurements at 4 K. Theoretically, the band gap is generally determined from the difference of the lowest unoccupied and highest occupied Kohn−Sham eigenvalues. The gap is significantly underestimated by DFT-LDA and DFT-GGA. On the contrary, hybrid functionals, with a typical 20−25% contribution of exact exchange, overestimate the anatase band gap.[99]

UV light absorption causes electrons to be excited in the conduction band with holes left in the valence band. The question whether charge carriers in TiO_2 behave as quasi-free electrons and holes or whether they are coupled to the lattice polarization to form polarons was debated at length.

The polaronic nature of the electron–hole couple (exciton) was demonstrated using the hybrid B3LYP functional in a bulk anatase supercell (96-atoms), by atomic relaxation of the triplet exciton.[100] The triplet exciton is highly localized on next neighboring sites, inducing a structural reorganization with an energy gain associated with this process of 0.6 eV. The computed photoluminescence (PL) of 2.6 eV satisfactorily agrees with the experimental one.

Electron polarons are usually identified as Ti^{3+} species, where the electron is trapped on a single Ti site, causing a local elongation of Ti–O bonds. Introduction of extra electrons in bulk anatase cannot be easily computed, as it is dependent on the method employed. Using B3LYP functional, 76% of the electron is localized on a single Ti site and the rest is mainly confined within a sphere of 6 Å in radius.[100] The electron trapping energy is computed to be 0.23 eV, suggesting that the electron is weakly bound to the bulk anatase lattice.

Concerning electron transport, the activation barrier for polaron hopping from one site to the other has been evaluated to be ~0.3 eV using DFT+U calculations.[101]

Self-trapping of the hole can be described by hybrid functionals,[100] the energy gain associated to hole trapping is computed to be 0.74 eV. The hole is found to be highly localized on an O_{3c} atom (85%) and its midgap state is deeper than that of the electron. The calculated values of the EPR hyperfine coupling constants with ^{17}O for the trapped hole are in fair agreement with the experiments.[102] Concerning hole transport, hopping barriers along different directions have been estimated to fall between 0.5 and 0.6 eV by DFT+U.[103]

1.3.2 Flat TiO_2 surface: slab model

The surface energies are essential in determine the thermodynamic, structural, and chemical properties of TiO_2 material, determining the relative stabilities and the crystal shape of different structures. Therefore, the surface energies are essential to understand the phase stability of different TiO_2 polymorphs.

The surface reactivity is related to the surface energies, generally low surface energy corresponds to a low reactivity.

First-principles calculations of the energetics of anatase surfaces have been reported by several groups.[104, 105, 106, 107, 108] The surfaces are usually modeled as slabs of finite thickness with periodic boundary conditions in the surface plane, and surface energies are determined from the difference between the total energy of the slab and the total energy of an equal number of TiO_2 units in the bulk phase, divided by the total exposed area. By hybrid functional B3LYP calculations on relaxed surface models, the relative energies follow the sequence (101) < (100) < (001) < (110), which can be related to the density of undercoordinated Ti surface atoms on different surfaces.[96] However, relaxation has a major effect on the surface energetics, and it can reduce the surface energy by more than 50%.

Once the surface energies are known, the equilibrium shape of a macroscopic crystal can be determined via the Wulff construction. The computed Wulff shape for anatase is shown in **Figure 1-20**. As typically found for natural samples, it consists of a truncated tetragonal bipyramid exposing majority (101) and minority (001) facets.

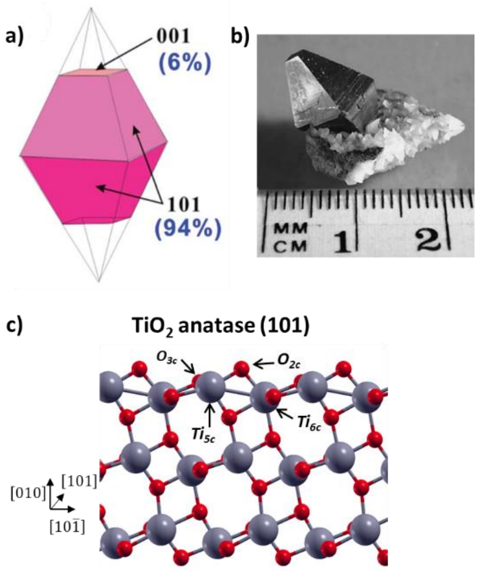

Figure 1-20 a) The equilibrium shape of a TiO_2 crystal in the anatase phase, according to the Wulff construction. Reprinted with permission from ref. 109. (b) Picture of an anatase mineral crystal. Reprinted with permission from ref. 4. (c) Ball-and-sticks representation of the (101) anatase surfaces. The coordination patterns of the exposed superficial atoms are indicated.

From LEED experiments,[110] it is known that the clean anatase (101) has the same (1 × 1) periodicity as the bulk-terminated surface, consistent with the low formation energy of this surface. **Figure 1-20** c shows the characteristic sawtooth profile of anatase (101) viewed along the [010] direction. The surface exposes both 5-fold (Ti_{5c}) and 6-fold (Ti_{6c}) coordinated Ti atoms, as well as 2-fold (O_{2c}) and 3-fold (O_{3c}) oxygens. The surface atoms undergo significant displacements from the ideal bulk-like positions upon relaxation.[96, 104, 105, 107]

In particular, Ti–O bonds between Ti and O_{2c} atoms are ~5–10% shorter than in the bulk, resulting in a rather rigid relaxed surface.

1.3.3 Anatase TiO_2 nanoparticles

Nanoparticles have gained considerable attention due to their unique properties not found in their bulk counterparts, which include high surface-to-volume ratio and high surface energy. Since most photochemical reactions mediated by TiO_2 are initiated by surface adsorption of a chemical species on TiO_2, the high surface exposure ensures an overall high density of reactive centres.

New physical and chemical properties occur when the size of the material becomes smaller and smaller, down to the manometer scale. Properties also vary as the shapes of nanomaterials change. Among the unique properties of nanomaterials, the motions of electrons and holes in semiconductor nanomaterials are governed mainly by the quantum confinement, and the transport properties related to phonons and photons are affected by the size and geometry of the materials.[111] Understanding the subtle interplay between the size/shape/surface functionalization of these materials is thus essential for further optimization of their technological applications.

Nanocrystals with different sizes have been investigated by Hummer et al. They have studied stoichiometric decahedral $(TiO_2)_n$ models with n up to 272. The models have been preliminary optimized with classical force fields and then relaxed with a standard DFT (PBE) method and a plane-wave basis set. In their work they have quantified the critical role of edges and vertices energies in determining the relative phase stabilities of anatase TiO_2 nanoparticles with respect to the rutile phase. As the particles grow, the bulk contribution in the free energy becomes more important, causing rutile to become stable at larger particle sizes.[112]

Liu et al. constructed truncated bipyramidal of TiO_2 anatase $(TiO_2)_n$ nanoparticles with different sizes (n = 58–449). They employed DFT calculations combined with a periodic continuum solvation model in order to compute the electronic structure of nanoparticles in aqueous solution.[113]

Nunzi et al. [114, 115] used differently sized models of anatase nanocrystals, i.e. (TiO_2)n (n = 161–918). First, geometrical optimizations with an approximate-DFT method (SCC-DFTB) were carried out, and then, single-point electronic structure calculations were performed using standard DFT methods with a plane wave basis set and hybrid DFT with localized basis functions. They have carried out an accurate computational analysis on the nature and distribution of electronic trap states in anatase TiO_2 structures, investigating the effect of the morphology on the electronic structure.

Regarding the spherical TiO_2 nanoparticles, only few theoretical works have been reported in literature, although TiO_2 nanoparticles are commonly synthesized and studied for many applications.[11] Naicker et al. performed molecular dynamics simulations of spherical anatase TiO_2 nanoparticles with a size in the range between 2 and 6 nm. No phase transformation was observed during the simulation time (3 ns), even though very high temperature (2000 K) has been explored. Interestingly, four-fold and five-fold coordinated Ti atoms on the surface showed shorter Ti–O bonds with respect to fully coordinated Ti atoms.[116]

Only recently first-principles DFT approaches have been employed to study realistic TiO_2 nanoparticle of ~3 nm size, made of several hundred TiO_2 units.[114, 117, 118]

In our group, TiO_2 spherical nanoparticles of different sizes (from 300 to 4000 atoms) were developed with a two-scale computational approach (**Figure 1-21**). Global optimization to obtain stable and equilibrated nanoparticles was performed with a self-consistent charge density functional tight-binding (SCC-DFTB) simulated annealing process, causing a considerable atomic rearrangement within the nanoparticles. Those SCC-DFTB relaxed structures were then optimized at the DFT(B3LYP) level of theory. They presented a systematic and comparative SCC-DFTB vs DFT(B3LYP) study of the structural properties, with particular emphasis on the surface-to-bulk sites ratio, coordination distribution of surface sites, and surface energy. From the electronic point of view, analysing the total and projected density of states, they compared HOMO–LUMO with Kohn-Sham gaps. Overall, the comparisons between DFTB and hybrid density functional theory show that DFTB provides a rather accurate geometrical and electronic description of these nanoparticles of realistic size (up to a diameter of 4.4 nm) at an extremely reduced computational cost.[118]

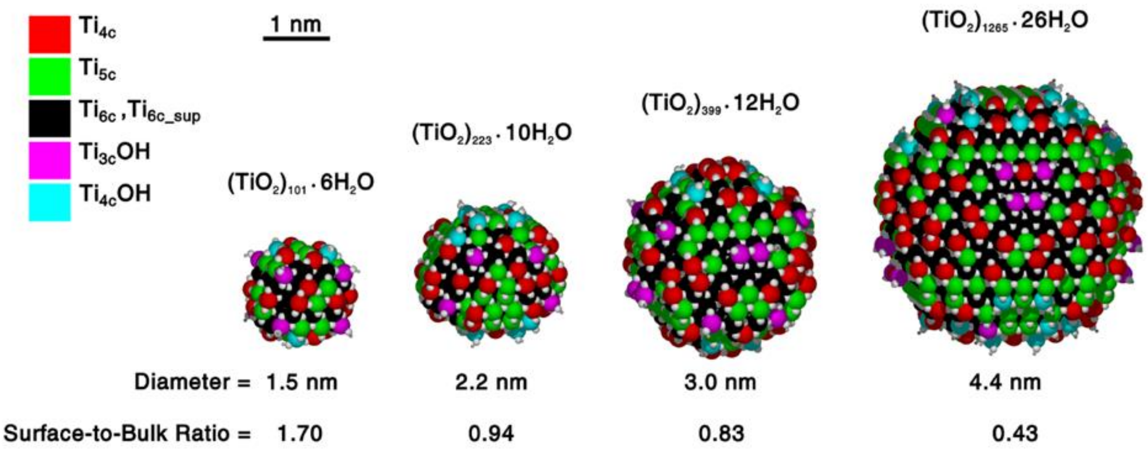

Figure 1-21 DFT(B3LYP) optimized structures, after simulated annealing, of the different nanoparticles. For each one, the stoichiometry, the approximate diameter, the surface-to-bulk ratio, and the position of the Ti atoms with different coordination are reported. Reprinted with permission from ref.118.

1.4 Outline of the PhD thesis

The atomistic understanding, through quantum chemical simulations, enables to predict the properties of complex systems, like a hybrid material composed by joining together two different components. The work aims at studying the interfaces between the semiconductive oxide TiO_2 and carbon-based monolayers. The latter is inorganic, i.e. graphene, or organic, such as a densely packed monolayer of organic molecules (DOPAC or TETT).

In this study, we employed state of the art computational methods and massively parallelized codes in order to perform highly accurate calculations of such extensive system in a reasonable time. Most calculations were based on density functional theory (DFT), using hybrid functionals and localized basis sets, which is a well-suited approach for the description of titanium dioxide. An approximate-DFT method, namely the self-consistent charge density-functional tight-binding (SCC-DFTB), was considered for the study of the largest systems and for the dynamical behaviour of the TiO_2 nanomaterial completely covered with the organic molecules. The theoretical methodologies employed in this work are discussed in Chapter 2.

The first part of the work was devoted to study the interface between graphene and the TiO_2 anatase (101) surface, considering even non ideal conditions, due to the presence of defects. In particular, we investigated the structural and electronic properties of the hybrid composite. Then, as a next step, we considered the reactivity of water at the interface of the two components, in order to define the possible reaction paths as discussed in Chapter 3.
Subsequently, we focused our attention on the photoresponsive properties of TiO_2 anatase. Consequently, starting from the realistic model of a TiO_2 spherical nanoparticle, developed in our group, we systemically investigated the adsorption modes of the catechol derivatives (DOPAC) at low coverage, considering the competition with water, as reported in Chapter 4. We identified the new molecular states in the band gap introduced by the adsorbed molecules and analysed the electronic charge-transfer. On top of that, we photoexcited the system with visible light and we modelled the possible life path of the photogenerated electron and hole: exciton formation, trapping, charge carrier diffusion, or recombination. As a further step, we considered a growing molecular layer on the nanoparticle and analysed the self-assembling mechanism and the effects on the electronic properties of the complex. Once we fully covered the nanoparticle surface, we performed molecular dynamics run at 300 K, in order to analyse the effect of the thermal treatment on the geometrical configuration. Further we want to understand if the molecule/surface or molecule/molecule interactions dominate in the model.

Finally, in the last part of the study, we functionalized the TiO_2 nanoparticle with organosilane molecules (TETT). First, we had to set the parameters for the efficient SCC-DFTB method to accurately describe the inorganic\organic interface. We compared the reliability of the SCC-DFTB results with DFT, as discussed in Chapter 5. Once we have defined the approach, we completely passivated the TiO_2 nanoparticle with the TETT molecules and investigated how they are adsorbed on the nanoparticle surface and how they interact in the dense monolayer. The configurational space of the complex nanoconjugate was sampled by means of several molecular dynamics runs at 300 K, and the conducted statistics allowed us to analyse how the molecules rearrange due to thermal treatment.

Chapter 2 Theoretical background

In this chapter, some fundamental aspects of electron structure theory will be introduced. We will start to present the foundation of the density functional theory (DFT) and its approximation in the density functional tight-binding (DFTB) method. Moreover, the conformational sampling by molecular dynamics (MD) will be presented.

2.1 The Schrödinger equation

A system consisting of interacting nuclei and electrons can be determined by the many-body wavefunction Ψ, which depends on the position of each electrons and each nucleus in the system. In the case on N electrons with coordinates $\mathbf{r}_1$, $\mathbf{r}_2$, …, $\mathbf{r}_N$ and M nuclei with coordinates $\mathbf{R}_1$, $\mathbf{R}_2$, … , $\mathbf{R}_M$ we have:

$$\Psi = \Psi\,(\mathbf{r}_1, \mathbf{r}_2, \dots, \mathbf{r}_\mathrm{N};\ \mathbf{R}_1, \mathbf{R}_2, \dots, \mathbf{R}_\mathrm{M}) \tag{2.1}$$

Applying the Hamiltonian operator to Ψ , we obtain the many-body Schrödinger equation:

$$\left[\begin{array}{c} -\sum_i \frac{\hbar^2}{2m_e}\nabla_i^2 - \sum_i \frac{\hbar^2}{2M_I}\nabla_I^2 + \frac{1}{2}\sum_{i\neq j}\frac{e^2}{4\pi\varepsilon_0}\frac{1}{\left|\mathbf{r}_i - \mathbf{r}_j\right|} \\ + \frac{1}{2}\sum_{I\neq J}\frac{e^2}{4\pi\varepsilon_0}\frac{Z_I Z_J}{\left|\mathbf{R}_I - \mathbf{R}_J\right|} - \sum_{i,I}\frac{e^2}{4\pi\varepsilon_0}\frac{Z_I}{\left|\mathbf{r}_i - \mathbf{R}_j\right|} \end{array} \right] \Psi = E_{tot}\Psi \tag{2.2}$$

The first and the second terms in eq. (2.2) are the kinetic energy of the N electrons and the M nuclei, respectively.

Regarding the potential energy terms, we can count all the possible pairs of charges in the system. We have the Coulomb repulsion between electron pairs (third term in eq. (2.2)), here the terms $i = j$ are excluded because an electron does not repel itself, and it is divided by 2 in order to count only one contribution per pair. Then, the fourth term in eq. (2.2) is Coulomb repulsion between pairs of nuclei, where Z_I and Z_J are the atomic numbers. And lastly, the Coulomb attraction between the electrons and nuclei (fifth term in eq. (2.2)).

Equation eq. (2.2) is almost everything that we need to know to study the materials at equilibrium. If we were to be rigorous, then we would include the time dependence, the interaction with external electromagnetic fields, and some corrections arising from the theory of relativity. However, despite the approximations introduced in eq. (2.2) the solution even for simplest systems (e.g. small molecules) is very challenging, and in most cases, it is still practically impossible. As a result, nowadays exists a hierarchy of approximations to eq.(2.2) which allows us to study materials at the atomistic level with different degrees of accuracy.

Equation (2.2) is rather general since it describes gases, liquids, and solids phases. Therefore, it is appropriate to restrict the range of possibilities and consider molecules and solids. While in the study of liquids and gases the nuclei can travel long distances, in the case of molecules adsorbed on solid surfaces the nuclei typically remain at near certain positions. Consequently, as a starting point, we can assume that the nuclei are in known positions. Since the nuclei are heavy compared to the electrons, we can set $M_I = \infty$ in eq. (2.2). Thus, we can neglect the kinetic energy of the nuclei, and that the Coulomb repulsion between them is simply a constant. For convenience, we bring the constant term to the right-hand side of eq. (2.2) by defining:

$$E = E_{tot} - \frac{1}{2} \sum_{I \neq J} \frac{e^2}{4\pi\varepsilon_0} \frac{Z_I Z_J}{|\mathbf{R}_I - \mathbf{R}_J|} \tag{2.3}$$

In the Born-Oppenheimer approximation the nuclear coordinates, R_I, are an external parameter, and Ψ is a function of the electron coordinates while ignoring its dependence on the nuclear coordinates: $\Psi = \Psi\,(\mathbf{r}_1, \mathbf{r}_2, \dots, \mathbf{r}_\mathrm{N})$. If we define the Coulomb potential of the nuclei experienced by the electrons as:

$$V_n(\mathbf{r}) = -\sum_I \frac{e^2}{4\pi\varepsilon_0} \frac{Z_I}{|\boldsymbol{r} - \boldsymbol{R}_j|} \tag{2.4}$$

eq.(2.2) becomes:

$$\left[-\sum_i \frac{\hbar^2}{2m_e}\nabla_i^2 + \sum_i V_n(\mathbf{r}_i) + \frac{1}{2}\sum_{i \neq j} \frac{e^2}{4\pi\varepsilon_0} \frac{1}{|\mathbf{r}_i - \mathbf{r}_j|}\right] \Psi = E\,\Psi \tag{2.5}$$

Eq. (2.5) is the fundamental equation of electronic structure, but further simplifications are still necessary to solve it.

In order to achieve a considerable simplification of the notation, it is convenient to measure energies in units of E_{Ha}, distances as a_0, the average radius of the electron orbital in the fundamental state of the H atom, and masses in units of the electron mass m_e; accordingly, the many-electron Hamiltonian is:

$$\widehat{H}(\mathbf{r}_1, \mathbf{r}_2, \dots, \mathbf{r}_N) = -\sum_i \frac{1}{2}\nabla_i^2 + \sum_i V_n(\mathbf{r}_i) + \frac{1}{2}\sum_{i \neq j} \frac{1}{|\mathbf{r}_i - \mathbf{r}_j|} \tag{2.6}$$

so that the eq.(2.5) can be written using the compact expression:

$$\widehat{H}\,\Psi = E\,\Psi \tag{2.7}$$

In addition, it is possible to define the single-electron Hamiltonian:

$$\widehat{H}_0(\boldsymbol{r}) = -\frac{1}{2}\,\nabla^2 + V_n(\boldsymbol{r}) \tag{2.8}$$

in a way that we can split the many-electron Hamiltonian as follows:

$$\widehat{H}(\mathbf{r}_1, \mathbf{r}_2, \dots, \mathbf{r}_N) = \sum_i \widehat{H}_0(\mathbf{r}_i) + \frac{1}{2}\sum_{i \neq j} \frac{1}{|\mathbf{r}_i - \mathbf{r}_j|} \tag{2.9}$$

If the electrons would not ‘see’ each other, we are allowed to eliminate from the eq.(2.5) the term describing the Coulomb repulsion between electrons. This dramatic simplification of the problem is called the independent electrons approximation. Using eq. (2.7) and (2.9) the Schrödinger equation becomes:

$$\sum_i \widehat{H}_0(\mathbf{r}_i)\,\Psi = E\,\Psi \tag{2.10}$$

Since the electrons are now independent, it is possible to write the solution of eq. (2.10) as a product:

$$\Psi = \Psi\,(\mathbf{r}_1, \mathbf{r}_2, \dots, \mathbf{r}_\mathrm{N}) = \phi_1(\mathbf{r}_1) \dots \phi_N(\mathbf{r}_N) \tag{2.11}$$

Suppose now that the wavefunctions, ϕ_1, were obtained as the solutions of the single electron Schrödinger equations:

$$\widehat{H}_0(\mathbf{r})\phi_i(\mathbf{r}) = \varepsilon_i\phi_i(\mathbf{r}) \tag{2.12}$$

with ε_1 the smallest eigenvalue and $\varepsilon_1 < \varepsilon_2 < \dots < \varepsilon_N$.

Therefore, replacing the trial solution of eq. (2.11) in eq. (2.12) we find:

$$E = \varepsilon_1 + \varepsilon_2 + \cdots + \varepsilon_N \tag{2.13}$$

the lowest-energy configuration of the system is obtained when we fill the lowest-energy eigenstates of the single-particle equation (2.12) with one electron in each state, starting from the lowest eigenvalue.

The independent electrons approximation as written in eq. (2.11) carries two important drawbacks. The first relates to the fact that the wavefunction, does not obey Pauli's exclusion principle. The second problem is that the Coulomb term eliminated from eq. (2.5) is of the same magnitude as the other terms, and therefore it cannot be ignored.

Slater pointed out that wavefunctions written as a Slater determinant (eq. (2.14)) satisfy the anti-symmetry requirement of the many-body wavefunction (Pauli's exclusion principle).

$$\Psi\,(r_1, r_2) = \frac{1}{\sqrt{2}}\begin{vmatrix} \phi_1(r_1) & \phi_1(r_2) \\ \phi_2(r_1) & \phi_2(r_2) \end{vmatrix} \tag{2.14}$$

Respect to eq. (2.11) the motion of electrons with the same spin is now correlated, but the motion of electrons with opposite spin is still not correlated.

2.2 The Hartree approximation

In Section 2.1 we mentioned that the approximation of ignoring the Coulomb repulsion between electrons in the many-body Schrödinger equation is too drastic. However, based on classical electrostatic consideration, the Coulomb repulsion between electrons can be re-introduced while assuming independent electrons.

Distribution of electron charge density is obtained by adding up the probabilities of finding electrons in each occupied state i:

$$n(\boldsymbol{r}) = \sum_i [\phi_i(\mathbf{r})]^2 \tag{2.15}$$

Consequently, the electronic charge distribution, $n(\boldsymbol{r})$ in eq. (2.15), will generate an electrostatic potential $V_\mathrm{H}(\mathbf{r})$ called Hartree potential:

$$\nabla^2 V_\mathrm{H}(\mathbf{r}) = -\,4\,\pi\,n(\mathbf{r}) \tag{2.16}$$

with the following solution:

$$V_\mathrm{H}(\mathbf{r}) = \int dr' \frac{n(\mathbf{r}')}{|\mathbf{r} - \mathbf{r}'\,|} \tag{2.17}$$

in which each electron in the system experiences the mean-field ‘average potential’ of the other electrons. The Hartree potential $V_\mathrm{H}(\mathbf{r})$ can be included in eq. (2.12):

$$\left[-\frac{\nabla^2}{2} + V_n(\boldsymbol{r}) + V_\mathrm{H}(\mathbf{r})\right]\phi_i(\mathbf{r}) = \varepsilon_i\phi_i(\mathbf{r}) \tag{2.18}$$

The equations (2.15), (2.16), and (2.18) must be solved simultaneously, and for this reason the approach is called self-consistent field method. The equations introduced by Hartree eq. (2.15), (2.16), and (2.18) represent a major simplification of our initial task of solving the complete many-body Schrödinger equation eq. (2.5), since one differential equation in 3N dimensions has been replaced by N three-dimensional equations.

In order to be more accurate, it is necessary to add to the equations (2.18) the exchange potential and the correlation potential.

2.3 The Hartree-Fock equations

Let us consider the quantum state Ψ with the lowest energy. The energy, E, of this state is obtained by multiplying both sides of eq. (2.7) by $\Psi^*$and integrating over all the variables:

$$E = \int dr_1 \dots dr_N \, \Psi \, \hat{H} \, \Psi^* \tag{2.19}$$

if we minimize the energy E with respect to variations of the functions $\phi_i(\mathbf{r})$ in the Slater determinant of eq. (2.14), and we require that these functions are orthonormal:

$$\frac{\delta E}{\delta \phi_i^*} = 0 \tag{2.20}$$

$$\int d\mathbf{r} \phi_i^*(\mathbf{r}) \phi_j^*(\mathbf{r}) = \delta_{ij} \tag{2.21}$$

where δ_{ij} is the Kronecker delta and is equal to 1 if $i = j$, 0 if $i \neq j$, then we obtain the Hartree–Fock equations:

$$\left[- \frac{\nabla^2}{2} + V_n(\mathbf{r}) + V_{\mathrm{H}}(\mathbf{r}) \right] \phi_i(\mathbf{r}) + \int d\mathbf{r}' V_x(\mathbf{r}, \mathbf{r}') \, \phi_i(\mathbf{r}') = \varepsilon_i \phi_i(\mathbf{r}) \tag{2.22}$$

An additional potential, V_x, called Fock exchange potential has been introduced with respect to the equation (2.18). The explicit expression of this potential is:

$$V_x(\mathbf{r},\mathbf{r}') = -\sum_j \frac{\phi_j^*(\mathbf{r}')\phi_i(\mathbf{r})}{|\mathbf{r}-\mathbf{r}'|} \tag{2.23}$$

the sum runs over the occupied single-particle states. The $V_x(\mathbf{r},\mathbf{r}')$ is a non-local exchange potential in single-particle equations. Its evaluation involves an integration over the additional variable $\mathbf{r}'$ that complicates enormously the solution of the Hartree–Fock equations. V_x arises from Pauli's exclusion principle and prevents that two electrons occupy the same quantum state.

To summarize the simplification introduced so far (Section 2.1), the independent particle model has been introduced, and the 3N-dimensional many-body Schrödinger equation has been transformed into N three-dimensional equations. In Section 2.2, the Coulomb repulsion between electrons has been considered using classical electrostatics. In Section 2.3 the exchange interaction (V_x) has been added in order to take into account the quantum nature of the electrons. So, the Hartree-Fock energy is:

$$E^{HF} = T + E_{V_n} + E_H + E_x + E_{ii} \tag{2.24}$$

The first term in eq. (2.24) is the kinetic energy (T), and the second term is the expectation value of the external potential V_n. The third term is the Hartee energy (E_H), followed by the energy involving the exchange operator (E_x), and finally the repulsion between the nuclei (E_{ii}). The only remaining element left out of the picture is the correlation between electrons. Owing to the Coulomb repulsion, the probability of finding an electron somewhere will decrease if there is another electron nearby. Therefore, it is possible to add in the single-particle equations an additional potential $V_c(r)$, where 'c' stands for correlation.

The exact correlation energy (E_c) is defined in terms of the exact energy (E_{exact}) and the Hartree-Fock energy (E_{HF}) by

$$E_c = E_{exact} - E_{HF} \tag{2.25}$$

In section 2.4, we will present the density functional theory, which is an independent particle approach that incorporates the effect of interactions and correlation among the particles.

2.4 The density functional theory

The density functional theory provides how to link rigorously the single-particle wavefunctions, ϕ_i, with the many-body wavefunction, Ψ, and how to determine the total E energy of the system.

The core concept of density functional theory is the observation that, if E is the lowest possible energy of the system, i.e., the energy of the ground state, then E is a functional of the electron density only:

$$E = F[n] \tag{2.26}$$

This observation is remarkable because the electron density $n(\mathbf{r})$ only depends on three variables, instead of three spatial and one spin coordinate for each N electron.

2.4.1 The Hohenberg–Kohn theorems

Quoting directly the Hohenberg-Kohn paper, the theorem statement that:

"The external potential $V_n(\mathbf{r})$ is (within a constant) a unique functional of $n(\mathbf{r})$; since $V_n(\mathbf{r})$ fixes $\hat{H}$ we see that the full many particles ground state is a unique functional of $n(\mathbf{r})$".

The statement can be demonstrated by reductio ad absurdum. Starting from the assumption that the same ground-state electron density can be obtained from two different external potentials, we will be obtained that this leads to a contradiction.

In order to outline the proof, it is helpful to introduce the kinetic energy and the Coulomb energy as:

$$\hat{T} = -\sum_i \frac{1}{2}\nabla_i^2 , \qquad \hat{W} = \frac{1}{2}\sum_{i\neq j} \frac{1}{|\mathbf{r}_i - \mathbf{r}_j|} \tag{2.27}$$

Introducing $\hat{T}$ and $\widehat{W}$ in the equation (2.19) the total energy become:

$$E = \langle \Psi \left| \sum_i V_n(\mathbf{r}_i) \right| \Psi \rangle + \langle \Psi | \hat{T} + \widehat{W} | \Psi \rangle \tag{2.28}$$

Using the electron density, the first term in eq. (2.28) can be written as:

$$E = \int d\mathbf{r}\, n(\mathbf{r})\, V_n(\mathbf{r}) + \langle \Psi | \hat{T} + \widehat{W} | \Psi \rangle \tag{2.29}$$

Let us assume that Ψ is the ground-state wavefunction for the potential V_n, with energy E and density n. Suppose there exists another potential, $V_n' \neq V_n$, which generates the same density n , and let us call $\widehat{H}'$, Ψ' and E' the Hamiltonian, the ground-state wavefunction, and the ground-state energy corresponding to this new potential, respectively. Since Ψ is not the ground state of V_n' we can write:

$$\langle \Psi | \widehat{H}' | \Psi \rangle > E' \tag{2.30}$$

The expectation value on the left-hand side can be decomposed into contributions from the kinetic energy, the Coulomb repulsion, and the external potential, in analogy with eq. (2.29):

$$\langle \Psi | \hat{T} + \widehat{W} | \Psi \rangle + \int d\mathbf{r}\, n(\mathbf{r})\, V_n'(\mathbf{r}) > E' \tag{2.31}$$

If we now combined the eq. (2.29) and (2.31) we obtain:

$$E - E' > \int d\mathbf{r}\, n(\mathbf{r}) [V_n(\mathbf{r}) - V_n'(\mathbf{r})] \tag{2.32}$$

Since we did not make any assumptions about the external potentials, we can repeat the entire reasoning by merely starting from V_n instead of V_n' in eq. (2.30). In this case, we would find:

$$E' - E > \int d\mathbf{r}\, n(\mathbf{r}) [V_n'(\mathbf{r}) - V_n(\mathbf{r})] \tag{2.33}$$

By adding the eq. (2.32) and eq. (2.33) we obtain 0 > 0, this is a contradiction. Therefore, the premise that two different potentials, $V_n' \neq V_n$, lead to the same ground-state density, n, must be false.

The second theorem of Hohenberg-Kohn establishes that the energy of the ground state is the lowest possible energy of the system, and all other states are higher in energy. It is called the 'Hohenberg–Kohn variational principle' and can be expressed as:

$$\left.\frac{\delta F[n]}{\delta n}\right|_{n_0} = 0 \tag{2.34}$$

This property is analogous to the variational principle that led us to write the Hartree–Fock equations in section 2.3.

2.4.2 The Kohn-Sham equations

The Hohenberg-Kohn theorems do not say anything about how to construct such functional; moreover, the exact form of this functional is still unknown.

By comparing eq. (2.26) and (2.29) the functional can be rewritten as follows:

$$F[n] = \int d\mathbf{r}\, n(\mathbf{r})\, V_n(\mathbf{r}) + \langle \Psi[n] | \hat{T} + \hat{W} | \Psi[n] \rangle \tag{2.35}$$

the first term in the functional depends explicitly on the density, $n(\mathbf{r})$, while for the kinetic energy and the Coulomb energy the dependence on the density is implicit. The idea of Kohn and Sham was to split these implicit therms into the kinetic and Coulomb energy of independent electron, as in eq. (2.18), plus an extra term E_{xc}:

$$\begin{aligned} E &= F[n] \\ &= \overbrace{\underbrace{\int d\mathbf{r}\, n(\mathbf{r})\, V_n(\mathbf{r})}_{\textit{External potential}} - \underbrace{\sum_i \int d\mathbf{r}\, \phi_i^*(\mathbf{r}) \frac{\nabla^2}{2}\, \phi_i(\mathbf{r})}_{\textit{Kinetic energy}} + \underbrace{\frac{1}{2} \iint dr\, dr' \frac{n(r)n(r')}{|\mathbf{r} - \mathbf{r}'|}}_{\textit{Hartree energy}}}^{\textit{The total energy in the independent electron approximation}} \end{aligned} \tag{2.36}$$

$$+\underbrace{E_{xc}[n]}_{XC\ energy}$$

The extra term E_{xc} contains what is left out, hiding all the difficult many-body effects, and it is called the exchange and correlation energy. The functional of the density, $F[n]$, in eq. (2.36) include the sum of known contributions taken from the independent electrons approximation, and unknown contribution, the exchange and correlation energy. If we knew the exchange and correlation energy, $E_{xc}[n]$, then we could calculate the total energy of the system in its ground state, $E = F[n]$, using the electron density. The remaining question is therefore how to determine the electron density. For the second theorem turns out that the ground-state density, n_0, is precisely the function that minimizes the total energy, $E = F[n]$. Hence, the functional derivative must be zero in order to lead an equation for the wavefunctions, $\phi_i(\mathbf{r})$, which can be used to construct the density, as in eq. (2.15). Subsequently, if we require these wavefunctions to be orthonormal (i.e., to satisfy eq. (2.21) then the Hohenberg–Kohn variational principle leads to:

$$\left[-\frac{\nabla^2}{2}+V_n(\mathbf{r})+V_{\mathrm{H}}(\mathbf{r})+V_{xc}(\mathbf{r})\right]\phi_i(\mathbf{r}) = \varepsilon_i\phi_i(\mathbf{r}) \tag{2.37}$$

where the external nuclear potential, V_n, the Hartree potential, V_{H}, and the kinetic energy, $-\frac{\nabla^2}{2}$, are identical to those in eq. (2.18). The extra term, V_{xc}, is given by:

$$V_{xc}(\mathbf{r}) = \left.\frac{\delta E_{xc}[n]}{\delta n}\right|_{n(\mathbf{r})} \tag{2.38}$$

and it is called the exchange and correlation potential. The set of equations given by eq. (2.37) are called Kohn–Sham equations and they form the basis of the Kohn–Sham theory. This set of equations constitutes a powerful tool for calculating many properties of materials starting from the first principles of quantum mechanics. We know that there must be a functional $E_{xc}[n]$ which gives the exact ground-state energy and density using the equations (2.37) and (2.38);

however, we do not know the expression of this functional. Therefore, the issue is to approximate $E_{xc}[n]$.

The Hartree functional in eq. (2.37) gives non-vanishing repulsion energy even for a system with only one electron, and it generates a spurious self-interaction energy. In the Hartree-Fock theory, this effect is automatically canceled in V_x eq. (2.23), but the same is not valid in the Kohn-Sham scheme, where any correction must be incorporated into the $V_{xc}[n]$, which will be discussed in section 2.4.3.

2.4.3 The exchange-correlation functionals

The E_{xc} functional must account not only for the self-interaction correction but also for the electronic correlation energies. Several approximated exchange and correlation functionals have been developed during the years, which will be presented in sections 2.4.3.1 and 2.4.3.2.

2.4.3.1 Local density approximation and generalized gradient approximation

The first successfully E_{xc} scheme in DFT was the Local Density Approximation (LDA). The idea considers that the electrons of a given system can be treated as homogeneous electron gas. The model also assumes that the E_{xc} functional can be separated into two independent terms, one for the exchange and one for the correlation energies, respectively:

$$V_{xc}[n(\mathbf{r})] = V_x[n(\mathbf{r})] + V_c[n(\mathbf{r})] \tag{2.39}$$

So that the E_{xc} is:

$$E_{xc}^{LDA} = \int n(\mathbf{r})\, V_x[n(\mathbf{r})]dr + \int n(\mathbf{r})\, V_c[n(\mathbf{r})]dr \tag{2.40}$$

For a homogeneous electron gas, the form of the exchange energy can be computed exactly:

$$E_x = -\frac{3}{4}\left(\frac{3}{\pi}\right)^{\frac{1}{3}} n^{\frac{4}{3}}\, V \tag{2.41}$$

where n in eq. (2.41) is the electron density defined as the total number of electrons divided by the volume V in which they are contained. In contrast to the exchange energy, for the correlation energy of the electron gas, we do not have a simple analytic expression such as eq. (2.41). Nevertheless, it has been possible to calculate the correlation energy for this simple model by directly solving the many-particle Schrödinger equation using stochastic numerical methods. The correlation energy of the electron gas can be extracted from the data of Ceperley et. al[119] by removing the known kinetic, Hartree and exchange contributions from the calculated total energies.

Many first-principles calculations on materials use more elaborate exchange and correlation functionals which also take into account the slopes of the electron density,[120] namely the Generalized Gradient Approximation (GGA):

$$E_{xc}^{GGA} = \int F_{xc}\,[n(\mathbf{r}), \nabla n(\mathbf{r})]dr \tag{2.42}$$

However, there is no systematic and straightforward way to improve exchange and correlation functionals (XC). For this reason, the development of exchange and correlation XC functionals constitutes a research field in its own right.

2.4.3.2 Hybrid functionals

One limitation of the LDA/GGA functionals is their inability of predicting correct band gap energies (E_g) in semiconductors and isolators, which are systematically underestimated in DFT calculations. This limitation is particularly important in the context of this work since the TiO_2 band gap is not well reproduced by LDA/GGA functionals. Experimentally, the TiO_2 E_g is 3.4 eV,[121] whereas PBE predicts 2.36 eV.[122] The inaccuracy is intrinsic to the DFT formalism itself. Despite that, it is consensual that the problem comes from the use of approximated XC functionals.

Band structures calculated through the GW method, where the many-body problem is handled via the Green Functions formalism, describe accurately the TiO_2 band gap (3.83 eV),[123] but such calculations are still too demanding to be applied even to modest size models. One widely used alternative to overcome the DFT limitation in predicting the band gap energy is to mix some amount of Hartree-Fock exchange into the LDA/GGA-XC functional; thereby producing a hybrid functional. The success of hybrid functionals in correcting the band gap values is often attributed to the fact that the HF exchange is an exact functional.[120] However, the HF Exchange, opposing the LDA/GGA, inducing over-localized electronic states. So, a proper balance between LDA/GGA and HF amount in the hybrid XC functional may lead to a useful cancelation of errors; and to correct band gap energies. The hybrid functional has the following expression:

$$E_{xc}^{hyb} = E_{xc}^{hyb} + \lambda(E_x^{HF} - E_x^{GGA}) \tag{2.43}$$

where λ is the fraction of HF exchange taken into account. One of the most popular hybrids functional is the B3LYP,[124,125,126] whose functional form is:

$$E_{xc}^{B3LYP} = (1-\alpha)E_{xc}^{LDA} + aE_x^{HF} + bE_x^{B88} + cE_c^{LYP} + (1-c)\,E_c^{LDA} \tag{2.44}$$

where E_x^{B88} is a GGA exchange functional and a, b and c are empirical parameters fitted to reproduce thermodynamic data, such as atomization and ionization potentials, proton affinities, and total atomic energies. This fitting procedure resulted in a = 0.20, b = 0.72 and c = 0.81. Although this functional was initially developed to investigate the electronic structure of molecules, it showed surprisingly good performances in many other chemical applications, including transition-metal chemistry and condensed-phase systems.

2.4.4 The DFT limitations

Today the combination of DFT with high-performance computing provides us with a powerful tool for understanding and predicting material properties starting from the first principles of quantum mechanics. Despite the success and widespread use of DFT, it is important to bear in mind that it addresses the electronic ground state of materials. Stated in other words, DFT is not designed to describe electronic excitations and non-equilibrium phenomena. However, in Chapter 4 we have computed the excited state energies as an open-shell triplet (T1) spin configurations. We can correctly calculate by DFT the triplet configuration because it is the lowest energy state for the corresponding spin multiplicities. Moreover, for many insulators and large gap semiconductors, including TiO_2 anatase, the triplet exciton state is the lowest excited state (**Figure 4-7**) and has a longer lifetime than the higher energy singlet exciton (S1).[127]

A general drawback of all common GGA functionals, including hybrids, is that they cannot describe long-range electron correlations that are responsible for van der Waals forces. The dispersive interactions play an important role in the hybrid interfaces investigated in this work. For example, they control the assembly of the graphene or a densely packed monolayer of molecules on the TiO_2 surface.

Grimme has developed an approach to include dispersion forces by correcting total energies and gradients. This correction can be applied to both DFT theory (Chapter 3, Chapter 4) and DFTB method (Chapter 4, Chapter 5).

2.5 Density functional based tight-binding method

Density-functional theory within the formulation by Kohn & Sham (DFT-KS) is a powerful method for the calculation of physical and chemical properties of molecules and condensed matter systems.

Although the DFT-KS scheme allows studying systems with remarkable size, there is demand for even faster but approximate methods to reach much larger system sizes and extended time scales in molecular dynamics simulations. Classical force field methods (molecular mechanics, MM), on the other hand, are several orders of magnitude faster than DFT, allowing to treat even millions of atoms and to follow their dynamics beyond the nanosecond time scale. Such classical force fields contain a large number of empirical parameters and do not consider quantum effects.

Semi-empirical (SE) quantum chemical methods are located in the middle between DFT and MM methods, being three orders of magnitude faster than DFT and slower than MM. The number of parameters in the SE methods is greater than in DFT, but significantly less compared to MM. These parameters require a reasonable effort in their determination, but most importantly, the SE methods can describe nearly all quantum effects accessible by DFT.

The semi-empirical tight-binding (TB) methods represent the counterpart to the SE quantum-chemical methods in the condensed phase with similar limitations. It was shown that a ‘TB’ scheme, i.e. the application of limited atomic orbital (AO) basis-set representation, can be used as the basis for an approximate treatment within the KS-DFT. These ideas have been further developed in the density-functional theory-based tight-binding (DFTB) method, which combines the computational efficiency of the semi-empirical quantum chemical methods to ‘TB’ methods; however, its parametrization is less empirical because it is related to a number of DFT calculations. Therefore, electron correlation in DFTB is included from the beginning owing to its descent from DFT. In the subsequent sections, the details of the self-consistent charge density functional tight-binding method (SCC-DFTB) will be discussed.

2.5.1 Approximated density-functional theory

The total energy of a system within DFT as reported in eq. (2.36) is the sum over occupied Kohn-Sham eigenstates (T + $E_{V_n} + E_H$), the exchange-correlation contribution (E_{xc}), and the nuclear repulsion (E_{ii}):

$$E^{DFT} = T + E_{V_n} + E_H + E_{xc} + E_{ii} \tag{2.45}$$

The idea of DFTB is to express the total energy as follow:

$$E^{DFT} \approx E^{DFTB} = E^{DFTB}_{Elec.} + E_{rep} \tag{2.46}$$

by assuming that the total energy of the system can be express as the sum of the eigenvalues ($E^{DFTB}_{Elec.}$) and the repulsive potential (E_{rep}), as in the tight-binding.

The derivation of the SCC-DFTB method starts by separating the electronic density n in eq. (2.36) in two terms: the references density n_0 chosen to be the superposition of the neutral-atom densities for all species in the system and the density fluctuation of the system δn:

$$n = n_0 + \delta n \tag{2.47}$$

Foulkes and Haydock[128] proposed to substitute the electronic density $n(\mathbf{r})$ in eq. (2.36) with eq. (2.47) in a way that E_{tot} may be written as follows:

$$\begin{aligned} E_{tot} = & \sum_{i}^{occ} \langle \psi_i \left| -\frac{\nabla^2}{2} + V_n[n_0(\mathbf{r})] + \frac{1}{2}\int \frac{n_0(\mathbf{r}') + \delta n(\mathbf{r}')}{|\mathbf{r} - \mathbf{r}'\,|} dr' \right| \psi_i \rangle \\ & + E_{xc}[n_0(\mathbf{r}) + \delta n(\mathbf{r})] + E_{ii} \end{aligned} \tag{2.48}$$

Then, eq. (2.48) can be rearranged in order to define the zero-order Hamiltonian $\widehat{H}_0$ that depends only on the reference's density $n_0(\mathbf{r})$:

$$\widehat{H}_0 = -\frac{\nabla^2}{2} + V_n[n_0(\mathbf{r})] + \int \frac{n_0(\mathbf{r}')}{|\mathbf{r} - \mathbf{r}'\,|} dr' + V_{xc}[n_0(\mathbf{r})] \tag{2.49}$$

So:

$$\begin{aligned} E_{tot} = & \sum_{i}^{occ} \langle \psi_i | \widehat{H}_0 | \psi_i \rangle - \frac{1}{2}\iint \frac{n_0(\mathbf{r}')\big(n_0(\mathbf{r}) + \delta n(\mathbf{r})\big)}{|\mathbf{r} - \mathbf{r}'\,|} dr dr' \\ & + \frac{1}{2}\iint \frac{\delta n(\mathbf{r}')\big(n_0(\mathbf{r}) + \delta n(\mathbf{r})\big)}{|\mathbf{r} - \mathbf{r}'\,|} dr dr' \\ & - \int V_{xc}[n_0(\mathbf{r})]\big(n_0(\mathbf{r}) + \delta n(\mathbf{r})\big)\, dr + E_{xc}[n_0(\mathbf{r}) + \delta n(\mathbf{r})] \\ & + E_{ii} \end{aligned} \tag{2.50}$$

The terms that depend linearly on $\delta n(\mathbf{r}')$ and $\delta n(\mathbf{r})$ will cancel each other for any $n_0(\mathbf{r})$ and eq. (2.50) becomes:

$$\begin{aligned} E_{tot} = & \sum_{i}^{occ} \langle \psi_i | \widehat{H}_0 | \psi_i \rangle - \frac{1}{2}\iint \frac{n_0(\mathbf{r}') n_0(\mathbf{r})}{|\mathbf{r} - \mathbf{r}'\,|} dr dr' \\ & + \frac{1}{2}\left(\iint \frac{1}{|\mathbf{r} - \mathbf{r}'\,|} dr dr' + \frac{\delta^2 E_{xc}}{\delta n(\mathbf{r}')\delta n(\mathbf{r})}\right) \delta n(\mathbf{r}')\delta n(\mathbf{r}) \\ & - \int V_{xc}[n_0(\mathbf{r})]\, n_0(\mathbf{r})\, dr + E_{xc}[n_0(\mathbf{r})] + E_{ii} \end{aligned} \tag{2.51}$$

At large distances, the second order exchange-correlation term is negligible in eq. (2.51); so that last term can be substituted by a pairwise potential:

$$\frac{1}{2}\left(\iint \frac{1}{|\mathbf{r} - \mathbf{r}'\,|} dr dr' + \frac{\delta^2 E_{xc}}{\delta n(\mathbf{r}')\delta n(\mathbf{r})}\right) \delta n(\mathbf{r}')\delta n(\mathbf{r}) \cong \frac{1}{2} \sum_{\alpha\beta}^{M} \gamma_{\alpha\beta} \Delta q_\alpha \Delta q_\beta \tag{2.52}$$

For $\alpha \neq \beta$, $\gamma_{\alpha\beta}$ is determined from the Coulomb interaction of two spherical charge distributions cantered in the atoms α and β, respectively. For $\alpha = \beta$, $\gamma_{\alpha\alpha}$ is approximated as the DFT chemical hardness of the atom α (U_α), also called Hubbard parameter, that is defined as the second derivative of the total energy of atom α with respect to the atomic charge:

$$\gamma_{\alpha\alpha} = U_\alpha = \frac{d^2E^\alpha}{dq_\alpha^2} \tag{2.53}$$

With the approximations introduced, it is possible to define the SCC-DFTB electronic energy expression:

$$E_{Elec.}^{DFTB} = \sum_i^{occ} \langle \psi_i | \hat{H}_0 | \psi_i \rangle + \frac{1}{2} \sum_{\alpha\beta}^{M} \gamma_{\alpha\beta} \Delta q_\alpha \Delta q_\beta \tag{2.54}$$

Further, we define a repulsive energy contribution E_{rep} by combining the nuclear repulsion and all the energy contribution depending on n_0 only in eq. (2.51):

$$\begin{aligned} E_{rep}[n_0(\mathbf{r})] = & -\frac{1}{2}\iint \frac{n_0(\mathbf{r}')n_0(\mathbf{r})}{|\mathbf{r}-\mathbf{r}'\,|} dr dr' - \int V_{xc}[n_0(\mathbf{r})]\, n_0(\mathbf{r})\, dr \\ & + E_{xc}[n_0(\mathbf{r})] + E_{ii} \end{aligned} \tag{2.55}$$

We may consider E_{rep} as practical equivalent to an XC-functional in DFT because it hides the cumbersome physics, while we approximate it with simple functions. The repulsive potential $E_{rep}(R)$ can be determinate as a function of distance for a references system:

$$\begin{gathered} E_{rep}(R) = \sum_{\alpha\neq\beta} V_{Rep}^{\alpha,\beta}\left(|R_\alpha - R_\beta\,|\right) \\ V_{Rep}^{\alpha,\beta}\left(|R_\alpha - R_\beta\,|\right) = E_{Total}^{DFT}\left(|R_\alpha - R_\beta\,|\right) - E_{Elec.}^{DFTB}\left(|R_\alpha - R_\beta\,|\right)\Big|_{\substack{reference \\ structure}} \end{gathered} \tag{2.56}$$

the interatomic distance $|R_\alpha - R_\beta\,|$ can be varied for calculating the DFT total energy $E_{Total}^{DFT}\left(|R_\alpha - R_\beta\,|\right)$ and the DFTB electronic energy $E_{Elec.}^{DFTB}\left(|R_\alpha - R_\beta\,|\right)$ of the reference structure, and then fitting the difference between them to a polynomial function. Once the repulsive potential has been defined, it can be stored in Slater-Koster tables for their respective elements pair.

To summarize, the SCC-DFTB total energy expression can be written as:

$$E_{Total}^{DFTB} = E_{Elec.}^{DFTB} + E_{rep} = \sum_{i}^{occ} \langle \psi_i | \hat{H}_0 | \psi_i \rangle + \frac{1}{2} \sum_{\alpha,\beta} \gamma_{\alpha\beta} \Delta q_\alpha \Delta q_\beta + E_{rep} \tag{2.57}$$

The single particle wave wavefunctions (ψ_i) can be expanded as linear combinations of nonorthogonal atomic orbitals ϕ_ν, denoting the expansion coefficients $c_{\nu\iota}$

$$\psi_i = \sum_{\nu} c_{\nu\iota} \, \phi_\nu \, (\mathbf{r} - \mathbf{R}_\alpha) \tag{2.58}$$

The coefficients are determined by solving a modified Schrödinger equation for the free neutral pseudoatoms:

$$\left[\frac{1}{2} \nabla_i^2 + v_{eff}[n_\alpha^0] + \left(\frac{r}{r_0}\right)^2\right] \phi_\upsilon(\mathbf{r}) = \epsilon_\upsilon \phi_\upsilon(\mathbf{r}) \tag{2.59}$$

In eq. (2.59) n_α^0 is the input density and $\left(\frac{r}{r_0}\right)^2$ is the contraction potential introduced by Eschrig and co-workers to generate an efficient basis set for molecular and solid-state systems.[129, 130] In the contraction potential r_0 is chosen to be about 1.85 times the atomic covalent radius.[131]

A self-consistent procedure is required to find the minimum of expression (2.57). It is noteworthy, that the self-consistency is given with respect to the charge fluctuations, estimated by the Mulliken population analysis, so inspiring the term “self-consistent-charge” in the method´s name. The fluctuations are calculated as $\Delta q_\alpha = q_\alpha - q_\alpha^0$, with q_α^0 the charge of an isolated atom and

$$q_\alpha = \frac{1}{2} \sum_{i}^{occ} n_i \sum_{\mu \in \alpha} \sum_{\upsilon}^{M} c_{\mu i}^{*} c_{\upsilon i} \, S_{\mu\upsilon} + c_{\upsilon i}^{*} c_{\mu i} S_{\upsilon\mu} \tag{2.60}$$

Given the atomic positions, a trial set of combination coefficients can be used in order to estimate the energies of the system via eq. (2.57). By applying the variational principle is possible to solve the general eigenvalue problem:

$$\begin{aligned} &\sum_{\upsilon} c_{\upsilon i}\,(H_{\mu\nu} - \varepsilon_i S_{\mu\upsilon}) = 0 \qquad \forall \mu, i \\ &H_{\mu\nu} = \hat{H}^0_{\mu\upsilon} + \frac{1}{2}\, S_{\mu\nu} \sum_{\tau} (\gamma_{\alpha\tau} + \gamma_{\beta\tau})\Delta q_{\tau} \qquad \forall \mu \in \alpha, \upsilon \in \beta \\ &S_{\mu\upsilon} = \langle \varphi_{\mu} | \varphi_{\upsilon} \rangle \qquad \forall \mu \in \alpha, \upsilon \in \beta \end{aligned} \tag{2.61}$$

The two-centre approximation allows to neglect several contributions in the $H_{\mu\nu}$ Hamiltonian obtaining:

$$\hat{H}^0_{\mu\upsilon} = \begin{cases} \epsilon_{\mu}^{neutral\ free\ atom} & if\ \mu = \upsilon \\ \langle \phi_{\mu}^{\alpha} \left| \frac{1}{2}\, \nabla_i^2 + \upsilon_{eff}\left[n_{\alpha}^0 + n_{\beta}^0\right] \right| \phi_{\upsilon}^{\beta} \rangle & if\ \mu \in \alpha, \upsilon \in \beta \\ 0 & otherwise \end{cases} \tag{2.62}$$

The indices α and β indicate the atoms on which the wave functions and potentials are centered. The diagonal terms in the Hamiltonian of the system are taken as DFT atomic eigenvalues of the free atoms, whereas all non-diagonal terms are obtained via DFT calculations for a α-β dimer. Since all non-diagonal elements depend on the distance between α and β, one has to construct a table, usually called Slater-Koster table, for each pair of atoms in the system containing the values of both the Hamiltonian and Overlap matrixes´ elements in the desired range of interatomic distances. Once constructed, the Slater-Koster tables can be accessed for any distance, which avoids the massive integral calculations during the SCC-DFTB simulation.

Given the optimal set of linear combination coefficients, one can calculate the gradients of E_{Total}^{DFTB} with respect to the atomic positions to derive the atomic forces necessary for geometry optimizations (section 2.7) and molecular dynamics simulations (section 2.8).

2.6 The basis sets

The unknown function, such as the one-electron wavefunction ψ_i in (2.58) is expanded in a set of known functions ϕ_i called basis set. There are two types of localized basis functions, also named atomic orbitals, commonly used in electronic structure calculations: Slater Type Orbitals (STO) and Gaussian Type Orbitals (GTO).

Slater type orbitals have the functional form shown in eq. (2.63):

$$\phi_v(r) = N\, Y_{l,m} r^{n-1} e^{\zeta r} \tag{2.63}$$

here N is a normalization constant, $Y_{l,m}$ are spherical harmonic functions and $e^{\zeta r}$ is the exponential dependence on the distance between the nucleus and electron. It seems to be a natural choice to use atom-centered basis sets for the DFTB method. The STOs, describe correctly the behaviour for r = 0 and the decay at large distances. However, the calculation of multicentred integrals with STOs are computationally expensive, therefore STOs are used where high accuracy is required, and in semi-empirical methods where all three- and four-centre integrals are neglected.

On the contrary, the integrals with the GTOs due to the r^2 dependence in the exponential eq. (2.64) can be easily calculated,

$$\phi_v(r) = N\, Y_{l,m} r^{2n-2-l} e^{\zeta r^2} \tag{2.64}$$

but more GTOs are necessary for achieving the same accuracy compared with STOs. The GTOs are inferior to the STOs in two respects. At the nucleus a GTO has a zero slope, in contrast to a STO which has a “cusp” (discontinuous derivative), and GTOs consequently have problems representing the proper behaviour near the nucleus. The other problem is that the GTO falls off too rapidly far from the nucleus compared with an STO, and the “tail” of the wave function is consequently represented poorly.

For all the DFT calculations we have employed GTOs split-valence basis sets as implemented in Crystal 14 code, where the core orbitals are described by only one contracted Gaussian function (large ζ) and the valence shell is instead represented by two or more set of contracted GTOs. Moreover, polarised functions, i.e., orbitals with higher angular momentum, and diffuse functions, characterized by small ζ exponents, have been added to the basis set to improve its quality.

Regarding our system of interest, the hybrid interface based on TiO_2, the use of plane waves might not be the best option because it requires a large number of plane waves, which might become computationally too demanding. Besides, the use of localized basis function furnishes a good description of electronic structure.

2.7 Equilibrium configurations and atomic forces

In sections 2.3, 2.4, and 2.5 we have discussed different quantum mechanical approaches to solve the many-body Schrödinger equations: Hartree-Fock, the Density Functional Theory and Density Functional Tight Binding. In all cases, the electronic structure calculations assume the Born-Oppenheimer approximation, with the nuclear wave-function decoupled from the electronic wave-function.

One of the ultimate aims of quantum simulations is to predict equilibrium atomic configurations of molecules and solids. In order to identify a minimum, it is necessary to sample the potential energy surface of the system.

During geometry optimization atomic forces can be calculated via the so-called Hellman-Feynman theorem,[132] which states that the force acting on a nucleus M is equal to the total energy derivative with respect to the position of M:

$$F_M = \frac{\partial E}{\partial R_M} = \int n(r) \frac{\partial V(r)}{\partial R_M}\, dr + \frac{\partial E_{Nucl}}{\partial R_M} \tag{2.65}$$

Where the $n(r)$ is the distribution of electrons which depends on the position of the nuclei (R_M) according to the solutions of Schrödinger equations. The $V_{ex}(r)$ is external potential provided by nuclei and $E_{Nucl} = \sum_{I \neq J} \frac{Z_I Z_J}{|\mathbf{R}_I - \mathbf{R}_J|}$ is the nucleus-nucleus repulsions. All the complexity of quantum mechanics goes into the determination of $n(r)$, once we know it, the calculation of forces is a classical problem.

2.8 Molecular dynamics

Molecular Dynamics simulation is a technique for computing the equilibrium and transport properties of many-body systems. In this context, the nuclear motion of the particles' system obeys the laws of classical mechanics. The evolution of the system can be distinguished various stages: initialization, equilibration, and production.

In the initialization step, it is necessary to define the initial conditions (e.g., initial temperature, number of particles, density, time step) of the M particles in the system of interest. The initial positions and velocities are assigned to all particles in the system, such that the total momentum is zero. The instantaneous temperature at the time t is:

$$k_B T(t) = \sum_{i=1}^{M} \frac{m v_{\alpha,i}^2(t)}{N_f} \tag{2.66}$$

where v_α is the α component of the velocity of the M particles

$$\langle v_\alpha^2 \rangle = \frac{k_B T}{m} \tag{2.67}$$

The instantaneous temperature $T(t)$ can be adjusted to match the desired temperature. The initial setting of temperature is not particularly critical, as the temperature will change during the equilibration.

As will appear later, we do not really use the velocity themselves to solve the Newton's equations of motion. Instead, we use the position of all the particle at present $r(t + \Delta\mathrm{t})$ and previous $r(t - \Delta\mathrm{t})$ time step combined with the knowledge of the force f acting on the particles, to predict the position in the next step.

The most time-consuming part of the molecular dynamics simulation is the calculation of the force acting on every particle. If a given pair of particles are close enough to interact, we compute the force between these particles and the contribution to the potential energy $V(r)$ at the DFTB level. For the x component the force is:

$$f_x(r) = -\frac{\partial V(r)}{\partial x} \tag{2.68}$$

Once the forces on every particle are calculated, it is possible to integrate the Newton's equation of motion. Many algorithms have been designed to do this. In particular, the Verlet algorithm has been used in the present work. Its derivation starts with the Taylor expansion of the coordinate around the time t:

$$r(t+\Delta\mathrm{t}) = r(t) - v(t)\Delta\mathrm{t} + \frac{f(t)}{2m}\Delta\mathrm{t}^2 - \frac{\Delta\mathrm{t}^3}{3!}\dddot{r} + O(\Delta\mathrm{t}^4) \tag{2.69}$$

where $\frac{f(t)}{m}$ is the acceleration and $\dddot{r}$ is the hyperacceleration. Similarly,

$$r(t-\Delta\mathrm{t}) = r(t) - v(t)\Delta\mathrm{t} + \frac{f(t)}{2m}\Delta\mathrm{t}^2 - \frac{\Delta\mathrm{t}^3}{3!}\dddot{r} + O(\Delta\mathrm{t}^4) \tag{2.70}$$

Summing eq. (2.69) and (2.70), we obtain

$$r(t+\Delta\mathrm{t}) + r(t-\Delta\mathrm{t}) = 2r(t) + \frac{f(t)}{2m}\Delta\mathrm{t}^2 + O(\Delta\mathrm{t}^4) \tag{2.71}$$

The estimate of the new position contains an error that is of the order $\Delta\mathrm{t}^4$, where Δt is the time step on our molecular dynamics. As the time step decreased, the trajectory becomes a better approximation to the "true" trajectory. However, a small-time step means that more steps are necessary for propagating the system for a given total time, increasing the computational cost.

The velocity can be derived from the knowledge of the trajectory:

$$\begin{gathered} r(t+\Delta\mathrm{t}) - r(t-\Delta\mathrm{t}) = 2v(t)\Delta\mathrm{t} + O(\Delta\mathrm{t}^3) \\ v(t) = \frac{r(t+\Delta\mathrm{t}) - r(t-\Delta\mathrm{t})}{2\Delta\mathrm{t}} + O(\Delta\mathrm{t}^2) \end{gathered} \tag{2.72}$$

Thereby, the velocities are used to compute the kinetic energy and the instantaneous temperature. After each step, the current potential energy and the total energy are calculated, considering that the total energy should be conserved.

During the production, the force calculation and the integration of Newton's equation are repeated until we have computed the time evolution of the system for the desired length of time. After completion of the simulation, it is possible to averages the quantities that we are interested (e.g., the total energy).

2.8.1 Molecular dynamics in various ensembles

Molecular dynamics simulations can generate a collection of configurations called ensemble, which yields a good representation of the phase space for the given property. This is based on the ergodic hypothesis, which assumes that the average obtained by following a small number of particles over a long time is equivalent to averaging over a large number of particles for a short time.

The microcanonical ensemble has been presented in section 2.8, which is the time evolution of a system of M particles in volume V, with the energy as a constant of motion (constant-NVE). However, since most experimental observations are performed at constant pressure and sometimes constant chemical potential, it is often convenient to perform simulation in another ensemble, isothermal-isobaric (NPT) and grand canonical (VEμ), respectively. In this work, we are interested to sample the potential energy surface of fully decorated TiO_2 nanoparticle with organic molecules. If we give enough energy to the system (300 K), which is related to the simulation temperature, it can overcome small barriers (0.025 eV) and sample the energy surface. In doing so, molecular dynamics is a method used for conformational sampling. There is no guarantee to find the global minimum, but it may generate a local minimum that is close in energy to the global minimum. Therefore, we have performed molecular dynamics at constant temperature (canonical ensemble, NVT) by bringing the system into thermal contact with a large bath. In the Nose-Hoover thermostat, the system is coupled to a “heat bath” which gradually adds or removes energy to/from the system with a suitable time constant.[133]

2.9 Modelling crystalline solids

The quantum chemical formalism described in the previous sections (2.3, 2.4, and 2.5) can be applied to molecule and periodic systems. The nanoparticle investigated in Chapter 4 and Chapter 5 has been treated as a large isolated molecule in the vacuum without any periodic boundary condition. Whereas in Chapter 3, and Chapter 4 a TiO_2 anatase slab model has been used, accordingly the essential aspect related to the periodic systems are presented in the following.

In periodic systems, due to the translational symmetry, a unit cell, defined by the $\boldsymbol{a}_1$, $\boldsymbol{a}_2$and $\boldsymbol{a}_3$ lattice vectors, can be identified in the crystal lattice. Given the lattice vectors in the direct space, the corresponding reciprocal lattice vectors in the reciprocal space, $\boldsymbol{b}_1$, $\boldsymbol{b}_2$and $\boldsymbol{b}_3$, are obtained applying the orthonormality condition $\boldsymbol{a}_i \boldsymbol{b}_j = 2\pi\delta_{ij}$, where δ_{ij} is the Kronecker delta. The equivalent of the unit cell in reciprocal space is the (first) Brillouin zone.

The Hamiltonian operator of the electrons in a periodic potential is periodic itself, since the external potential $\mathrm{V_n}$ $(\mathbf{r})$ must obey to the periodicity of the lattice:

$$V_n(\mathbf{r}) = V_n(\mathbf{r} + N_j a_j) \qquad j = 1, 2, ..., \tag{2.73}$$

where a_j are the lattice vectors and the N_j are integer numbers. The Bloch theorem[134] stated that the eigenfunctions of such periodic Hamiltonian can be factorized in a plane-wave $e^{i\mathbf{kr}}$ and a periodic function $u_{\mathbf{k}}(\mathbf{r}_i)$, called Bloch or crystalline orbital:

$$\psi_{\mathbf{k}}(\mathbf{r}_i) = e^{i\mathbf{kr}} u_{\mathbf{k}}(\mathbf{r}_i) \tag{2.74}$$

where the **k** is the reciprocal space vector, which is the equivalent of the direct space vector **r**. The theorem provided that the electronic structure reflects the symmetry of the lattice.

Aa a consequence of the block theorem, the eigenvalues of the Hamiltonian operator are continuous functions of **k** and do not form discrete energy levels but form continuous energy bands.

The integrations of the occupied bands, below the Fermi level, over all the k-points gives the total energy of the system.

Another property that can be extracted from the eigenvalue is the energy distribution of the energy bands in the system which is called density of state (DOS). For the n*th* bands is given by

$$g_n(\varepsilon) = \int \frac{d\mathbf{k}}{4\pi}\, \delta\,(\varepsilon - \varepsilon_n(\mathbf{k})) \tag{2.75}$$

where δ is the Dirac's delta function. The integral is over all the electronic state in the first Brillouin zone and count the total number of electronic states with given eigenvalue $\varepsilon_n(\mathbf{k})$ numerically equal to a given reference energy ε.

To compute the total energy, the band structure and the density of states of the solids it is necessary to choose an adequate k-points sample in reciprocal space. The Monkhorst-Pack grid has been used in this work.[135]

2.10 The models

2.10.1 The anatase (101) TiO_2 surface

In this work the anatase (101) surface is modeled as slabs of finite thickness, it contains three triatomic layers with 144 atoms and 4x2 periodicity along the $[10\bar{1}]$ and [010] directions; no periodic boundary conditions were imposed in the direction perpendicular to the surface. The atoms in the bottom layer were kept fixed to the bulk position during all relaxations to mimic a semi-infinite solid. The optimized lattice parameters for the slab supercell are obtained from the optimized TiO_2 bulk. These supercell models should be sufficiently large to eventually considered the presence of defects at low concentrations in the surface model.

The anatase (101) surface has the characteristic sawtooth profile (**Figure 2-1**). The surface exposes both 5-fold (Ti_{5c}) and 6-fold (Ti_{6c}) coordinated Ti atoms, as well as 2-fold (O_{2c}) and 3-fold (O_{3c}) oxygens.

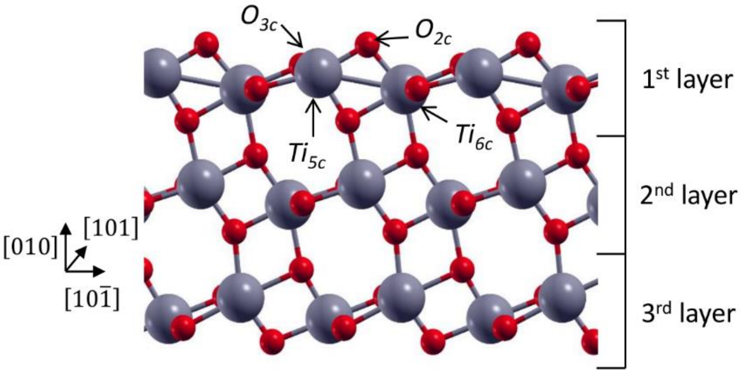

Figure 2-1 Side view of the anatase (101) TiO_2 surface. Small red and dark grey balls represent O atoms and Ti atoms, respectively. The numbers of layers and the crystallographic direction are also given. The arrow point out the low coordinated atoms.

2.10.2 TiO_2 nanoparticle modelling

The 2.2 nm nanoparticle (NP) model considered in this work has been developed in our group. The nanoparticle has been carved from optimized bulk anatase TiO_2 supercell. A Ti atom was set at the origin of the coordinate axis and an overall D_{2d} point group symmetry was kept when cutting the nanoparticle. The too low-coordinated Ti and O atoms of the surface have been saturated with dissociated H_2O molecules: three-fold and some four-fold Ti atoms were coordinated to hydroxyl groups; whereas mono-coordinated O atoms were saturated with H atoms. These operations result in the creation of stoichiometric nanoparticle saturated with a bunch of dissociated water molecules. It was reported that some water adsorbates on spherical nanoparticles cannot be completely eliminated even after annealing at 600 K.[136]

2.10.2.1 The simulated annealing of TiO_2 nanoparticles

Once the models were carved and saturated as described (section 2.10.2), the authors have performed a conjugate-gradient geometry optimization at both the DFTB and DFT levels of theory to obtain total reference energy for a geometrically constructed nanoparticle.

The search for a global minimum is not achievable at the DFT level. Therefore, DFTB molecular dynamics simulations were conducted at a reduced computational cost, considering that its accuracy is comparable to ab initio methods. The optimized 2.2 nm NPs have been used as a starting point for a series of simulated annealing calculations at different target temperatures 700 K, 500 K, and 300K (**Figure 2-2**).

During the molecular dynamics, the temperature profile has been divided into three temporal regions:

I. Heating region: the systems have been heated up to the target temperature in a short time, starting from an initial Boltzmann velocity distribution generated at 150 K.
II. Equilibration region: the systems have been equilibrated to the target temperature until the temperature profile was found flat.
III. Cooling region: the systems have been cooled down slowly to 0 K in order to find the global minimum.

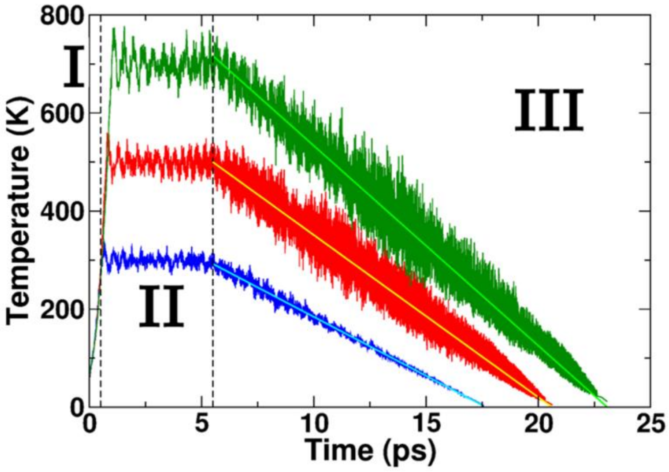

Figure 2-2 Simulated annealing temperature profiles for the 2.2 nm nanoparticles. Green curves refer to the profile with 700 K of target temperature, red curves refer to the profile with 500 K of target temperature, and blue curves refer to the profile with 300 K of target temperature. Heating (I), equilibration (II), and cooling (III) regions have been indicated. Reprinted with permission from ref.118

Finally, one selected structure for each nanoparticle obtained with the simulated annealing processes has been optimized again both at the DFTB and DFT(B3LYP) levels of theory. They selected the most stable one in terms of energy difference with respect to the not annealed “0 K” NP. The smallest 2.2 nm NP result more stable when annealed at 300 K. At higher temperatures, the surface presents some localized amorphous areas, causing a loss instability.

2.10.2.2 The structural analysis of TiO_2 nanoparticles

The 2.2 nm nanoparticle obtained by our group with the annealing process present crystalline core and rearranged surfaces. In particular, the high curvature characteristic of nanoparticles plays a fundamental role in determining the properties of these nano-objects, like the enhance reactivity and affinity toward chemical adsorbates or ligands (section 4.3).

The coordination/undercoordination of all the atomic species in the designed nanoparticles is detailed in **Table 2-1**.

Table 2-1 Number of Ti atoms with specific coordination and their percentage with respect to the total number of Ti atoms for the 2.2 nm NP geometries optimized with DFTB. The number and the percentage of Ti atoms in NP geometries optimized with DFT(B3LYP) are reported in parentheses. Reprinted with permission from ref.118.

DFT [DFT(B3LYP)]	2.2 nm NP	
Ti site	Number	%
Ti_{4c}	36 [36]	16.1 [16.1]
Ti_{5c}	43 [49]	19.2 [22.0]
Ti_{6c_sup}	28 [24]	12.6 [10.8[
Ti_{6c}	96 [94]	43.1 [42.1]
$Ti_{3c}(OH)$	8 [8]	3.6 [3.6]
$Ti_{4c}(OH)$	12 [12]	5.4 [5.4]

2.10.2.3 The electronic properties of TiO_2 nanoparticles

The nanoparticle is a molecular system of finite size; therefore, one cannot define true band states and band gaps in the nanoparticle electronic structure. However, it is possible to distinguish between localized states and states that are delocalized on several atoms of the nanoparticle, similar to periodic systems (i.e., "pseudo band" states). Thus, two different kinds of energy gaps can be defined: the canonical HOMO-LUMO gap (ΔE_{H-L}), which is the energy difference of the frontier orbitals in the nanoparticle, and the Kohn-Sham band gap (ΔE_{gKS}), which is the energy difference of the highest occupied delocalized valence state and the lowest unoccupied delocalized conduction state. The definition of the delocalized or "pseudo band" state is not straightforward since the transition from localized to delocalized states is not observed. In the work of Selli et al.[118] they have defined a criterion to select the delocalized states. It is based on the maximum squared coefficient (max_c) of each eigenstate: the first delocalized state is the one with max_c lower than a threshold of 0.02, in the valence and conduction region, respectively. In this way, ΔE_{gKS} is rigorously defined and values for different NPs and for different methods can be compared. In **Table 2-2** are reported the value of ΔE_{H-L} and ΔE_{gKS}.

Table 2-2 HOMO-LUMO electronic gap (ΔE_{H-L}) and Kohn-Sham electronic gap (ΔE_{gKS}.) (expressed in eV) calculated for the 2.2 nm NP with both DFTB and DFT(B3LYP) methods and with DFTB on top of the DFT(B3LYP) optimized geometries [DFTB/DFT(B3LYP)]. Reprinted with permission from ref.118.

	ΔE_{H-L}			ΔE_{gKS}.		
NS diam.	DFTB	DFT (B3LYP)	DFTB/DFT (B3LYP)	DFTB	DFT (B3LYP)	DFTB/DFT (B3LYP)
2.2	3.11	4.13	3.38	3.55	4.31	3.83

Chapter 3 Graphene-coated TiO_2: role of the atomic vacancy

3.1 Introduction

Graphene, as the prototype of two dimensional (2D) materials, shows excellent properties and has been widely studied.[137, 138, 139] Moreover, graphene can effectively anchor or wrap metal and metal oxide nanoparticles to form various nanocomposites, which show great potential in catalytic applications.[140, 141, 142, 143] Among these nanocomposites, TiO_2-graphene nanocomposites have drawn great attention because TiO_2 possesses superior photocatalytic performance, good biocompatibility and remarkable chemical and thermal stabilities.[144, 145, 146] In recent years, graphene coated TiO_2 nanoparticles have also been synthesized in experiments and found to show enhanced photocatalytic activity.[147, 148, 149, 150] The observed improved performance in photocatalysis and photovoltaics of TiO_2-graphene nanocomposites is attributed to the presence of the graphene layer.[144, 145, 146] On one hand, graphene can act as an electron-acceptor to effectively hinder the electron–hole pair recombination upon UV irradiation of TiO_2;[144, 145, 147, 151, 152, 153, 154] on the other, if TiO_2-graphene nanocomposites are exposed to visible light, graphene can act as sensitizer with electrons being photoexcited within the graphene states and then eventually trapped by Ti atoms, after direct transfer to the TiO_2 conduction band.[146, 155, 156] Moreover, graphene coated TiO_2 nanoparticles exhibit great applications in lithium ion batteries,[157, 158, 159] in biosensors[160] and are also rather promising in the field of nanomedicine because graphene and TiO_2 have a good performance as carriers for bioactive molecules[161] and for photodynamic therapy,[162] respectively.

In real samples of TiO_2-graphene nanocomposites, graphene is expected to present defects[163] that may play an important role. Carbon vacancies can naturally form during the growth process. Eventually, they could also be generated on purpose through particle irradiations or chemical treatments.[164] For example, one widely used approach to prepare graphene-based/TiO_2 composite photocatalysts is the reduction of graphene oxide (GO).[165] This reduced GO (RGO) inevitably contains residual few amounts of oxygenated functional groups and a particularly large population of defects. Another very common approach to obtain graphene-TiO_2 composite is graphite dispersion and exfoliation,[166, 167] which also leads to defective graphene samples that present carbon vacancies, as experimentally observed by TEM.[168, 169] Defects not always appear as unfavourable factors, reducing or even degrading the excellent qualities of graphene. They can also be used, exploited, and even properly designed to suite desirable purposes. For instance, vacancies in graphene sheets or nanotubes can be used as traps for metal atoms, by providing strong C–metal bonds.[170, 171] Vacancies are good anchoring points for deposition of nanoparticles[170, 172, 173, 174] and can enhance the catalytic activity of the nanoparticles. The CO oxidation barrier[172] and O_2 dissociation activation energy[173] on small platinum nanoparticles are reduced when the platinum nanoparticles are supported on defective graphene. Moreover, defective graphene is also promising in the fields of hydrogen storage[175, 176] and air purification.[177] A recent theoretical study shows that vacancy defects can highly enhance the binding between graphene and metal surfaces (Cu and Pt) by forming strong organometallic bonds.[178] Therefore, defects may have a big influence on the graphene/TiO_2 interface and, thus, affect the performance of TiO_2-graphene nanocomposites.

Many exciting results have been recently achieved exploiting the confined space between graphene or other 2D materials and an underlying support for different reactions of small molecules, like H_2, O_2, CO, and H_2O. For example, intercalated CO at the graphene/Pt(111) interface shows weaker interactions with the metal as well as lower desorption temperatures and a lower reaction barrier for oxidation compared to bare Pt(111).[141, 179, 180, 181] The desorption of H_2 on Pt (111) surface is facilitated in the presence of either graphene or h-BN monolayer due to the cover effect.[182] Recent experiments show that oxygen can reach the graphene/Cu interface and lead to a partial oxidation of Cu.[183, 184] Differently, dissociation of O_2 at boron-doped graphene/Cu(111) interface leads to the competitive oxidation of the graphene sheet in the proximity of the dopant.[185] It is shown that water can reach the interface between graphene and different substrates, such as HfO_2[186], silica[187], or $BaTiO_3$[188], Ni(111) surfaces,[189] by intercalation. Water intercalation under the epitaxial graphene on Ru(0001) surface can efficiently split the graphene along line defects into numerous fragments at temperatures as low as 90 K.[190] On Cu(111), however, the water-induced splitting of graphene is far less effective.[190] At the interface of graphene with carbon vacancies on Cu(111) surface, water is capable of breaking the C−Cu bond by dissociating at the undercoordinated carbon atom of the vacancy, restoring the weak van der Waals type of interaction at the interface.[178] The same is not true in the case of Pt(111) surface, where C−Pt bonds are much stronger. Recent DFT calculations show that graphene-on-Cu is a good catalyst for water splitting and is suitable for the low-temperature process.[191] By X-ray absorption spectra, Böttcher and co-workers proposed that on Ni(111) supported graphene[192] water is not just physisorbed as on free-standing graphene[193] but it is chemically bound inducing a p-type doping.[194] Moreover, water is expected to dissociate within the graphene/Ni(111) interface at room temperature, providing a hydrogenated graphene sheet with a gravimetric density competitive with current technology for hydrogen storage.[189]

Water is ubiquitous in normal environmental conditions and especially in human bodies. Thus, the behaviour of water at the interface of graphene coated TiO_2 (i.e. G/TiO_2) is of great interest and significance for the applications of TiO_2-graphene nanocomposites in photocatalysis, lithium ion batteries, biosensor and nanomedicine. Recently, the reactivity of water molecules on top and at the interface of non-defective G/TiO_2 composite was studied by DFT calculations.[195] On top of G/TiO_2, water was found to physically adsorb on the graphene layer with an adhesion energy slightly larger than that on free-standing graphene. At the interface water prefers to adsorb on TiO_2 rather than on the carbon sheet, leading to adsorption configurations very similar to those on bare TiO_2. Thus, the presence of graphene does not improve the activity for water dissociation. However, the presence of carbon vacancies in the graphene layer could play a role but this is still an open question.

In this work, by means of dispersion corrected hybrid density functional theory (DFT) calculations, we investigate two atomic defects in the hybrid G/TiO_2 interface: C monovacancy in graphene and O vacancy in TiO_2. The C monovacancy can be considered a prototype defect in graphene since the undercoordinated C atoms appearing in the structure are analogous to those that would appear in the presence of larger (pluriatomic) vacancies, or in the presence of extended edges. The O vacancy is a prototype defect for reduced TiO_2 samples, which are those commonly obtained after annealing. First, we study the structural and electronic properties of C monovacancy in graphene, and then the interface between graphene with one C monovacancy (VG) and the stoichiometric anatase $TiO_2(101)$ surface (VG/TiO_2). As a next step, we analyze the behavior of water at the interface. Finally, we consider the effect of the presence of one O vacancy in the TiO_2 support. Our results show that the characteristic magnetism of free-standing VG[196] quenches in the presence of an underlying anatase $TiO_2(101)$ surface and a C-O bond may occur at the interface. Dissociated rather than molecular water is preferred at the interface VG/TiO_2 in contrast with what observed on bare TiO_2 surface. O atoms at the interface may diffuse into the reduced TiO_2 sublayers to heal O vacancies. This study is helpful to understand how the presence of water in the surrounding environment affects structural and electronic properties of the graphene/TiO_2 interface, and, thus, its application in photocatalysis, electronic devices and nanomedicine.

3.2 Computational details

All the calculations were performed with the CRYSTAL14 code[197], where Kohn-Sham orbitals are expanded in Gaussian type functions (the all-electron basis sets are O 8-411(d1), Ti 86-411 (d41), C 6-31(d1) and H-11(p1)). The hybrid functional B3LYP[198, 199] was adopted for all the calculations. To properly take into account the long-range van der Waals interactions, dispersion correction was introduced with the Grimme approach.[200, 201]

For the free-standing graphene, three supercell models were used: 6×6 (71 C atoms), 8×8 (127 C) and 16×16 (511 C), with Monkhorst-Pack k-point grid[135] of 12×12×1, 10×10×1, or 4×4×1 with B3LYP-D*, and of 12×12×1, 10×10×1 or 8×8×1 with PBE-D2, respectively. The band structures were obtained for 4×4, 8×8 and 16×16 supercells with 30×30×1, 15×15×1 and 10×10×1 k-point grids. The hexagonal lattice parameter of pure graphene is computed to be 2.463 Å for B3LYP-D* and 2.472 Å for PBE-D2 and was kept fixed in all the calculations.

The lattice parameters of anatase were calculated to be 3.764 and 9.793 Å, for a and c, respectively. The anatase (101) TiO_2 surface was modelled by a three triatomic layers slab (144 atoms) with the bottom layer fixed. A (5 × 6) supercell for graphene and a (4 × 2) supercell for anatase (101) slab were used to build the co-periodic lattice of graphene/anatase (101) hybrid system. An angle of 50° exists between the vectors of the supercells of graphene and anatase (101) TiO_2 surface. Here the lattice of graphene was slightly stretched in x direction and compressed in y direction (see **Figure 3-1**) to fit the anatase lattice. Thus, a slightly tensile strain along x axis (+1.9 %) and compressive strain along y axis (-0.6 %) were introduced. Therefore, two configurations appear for free-standing graphene with monovacancy, VG_{ab} and VG_{bc}, depending on the rearrangement of carbon atoms at vacancy site as shown in **Figure 3-1**. One carbon single vacancy was created in one supercell of VG/TiO_2 resulting in a distance larger than 11 Å between two periodically repeated defects and in a vacancy concentration of 1.67%. The difference between VG_{ab} and VG_{bc} is just the vacancy pattern when we repeat the supercell. VG_{bc} is 0.21 eV higher in energy than VG_{ab}. Thus, for the VG/TiO_2 interface, only VG_{ab} is presented in the manuscript. To make sure that we always get the reasonable VG/TiO_2 interface, VG_{bc}/TiO_2 interfaces were also calculated, which are always higher in energy compared with VG_{ab}/TiO_2 interfaces.

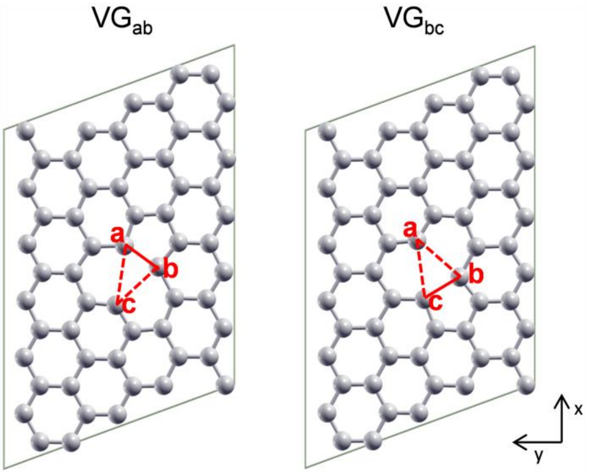

Figure 3-1 Two ball-and-stick configurations of slightly strained free-standing graphene with a single C vacancy: VG_{ab} and VG_{bc}. The red triangles indicate the vacancy defect. The solid red lines represent elongated C-C bonds and the dotted lines indicate no C-C bond. The three C atoms at the vacancy are marked with a, b and c.

The geometry optimizations for the VG/TiO_2 interface were done using a 2 × 2 × 1 k-point mesh. A dense k-point mesh of 15×15×1 was adopted in the calculations for density of state (DOS) to get a good description of the electronic properties.

The adhesion energy of the interface VG/TiO_2 is defined as:

$$\Delta E_{adh} = E(VG/TiO_2) - [E(VG) + E(TiO_2)] \tag{3.1}$$

where $E(VG/TiO_2)$ is the energy of the VG/TiO_2 interface, $E(VG)$ is the energy of free-standing VG and E(TiO_2) is the energy of the TiO_2 slab.

The adsorption energy (ΔE_{ads}) and dissociation energy (ΔE_{diss}) of water on free-standing VG are computed as follows:

$$\Delta E_{ads\ or\ diss} = E(VG + H_2O) - [E(VG) + E(H_2O)] \tag{3.2}$$

where $E(VG + H_2O)$ is the total energy of molecular or dissociated H_2O on VG, VG is the energy of free-standing VG and $E(H_2O)$ is the energy of an isolated $E(H_2O)$ molecule.

The same quantities (ΔE_{ads} and ΔE_{diss}) for water on bare TiO_2(101) surface are computed as follows:

$$\Delta E_{ads\ or\ diss} = E(TiO_2 + H_2O) - [E(TiO_2) + E(H_2O)] \tag{3.3}$$

where $E(TiO_2 + H_2O)$ is the total energy of molecular or dissociated H_2O on TiO_2, $E(TiO_2)$ is the energy of the TiO_2 slab and $E(TiO_2)$ is the energy of an isolated H_2O molecule.

The same quantities (ΔE_{ads} and ΔE_{diss}) for water on top or at the interface of VG/TiO_2 are computed as follows:

$$\Delta E_{ads\ or\ diss} = E(VG/TiO_2 + H_2O) - [E(VG/TiO_2) + E(H_2O)] \tag{3.4}$$

where $E(VG/TiO_2 + H_2O)$ is the total energy of molecular or dissociated H_2O on top or at the interface of VG/TiO_2, $E(VG/TiO_2)$ is the energy of the most stable configuration of the interface VG/TiO_2 and $E(H_2O)$ is the energy of an isolated H_2O molecule.

In the following we define the nomenclature that will be used in the chapter. We name the hybrid interface between graphene and the anatase TiO_2 (101) surface as "G/TiO_2" (section 3.4). In the presence of one C monovacancy in G/TiO_2, we may observe interaction of the vacancy either with a 2-fold coordinated bridging oxygen (O_{br}) or a five-fold coordinated Ti atom (Ti_{5c}) on the anatase TiO_2 (101) surface. If the type of interaction is C-O covalent bond at the interface we represent it by the symbol "—" (VG—O_{br}); if it is a weak van der Waals interaction we represent it by the symbol "---" (VG---O_{br} or VG---Ti_{5c}).

For the configurations of molecular water adsorption on VG/TiO_2 (section 3.5.1) we use the symbol "/" when on top (H_2O/VG—O_{br}) and a second "/" when between the two materials (VG/H_2O/TiO_2).

For the configurations of dissociated water (in OH+H or O+H+H) further details must be given (section 3.5.2). When on free-standing defective graphene, we add subscripts a, b or c to each fragment of dissociation (e.g. OH_aH_b or $O_aH_bH_c$ or $O_{ab}2H_c$) that identify which uncoordinated C atoms at the vacancy site are involved in the bonding (see **Figure 3-1** left or **Figure 3-6** for the definition of C atoms a, b, c). When the dissociation takes place on top or at the interface of VG/TiO_2, we do not explicitly mention VG/TiO_2 in the label, but we use the generalized label ".../.../..." where the first "/" distinguishes what is on VG from what is at the interface and the second "/" distinguishes what is at the interface from what is on TiO_2: the fragments of dissociation bound to VG go on the left part of the label (e.g. OH_a/.../...), the fragments at the interface between VG and TiO_2 go in the central part of the label (e.g.

…/OH_a/…), and the fragments on TiO_2 go on the right part of the label (e.g. …/…/$O_{br}H$ or …/…/$Ti_{5c}OH$) where O_{br} is a twofold coordinated O and Ti_{5c} is a fivefold coordinated Ti on the anatase TiO_2 (101) surface. Accordingly, dissociated water on bare TiO_2 surface was simply labelled as "$Ti_{5c}OHO_{br}H$" (section 3.5.2.3).

All the calculations reported in this work were performed including spin polarization when it was necessary.

3.3 The carbon monovacancy in free standing-graphene

As a preliminary study we have modelled the carbon monovacancy in free-standing graphene considering different supercells and functionals **Table 3-1**. The carbon monovacancy is created by removing one C atom in the graphene lattice, which costs about 8 eV, as detailed in **Table 3-1**.

Table 3-1 Formation energy ($E_{formation} = (E_{VG} + E_C) - E_G$), where VG is the C monovacancy model, C is a single C atom in a non defective graphene model and G is the non defective graphene model) for a C monovacancy (ground state spin configuration) in cells of different size, as obtained with B3LYP-D* and PBE-D2.

	B3LYP-D*	**PBE-D2**
Cell	$E_{formation}$ (eV)	
6×6 (71 C)	8.18	7.90
8×8 (127 C)	8.12	7.82
16×16 (511 C)	8.05	7.74

Depending on the local point group symmetry imposed to the defective lattice, different electronic solutions can be obtained, as described in **Figure 3-2**: for D_{3h} symmetry a ferromagnetic quintet (Q, the highest possible spin configuration); for the C_{2v} symmetry a ferromagnetic triplet (T); and for the C_s symmetry an antiferromagnetic open shell singlet (S_{os}) or a diamagnetic closed shell singlet (S_{cs}) solution.

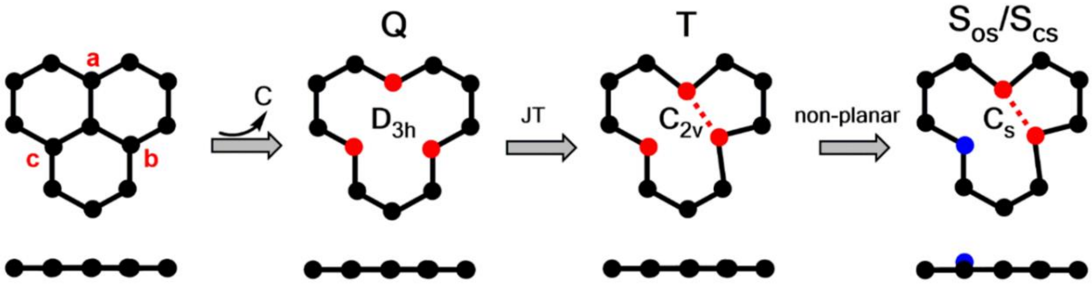

Figure 3-2 Schematic top and side view representations of the C monovacancy defect in graphene with spin multiplicity of quintet (Q), triplet (T), closed-shell (S_{cs}) and open-shell (S_{os}) singlets. The local point group symmetry is shown together with the type of distortion involved: JT (Jahn-Teller) and non-planar. Undercoordinated carbon atoms (a, b and c) are in red. Out-of-plane C atom is in blue.

The Q solutions are always much higher in energy (> 1.5 eV) and therefore they have not been considered further in the analysis. Results for all the other three electronic configurations in the case of supercell models of increasing size are reported in **Table 3-2**, using both the dispersion-corrected B3LYP functional (B3LYP-D*) and the dispersion corrected PBE functional (PBE-D2).

The T solution is always the most stable, although the S_{os} is only slightly above in energy, by less than 0.08 eV. We may note that only the T solutions are characterized by a planar geometry, since the d_z parameter (**Table 3-2**) is an indicator of the out-of-plane distortion caused by a lift of one undercoordinated C atoms. T and S_{os} are very close in energy because going from T to S_{os}, and keeping the geometry fixed to that of T, there is only an energy cost to flip the spin of one of the two unpaired electrons. This cost corresponds the loss of the exchange energy (estimated to be +0.10 eV for the 6×6 model). Note, however, that S_{os} has been fully optimized and, thus, the final energy difference reported in **Table 3-2** is slightly smaller (+0.08 eV for the same 6×6 model). The relaxed S_{os} structures are not planar (d_z = 0.18-0.46 Å, depending on the supercell with B3LYP-D* in **Table 3-2**; values for PBE-D2 are also reported). Even less planar are the S_{cs} optimized structures (d_z = 0.55-0.70 Å, depending on the supercell with B3LYP-D* in **Table 3-2**; values for PBE-D2 are also reported). In this last case (S_{cs}) a robust lift of the undercoordinated atom is necessary in order to obtain a good overlap between the sp^2 orbital and the $v\pi$ state, resulting in the pairing up of the two electrons and, thus, in the complete quenching of the magnetization.

Table 3-2 Magnetization (μ), out-of-plane distortion (d_z) and relative energy (ΔE) referred to the T, for T, S_{os} and S_{cs} spin configurations of VG for increasing size cells (6×6, 8×8 and 16×16), as obtained with B3LYP-D*, and PBE-D2. d_z is defined as the difference between the z cartesian coordinate of the undercoordinated C atom (**Figure 3-2**) and the average value for all the other carbon atoms in the cell.

Cell	Spin Multeplicity	**B3LYP-D***			**PBE-D2**		
		$\mu(\mu_B)$	**d_z(Å)**	**ΔE(eV)**	**$\mu(\mu_B)$**	**d_z(Å)**	**ΔE(eV)**
6x6 (71C)	T	2.00	0.00	0.00	1.59	0.00	0.00
	S_{os}	0.00	0.18	0.08	0.32	0.38	0.02
	S_{cs}	0.00	0.55	0.33	0.00	0.48	0.07
8x8 (127C)	T	2.00	0.00	0.00	1.54	0.00	0.00
	S_{os}	0.00	0.38	0.07	- (-)[a]	- (-)[a]	- (-)[a]
	S_{cs}	0.00	0.62	0.34	0.00	0.55	0.11
16x16 (511 C)	T	2.00	0.00	0.00	1.49	0.00	0.00
	S_{os}	0.00	0.46	0.05	- (-)[a]	- (-)[a]	- (-)[a]
	S_{cs}	0.00	0.70	0.31	0.00	0.67	0.11

[a] During relaxation, S_{os} collapses into T.

In the case of the B3LYP-D* functional, the computed magnetic moment for the electronic ground state is fully coherent with a T spin configuration, since it corresponds to 2 μ_B after spin relaxation. This does not hold for the PBE-D2 calculations, where the total relaxed magnetic moments span the range from 1.59 to 1.49 μ_B, going from the smallest to the largest supercell model considered. Analogously, for the S_{os} spin configuration, with B3LYP-D* the magnetic moments is 0 μ_B, as expected for an antiferromagnetic solution, whereas with PBE-D2 it is 0.32 μ_B, which is a sort of uncompensated antiferromagnetism (value obtained with 6×6 cell model since with the 8×8 and 16×16 cells the solution collapsed on the T spin configurations during optimization).

The partial quenching of the magnetic moment of defective graphene with DFT/GGA calculations has been often previously[202, 203] reported and rationalized in terms of a partial charge transfer from the vπ^{α} to the vπ^{β} band, since both bands cross the Fermi level, as it is clearly observable, for the present study, in the band structures in the lower panels of **Figure 3-3**. The vπ^{α} and vπ^{β} bands become closer for increasing cell size, but for all the three sizes considered, they both cross the Fermi level, leading to a partial magnetization passivation.

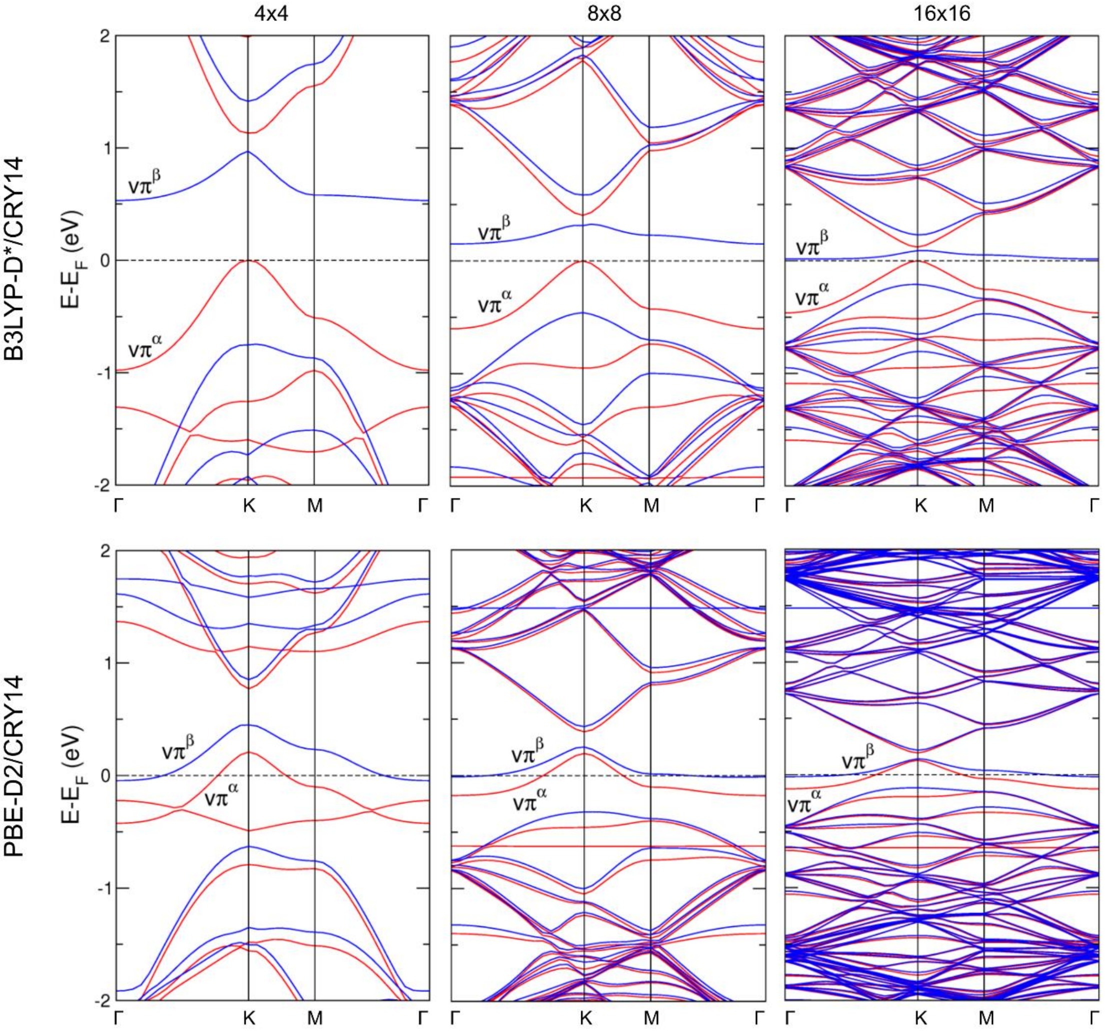

Figure 3-3 Band structure of the ground T state for the C monovacancy in 4×4, 8×8 and 16×16 cell models as obtained with B3LYP-D* (top panel) and PBE-D2 (bottom panel). α bands are in red and β bands are in blue. The zero energy is set at the Fermi level (dashed line).

What is striking is that a very different situation emerges from the B3LYP-D* calculations, shown in the upper panels of **Figure 3-3**. Here, the vπ^{α} band is always below the Fermi level, whereas the vπ^{β} band is always above the Fermi level, getting closer in energy for increasing supercell size, but still clearly separated in energy (30 meV for the 16×16 cell). This means that in the case of B3LYP-D* calculations, no charge transfer takes place, which is the reason for no partial π magnetic moment quenching. This result is in excellent agreement with the recent STS experiment proving that the π magnetization is caused by a splitting of about 20-60 meV between two spin-polarized vacancy π states (two distinct peaks in the spectra).[204] Thus, B3LYP-D*, at odds with PBE-D2, is capable of reproducing this very delicate but extremely relevant experimental quantity. This is because of a more accurate treatment of the exchange energy and of the partial correction for the self-interaction error for hybrid functional methods.[205, 206] The unpaired electron in the $v\pi^{\alpha}$ benefits from the exchange with the other unpaired electron in the sp^2 orbital in the σ plane. No π passivation, as observed in B3LYP-D* calculations, results in more exchange energy, which is the reason why a total 2 μ_B magnetic moment is always obtained with hybrid functional calculations.

We investigated further whether there is a trend in the degree of magnetization with the increasing portion of exact exchange (EXX) in the hybrid functional. Indeed, this trend exists and it is evident when observing the computed magnetic moments in **Figure 3-4**. We considered five values of % of exact exchange, going from 0 to 20% (B3LYP-D*). The magnetic moment for 0% of EXX is similar to that computed with PBE-D2 (1.47 vs 1.59 μ_B), but increases rapidly and converges to 2 μ_B already for 15% of exact exchange contribution to the exchange functional. These results prove the crucial role played by the exact exchange in determining the correct magnetic moment of the defective graphene model. Even a small contribution of exact exchange is capable of largely increasing the resulting free magnetization.

We tested other hybrid functionals to prove that this is not a peculiar behavior of B3LYP. We considered both HSE06-D2[207], B3PW91[199, 208] and PBE0.[209] B3PW91 was chosen because it was found to be particularly suitable for metal and magnetic system.[210] All these hybrid functional methods provide a magnetization of 2 μ_B, in agreement with B3LYP-D* calculations. The band structures for the 8×8 cell model are reported in **Figure 3-5** and can be compared to the corresponding B3LYP-D* one in **Figure 3-3**.

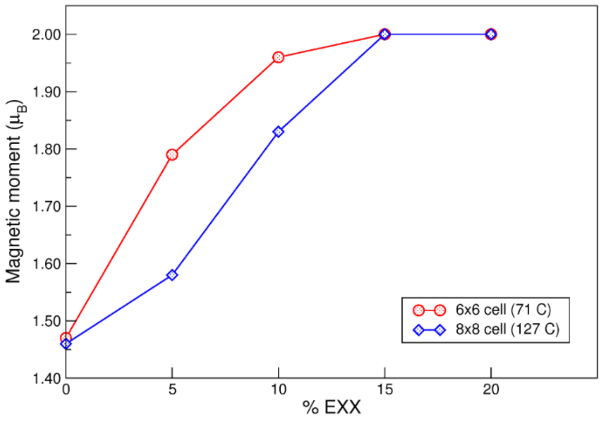

Figure 3-4 Magnetic moment values for the C monovacancy (in 6×6 or 8×8 cells) as a function of the exact exchange (EXX) percentage. The 20% exact exchange functional corresponds to the B3LYP-D* used throughout this work.

3.4 Interface between defective graphene and $TiO_2(101)$ surface

Once we have defined the method to describe the carbon monovacancy in free-standing graphene, we introduced the defect in the (5 × 6) supercell of graphene, which is co-periodic with the lattice of anatase(101) surface in order to build the VG/TiO_2 hybrid interface (section 3.2). The ground state for VG in the (5 × 6) supercell is calculated to be triplet with a planar configuration, as explained in section 3.3.[196] After the formation of one single vacancy in the graphene sheet, there is a dangling bond on the C_c atom with a sp^2 hybridization, whereas the other two carbon atoms (a and b) get closer to form an elongate C-C bond (labelled as VG_{ab} in **Figure 3-1**). The singlet closed shell solution for VG was found to be 0.50 eV higher in energy than the corresponding triplet solution. However, considering that the magnetism may quench in the present of $TiO_2(101)$ surface, both triplet and singlet closed shell solutions were considered for the VG/TiO_2 interface.

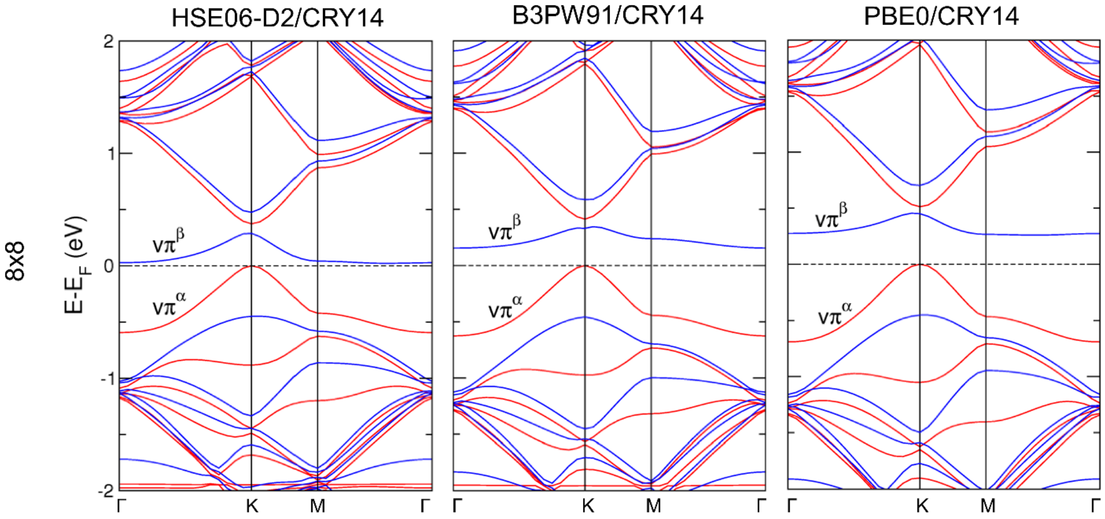

Figure 3-5 Band structure of the ground T state for the C monovacancy in 8×8 cell models as obtained with HSE06-D2 (left), B3PW91 (middle) and PBE0 (right). α bands are in red and β bands are in blue. The zero energy is set at the Fermi level (dashed line).

Various configurations of the VG/TiO_2 interfaces have been considered to search for the most stable one, including different relative positions between graphene and TiO_2 surface, as well as the mirror flipping of graphene. Some selective configurations of VG/TiO_2 interfaces are listed in **Figure 3-6**. First, we focus on the singlet closed shell structures.

When the VG was put close to the TiO_2 surface and above one bridge oxygen atom, the most stable interface VG—O_{br} model could be obtained after geometry optimization with an adhesion energy of -3.18 eV per supercell. The ground state of this configuration is singlet closed shell state, in which the carbon atom *c* (marked in **Figure 3-6**) is oxidized and forms a strong covalent bond with the O_{br} atom. The C-O bond length at the interface is 1.35 Å. One of the original two O-Ti bonds is broken and the other one is elongated from 1.82 Å to 1.84 Å. This C-O-Ti bond agrees well with X-ray photoelectron (XPS) and Fourier transform infrared (FTIR) spectra of TiO_2/graphene nanocomposites in previous experiments.[211, 212, 213] This additional chemical bond between graphene and TiO_2, which is otherwise just attracted by dispersion forces, is crucial because it was shown to facilitate the interfacial charge-transfer, improving the photocatalytic activity of TiO_2–graphene composites.[151, 214]

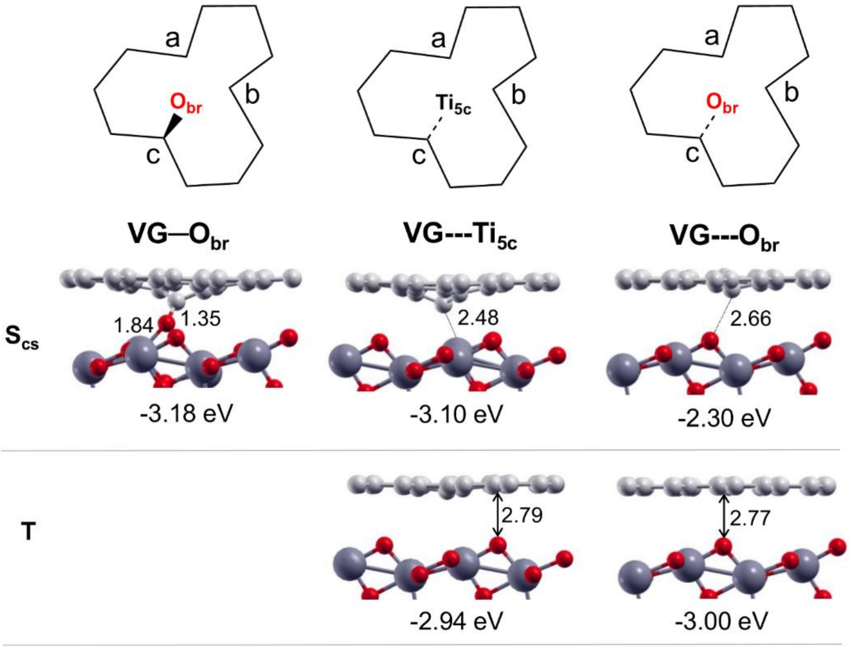

Figure 3-6 Schematic top views of the C monovacancy defect in VG/TiO_2 interfaces (top line). Side views of selected configurations of VG/TiO_2 interfaces in the singlet closed shell (S_{cs}) (middle line) and in the triplet (T) solutions (bottom line). For labels see Computational methods (section 3.2). Adhesion energies per supercell calculated according to equation (3.1) are listed below each configuration. Small red and light grey balls represent O atoms and C atoms. Big dark grey balls represent Ti atoms. Distances are in Å.

Another metastable singlet configuration is the VG---Ti_{5c}, which is 80 meV higher in energy than VG—O_{br}. For VG---Ti_{5c}, in which the vacancy is above one five-fold Ti atom on the TiO_2 surface, the carbon atom *c* moves down toward the Ti_{5c} atom to establish an interaction. However, the C-Ti distance is as long as 2.48 Å, much larger than the normal a C-Ti bond length in a C-Ti alloy (2.11 Å to 2.16 Å), implying that there is no true chemical bond at the interface. Actually, we never succeed in getting a C-Ti bond at the interface even when starting from a very short interface distance, which is in agreement with previous theoretical results about TiO_2 nanostructures on graphene[215]. Only for very small $(TiO_2)_n$ clusters ($n \leq 15$) on VG, some Ti-C bonds have been reported in the literature.[216] Another less stable singlet state configuration for the interface is named as VG---O_{br}, in which the carbon atom *c* has moved down towards one O_{br}. However, the C-O distance is very high (2.66 Å). Thus, there is no true chemical bond in this configuration at the interface and the adhesion energy is much smaller when compared with VG—O_{br}.

Now we turn to the triplet solutions. The most stable two triplet configurations are shown in **Figure 3-6**. We observe that the triplet solutions for VG/TiO_2 are always characterized by a planar geometry of VG on TiO_2 surface with an equilibrium distance between graphene and TiO_2 surface of about 2.8 Å, indicating weak van der Waals interactions at the interfaces. The adhesion energies at the interfaces are -2.94 eV and -3.00 eV per supercell for VG---Ti_{5c} and VG---O_{br}, respectively.

On the basis of the results above, we conclude that the magnetism of VG is quenched when it is supported on a TiO_2(101) surface since the singlet state configurations for VG—O_{br} and for VG---Ti_{5c} are the most stable ones. The chemical adsorption of VG on TiO_2(101) (VG—O_{br}) involves the breaking of one O-Ti bond. Thus, we expect an energy barrier between physical and chemical adsorption. We suppose that after the transfer of graphene from the substrate for growth (for example Cu or Ni) to the TiO_2 anatase (101) surface, the interface presents a mixture of VG—O_{br} and VG---Ti_{5c}. So, hereafter, we will focus our work on these two most stable singlet closed shell configurations.

The top and side views of G/TiO_2, VG—O_{br} and VG---Ti_{5c} interface models are shown in **Figure 3-7**, where the relative position of the vacancy on the TiO_2 surface is clearly displayed. To further investigate and understand their electronic properties, the projected density of states (PDOS) is plotted under each structure. In all three systems, we observe that the C 2p states largely fill the TiO_2 band gap region. This can explain the broad background absorption in the visible-light region of TiO_2–graphene nanocomposites.[211, 217] For the non-defective G/TiO_2 interface, the Dirac cone at the Fermi level originating from free-standing graphene is quite preserved and the total density of states is almost the superimposition of those from free-standing graphene and from TiO_2 surface, due to the weak interaction at the interface, even though a small band gap opening is registered (0.14 eV).[155] We wish to recall, from a previous section 3.3,[196] that a small band gap opens also when the C monovacancy is introduced in the

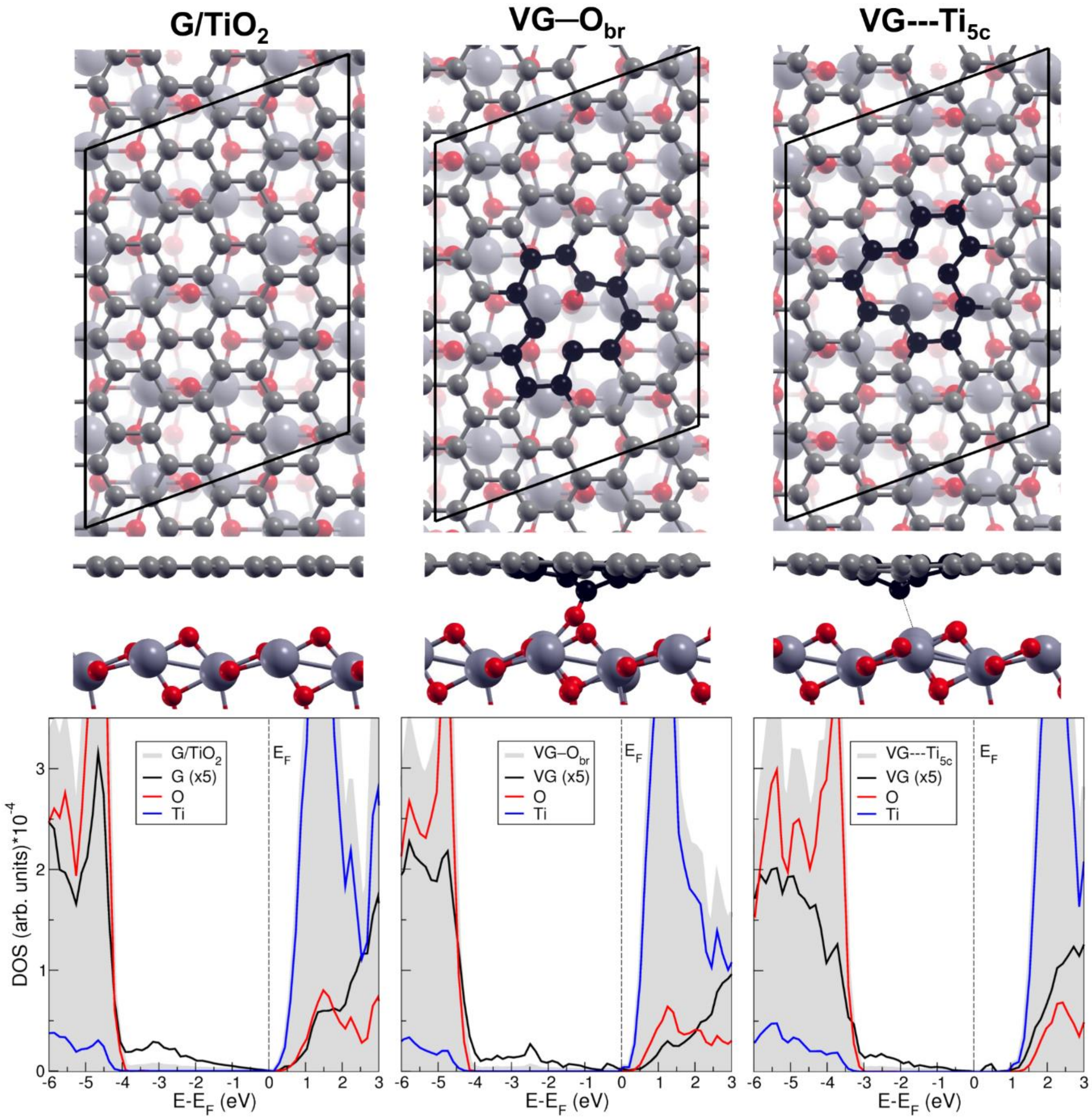

Figure 3-7 Top and side views of G/TiO$_2$, VG—O$_{br}$ and VG---Ti$_{5c}$ interfaces (top and middle lines) along with the density of states (bottom line). The C atoms at the vacancy are highlighted in black and the other C atoms are shown in light grey. Small red balls represent O atoms and big dark grey balls represent Ti atoms. In the DOS, the filled grey area represents the total DOS, the black line is DOS projected on graphene (G or VG), which is magnified by five for clarity. The red and blue lines are DOS projected on all O and all Ti atoms in the TiO$_2$ slab, respectively. Fermi energy (E$_F$) is set at the eigenvalue of the highest occupied states.

free-standing graphene (VG). This is 0.26 eV with the computational setup for the VG/TiO$_2$ interface. It is very interesting to observe what happens when VG is now put on TiO$_2$. In the case of VG—O_{br} interface, the DOS presents some states originating from Ti atoms at the Fermi level, thus there is no band gap but a metallic character is exhibited. This is a consequence of the Ti-O bond breaking at the TiO_2 surface that results in a non-fully oxidized TiO_2 surface. The metallic character of VG—O_{br} interface can be more clearly noted in the zoomed DOS shown in **Figure 3-8**a. On the contrary, for the VG---Ti_{5c} interface, a band gap of 0.27 eV is observed (see **Figure 3-8**b), due to the presence of the C vacancy, in line with the case of free-standing VG (section 3.3).[196]

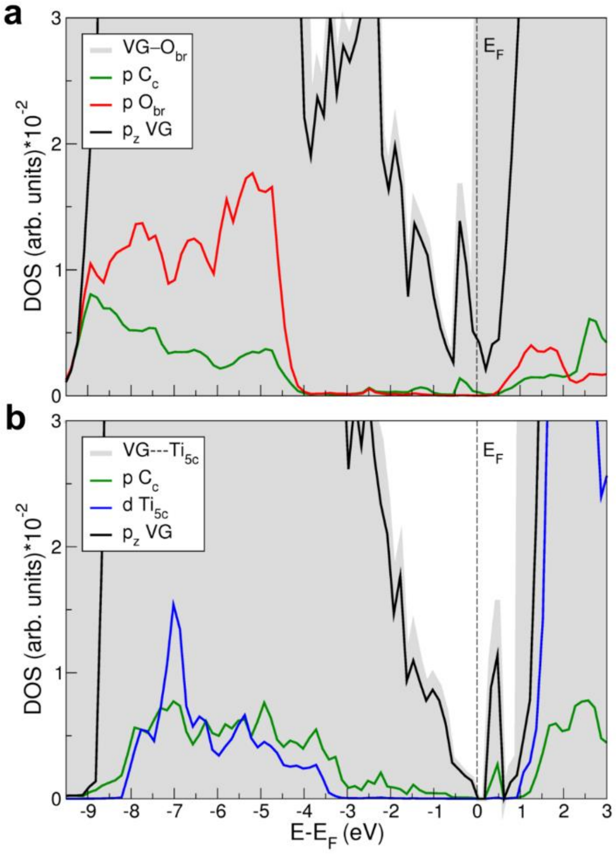

Figure 3-8 Total and projected DOS for the VG—O_{br} (a) and VG---Ti_{5c} (b) interfaces in a larger range of energies but in a zoomed range of density with respect to **Figure 3-7**. The green lines in (a) and (b) are DOS projected on the p states of the C atom c marked in **Figure 3-1** and **Figure 3-6**. The red line in (a) is DOS projected on the p states of the O_{br} atom on the TiO_2 surface bonding to the C atom c at the interface VG—O_{br}. The blue line in (b) is DOS projected on the d states of the Ti_{5c} atom interacting with the C atom c at the interface VG---

Ti_{5c}. The black lines in (a) and (b) are DOS projected on the p_z states of all C atoms in VG. See **Figure 3-6** and **Figure 3-7** for structures. Fermi energy (E_F) is set at the eigenvalue of the highest occupied states

To gain more insight on the interaction at the interfaces of VG—O_{br} and VG---Ti_{5c}, the projected density of states on C_c, O_{br} and Ti_{5c} atoms are calculated and shown in **Figure 3-8**a and **Figure 3-8**b, respectively. For VG—O_{br} interface, a clear hybridization between C_c p and O_{br} p orbitals exist in the energy range between -4 eV to -9.5 eV below the Fermi level, due to the C-O chemical bond at the interface. For VG---Ti_{5c}, some hybridization between C_c p and Ti_{5c} d orbital can be seen in the energy range between -3 eV to -8 eV, in line with a strong interaction at the interface.

3.5 Reactivity with water

In this section, we describe the water reactivity with the VG/TiO_2 interface in terms of molecular (section 3.5.1) and dissociated (section 3.5.2) adsorption modes. We consider the possibility that either water molecules approach from the top of the interface or they are intercalated, through graphene edges or large carbon holes in the graphene sheet, in the confined zone between the two materials. Then, we evaluate the cover effect on the energetics of water dissociation on TiO_2(101) surface (section 3.5.2.1). Finally, we investigate the electronic properties of hydrated VG/TiO_2 (section 3.5.2.2) and the effect of an underlying reduced TiO_2 surface (section 3.5.2.3).

3.5.1 Molecular adsorption

We compare energy of adsorption (ΔE_{ads}), as defined in detail in the section 3.2. By comparing the systems in the top panel of **Figure 3-9**, it is evident that water binds more strongly on a fivefold coordinated titanium (Ti_{5c}) of the anatase (101) TiO_2 surface (-0.97 eV) than on a defective graphene sheet (-0.22 eV), where it just weekly physisorbs by pointing the H atoms down towards the π electron density of the C layer.

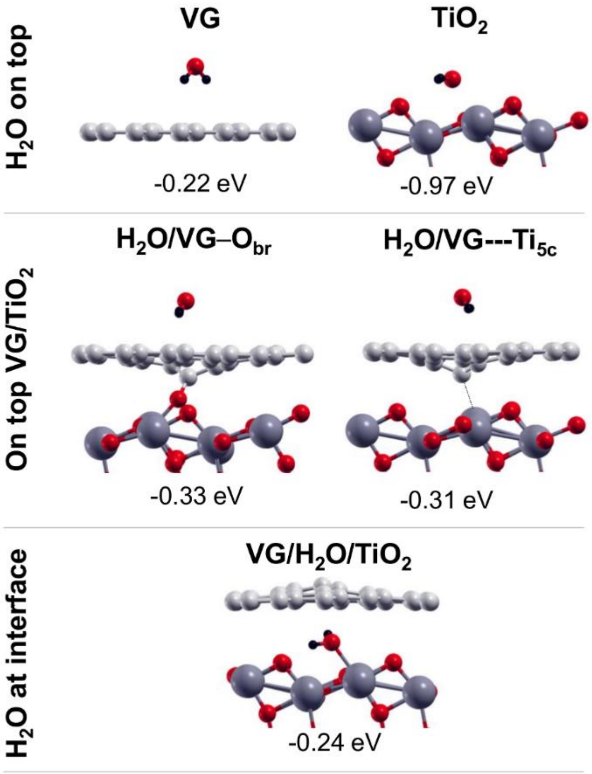

Figure 3-9 Side views of molecular water adsorption on top of free-standing VG and TiO_2 (101) surface (top line), side views of molecular water adsorption on top of the most stable two VG/TiO_2 interfaces (middle line) and molecular water adsorption at the VG/TiO_2 interface (bottom line). Labels and adsorption energies are reported above and below each configuration, respectively, and defined in section 3.2 of Computational methods. Small red, light grey and black balls represent O atoms, C atoms and H atoms, respectively. Big dark grey balls represent Ti atoms.

As a next step, in the central panel of **Figure 3-9**, we consider that water comes from the top side of the two most stable interface configurations (see **Figure 3-6**). The adsorption energy (ΔE_{ads}) slightly increases with respect to the free-standing case by about -0.1 eV, which is probably due to some surface polarization induced by the presence of the titania substrate that enhanced the weak Van der Walls interaction between the defective graphene sheet and the water molecule.

Finally, we have the water at the interface between the two materials, binding to a Ti_{5c} and with the two H atoms pointing towards the π electron density of the graphene sheet. However, the adsorption energy in this configuration is much smaller than on the top of TiO_2 surface (-0.24 vs -0.97 eV). The reason is that the graphene sheet must largely distort upwards to give enough space to the water molecule, which accounts for a relevant energy cost. Moreover, the C sheet uplift highly reduces the adhesion energy between the two surfaces, which is a second relevant energy cost. The net balance (ΔE_{ads}) is still negative and comparable with water adsorption on top of VG/TiO_2 (-0.31/-0.33 eV).

3.5.2 Dissociated adsorption

Water dissociation is typically in two fragments: OH and H. On a free-standing graphene sheet, as shown in the top panel of **Figure 3-10**, the OH fragment covalently binds to an undercoordinated C atom of the vacancy, whereas the H atom covalently binds to another one.

We have investigated more possibilities, among which the two lowest in energy are those shown in **Figure 3-10**: one with the OH on the C_b atom and the H on the C_c atom (OH_bH_c) and the other with the OH on the C_a and the H on the C_c (OH_aH_c).

The dissociation energy values (ΔE_{diss}) are very similar and amount to about -1.9 eV. The dissociation energy becomes slightly smaller (by about 0.15-0.2 eV) when these types of dissociation happen on a TiO_2 supported graphene sheet, as a consequence of a reduced adhesion energy between the two materials due to the additional distortions. On the contrary, it becomes larger when the dissociation takes place at the interface (up to 2.10 eV). This is because the OH fragment establishes an additional stable bond with the Ti_{5c} on the anatase surface.

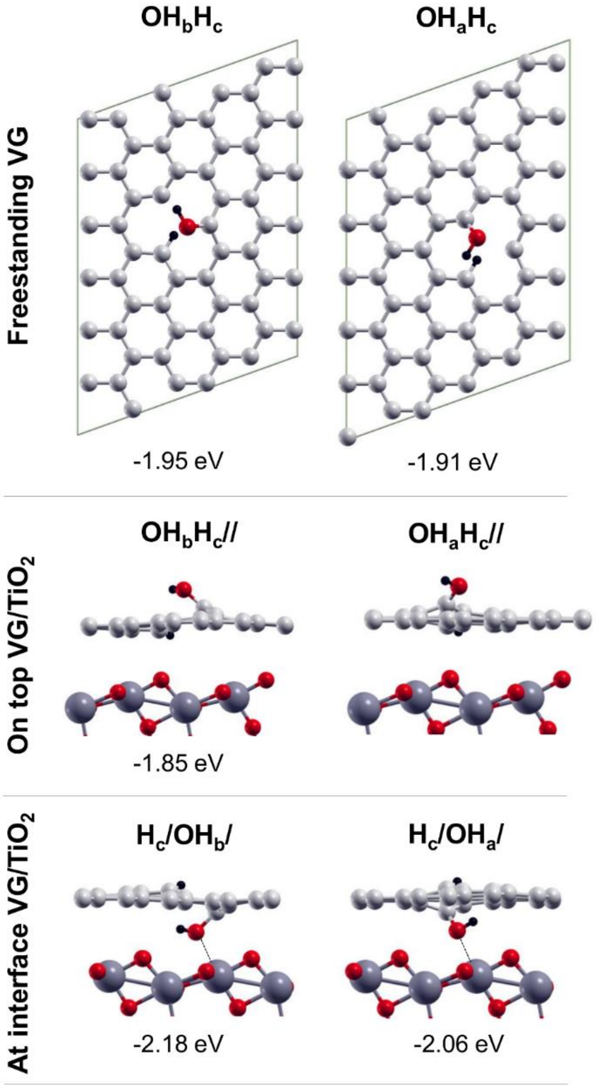

Figure 3-10 Top views of the partially dissociated products of water (OH+H) on free-standing VG (top line), side views of the partially dissociated products of water on top of VG/TiO$_2$ (middle line) and at the interfaces of VG/TiO$_2$ (bottom line). Labels and dissociation energies are reported above and below each configuration, respectively, and defined in section 3.2 of Computational methods. Small red, light grey and black balls represent O atoms, C atoms and H atoms. Big dark grey balls represent Ti atoms.

When these dissociation processes happen on a supported graphene sheet, the energy gain is slightly less negative but the $O_{ab}2H_c$// configuration is still the most favorable (-4.32 eV). On the contrary, when these dissociations take place at the interface, we observed that the O of the keto group for the first two systems on the left side is largely stabilized by a strong interaction with the Ti_{5c} on the anatase surface. Therefore, an inversion in the relative stability is clearly observed and water dissociation at the VG/TiO_2 interface in the $H_bH_c/O_a/$ configuration becomes very stable with a ΔE_{diss} of -4.29 eV, similar to that of $O_{ab}2H_c//$.

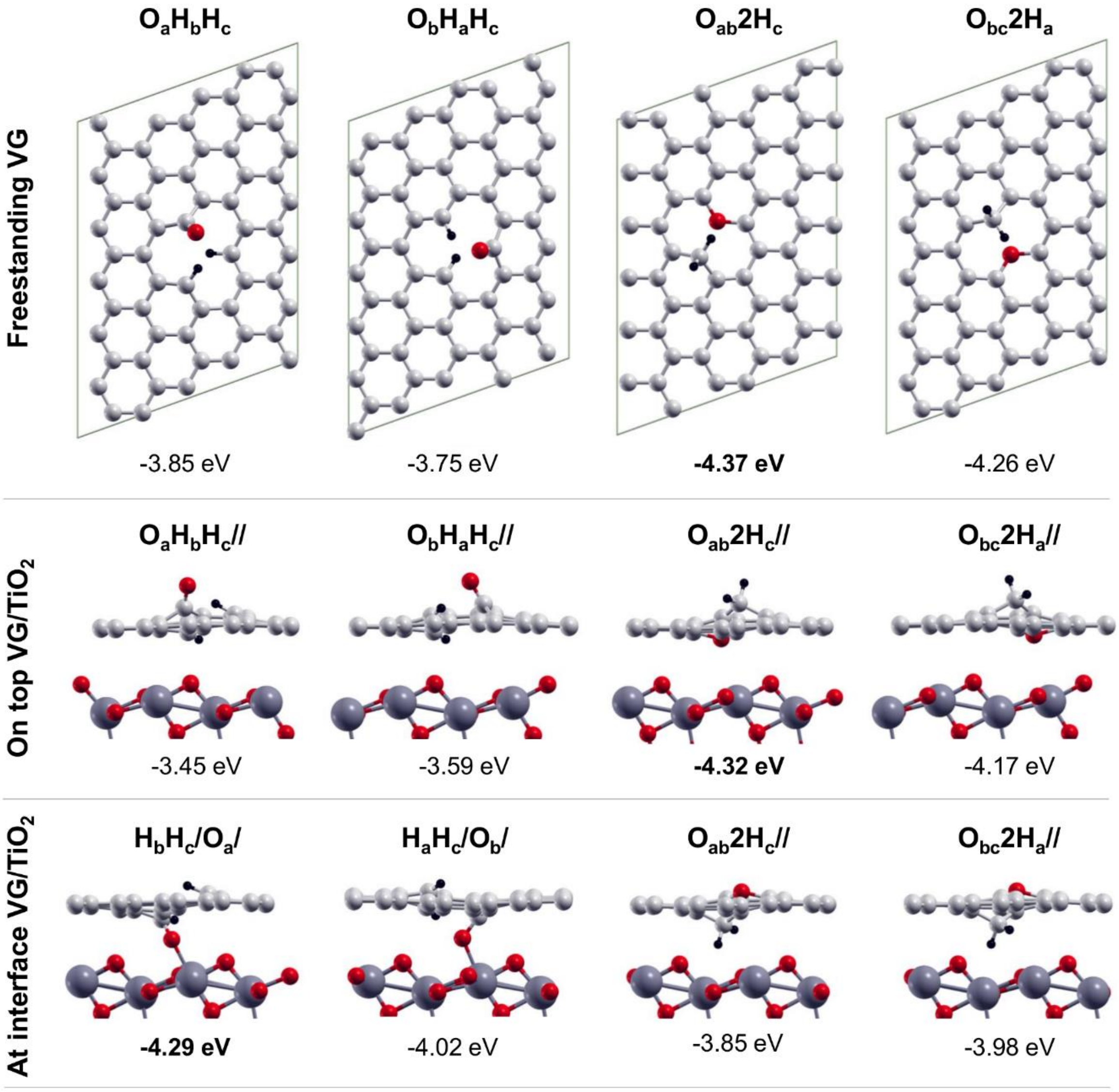

Figure 3-11 Top views of the fully dissociated products of water on free-standing VG (top line); side views of the fully dissociated products of water (O+H+H) on top of VG/TiO_2 (middle line) and at the interfaces of VG/TiO_2 (bottom line). Labels and dissociation energies are reported above and below each configuration, respectively,

and defined in section 3.2 of Computational methods. Small red, light grey and black balls represent O atoms, C atoms and H atoms. Big dark grey balls represent Ti atoms.

In **Figure 3-12** we show a number of configurations where either one or two H atoms are transferred to the TiO_2 surface. In one case, we even form an H_2 molecule that is physisorbed on the surface. However, as it is evident from analyzing the energies of dissociation, all these configurations are less stable than those proposed in **Figure 3-11**, where both the H atoms saturated two undercoordinated C atoms of the defective graphene layer. Note that if one H atom is transferred, the O atom coming from the water saturates two C atoms by forming an ether group, whereas when both H atoms are transferred, the remaining O atoms replaces the missing carbon in the graphene sheets and is three-fold coordinated to the three undercoordinated C atoms of the vacancy (O_{abc}).

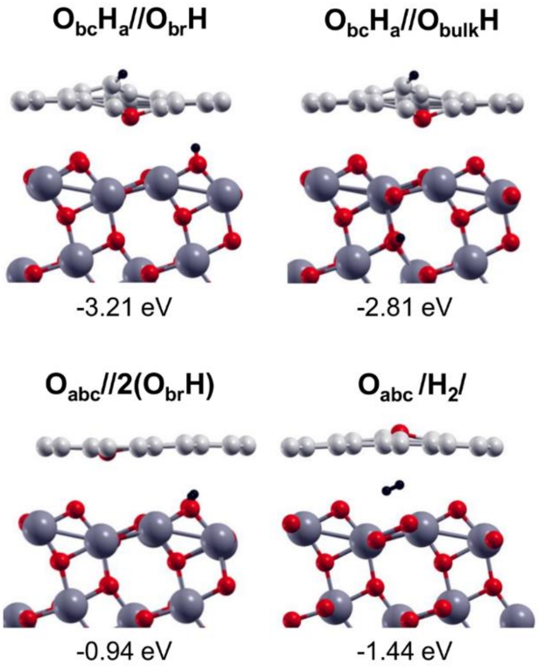

Figure 3-12 Side view of the total dissociation of water (O+H+H) with one H atom transferred to the O_{br} of the TiO_2 surface (top line, left) and the consequent diffusion of the H in the subsurface layer (top line, right). Side view of the total dissociation of water (O+H+H) with both H transferred to O_{br} atoms of the TiO_2 surface (bottom line, left) and, finally, side view of the desorption of a H_2 molecule at the VG/TiO_2 interface (bottom line, right). Labels and dissociation energies are reported above and below each configuration, respectively, and defined in

section 3.2 of Computational methods. Small red, light grey and black balls represent O atoms, C atoms and H atoms. Big dark grey balls represent Ti atoms.

In the last part of this section devoted to water dissociation on and at the interface of VG/TiO_2, we are going to present an overview, as sketched in **Figure 3-13**, on what can actually happen when water comes from the top or is intercalated in the confined zone between the two materials, considering all the configurations discussed above.

If water comes from the top, it may first physisorb (H_2O//) and then dissociated into two fragments (OH_bH_c//) and, then, further into three ($O_{ab}2H_c$// or $O_{ab}H_bH_c$//). The final product $O_{ab}2H_c$// is very stable (ΔE_{diss} = -4.32 eV) and more stable than $O_{ab}H_bH_c$//, however, the latter could eventually further evolve into the product H_bH_c/O_a/, where the O atom coming from the water full dissociation is bridging between a C atom of the graphene sheet and a Ti_{5c} atom on the TiO_2 surface. This final product is also extremely stable (ΔE_{diss} = -4.29 eV) and competes with $O_{ab}2H_c$//.

If water successfully intercalates in the interface zone, molecularly bound to a Ti_{5c} atom of the TiO_2 surface, there are several possibility for the next chemical step: the water dissociation into two fragments (OH+H) may result i) into an OH that is bridging between the two materials and the H bound to an undercoordinated C atom on graphene (H_c/OH_a/ and H_c/OH_b/) or ii) into an OH that is bridging between the two materials and the H bound to the same C atom as the OH (H_c/OH_c) or iii) into an OH that is bridging between the two materials and the H bound to a two-fold O atom on the TiO_2 surface (/$OH_c/O_{br}H$). Each of these four (OH+H) configurations can evolve in a fully dissociated product (O+H+H), as described in **Figure 3-13**. The most stable final configuration is again the H_bH_c/O_a/, which was already discussed above (-4.29 eV). We wish to note that the OH species in the H_c/OH_b/ configuration is found to preferentially evolve into H_aH_c/O_b/ than into $H_c/O_b/O_{br}H$: -4.02 eV vs -2.09 eV.

Therefore, this analysis allows us to conclude that one of the most stable products, independently of the water origin, from the top or through the interface, is H_bH_c/O_a/, where there is an O atom strongly linked to both the materials: to graphene with a C-O covalent bond (1.26 Å) and to TiO_2 with a Ti-O strong covalent bond (2.06 Å).

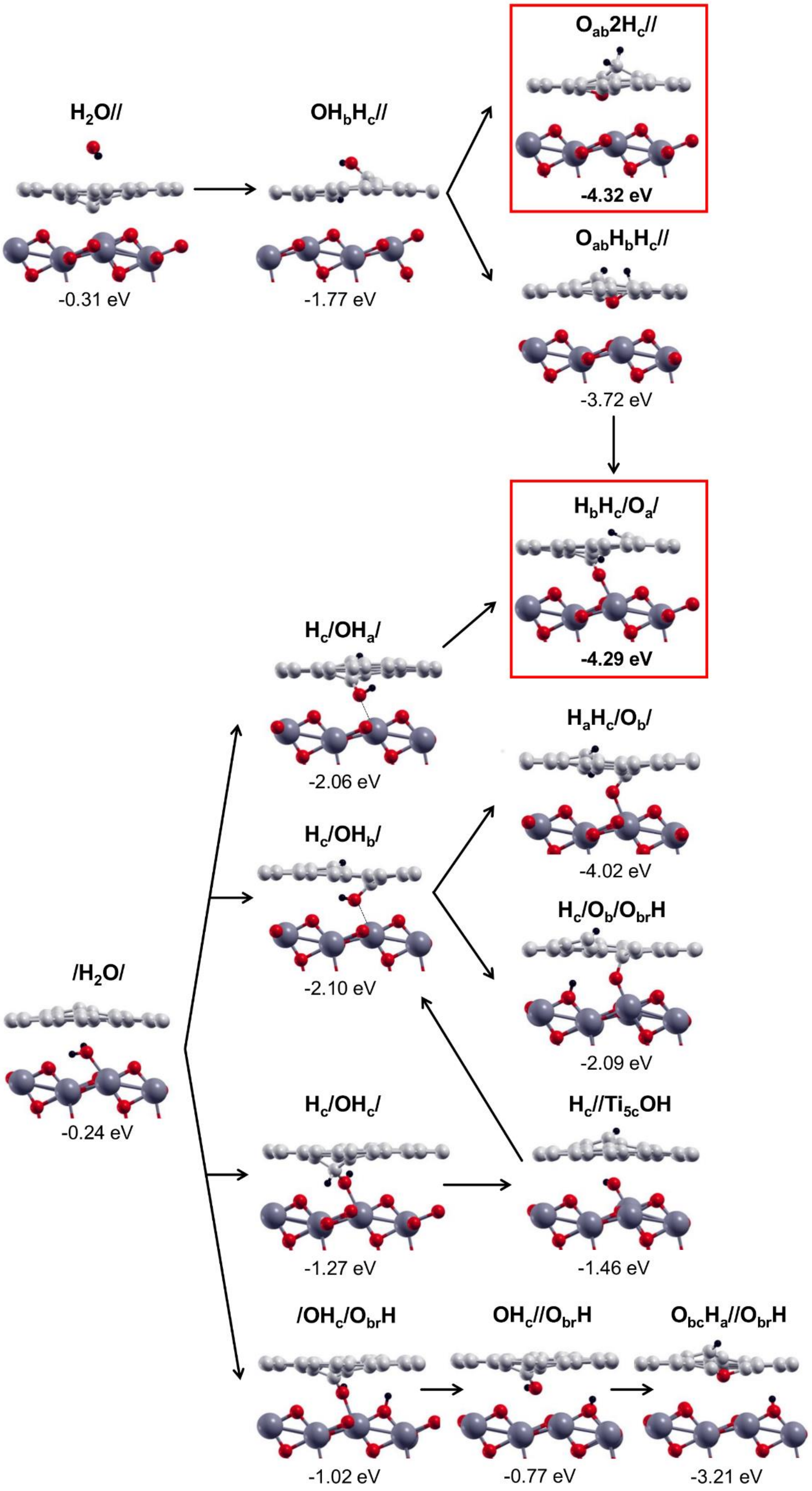
H_2O//
-0.31 eV
OH_bH_c//
-1.77 eV
$O_{ab}2H_c$//
-4.32 eV
$O_{ab}H_bH_c$//
-3.72 eV
H_bH_c/O_a/
-4.29 eV
H_c/OH_a/
-2.06 eV
H_aH_c/O_b/
-4.02 eV
H_c/OH_b/
-2.10 eV
H_c/O_b/$O_{br}H$
-2.09 eV
/H_2O/
-0.24 eV
H_c/OH_c/
-1.27 eV
H_c//$Ti_{5c}OH$
-1.46 eV
/OH_c/$O_{br}H$
-1.02 eV
OH_c//$O_{br}H$
-0.77 eV
$O_{bc}H_a$//$O_{br}H$
-3.21 eV

Figure 3-13 Side views of water adsorption on top or at the VG/TiO_2 interface (left column); side views of partial water dissociation in OH and H on top and at the VG/TiO_2 interfaces (middle column) and finally side views of the various possible step of total water dissociation (right column). Labels and adsorption/dissociation energies are reported above and below each configuration, respectively, and defined in section 3.2 of Computational methods. Small red, light grey and black balls represent O atoms, C atoms and H atoms. Big dark grey balls represent Ti atoms.

3.5.2.1 Cover effect

In this last section, we analyze the cover effect on water dissociation. Whereas the cover effect on molecular water adsorption on TiO_2 is a negative one (from -0.97 to -0.24 eV), as shown in **Figure 3-9** and discussed in section 3.5.1, in the case of dissociated water the cover effect is positive and largely stabilizes the OH+H dissociation (from -0.63 to -1.02 eV) by forming a bridging species with the OH bound to both a C atom of the graphene sheet and a Ti atom on the TiO_2 surface (see **Figure 3-14**).

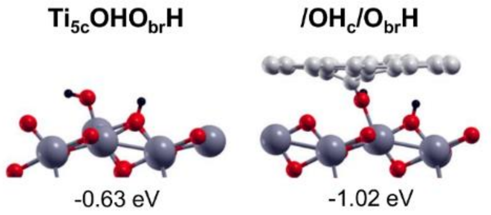

Figure 3-14 On the left side view of water dissociation on bare TiO_2 (101) surface and on the right the cover effect of defective graphene on water dissociation at TiO_2 surface. Labels and dissociation energies are reported above and below each configuration, respectively, and defined in section 3.2 of Computational methods. Small red, light grey and black balls represent O atoms, C atoms and H atoms. Big dark grey balls represent Ti atoms.

3.5.2.2 Electronic properties of hydrated VG/TiO_2

We investigated the electronic properties of the two most stable structures resulting from water full dissociation on VG/TiO_2, which are $O_{ab}2H_c//$ and $H_bH_c/O_a/$. The aim is to determine the water effect on the electronic properties of the composite. We recall from section 3.4 that VG—O_{br} is metallic whereas VG---Ti_{5c} is semiconducting with a 0.27 eV band gap (see DOS in **Figure 3-7**). After water dissociation, we observe a semiconducting character in the DOS

(**Figure 3-15**) of both the hydrated structures ($O_{ab}2H_c$// and H_bH_c/O_a/) with a band gap of 0.49 and 0.40 eV, respectively.

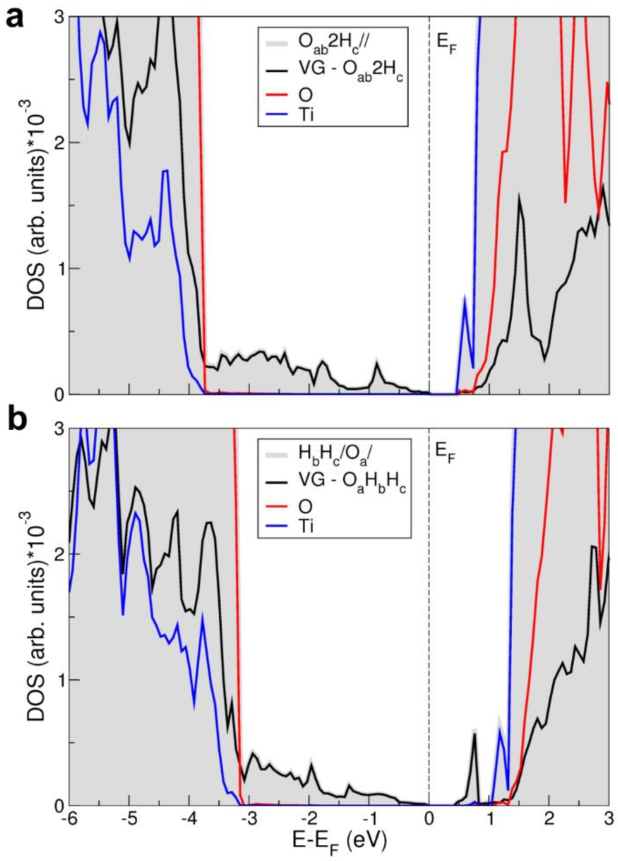

Figure 3-15 Total and projected DOS for $O_{ab}2H_c$// (a) and H_bH_c/O_a/ (b). In the DOS, the filled grey area represents the total DOS, the black lines are DOS projected on graphene (G or VG) together with the fragment coming from water dissociation (O+H+H). The red and blue lines are DOS projected on all O atoms and all Ti atoms in the TiO_2 slab, respectively. The structures of $O_{ab}2H_c$// and H_bH_c/O_a/ can be seen in **Figure 3-13**. Fermi energy (E_F) is set at the top of the occupied states.

3.5.2.3 Effect of an underlying reduced TiO_2 surface

In this last section we discuss what could happen if the TiO_2 system were reduced, as often it is the case in real samples. We, thus considered the possibility that the water full dissociation (configuration H_bH_c/O_a/) takes place on a non-stoichiometric TiO_2 slab presenting an oxygen vacancy V_O in the second layer of the slab ($H_bH_c/O_a/V_O$), as shown on the left side of **Figure 3-15**. Considering that excess O atoms on the surface are known to diffuse into the bulk of

TiO_2 to heal eventual subsurface or bulk oxygen vacancies in anatase TiO_2,[218] we transferred the O atom from the interface to the V_O site and fully relaxed the structure (H_bH_c//), as shown on the right side of **Figure 3-15**. The energy gain that is computed is rather large since it amounts to -1.76 eV. Therefore, we may conclude that the presence of an underlying reduced metal oxide support may further complete the water splitting at the VG/TiO_2 interface by attracting the oxygen atom from water into the subsurface layers or in the bulk of the oxide where vacancies are present.

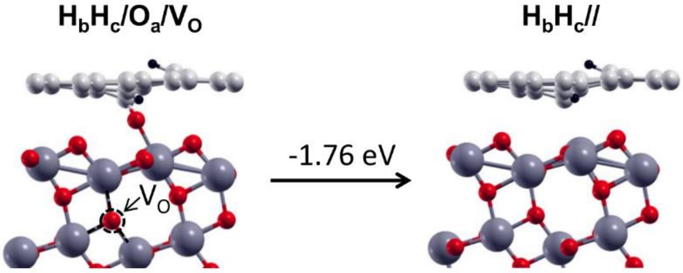

Figure 3-16 On the left, side view of the fully dissociated product of water at the VG/TiO_2 interface with one oxygen vacancy (V_O) in the subsurface layer of TiO_2. On the right, the oxygen O_a from the water heals the V_O in TiO_2. The energy gain during the transfer/healing process is shown on top of the arrow. Labels are reported above each configuration. Small red, light grey and black balls represent O atoms, C atoms and H atoms. Big dark grey balls represent Ti atoms. The dotted black circle represents the V_O in TiO_2.

3.6 Conclusions

To summarize and conclude this chapter, we first want to stress that a comparative investigation of the C monovacancy in graphene, comparing a GGA functional, i.e. PBE-D2, and a hybrid functional, i.e. B3LYP-D*, has clearly evidenced that the former is not suited or accurate enough to study these magnetic systems. Although PBE-D2 is capable of reproducing a magnetic ground state, the magnetic moment is found to be partially quenched (from 2 to about 1.5 μ_B) because of a spurious charge transfer from the $v\pi^\alpha$ band to the $v\pi^\beta$ one, which can be evidenced by both the band structure or the density of states. The partial passivation induced by the charge transfer is not observed when a hybrid functional is applied (this is not true only for B3LYP-D*, but we have also tested HSE06-D2, B3PW91 and PBE0, as discussed above) because the two bands are found not to cross the Fermi level, resulting in a fully occupied $v\pi^{\alpha}$ band and a fully unoccupied $v\pi^{\beta}$ one (total magnetization 2 μ_B). Notably, such splitting was recently experimentally determined to be in the range of 20-60 meV,[204] in excellent agreement with the value computed by B3LYP-D* of 30 meV (for the 16×16 cell).

The B3LYP-D* magnetization is not sensible to the supercell size and the k-point mesh density, as it is observed, both in the present and in previous works, for PBE-D2. The hybrid functional results are thus very robust and were also successfully tested against antiferromagnetic (S_{os}) and diamagnetic (S_{cs}) solutions, whose structures present a peculiar out-of-plane distortion of one of the undercoordinated C atom.

The atomic structure of the interface between defective graphene and anatase TiO_2 surface, together with its electronic properties and chemical reactivity with water molecules were systematically investigated by dispersion-corrected hybrid density functional calculations. The magnetism observed for the carbon monovacancy model in graphene (VG) is found to quench when VG is put on $TiO_2(101)$ surface. The interaction at the VG/TiO_2 interface is typically based on van der Waals or dispersion forces. However, after overcoming some energy barrier, a C-O bond may be formed at the interface. The chemical adsorption of VG on $TiO_2(101)$ leads to a metallic character of the hybrid system, whereas the physical adsorption presents semiconducting properties with a small band gap of 0.27 eV. The adsorption energy of molecular water on top of VG/TiO_2 interface is slightly increased with respect to the free-standing case by about -0.1 eV. Water molecules can dissociate either on top or at the VG/TiO_2 interface. Our study allowed the definition of the possible reaction paths and of the most stable dissociation products. Full dissociation into O+H+H is found to be largely preferred. Those configurations involve the formation of a methylene (CH_2) and one ether (-COC-) group at the C vacancy site in VG ($O_{ab}2H_c$//) or two CH bonds and the O atom strongly linked to both materials forming a C-O bond on one side and a O-Ti_{5c} bond on the other (H_bH_c/O_a/). This O atom is an interface species. Very importantly, if the underlying TiO_2 substrate is partially reduced, with oxygen vacancies in the subsurface layers, this interface O atom is found to be subject to a force that would favourably drive it down to heal the vacancy (by -1.8 eV). Then, water splitting is fully achieved since the two H atoms are left on the graphene layer, whereas the O atom is deep in the TiO_2 bulk.

To conclude, this comprehensive study provides important information on the details of the atomic structure and electronic properties of graphene/titania composites, even when the conditions are not as ideal as one would wish, i.e., in the presence of C vacancies in the graphene sheet prepared on top of the TiO_2 sample, in the presence of unwanted water molecules in the experimental conditions, and in the presence of oxygen vacancies when the TiO_2 sample is not fully stoichiometric because of reducing preparation conditions or because of severe annealing processes. The results give a clear overview of what chemistry would take place in these real complex composite systems.

Chapter 4 Functionalized TiO_2 nanoparticles for bio-conjugation: DOPAC linker

4.1 Introduction

Bionanotechnology can be defined as the field representing all facets of research at the intersection of biology and nanomaterials. One of the goals is that of utilizing the unique properties available to nanomaterials within a biological setting. For example, using nanoparticles (NPs) to mediate targeted drug delivery or in vivo imaging, with the intent of overcoming many of the problems associated with the systemic administration of drugs and of contrast agents.

As synthesized, many metal, semiconductor, and carbon-based NPs are hydrophobic and need to be made hydrophilic and biocompatible by chemical modification of their surfaces (e.g. PEG coating). The ligands may also provide additional chemical "handles" that can act as sites for subsequent bioconjugation.

Various types of NP bioconjugates can be designed,[30] which are capable of multiple and simultaneous activities, such as tumor-targeting, active sensing, diagnostics, and delivery of drugs or imaging contrast agents.[219]

NPs bioconjugation should ideally be achieved with control over several aspects, such as: i) the number of conjugating sites on the NP; ii) the number of biomolecules that can be tethered; iii) the distance between the biomolecule and the NP; iv) the type of linkage (e.g. permanent or labile); v) the preservation of function and activity of both the NP and the biomolecule.

The type of linkage of biomolecules to NPs is a crucial factor, which is specifically dependent on the desired application. The conjugation could be based on non-covalent interactions (H-bonding, dispersion forces, electrostatic interactions) or covalent bonds.

Bifunctional linkers provide an interesting bioconjugation strategy mostly because they behave as spacers between the NP and the biomolecules, which helps in maintaining their optimal respective functions and activities. Moreover, by the use of bifunctional linkers it is possible to control the binding strength between the NP and the biomolecule with the proper choice of the two functional groups used for anchoring the surface and for tethering the biomolecule.[36] Additionally, it is possible to bridge the electronic properties of the NP material to those of the biomolecule (e.g. protein, oligonucleotides, DNA fragments, etc.).[220]

Catechol derivatives are an effective class of bifunctional linkers for metal oxide NPs since they can stably anchor the oxide surface by forming relative strong coordination bonds with undercoordinated surface metal atoms.[221] Among them, DOPAC (3,4-dihydroxyphenilacetic acid), is one of the most relevant bifunctional linkers used for direct conjugation to metal oxide NP surfaces.[222] On one side of the benzene ring, the enediol portion binds the surface through coordinative bonds, whereas on the other side, the carboxylic acids remains exposed to the surrounding environment, imparting water dispersibility and acting as a potential handle for biomolecules. The OH dissociative binding of catechol to metal atoms is preferred to carboxylic and phosphonic groups since a higher ligand-metal oxide electronic coupling is observed.[223]

Among metal oxides, iron oxides[224, 225] and titanium dioxide are the most popular in the biomedical applications. The interest in titanium dioxide is motivated by its unique photocatalytic properties, excellent biocompatibility, high chemical stability and low toxicity.[226] It is also an inexpensive material. Recent advances in the biomedical applications of TiO_2 range from photodynamic therapy for cancer treatment,[84, 227, 228] drug delivery systems,[229] cell imaging,[230, 231, 232] biosensors, antimicrobial and bactericidal action and genetic engineering.[92, 233]

Titanium dioxide NPs are typically prepared through sol-gel chemistry. Below 10-15 nm, the anatase phase is preferred. The thermodynamically most stable anatase NP shape is a decahedron where the two surfaces are exposed: (101) and (001). However, concentration and pH condition are growth-determining factors and in condition of high dilution, the faceted NPs partially dissolve and acquire a spherical shape.[11] This is more interesting for biomedical application since curved nanoparticles present a higher number of low-coordinated sites[118, 234] that are better suited for the linker anchoring.

Catechol and catechol derivatives can bidentate to surface fivefold coordinated Ti atoms or even chelate to fourfold coordinated Ti sites.[81, 235, 236, 237] Interestingly, their presence on the surface is capable of shifting the absorption properties of TiO_2 from the UV to the vis region[11] because they introduce molecular states in the band gap. For the DOPAC/TiO_2 NP system, an effective charge transfer mechanism was reported by surface-enhanced Raman spectroscopy (SER) measurements with an unexpected dependence on coverage and shape. This effective charge transfer is probably at the basis of the instantaneous charge separation observed in peptides/DOPAC/TiO_2 NPs triads.[238] The Raman signal intensity was also found to depend on the number of surface binding sites, electron density of the ligands and dipole moment. Biofunctionalized TiO_2 nanomaterials through DOPAC linker are capable of bio-manipulation via altering intracellular biochemical pathways.[228] DOPAC attached epidermal growth factor receptor allowed for both cellular and subcellular NP delivery,[239] whereas DOPAC attached antibody allowed for targeted cancer therapy.[84] Although bifunctional linkers on metal oxides are commonly used in biomedical applications, as presented above, still little is known of the atomistic details and electronic properties of these hybrid systems at the nanoscale level.

In this work, we present a computational multiscale investigation of DOPAC/TiO_2 NP composite system, where realistic sized TiO_2 NPs of 700 atoms are used (2.2 nm)[118, 234] We investigate several aspects related to both structural and electronic properties. First, we consider the low coverage regime and compare different adsorption modes of the catechol-like molecules on a spherical TiO_2 nanoparticle model. Then, we analyze the electronic structure details and the effect of light irradiation for the composite: exciton formation, trapping, charge carriers diffusion and recombination processes. Further, we go to an increasing coverage regime on the NP, up to full coverage (46 DOPAC molecules anchored to the surface). We learn how the molecules self-assemble on the surface and what is the coverage effect on the electronic properties of the composite systems. For the fully covered NPs, we perform molecular dynamics runs and observe how the molecules rearrange on the surface. All the calculations for the low coverage regime are done at both hybrid density functional theory (DFT-B3LYP) and self-consistent-charge density functional tight-binding (SCC-DFTB) level of theory, which allows to assess the accuracy of DFTB in the description of both structural and electronic properties of these complex systems. The high coverage regime has been investigated by means of DFTB static and dynamic calculations, except for the electronic properties that were determined through single point DFT calculations on the DFTB geometries for a correct description of the TiO_2 band gap.

Our computational results are discussed through a comparative analysis with all the available experimental observations and data, regarding the mode of adsorption, the absorption properties, the charge separation effects, the effects of increasing coverage and stoichiometry of the nanoparticle/linkers complex. The size of the real TiO_2 nanoparticles used in the experiments is similar to that of the simulated systems. The experimental findings are mainly based on spectrophotometric measurements, electron paramagnetic resonance (EPR), nuclear magnetic resonance (NMR), X-ray absorption measurements (XANES and EXAFS), infrared (IR) and surface-enhanced Raman spectroscopy (SER).[11, 81, 235, 238, 240, 241, 242, 243, 244]

4.2 Computational details

In this work, we used two levels of theory: density functional theory (DFT) and self-consistent charge density functional tight-binding (SCC-DFTB).[245, 246] Both methods have been employed for geometry optimization and electronic structure calculations. The molecular dynamics simulations have been performed only by using the SCC-DFTB approach.

All the DFT calculations have been carried out with the CRYSTAL14 simulation code,[197] where the Kohn-Sham orbitals are expanded in Gaussian-type orbitals. The all-electron basis sets are Ti 86-4111(d41), O 8-4111(d1) for the oxygens of TiO_2; H 5-111(p1), C 6-31111 (d1), and O 8-41111 (d1) have been employed for hydrogen, carbon, and oxygen of the adsorbed DOPAC molecule. We used the B3LYP functional,[198, 199] corrected by Grimme's D* to include dispersion forces.[200, 201] The cut-off limits in the evaluation of Coulomb and exchange series/sums appearing in the SCF equation were set to 10^{-7} for Coulomb overlap tolerance, 10^{-7} for Coulomb penetration tolerance, 10^{-7} for exchange overlap tolerance, 10^{-7} for exchange pseudo-overlap in the direct space, and 10^{-14} for exchange pseudo-overlap in the reciprocal space. The condition for the SCF convergence was set to 10^{-6} a.u. on the total energy difference between two subsequence cycles. The equilibrium structure is determined by using a quasi-Newton algorithm with a BFGS Hessian updating scheme.[247] Geometry optimization was performed without any symmetry constraint, forces were relaxed to be less than 4.5 × 10^{-4} au and displacements to be less than 1.8 × 10^{-3} au.

For all the SCC-DFTB calculations we used the DFTB+ open source package.[248] We employed the MATORG parameterization set[249] for the pairwise interaction of the atoms of both TiO_2 and adsorbed molecules. The description of the hydrogen bonding has been further improved with the inclusion of the empirical HBD correction ($\zeta = 4$).[250, 251] For geometry relaxations, the threshold for the convergence of the self-consistent charge (SCC) procedure was set to 10^{-6} charge au and forces were relaxed to less than 10^{-4} au.

The anatase TiO_2 spherical nanoparticle (NP) model used throughout this work has been designed through global optimization with a simulated annealing process at the SCC-DFTB level of theory in a previous work by our group.[118] The stoichiometry of the model is $(TiO_2)_{223}\cdot 10H_2O$ and it is characterized by an equivalent diameter of 2.2 nm. The nanoparticle has been treated as a large isolated molecule in the vacuum without any periodic boundary condition.

For the slab calculation (section 4.3.1), we modeled the (101) anatase surface by a three tri-atomic layers of TiO_2 slab. The bottom layer was kept fixed to the optimized bulk positions during the geometry optimization. Periodicity was considered only along the $[10\bar{1}]$ and [010] directions, while no periodic boundary conditions were imposed in the direction perpendicular to the surface. We used a 1×4 supercell model (144 atoms), already described in Chapter 3. Configurations have been optimized using a k-point mesh of 2×2×1 to ensure the convergence of the electronic structure.

The total adsorption energy per DOPAC molecule on the spherical nanoparticle has been defined as:

$$\Delta E_{ads}^{mol} = (E_{(NP/slab)+n_{mol}} - [E_{(NP/slab)} + n_{mol}E_{mol}])/n_{mol} \tag{4.1}$$

where $E_{(NP/slab)+n_{mol}}$ is the total energy of the whole system, $E_{NP/slab}$ is the energy of the NP/slab models, E_{mol} is the energy of the molecule in the gas phase and n_{mol} is the number of molecules adsorbed on the NP/slab.

Vertical and adiabatic ionization potentials (IP) are computed by removing one electron from the model of functionalized nanoparticle in its original geometry and by performing full atomic relaxation, respectively. Vertical and adiabatic electron affinities (EA) are computed by adding one electron to the model of functionalized nanoparticle in its original geometry and by performing full atomic relaxation, respectively.

Trapping energies (ΔE_{trap}) are computed as the energy difference between the isolated charges or electron−hole pairs in the trapping geometry and the delocalized solution in the neutral ground state geometry. Distortion energies ($\Delta E_{dist} = E[S_0(T_1)] - E[S_0]$) are obtained as the difference between the energy in the trapping geometry and in the optimized geometry for the S_0 state. Emission energies ($\Delta E_{em} = E[S_0(T_1)] - E[T_1]$) are the energy differences between the S_0 and T_1 both in the T_1 optimized geometry. When they are negative, we can observe radiative emission.

Simulated total densities of states (DOS) of the nanoparticles have been obtained through the convolution of Gaussian peaks ($\sigma = 0.005$ eV for DFT calculations, $\sigma = 0.05$ eV for DFTB) centered at the Kohn-Sham energy eigenvalue of each orbital. Projected densities of states (PDOS) have been obtained by using the coefficients in the linear combination of atomic orbitals (LCAO) of each molecular orbital: summing the squares of the coefficients of all the atomic orbitals centered on a certain atom type results, after normalization, in the relative contribution of each atom type to a specific eigenstate. Then, the various projections are obtained from the convolution of Gaussian peaks with heights that are proportional to the relative contribution. For spin polarized systems, (projected) densities of states are calculated using the Kohn-Sham eigenvalues of alpha or beta population separately. The zero energy for all the DOS is set to the vacuum level, corresponding to an electron at an infinite distance from the surface.

Born−Oppenheimer molecular dynamics simulations were performed on the high coverage functionalized nanoparticle models within the canonical ensemble (NVT). The Newton equations of motion were integrated with the velocity Verlet algorithm, with a time step of 0.5 fs. During the molecular dynamic simulation, the temperature has been kept constant to 300 K by using the Nosé − Hoover thermostat (time constant of 0.04 ps) and the system has been let evolve for 10 ps.

4.3 Single linker adsorption on TiO_2 spherical nanoparticle

In this section, we will present the study of a single DOPAC molecule adsorption on a realistic model of spherical anatase TiO_2 nanoparticle (**Figure 4-1**a). Different adsorption modes are considered. For few selected configurations, we also investigate electronic properties by means of the total (DOS) and projected density of states (PDOS). For the most stable adsorption configuration we analyze the effect of light irradiation in terms of the result of a vertical excitation (exciton formation), atomic relaxation in the excited state (exciton self-trapping) and charge carriers dynamic evolution through charge hopping.

The spherical NPs that are used in this work present a diameter of 2.2 nm, similar to those used in several experimental works of NP+linker (DOPAC or dopamine) complexation.[81, 84, 228, 238, 242, 243, 244] Experimental characterization of this type of NPs was obtained by XANES spectroscopy.[240] Four-, five- and six-fold coordinated Ti atoms were identified according to the position and the intensity of the preedge peaks. As the size of the NP decreases, the number of low coordinated sites increases. In several experimental studies, the fraction of surface TiO_2 in these NPs was estimated based on the number density of Ti on different lattice planes and on an assumed equal probability of exposure for different lattice planes.[241] According to this approach, the superficial Ti atoms are proportional to $\frac{12.5}{d}$, where d is the diameter of the NP in Å. For a NP with diameter of 2.2 nm, the fraction of surface TiO_2 is expected to be 56%. We have applied the formula $[Ti_{surf}] = [TiO_2] \times \frac{12.5}{d}$ to evaluate the number of surface Ti site per particle, considering a perfect spherical volume ($\frac{4}{3}\pi r^3$) and the anatase density of 3.78 g/cm^3. We obtain 90 surface Ti sites that rather nicely compares with the actual number of Ti surface sites in the NP model (Ti_{4c}+Ti_{5c} in **Figure 4-1**a), which is 106 (44+62, respectively). This confirms that our model satisfactorily resembles experimental NPs.

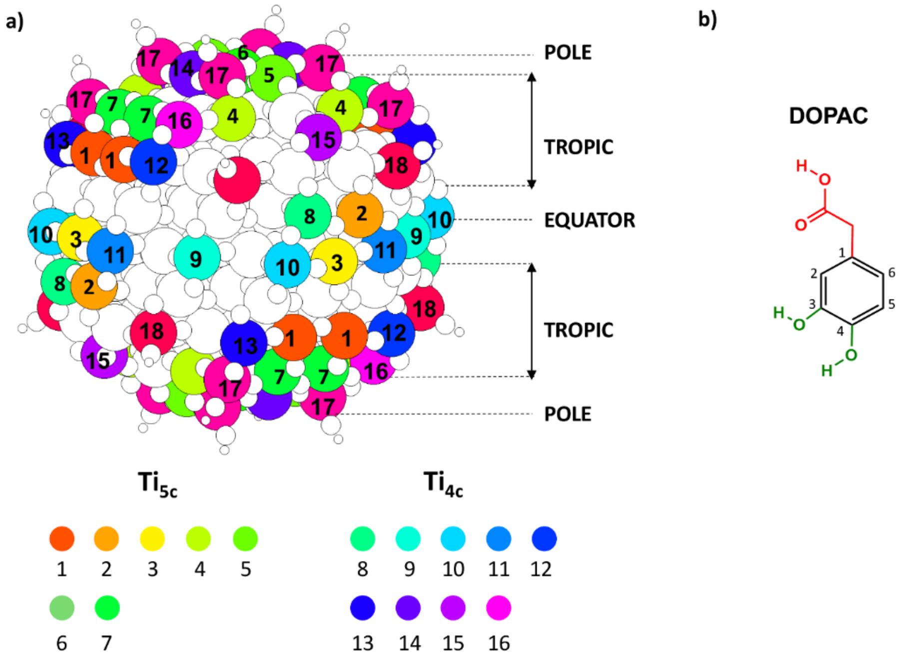

Figure 4-1 a) Map of the Ti atoms of the spherical anatase TiO_2 nanoparticle with different coordination environment, visually shown by the color-coding and numbering. Different areas of the sphere are identified: pole, tropic and equator. b) The structure of the DOPAC [3,4 dihydroxyphenilaceticacid] with the enediol group in green and the carboxylic group in red.

4.3.1 DOPAC adsorption modes

DOPAC is a bifunctional linker molecule (see **Figure 4-1**b). It is an enediol species, a derivative of catechol, with an additional carboxyl group on the ring. Diols bind quite strongly to metal oxide surfaces and have been utilized successfully in a range of conjugation protocols. Among diols, catechol and catechol derivatives are particularly strongly binding. While the bidentate catechol portion of DOPAC binds to the oxide surface through coordinative bonds, the carboxyl group could remain exposed to the surrounding environment, improving the water dispersibility of the nanoparticle and providing a hook to tether biomolecules or drugs. However, the carboxylic group is known to strongly bind undercoordinated Ti atoms on TiO_2 surface, for which is commonly used to anchor dyes in DSSC.[252] Therefore, the carboxylic group could be competitive to the catechol functionality for the surface attachment.

Base on that, we performed a preliminary DFT study of DOPAC adsorbed on a slab model of the flat anatase (101) TiO_2 surface, because no data was present in literature. We analysed two different binding modes: bidentate and tetradentate. The bidentate mode can take place via carboxylic group or via vicinal hydroxyl groups. The adsorption via hydroxyl groups is preferable (by 0.11 eV) compared to the adsorption via the carboxylic group.

Therefore, after anchoring DOPAC by the two hydroxyl groups, we performed molecular dynamics (NVT ensemble, T=300 K, DFTB, 20 ps) to simulate the optimal position of the molecule relative to the slab. From our simulation there is evidence that the carboxylic group in DOPAC gets closer to the surface, driven by the interaction of the carbonyl (=O) oxygen with the underlying five-fold coordinated Ti atom (2.77 Å). The simulation time was not sufficient to observe the dissociation of the carboxylic group, although our estimations showed that the total deprotonation of DOPAC (tetradentate configuration) is energetically favourable, with a binding energy of -2.46 eV. In this configuration (**Figure 4-2** c), DOPAC binds to four different Ti atoms in a bidentate fashion, both on the side of the catechol functionality and on that of the carboxylic group.

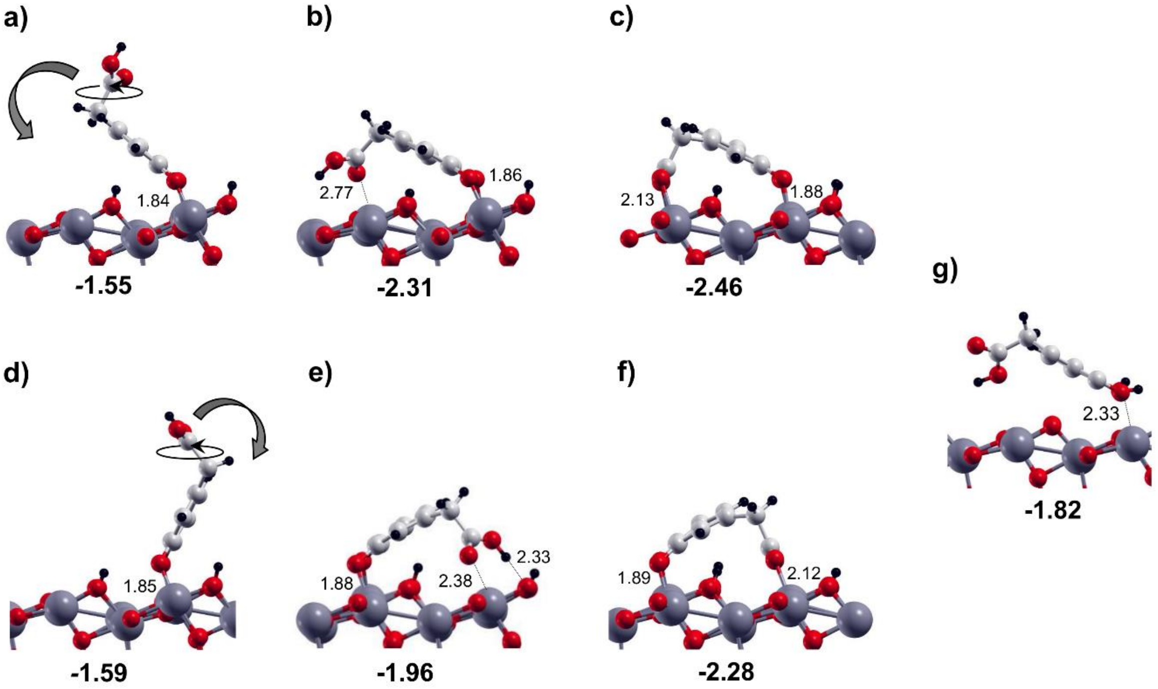

Figure 4-2 Ball and stick representation (side views) of DOPAC in the bidentate mode with the catechol moieties and bent to the left a) and right d) respect to the [010] direction. The consequentially step during the DOPAC approaching on the TiO_2 surface (b, e) ending with the tetradentate c, f) configurations are also shown. On the right, the undissociated configuration. Labels and dissociation energy (in eV) are reported above and below

each configuration, respectively. In light grey C atoms, in red O atom, in dark grey Ti atoms and in black H atoms. Relevant distances are reported in Å.

In **Figure 4-3** the configurations that have been considered for the spherical nanoparticle model are presented. The DOPAC molecules can adsorb through dissociation of the two OH groups with the two dissociated protons transferred to O_{2c} atoms. The binding may take place either in a bidentate ("B") or in a chelated ("C") fashion. The map of the under-coordinated Ti atoms present on the nanoparticle's surface is shown in **Figure 4-1**a. Later on, for the tag labeling of the binding Ti atoms, we will refer to the numbering presented in **Figure 4-1**a.

Differently from the adsorption on the surface, the structure bound to four Ti atoms in bidentate adsorption modes on the NP surface, i.e. $B^{3,11}B^{1,1'}$ (**Figure 4-3**) is not the most stable one. Note that the first B stands for bidentate by the catechol functionality and the second B stands for bidentate by the carboxylic group (Ti [1] and Ti [1'] are symmetry equivalent). The most favored configuration on the NP is $B^{11,9}C^{12}$ (B bidentate for catechol and C chelated for carboxylic group, respectively), with an adsorption energy of -5.18 eV. This energy is double of what computed for the slab adsorption because, here, two of the surface Ti atoms involved in the binding are fourfold coordinated or Ti_{4c}. In **Figure 4-3** we show that when the carboxylic group is monodentate (M) to the same Ti atom, the binding energy drops to -4.54 eV ($B^{11,9}M^{12}$). Doubly chelated structure $C^{11}C^{12}$ (**Figure 4-3**) and $C^{10}C^{13}$ (**Figure 4-5**) are not particularly favored (-4.07 eV and -4.01 eV, respectively).

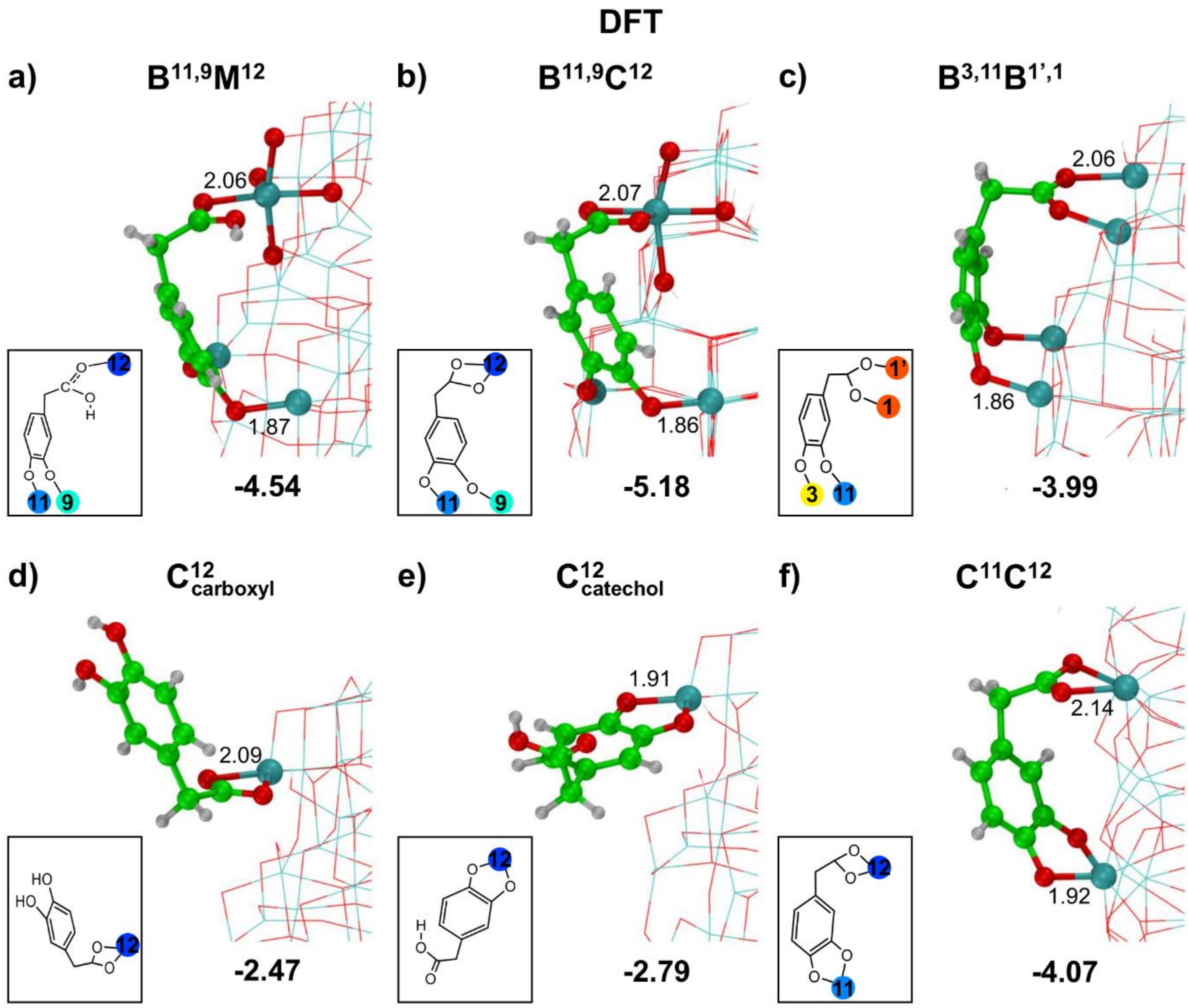

Figure 4-3 Adsorption configurations (side views) and energies per molecule in eV $\left(\Delta E_{ads}^{mol}\right)$ for one DOPAC molecule on the surface of the spherical NP, as obtained by DFT calculations. (a) Bidentate and bent towards the surface making a covalent bond ($B^{11,9}M$); (b) bidentate and chelated making a covalent bond ($B^{11,9}C^{12}$); (c) bidentate and bent towards the surface making a covalent bond ($B^{3,11}B^{1',1}$); (d) chelated by the carboxyl group ($C^{12}_{carboxyl}$); (e) chelated by catechol and bent towards the surface making a covalent bond ($C^{12}_{catechol}$); (f) chelated and bent towards the surface making a covalent bond ($C^{11}C^{12}$). Relevant distances are reported in Å.

A further question that arises is whether all four O–Ti bonds in $B^{11,9}B^{1,1'}$ are sufficiently strong to compete with water molecules for adsorption. We analyzed this issue by comparing the total energy of two situations (**Figure 4-4**), where: 1) the molecule in the $B^{11,9}C^{12}$ adsorption mode is surrounded by a full monolayer of adsorbed water molecules on the nanoparticle surface and 2) the molecule in the $B^{11,9}D^{H\text{-}bond}$ adsorption mode bidentates the surface Ti atoms from the catechol group side and it is only H-bonded to the water molecules of the monolayer of water around the nanoparticle.

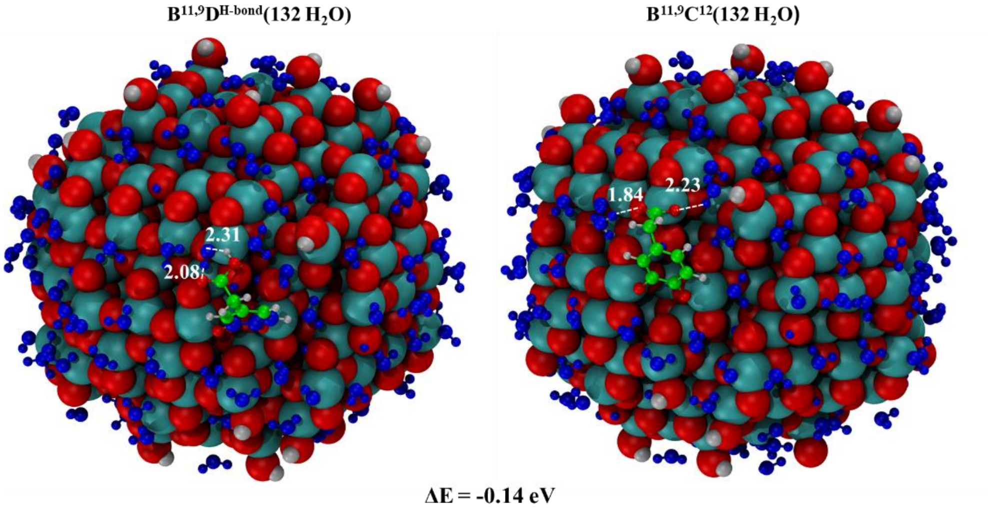

Figure 4-4 Optimized geometry for the $B^{11,9}D^{H\text{-bond}}$ (132 H_2O) and $B^{11,9}C^{12}$(132 H_2O) configurations. Ball and stick representation for the Ti site involved in the DOPAC adsorption, the water of the monolayer and the DOPAC molecule. The energy difference between the structure is reported below. In green C atoms, in red O atoms, in cyan Ti atoms, in white H atoms and in blue the O belonging to the water monolayer. H-bond distances are reported in Å.

The total number of water molecules in the two calculations is the same. We observe that $B^{11,9}C^{12}$ is more stable than $B^{11,9}D^{H\text{-bond}}$ by -0.14 eV, which is an indication of the stronger binding of the carboxylic group with respect to water molecules.

Furthermore, we compare structures in the up configuration that involved one functional group, catechol or carboxylic, in the chelated adsorption mode on the Ti[12]: the catechol functionality is preferred with respect to the carboxylic group (-2.79 vs -2.47 eV). We focus on the chelated binding mode because it is relevant for the high coverage assembling since, in that case, the number of occupied sites by a single molecule must be minimized.

For completeness, we also consider other down configurations, as shown in **Figure 4-5**, although they are less relevant for the full coverage model.

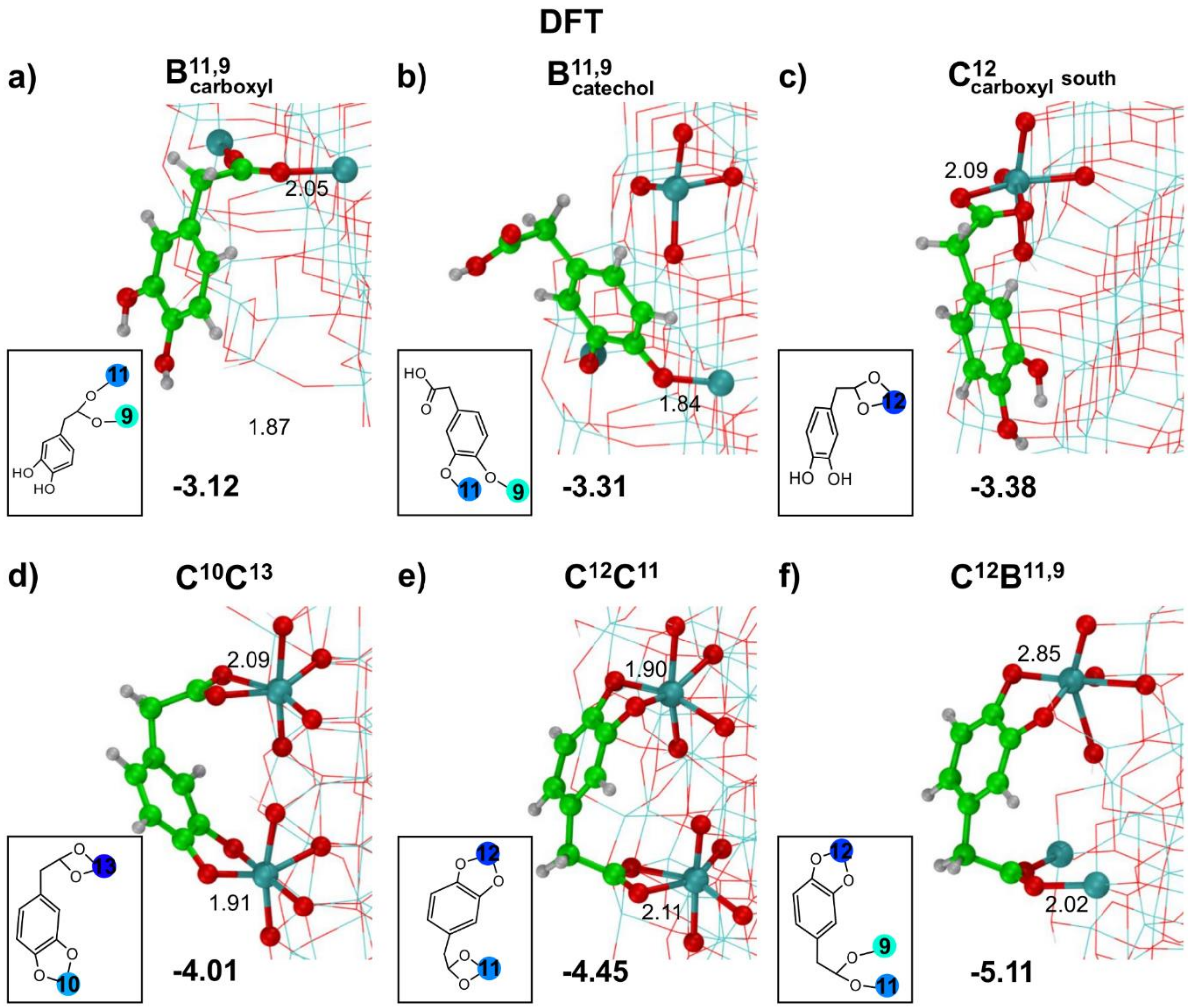

Figure 4-5 Adsorption configurations (side views) and energies per molecule in eV $\left(\Delta E_{ads}^{mol}\right)$ for one DOPAC molecule on the surface of the spherical NP, as obtained by DFT calculations. (a) Bidentate by carboxyl group ($B_{carboxyl}^{11,9}$); (b) bidentate by enediol group ($B_{catechol}^{11,9}$); (c) chelated and bent towards the south pole of the surface ($B_{carboxyl}^{12}$ south); (d) chelated by the carboxyl and enediol groups ($C^{10}C^{13}$); (e) chelated by catechol and bent towards the surface making a covalent bond ($C^{12}C^{11}$); (f) chelated and bent towards the surface making a covalent bond ($C^{12}B^{11,9}$). Relevant distances are reported in Å.

4.3.2 Electronic properties of the nanoconjugate

For the DOPAC/TiO_2 NP complex at low coverage (5%), experimental observations indicate a shift of the absorption onset to the visible range from 380 nm (bare NP) to 800 nm, due to charge transfer excitations.[238, 244] In order to rationalize this large shift, we analyze the electronic structure of the most stable DOPAC/TiO_2 NP complex configuration ($B^{11,9}C^{12}$) by means of the total and projected density of states. The calculations were performed at three different levels of theory: i) DFTB, ii) single-point DFT calculation on the DFTB optimized geometry (DFT/DFTB) and iii) DFT (see **Figure 4-6**)

The DOS obtained by DFTB (**Figure 4-6** a) is characterized by the presence of one mid-gap state while those by DFT/DFTB (**Figure 4-6** b) and DFT calculations (**Figure 4-6** c) present two mid-gap states. HOMO is mainly related to the C and O atoms of the DOPAC and HOMO-1 peak is ascribed to the C atoms. In the DFTB calculations, the HOMO-1 state is inside the valence band due to the underestimated band gap value.

On this basis, we can infer that DFTB is generally not accurate enough for such delicate functionalized metal oxide systems. However, we learn that performing DFT single point calculations on DFTB optimized geometries effectively improves the description of the electronic structure, providing results in close agreement with DFT. Therefore, one can safely recourse to this cheap approach when studying high coverage densities or, in general, when performing a full DFT optimization is too expensive and time consuming.

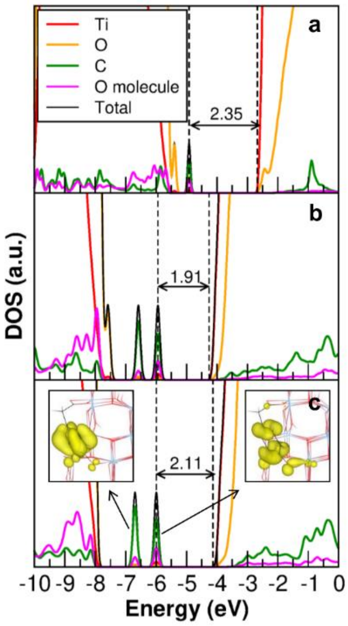

Figure 4-6 Total (DOS) and projected (PDOS) density of states for the $B^{11,9}C^{12}$ configuration of single DOPAC molecule adsorption on the TiO_2 anatase nanoparticle as calculated by DFTB (a), DFT/DFTB (b) and DFT (c).

The HOMO-LUMO gap is reported for each plot by dashed lines. The zero energy is set to the vacuum level. Electronic density plot for the HOMO and HOMO-1 of $B^{11,9}C^{12}$ configuration. Iso-value=0.005 e/Å^3.

4.3.3 Effect of the light irradiation on the nanoconjugate

We follow the light irradiation process for the DOPAC/TiO_2 NP composite by computing first the vertically excited state (v), in the Franck-Condon approximation, from the S_0 to the T_1 state by means of a spin-constrained calculation (see **Figure 4-7** and **Figure 4-8**).

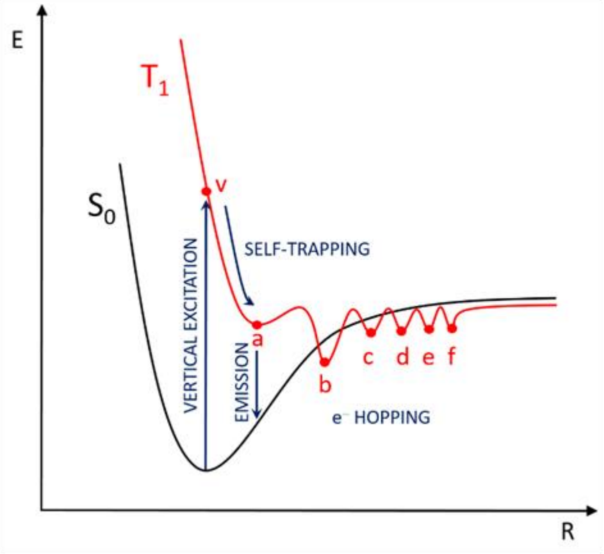

Figure 4-7 Schematic representation of the process involving e^-/h^+ pair: the vertical excitation $S_0 \rightarrow T_1$ (v), the self-trapping relaxation (a), the $T_1 \rightarrow S_0$ emission and the electron hopping follow by the non-radiative emission (b, c, d, e, f).

We are aware of the fact that this is a spin forbidden excitation, however after atomic relaxation it will allow to localize the self-trapped triplet exciton (a), which is what could be observed in photoluminescence experiments, due to its longer lifetime with respect to the singlet one. We compute a self-trapping energy (ΔE_{trap}) of -1.04 eV and an emission energy (for $T_1 \rightarrow S_0$, ΔE_{em}) of -0.25 eV. In the triplet self-trapped exciton $\left[B^{11,9}C^{12}\right]_a^{T_1}$, the hole is fully localized on the π orbital of the aromatic ring in DOPAC, whereas the electron is localized a single Ti atom of the subsurface Ti_{6c} (see **Figure 4-8**).

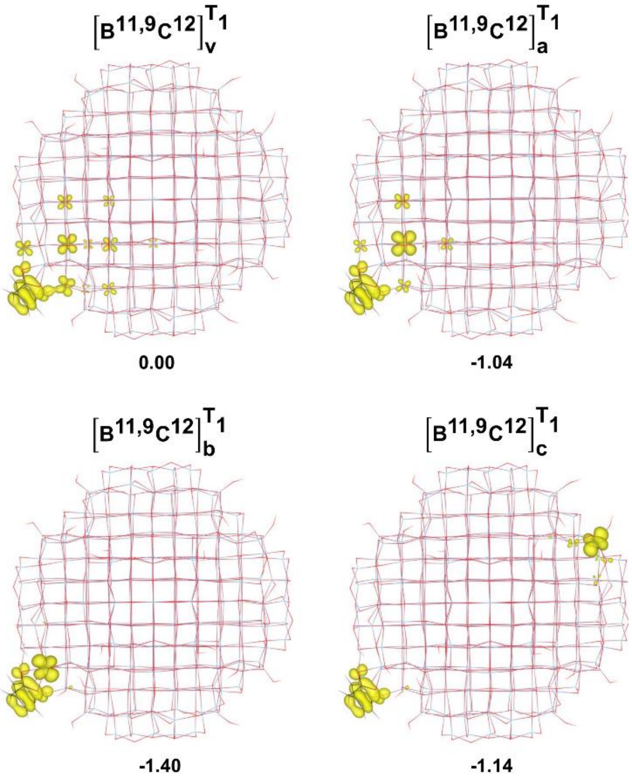

Figure 4-8 Top views of the spin density of the $B^{11,9}C^{12}$ configuration (see **Figure 4-3**) for the (v configuration) vertical triplet state, (a configuration) self-trapped triplet exciton, (b configuration) triplet exciton involving the Ti atom chelated by the carboxylic group, and (c configuration) separated charges with the hole on the DOPAC molecule and the electron on a distant Ti atom. Below each structure, the energy gain in eV with respect to $\left[B^{11,9}C^{12}\right]_v^{T_1}$ (ΔE_{trap}) is reported. Iso-value=0.005 e/Å^3.

If, as a further step along the post-irradiation processes, we suppose that electron hopping is faster than radiative recombination then the electron could localize on a different Ti atom (electron hopping barrier was estimated to be about +0.09 eV).[253] Clearly, the nearby positions are reached first and there is one where the electron is found to be particularly stable and still in close contact with the hole (configuration b, see **Figure 4-8**). The total trapping energy (ΔE_{trap}) in this case is much larger (-1.40 eV, with respect to the energy of the v configuration). The hole is still localized in the DOPAC molecule, whereas the electron is now trapped at the Ti atom involved in the chelation of the carboxylic group. The S_0 state curve lies above this T_1 minimum structure b (confirmed by a single point calculation in the closed-shell configuration) by +0.37 eV. Therefore, decay to the S_0 ground state geometry can only take place through a non-radiative process through the conical intersection on the left of b, shown in **Figure 4-7**.

Further hopping to more distant Ti sites (i.e. $\left[B^{11,9}C^{12}\right]_{c}^{T_1}$ in **Figure 4-8** and $\left[B^{11,9}C^{12}\right]_{d}^{T_1}$, $\left[B^{11,9}C^{12}\right]_{e}^{T_1}$ and $\left[B^{11,9}C^{12}\right]_{f}^{T_1}$ in **Figure 4-9**) does not provide any energy stabilization, but on the contrary, these configurations are higher in energy than $\left[B^{11,9}C^{12}\right]_{b}^{T_1}$.

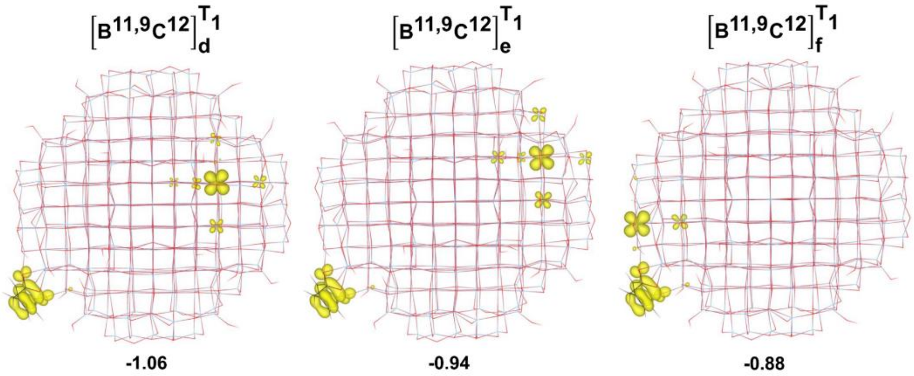

Figure 4-9 Top views of the spin density of the $B^{11,9}C^{12}$ configuration (see **Figure 4-3**) for the (d configuration) separated charges with the hole on the DOPAC molecule and the electron on a distant Ti atom (on the left). Spin density of the $B^{11,9}C^{12}$ for the (e and f configurations) separated charges with the hole on the DOPAC molecule and the electron on a distant Ti atom. Below each structure, the energy gain with respect to $\left[B^{11,9}C^{12}\right]_{v}^{T_1}$ (ΔE_{trap}) is reported. Iso-value=0.005 e/Å^3.

Therefore, it is highly improbable that the electron will have the chance to reach other sites far apart from the adsorbed molecule. The hole is formed in a π state of DOPAC, where it is very stable due to large structural deformation involving the elongation of C_3–C_4 and Ti–O bonds by ~0.07 and ~0.17 Å, respectively. It is relevant to note (see **Table 4-1**) that the smallest distortion energy value is registered for the self-trapped exciton (1.20 eV), whereas for all the other electron/hole configurations we observe rather larger distortion energies from 1.47 to 2.11 eV, which are the cause of a positive ΔE_{em}.

Table 4-1 Trapping energy (ΔE_{trap}) in eV of photoexcited charge carriers at different sites for the adsorbed DOPAC configuration $B^{11,9}C^{12}$ on the spherical TiO_2 nanoparticle in the T_1 excited state, with respect to $\left[B^{11,9}C^{12}\right]_{v}^{T_1}$, degree of localization (%electron or %hole), structural distortion energy with respect to the ground state ($\Delta E_{dist} = E[S0(T_1)] - E[S_0]$), and $\Delta E_{em} = E[S_0(T_1)] - E[T_1]$ energy difference in eV. No symmetry constrains are imposed in all the calculations. The binding site numbering is defined graphically in **Figure 4-1** whereas the charge carrier localization configuration is defined in **Figure 4-8** and **Figure 4-9**.

	ΔE_{trap} (eV)	%electron	%hole	ΔE_{dist} (eV)	ΔE_{em} (eV)
$[\mathbf{B}^{11,9}\mathbf{C}^{12}]_{\mathbf{v}}^{T_1}$	0.00	19%	97%	0.00	-
$[\mathbf{B}^{11,9}\mathbf{C}^{12}]_{\mathbf{a}}^{T_1}$	-1.04	77%	96%	1.20	-0.25
$[\mathbf{B}^{11,9}\mathbf{C}^{12}]_{\mathbf{b}}^{T_1}$	-1.40	97%	97%	1.47	+0.37
$[\mathbf{B}^{11,9}\mathbf{C}^{12}]_{\mathbf{c}}^{T_1}$	-1.14	91%	97%	2.11	+0.75
$[\mathbf{B}^{11,9}\mathbf{C}^{12}]_{\mathbf{d}}^{T_1}$	-1.06	77%	96%	1.67	+0.24
$[\mathbf{B}^{11,9}\mathbf{C}^{12}]_{\mathbf{e}}^{T_1}$	-0.94	69%	97%	1.56	+0.07
$[\mathbf{B}^{11,9}\mathbf{C}^{12}]_{\mathbf{f}}^{T_1}$	-0.88	91%	97%	1.89	+0.27

To rationalize the reason why the b configuration of $B^{11,9}C^{12}$ in the T_1 state is so stable with respect to a configuration and even lower in energy than the corresponding S_0 state in those atomic distorted positions, we must analyze the DOS in detail and compare results for configurations a and b (see **Figure 4-10**). The critical feature is the position of the highest occupied state (HOMO) for the α or up component. For $[B^{11,9}C^{12}]_{a}^{T_1}$, this peak is very high in energy (at -4.88 eV), just below the bottom of the conduction band, whereas for $[B^{11,9}D^{12}]_{b}^{T_1}$ it is deeper in the gap (at -5.23 eV) by about -1.2 eV. This HOMOα state is the one hosting the excited electron, whereas the LUMOβ is the state associated to the hole. The recombination process is essentially the transfer of the electron from the HOMOα state to the LUMOβ one, leading to the electronic structure shown in (c) and (d) panels of **Figure 4-10**. Therefore, whereas in $[B^{11,9}C^{12}]_{a}^{T_1}$ the recombination process is favored since the LUMOβ is below the HOMOα state, in $[B^{11,9}C^{12}]_{b}^{T_1}$ the recombination is not an energetically favorable process since LUMOβ is just slightly above the HOMOα state in the T_1 and, consequently, the resulting HOMO for $S_0(T_1)$ in panel (d) is higher in energy than the HOMOα in panel (b) for T_1. In this geometry T_1 is preferable than S_0, as schematically shown in **Figure 4-7**.

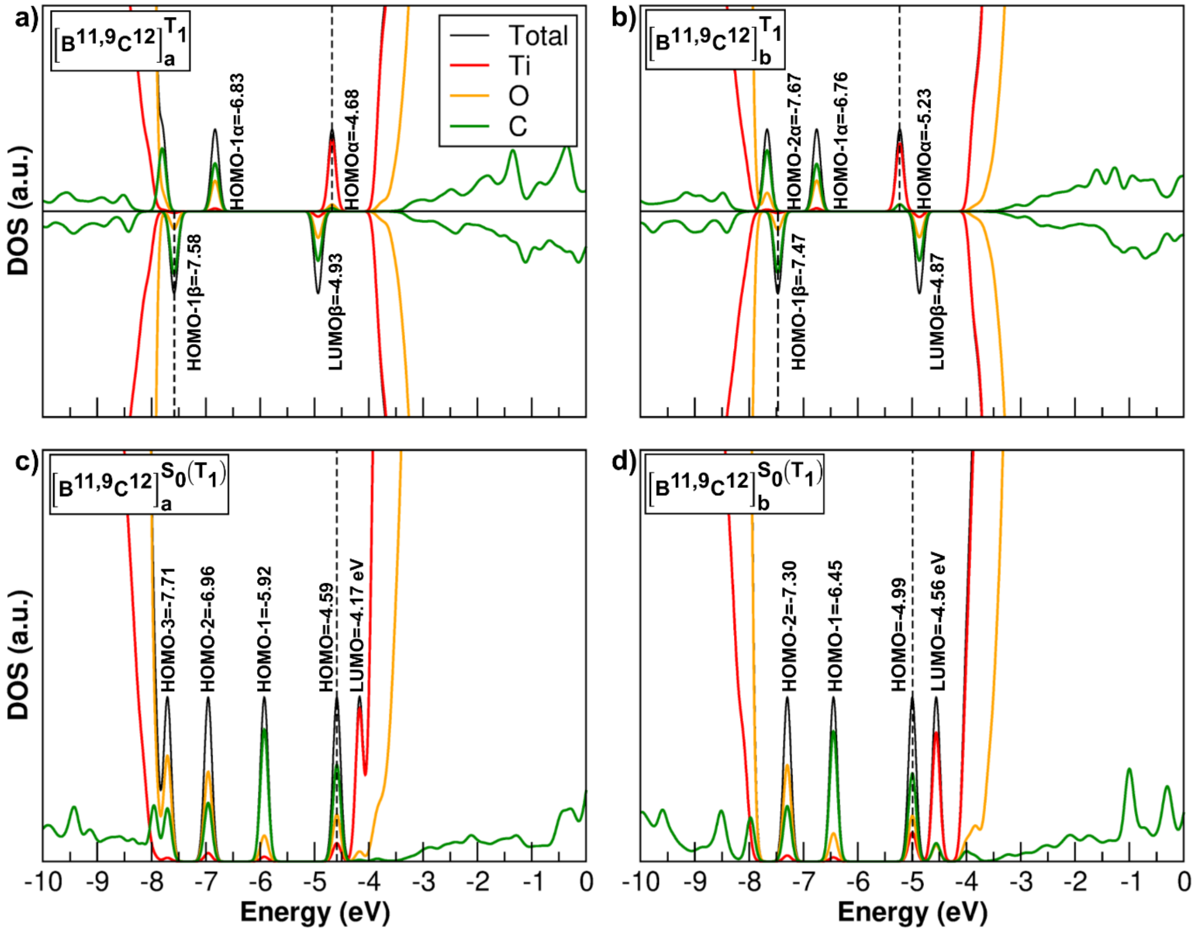

Figure 4-10 Total (DOS) and projected (PDOS) density of states for a) $[B^{11,9}C^{12}]_a^{T_1}$, b) $[B^{11,9}C^{12}]_b^{T_1}$, the recombined singlet in the T_1 optimized geometry for c) a and d) b configurations. Ti is represented in red, O is orange, C is green, and N is reported with a blue line. The zero energy is set to the vacuum level. The energy in eV of all the mid-gap states are reported on each plot.

Based on the results presented in this section, we may conclude that in the photoexcited DOPAC/TiO_2 anatase NP complex there is an intrinsic and effective charge separation, since the hole is localized on the DOPAC and is not coupled with phonons of the TiO_2 lattice, whereas the electron sits on Ti ions of the NP. The hole localization on the DOPAC has the beneficial effect of lowering the oxidative power of TiO_2 NP under light irradiation. This we can prove by computing the vertical and adiabatic ionization potentials (IP) for the bare NP and compare them to the values for the DOPAC/TiO_2 NP complex in the lowest energy $B^{11,9}C^{12}$ configuration (see **Table 4-2**). The reduction in the adiabatic IP value is of about 1.5 eV.

We have also estimated the electron affinity (EA) of the DOPAC/TiO_2 NP complex in the lowest energy $B^{11,9}C^{12}$ configuration. In this case, we do not expect large differences from the bare TiO_2 NP because in DOPAC/TiO_2 complex the electron is delocalized/localized on Ti atoms. This is confirmed by the data since, when comparing EAs for corresponding electron position on the DOPAC/TiO_2 NP complex and bare NP, the observed differences are small. Only for the $[B^{11,9}C^{12}]^{-}_{b}$ configuration, where the electron is trapped at the Ti atom that is chelated by the carboxyl group of DOPAC, the electron trapping ability of that Ti site is slightly enhanced.

Table 4-2 Trapping energy (ΔE_{trap}) in eV for an excess electron and hole at the different sites with the charge localization (%electron or %hole) in the $B^{11,9}C^{12}$ configuration. The references zero for the ΔE_{trap} is obtained by adding one electron in the former case and removing one electron in the latter with no atomic relaxation. The charge localizations (%electron or %hole) are also given. The electron affinity (EA) of one extra electron coming from the vacuum and ionization potential (IP) of the most external, less bound, electron to the vacuum level are reported, together with a comparison with the values for the EA and IP of the bare NP. The binding site numbering is defined graphically in **Figure 4-1**, whereas the charge carrier localization configuration is defined in **Figure 4-7**. Spin plots are shown in **Figure 4-11**.

Excess electron	ΔE_{trap} (eV)	**%electron**	**EA**	**EA BARE NS**
$[\mathbf{B^{11,9}C^{12}}]^{-}_{\mathbf{v}}$	0.00	4.8%	3.29	3.27[1]
$[\mathbf{B^{11,9}C^{12}}]^{-}_{\mathbf{b}}$	-0.60	97%	3.89	3.67[1]
$[\mathbf{B^{11,9}C^{12}}]^{-}_{\mathbf{d}}$	-0.25	77%	3.55	3.51[1]
Excess hole	ΔE_{trap} (eV)	**%hole**	**IP**	**IP BARE NS**
$[\mathbf{B^{11,9}C^{12}}]^{+}_{\mathbf{v}}$	0.00	95%	7.04	8.35[2]
$[\mathbf{B^{11,9}C^{12}}]^{+}_{\mathbf{r}}$	-1.02	96%	6.02	7.50[2]

[1] Values calculated for the annealed NP used throughout this work.

[2] Values reported in ref.[254]

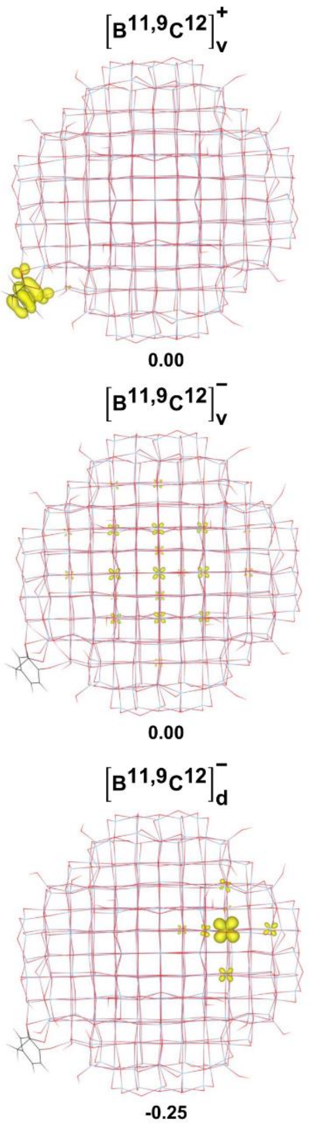

Figure 4-11 Top views of the spin density plots of the $B^{11,9}C^{12}$ configuration (see **Figure 4-3** b and **Table 4-2)** for an excess hole and electron at the different sites. The references zero for the ΔE_{trap} is obtained by removing

one electron in the former case $\left[B^{11,9}C^{12}\right]_v^+$ and adding one electron in the latter $\left[B^{11,9}C^{12}\right]_v^-$ with no atomic relaxation. Below each structure, the energy gain (ΔE_{trap}) is reported. Iso-value=0.005 e/Å^3.

4.4 Increasing linker coverage on TiO_2 spherical NP

4.4.1 Adsorption mode and packing

In this section, we discuss the effect of binding an increasing number of DOPAC molecules on the adsorption energy and on the electronic properties of the DOPAC/TiO_2 NP composite system. To obtain the full coverage, the DOPAC molecules were adsorbed in a mixture of bidentate and chelated fashion and with the carboxyl groups pointing up toward the vacuum. The DOPAC molecules were added to the surface of the NP in a multiple steps. we were able to adsorb 46 DOPAC molecules (32 chelated and 14 bidentate, $TiO_2^{46\text{-}DOPAC}$) on the surface of the nanoparticle, as shown in **Figure 4-12** a.

All the twelve Ti_{4c} sites at the NP equator are chelated to DOPAC molecules (C^9, C^{10}, C^{11}). It is necessary to emphasize that we were not able to adsorb molecules on all the Ti_{5c} and Ti_{4c} undercoordinated sites on the NP due to steric hindrance and to geometrical arrangement of Ti sites on the surface, but we were able to reach up to ~61% of coverage (calculated as the ratio between the number of adsorbed molecules and the total number of binding sites on the NP model). The addition of DOPAC molecules up to full coverage is an energetically favourable process, even though the energy gain at each step decreases. The adsorption energy calculated by DFTB for one isolated molecule is -3.68 eV, while in the full coverage the adsorption energy per molecule drops to -2.59 eV. At full coverage, due to the high packing of the DOPAC molecules at the equator we observe the formation of H-bonds and π-π stacking interactions that stabilize the completely decorated NP model.

4.4.2 Electronic properties at increasing coverage

Absorption spectra of colloidal 5 nm TiO_2 nanoparticles functionalized with DOPAC (~ 50 molecules/particle) have been investigated experimentally.[238] The wavelength of the absorption onset is found to largely shift up to 700/800 nm. Based on measurements for increasing concentrations of linker and on the Job's method,[242] it was possible to determine both the constant of complexation (1400 M^{-1}) and the stoichiometric ratio between DOPAC and Ti surface sites of 2:1, which is very close to the 2.3:1 ratio in the $TiO_2^{46\text{-DOPAC}}$ model of the present study.

At the full coverage the system has 1619 atoms. Due to the large size of these structures a full geometry optimization at the hybrid DFT level of theory is prohibitive. On the other hand, as we discussed in Section 4.3.2, the electronic structure obtained using DFT/DFTB method is qualitatively accurate enough to describe the electronic properties as compared to hybrid DFT calculations. Therefore, in the following we will discuss the results obtained by performing single point calculations at the hybrid DFT (B3LYP level of theory) on the DFTB optimized geometries (labeled as DFT/DFTB).

In **Figure 4-13** we show the electronic structure for the DOPAC/TiO_2 NP systems with 46 dopamine molecules. The values for the HOMO-LUMO gap and an approximation of the band gap (E_g), calculated as the difference between the bottom of the conduction band and the top of valence band, are reported in the plot.

By adsorbing more molecules on the surface, new localized peaks appear both inside the band gap and on top of the valence band, causing a shrinking of the band-gap value. At higher coverages, the electronic structures become more complicated. Due to the increasing density coverage, the molecules interact both with each other and with the NP surface. Therefore, the peaks are highly hybridized and assigning them to a specific atom is not trivial. Nevertheless, we can still notice the predominant contribution of both C. Notably, we can observe that the HOMO-LUMO energy difference is only 0.74 eV. Since, the localized peaks inside the gap and on top of the valance band merge to create a unique large band (see **Figure 4-13**).

4.5 Dynamics at full coverage of DOPAC on TiO_2

To investigate the effect of temperature on the rearrangement of the as-deposited DOPAC molecules in the $TiO_2^{46\text{-DOPAC}}$ model, we performed DFTB molecular dynamics runs at 300 K for 10 ps. In the optimized $TiO_2^{46\text{-DOPAC}}$ model, even before MD, we observe H-bonds between the carboxylic groups of the DOPAC molecules and the hydroxyl groups on the surface of the

NP (~28% of the molecules make a H-bond of length in the range of 1.56-1.92 Å). We also note that there are some H-bonds between the carboxylic groups of pairs of DOPAC molecules (12 H-bonds of length in the range of 1.36-2.20 Å). After performing MD at 300 K and fully relaxing the structure we obtain a new configuration shown in **Figure 4-12** b.

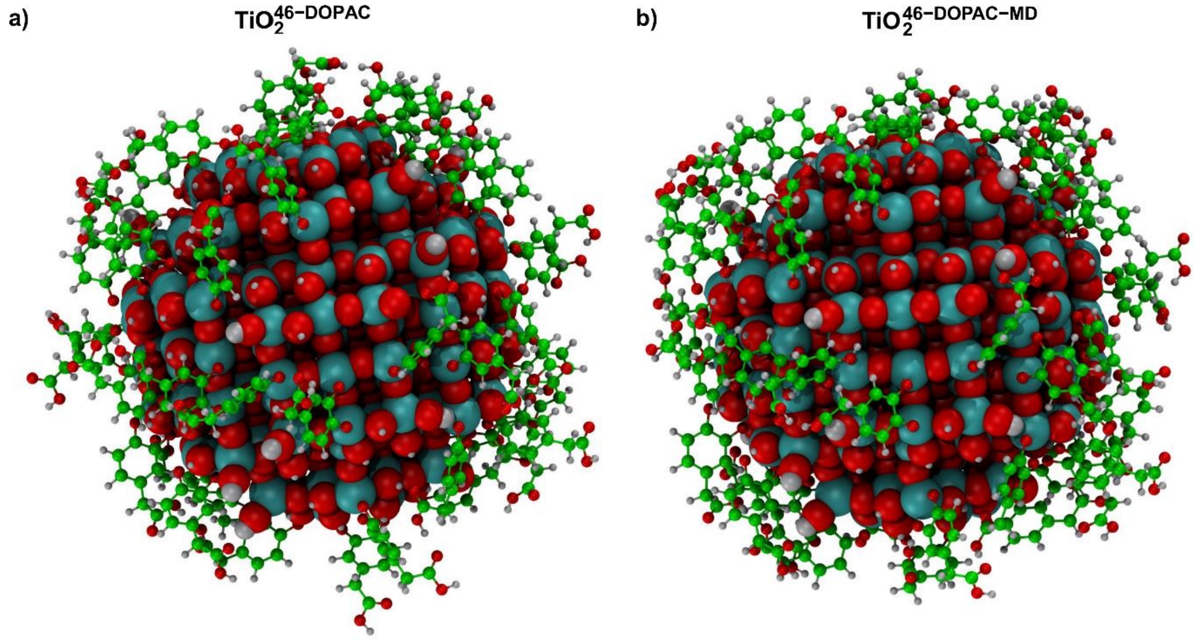

Figure 4-12 3D structure for the high coverage models before and after the molecular dynamics $TiO_2^{46\text{-}DOPAC}$ in a and $TiO_2^{46\text{-}DOPAC\text{-}MD}$ in b, respectively.

Here, ~37% of the carboxylic groups of the DOPAC molecules make H-bonds with the surface of the NP (length in the range of 1.62-1.91 Å), which indicates a tendency of the molecules to get closer to the surface with some thermal treatment. Moreover, we also observe the formation of five doubly H-bonded carboxylic group dimers (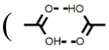) that further reduces its availability for bioconjugation.

The electronic structure for the optimized $TiO_2^{46\text{-}DOPAC}$ configuration after 10 ps MD at 300 K is shown in **Figure 4-13** and can be directly compared with that of the optimized configuration before MD. The molecular rearrangement following the MD causes a different resulting dipole of the molecular layer on the NP surface that affects the position of the NP valence and conduction bands with respect to the vacuum. We register a rigid shift of 0.18 eV. On the contrary, the DOPAC states are stabilized after MD because of a more favorable disposition by 0.12 eV. The net result is a widening of the HOMO-LUMO gap from 0.74 eV to 0.92 eV.

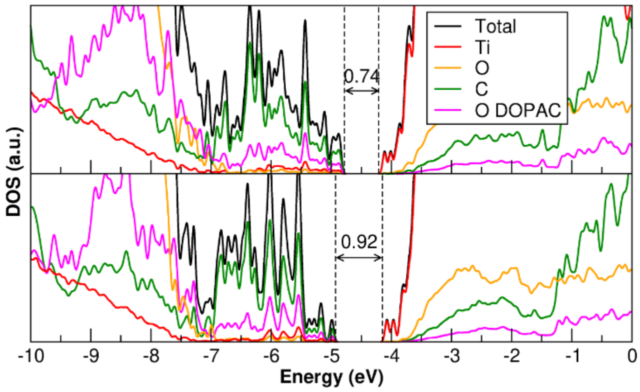

Figure 4-13 Total (DOS) and projected (PDOS) density of states for the 46-DOPAC high coverage model on the TiO_2 NP calculated by DFT/DFTB before (upper panel) and after (lower panel) molecular dynamics simulation. Ti is represented in red, O of the TiO_2 NP is orange, while O of the DOPAC is marked in violet, and C is green. The HOMO-LUMO gap is reported for each plot by dashed lines. The zero energy is set to the vacuum level.

4.6 Conclusions

In this chapter, we presented a density functional theory based study on the structural, electronic, self-assembling properties of catechol-derivatives (DOPAC) adsorption on curved TiO_2 NPs of realistic size (2-3 nm size with ~700 atoms). The investigation spanned from single-molecule adsorption to a full coverage regime.

For the low coverage, we have determined the favorable molecular adsorption modes and analyzed the electronic charge-transfer effects, identifying the new molecular states in the band gap introduced by the adsorbed linker species. On top of that, we have investigated the processes following vis-light photoexcitation of the charge transfer complex: exciton formation, trapping, charge carriers diffusion or recombination. We learnt that the photoexcited hole is trapped in the π-states of the aromatic ring, whereas the photoexcited electron can hope on different Ti sites, leading to an effective charge transfer separation. Interestingly, the one that provides the strongest binding is the surface Ti atom involved in the bonding with the –

COOH functional group in DOPAC. The hole trapping has a beneficial effect of lowering the oxidative power of TiO_2 NP under light irradiation.

As a further step, we then consider a growing molecular layer on the NP and analyze the self-assembling mechanism and the effects on the electronic properties of the complex. To achieve very high coverage most of the molecules have been chelated to fourfold coordinated Ti atoms, and bidentate to pairs of fivefold coordinated ones. All the molecules are positioned in an upward configuration to reduce the steric hindrance and maximize the dispersion interactions between them. Molecular states in the gap increase progressively, until they form a continuous band from the top of the valence band of the TiO_2 NP to about 0.7 eV from the bottom of its conduction band.

At the maximum coverage (46 molecules per NP), we perform molecular dynamics runs at 300 K to compare the molecular configuration and electronic properties of the NP/linkers complex before and after thermal treatment to better account for the competition between molecule/surface and molecule/molecule interactions. Considering, the high affinity of the carboxylic group towards the oxide surface, we may conclude that the DOPAC is not an effective bifunctional linker for bioconjugation.

Chapter 5 Functionalized TiO_2 nanoparticles for bio-conjugation: TETT linker

5.1 Introduction

TiO_2 nanoconjugates have gained increasing attention during the last few years in nanobiotechnology and biomedicine.[11] In particular, spherical nanoparticles (NPs) can be easily conjugated with bioactive molecules, due to the large numbers of undercoordinated sites, leading to hybrid multifunctional nanodevices for photodynamic therapy, drug delivery and imaging.[1]

As synthesized, TiO_2 NPs are hydrophobic and need to be made hydrophilic and biocompatible by chemical modification of their surfaces. Organofunctional silanes are widely used to modify NPs surfaces due to the combination of hydrophilic features with chemical and physical stability. Indeed, the formation of a cross-linked shell of silicon ligands is a way to reduce particle aggregation. In particular, the silica coating shields the functional core from the biological environment, protecting the NPs toward oxidation and reducing their toxicity.[33]

Organofunctional silanes act as coupling agents since they connect the organic and inorganic phases. The general formula is $Y\text{-}R\text{-}Si\text{-}X_3$, where X is a hydrolysable leaving group (e.g. methoxy, ethoxy, etc), which provides a site for attaching Si to the surface, while Y is a functional group (e.g. carboxyl group, amine, etc.) and R is an alkyl chain. The silane reacts with water to form a silanol group Si—OH and, by condensation of surface hydroxyls on the NP with these Si-OH bonds a silane—surface bond is formed. The use of multidentate anchoring groups and the strength of the formed covalent bonds ($\Delta H_{Si\text{-}O} = 466$ kJ/mol)[255]

---

[1] The work presented in this chapter has been done in collaboration with the Prof. Gotthard Seifert and the Dr. Igor Baburin.

ensure the stability of the nanoconjugate. The available functional groups Y in the silane provide a chemical handle for secondary modification of NPs with biomolecules or other desired polymers.

Several reports have described protocols for the conjugation of biomolecules onto TiO_2 surfaces and these have been partially reviewed in work of Beutner et. al.[256] For example, TiO_2 NPs have been functionalized to yield amino-functionalized NPs with 3-amino-propyl-triethoxysilane (APTES).[257] The amino groups can anchor the biotin molecules, which usually are conjugated to an enzyme, antibody or target protein to form a selective complex for many metabolic processes.[258, 259, 36]

Water-dispersible Gd_2O_3 NPs were obtained by the exchange of oleate ligands with a carboxylic silane, namely N-(trimethoxysilylpropyl) ethylene diamine triacetic, acid trisodium salt (TETT). The abundant carboxylic groups of the attached TETT silane allow the coupling of the polyethylene glycol polymer (PEG) to form PEG coated Gd_2O_3 NPs. The biocompatible PEG layer further helps to stabilize Gd_2O_3 NPs, to enhance the blood circulation and to improve the water dispersibility. Also, the PEG coated Gd_2O_3 NPs have been exploited as a glioma-targeted contrast agent. Target specificity is another critical requirement for a successful diagnosis and makes the contrast agent safer by reducing the dosage and minimizing the damage to healthy tissues.[260]

The same ligand TETT was covalently attached to the surface of MnO NPs, and then the MnO-TETT was conjugated with the folic acid (FA) to produce MnO-TETT-FA NPs. The folic acid has been utilized as an effective targeting molecule toward glioma since it shows a high affinity toward a folate receptor that is overexpressed in brain cancer. The biocompatibility of MnO-TETT-FA NPs was proved *in vitro* and *in vivo*; therefore the nanomaterials could be used as magnetic resonance imaging contrast agents for the early diagnosis of brain gliomas.

Besides imaging, TETT ligand is also suitable for drug delivery. Ying et al.[261] have succeeded in loading on TiO_2 nanoparticle the chemotherapy drug doxorubicin (DOX), without affecting the biological activity of the drug. The success of the nanocomposite relies on the abundant amount of carboxylic group provided by TETT, which imparts to TiO_2 excellent water dispersibility and allows for an easy conjugation of the drug.

In contrast to a large number of fundamental studies on bulk and surfaces, TiO_2 nanoparticles, which are the key system for biomedical applications have only been studied experimentally, in relation to their synthesis and medical applications.[261] Only few computational studies exist about organic molecule adsorption on titanium dioxide nanoparticles, based on force-field methods[262, 263] or classical molecular dynamics,[264, 265, 266] which intrinsically lack the description of electronic properties and the chemical processes at the interface.

The objective of this work is to systematically investigate by DFTB calculations the structural properties of the TETT-functionalized TiO_2 nanoparticles. Firstly, we have considered the low coverage regime and studied the possible adsorption modes of the silanol-like molecule on the NP model.

Secondly, through molecular dynamics simulations, we have explored the configurational space of the linker adsorbed on the TiO_2 nanoparticle and analyze how the chain of the linker can interact with the surface of the nanoparticle.

As a next step, we covered the TiO_2 nanoparticle with more molecules up to 22 for the medium coverage, and up to 40 molecules in the full coverage to form a densely packed monolayer of organic ligands.

5.2 Computational details

In this work, we used a self-consistent charge density functional tight-binding (SCC-DFTB)[245, 246] approach for geometry optimization, molecular dynamics simulations and electronic structure calculations.

For all the SCC-DFTB calculations we used the DFTB+ 18.2 open-source package.[248] We employed the MATORG[249] parameterization set for the Ti-O pairwise interaction in the TiO_2 atoms, and C, N, O, and H of the adsorbed molecules. Whereas for the Si-Ti, Ti-Ti, and Si-Si pairwise interaction we used an extra set of parameters (for further details refer to section 5.3).

The description of the hydrogen bonding[250, 251] has been further improved with the inclusion of the empirical hydrogen bonding damping (HBD) function $\gamma_{\alpha H}$, only for the interaction between an atom α and a hydrogen atom

$$\mathrm{\gamma_{\alpha H}} = \frac{1}{\mathrm{r_{\alpha H}}} - \mathrm{S_{\alpha H}} \times \mathrm{f_{\alpha H}} \tag{5.1}$$

$$\mathrm{f}_{\alpha\mathrm{H}} = \exp\left[-\left(\frac{U_\alpha + U_H}{2}\right)^{\varsigma} r_{\alpha H}^2\right] \tag{5.2}$$

where U_α and U_H are the atomic Hubbard parameters, which are linked to the chemical hardness of atom α and the corresponding hydrogen, respectively. The parameter $\zeta = 4$ is generally determined by fitting to hydrogen-bonding energies from high level ab initio calculations. As a result, $\gamma_{\alpha H}$ becomes more positive in the short range, leading to stronger polarization for the atoms forming H-bonds, thus increasing the accuracy of describing hydrogen bonds.

The anatase TiO_2 spherical nanoparticle model used throughout this work has been designed in previous work by our group.[118] However, we have substituted the Ti-Ti Slater-Koster file in the MATORG set, and then we have reoptimized the nanoparticle model. The stoichiometry of the model is $(TiO_2)_{223}\cdot 10H_2O$, and the NP has an equivalent diameter of 2.2 nm. The nanoparticle has been treated as a large isolated molecule in vacuum without any periodic boundary condition.

For geometry relaxations, the threshold for the convergence of the self-consistent charge (SCC) procedure was set to 10^{-6} au and forces were relaxed to less than 10^{-4} au.

The total adsorption energy per TETT linker on the spherical nanoparticle has been defined as:

$$\Delta E_{ads}^{mol} = (E_{NP+n_{mol}} - [E_{NP} + n_{mol}E_{mol}])/n_{mol} \tag{5.3}$$

where $E_{(NP+n_{mol})}$ is the total energy of the whole system, E_{NP} is the energy of the NP, E_{mol} is the energy of the molecule in the gas phase, and n_{mol} is the number of the molecules adsorbed on the NP.

Born−Oppenheimer molecular dynamics (MD) simulations were performed within the canonical ensemble (NVT). The Newton equations of motion were integrated with the velocity Verlet algorithm, and a relatively small time step of 0.5 fs was used. During the molecular dynamics simulation, the temperature has been kept constant to 300 K by using the Nosé−Hoover thermostat (time constant of 0.04 ps) and the system has been evolved for 20 ps. For the medium (1689 atoms) and high coverage (2499 atoms) the time step was set to 1 fs, and the system has been let evolve for 15 ps and 5 ps, respectively, due to the large number of atoms.

For each run of the MD simulations the initial velocity was randomly generated with the Boltzmann distribution at 300 K.

All the DFT calculations have been carried out with the CRYSTAL14[197] simulation code where the Kohn−Sham orbitals are expanded in Gaussian-type orbitals. The all-electron basis sets are Ti 86-4111(d41), O 8-4111(d1) for the titanium and oxygen atoms of TiO_2; Si 86-311 (d1), H 5-111(p1), C 6-31111 (d1), O 8-41111 (d1), and N 6-311(d1) have been employed for silicon, hydrogen, oxygen, and nitrogen atoms of the adsorbed TETT linker, respectively. We used the B3LYP functional,[198, 199] corrected by Grimme's D* to include dispersion forces.[200, 201] The cut off limits in the evaluation of Coulomb and exchange series/sums appearing in the SCF equation were set to 10^{-7} for Coulomb overlap tolerance, 10^{-7} for Coulomb penetration tolerance, 10^{-7} for exchange overlap tolerance, 10^{-7} for exchange pseudo-overlap in the direct space and 10^{-14} for exchange pseudo-overlap in the reciprocal space. The condition for the SCF convergence was set to 10^{-6} au on the total energy difference between two subsequent cycles. The equilibrium structure is determined by using a quasi-Newton algorithm with a BFGS Hessian updating scheme.[247]

Geometry optimization was performed without any symmetry constraint; forces were relaxed to be less than 4.5×10^{-4} au, and displacements to be less than 1.8×10^{-3} au.

5.3 Assessment of the Ti-Si parameters in the MATORG set

DFTB is not a semi-empirical method in a strict sense since its parametrization procedure is completely based on DFT calculations and no fit to empirical data has to be done. In contrast to most semi-empirical methods DFTB is a non-orthogonal method. The non-orthogonality of the atomic-like orbitals is a crucial factor for transferability, which means that the parameters perform sufficiently well also for chemical environments not included in the parametrization procedure.

The MATORG parameters have been designed to describe the hybrid interface between TiO_2 and organic molecules. For our system of interest, we have introduced in the MATORG set the

Ti-Si and Si-Ti Slater-Koster files and replaced the homonuclear Ti-Ti and Si-Si parameters with the ones that are parametrized for the heteronuclear pairs, Ti-Si and Si-Ti.

5.3.1 Validation of the combined set of parameters

We have evaluated the combined set of parameters by comparing the energy condensation of small molecules, the elastic properties for the TiO_2 anatase bulk, and Ti charge distribution in the TiO_2 spherical nanoparticle model to DFT results.

Regarding the energy condensation we have considered the simplest test system. The new set of parameters has been evaluated based on the energetics of the homonuclear and heteronuclear condensation of small molecules. In particular, we have studied silicic acid $Si(OH)_4$ and titanium hydroxide $Ti(OH)_4$. The combined set has provided reasonable geometries. However, the DFTB homonuclear and heteronuclear energy condensations reported in **Table 5-1** are overestimated by a factor of three with respect to DFT(LDA) values. For Ti-O and Si-O-Ti, whereas for Si-O the results agree quite well with DFT LDA, but still over bound compared to PBE.

Table 5-1 Comparison between the condensation energies (ΔE, in eV) for small molecule like $Si(OH)_4$ and $Ti(OH)_4$ with the DFT(B3LYP, PBE, LDA) and the DFTB methods. Both homonuclear and heteronuclear condensations are considered. Dispersion forces are not taken into account.

	ΔE(eV)			
	DFT(B3LYP)	DFT(PBE)	DFT(LDA)	DFTB
$2\ Si(OH)_4 \rightarrow Si(OH)_3OSi(OH)_3 + H_2O$	-0.28	-0.19	-0.38	-0.39
$2\ Ti(OH)_4 \rightarrow Ti(OH)_3OTi(OH)_3 + H_2O$	-0.27	-0.40	-0.40	-1.22
$Si(OH)_4 + Ti(OH)_4 \rightarrow Si(OH)_3OTi(OH)_3 + H_2O$	-0.25	-0.31	-0.46	-1.07

In order to identify the possible source of over binding, we have analyzed the behavior of the Ti-O repulsive potential performed by the parameters. Therefore, we have studied the elastic properties of the bulk titanium dioxide anatase. An indicator is the bulk modulus, which is a measure of resistance to volume change by the applied pressure. Hence, we have stretched and shrunk the lattice vector by 5% and fitted the parabola shown in **Figure 5-1**. The calculated

DFTB bulk modulus is overestimated by a factor of two compared to the experimental value and the calculated one with DFT(B3LYP), as reported in **Table 5-2**. Nevertheless, we have observed that the DFTB curvature of the Ti-O potential around the equilibrium volume is harmonic. Therefore, a possibility to correct the over binding is to shift the DFTB potential curve rigidly to the DFT one by applying a scaling factor.

Table 5-2 Comparison between the experimental value of bulk modulus in GPa and calculated by DFT(B3LYP) and DFTB methods, respectively.

B_0(GPa)		
Exp[a]	DFT(B3LYP)[b]	DFTB
179	178	250

[a] Phy.Rev. B 61, 14 (2000)

[b] Phy.Rev. B 63, 155409 (2001)

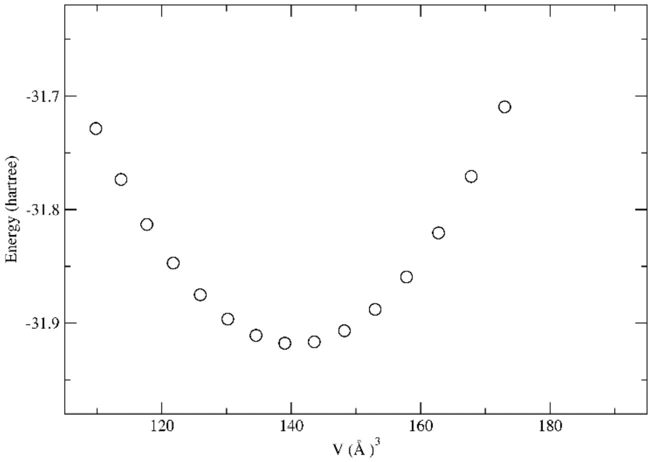

Figure 5-1 Parabolic fit for total energy vs total volume of bulk anatase.

We are allowed to scale scaled the energies afterwards for the evaluation since the relative energies are well reproduced with the DFTB method as compared with DFT (**Table 5-3**), so we corrected the over-binding by applying a factor to the calculated DFTB energies. The scaling factor applied (0.63) is calculated as the average of the ratio between bi-dentate to mono-dentate and tri-dentate to mono-dentate adsorption energy, which is in agreement with both DFT and DFTB methods, as shown in **Table 5-3**.

Table 5-3 Comparison between the mono-, bi- and tri-dentate adsorption mode (ΔE, in eV) for the TETT linker on the TiO_2 nanoparticle with the DFT(B3LYP-D*) and the DFTB method for the tri-site C. The energy gain per bond is reported in parenthesis for each adsorption mode taken in account. The ratio monodentate/monodentate, bidentate/monodentate and tridentate/monodentate is also given.

	ΔE (eV)			
	DFT(B3LYP-D*)		DFTB	
	per ligand (per bond)	ratio	per ligand (per bond)	ratio
mono-	-1.91 (-1.91)	1	-2.49 (-2.49)	1
bi-	-2.23 (-1.11)	0.58	-3.35 (-1.68)	0.67
tri-	-2.64 (-0.88)	0.46	-4.15 (-1.38)	0.56

Another possibility is to reparametrize the Ti-O and Si-O pairwise interaction and then check the "transferability" to the mixed Ti-O-Si system. However, the success is not guaranteed.

To further validate the new set of parameters, we compared the DFT(B3LYP) and DFTB Ti charge distribution in the TiO_2 NP. We plotted for each Ti in the NP the difference with respect to the Ti charge in the anatase bulk. As shown in **Figure 5-2**, the DFTB provides adequate charge description compared with DFT results. In both graphs we can distinguish two areas: in the first one the charges are bulk-like since they are in the core of the nanoparticle (R<6 Å), and in the second area the charge values oscillate since Ti atoms are far from the centre of the nanoparticle (6<R>12 Å) and the surface effect dominates.

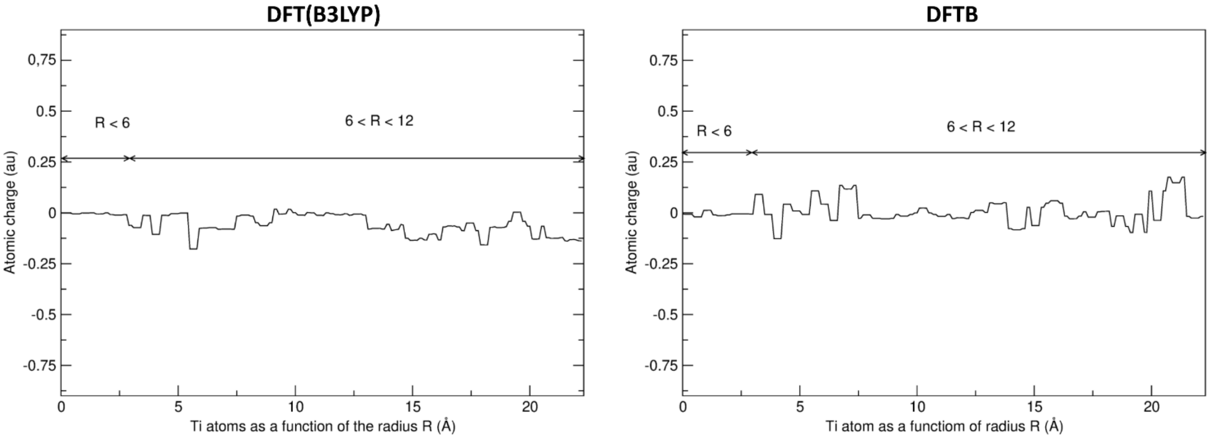

Figure 5-2 Ti charge (in au) distribution as a function of the nanoparticle radius with DFT(B3LYP) and DFTB methods. The zero is set to the charge of the Ti in the anatase bulk for DFT(B3LYP) and DFTB, respectively. The double arrow distinguishes the Ti atoms in the core (R<6 Å) from the Ti atoms in the surface (6<R>12).

5.3.2 Modifying the combined set of parameters

During the calculations, we faced a numerical problem related to a linear dependency in the overlap matrix and much effort has been made to solve the diagonalization failure.

We observed that the matrix elements, which involve the Ti-4p atomic like-orbital, are unexpectedly large at long distances. For that reason, we scaled the Hamiltonian and the overlap matrix elements pdσ, pdπ, ppσ, and ppπ until the numerical problem was overcome. We have learnt that reducing integrals shown in **Figure 5-3** by 40% is enough to succeed in the diagonalization procedure.

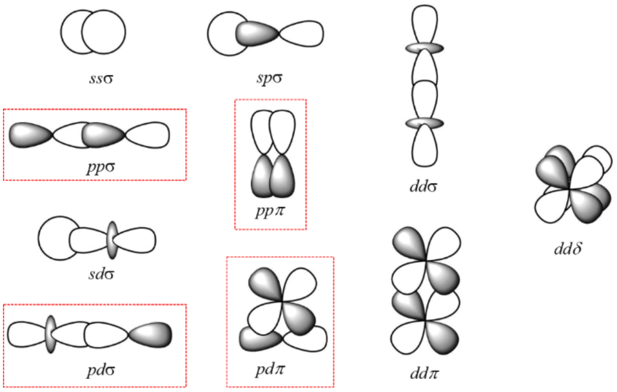

Figure 5-3 Representation of the fundamental bond integrals used to construct the tight-binding Hamiltonian. The red boxes identify the modified bond integrals in the Slater-Koster table used throughout this work.

5.4 How to model the TETT linkers condensation on the TiO_2 NP

The silanization of the TiO_2 nanoparticle involve the -OH groups present on the surface, which are coming from the nanoparticle synthesis.

Commonly, the spherical TiO_2 nanoparticles are prepared by sol−gel or hydrothermal methods, in which water is used as a primary reaction solvent. The synthesis process involves three steps: hydrolysis, condensation, and oxolation. In the hydrolysis step, Ti forms aquo, hydroxo, or oxo complex with water. The condensation step follows the hydrolysis, in which two (or more) complexes can condensate to give the Ti−O−Ti bonds. After that, oxolation can occur with the formation of additional oxo bridges between Ti fragments through nucleophilic addition. Usually, this step is accompanied by water elimination and the Ti−O−Ti bonds are finally formed.[267]

Each step shows different rates at different pH values, therefore, depending on the reaction conditions, hydrolysis can be promoted by either increasing dehydroxylation (a water molecule is removed from a Ti−OH group) or deprotonation (a OH^- attacks a Ti centre to form a Ti−OH bond).[268] At the end of the synthesis process, the residual OH groups on the nanoparticle surface can be further involved in the condensation reaction with the alkoxysilanes. As a result of the reaction bonds are formed at the interface between the inorganic component, titanium dioxide, and the organic component, alkoxysilanes.

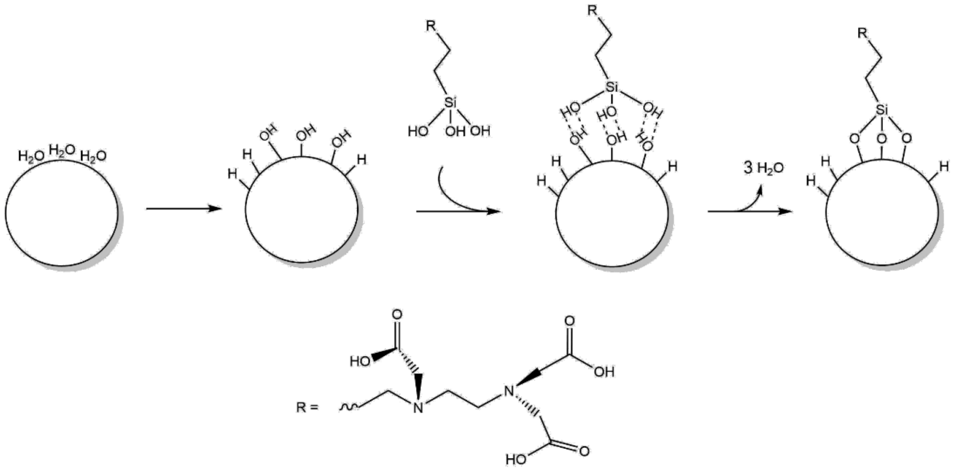

Figure 5-4 Schematic representation of the silanization reaction of the TETT (R) linker on the metal oxide NP. Starting from the right the synthesis of TiO_2 NP in aqueous environment, hydrolysis, and condensation of the TETT linker.

The classical mechanism for surface reactivity of silanes (e.g., trialkoxysilanes) involves hydrolysis of the silane reagent to the trisilanol, followed by surface reaction with the OH groups present on the metal oxide surface (**Figure 5-4**).

Schlecht et al. observed that the hydrolysis of trialkoxysilanes to trisilanols is unlikely prior to surface reaction. In their work, they proposed a second mechanism[269] in which trialkoxysilanes react directly with surface hydroxyl groups via an addition–elimination type mechanism, with the central silicon atom forming a pentavalent intermediate.

In this context, to simplify the reactions steps, we just dissociatevely adsorbed the trisilanol on the undercoordinated Ti sites and put the hydrogen on the closest two-fold oxygen (O_{2c}) of the nanoparticle.

5.4.1 Preliminary water dissociation

In order to study the TETT condensation, we have assumed that water molecules could be present on the NP surface. Considering that the synthesis of the NP takes place in an aqueous environment and involves hydrolysis and condensation reactions, we may expect the presence of residual water molecules on the nanoparticle surface. Also, the real samples of nanoparticles are in solution and interact with their surroundings via hydration shells, and it is experimentally proved that a small quantity of bound water on nanoparticles is present up to 600−700 K.[136]

Based on the previous work by our group, we know the relative reactivity at each Ti site of the spherical nanoparticles towards one water molecule.[270] The authors have distinguished sites where water molecules dissociate into OH^- on undercoordinated Ti atoms and H^+ on bridging O atoms, from sites where water molecules are adsorbed in the molecular form on undercoordinated Ti atoms.

Since the NP model ($(TiO_2)_{223}\cdot 10\ H_2O$) contains 10 intrinsic water molecules, 10 -OH groups are already available on the nanoparticle surface. However, to study the possible multidentate adsorption mode of the TETT linker, we have not taken for granted that the hydroxyl groups involved in the condensation reaction can stably coexist on closely Ti atoms. Consequently, before we have adsorbed the linker in a tri-dentate mode, we have ensured whether each Ti in the three-site can host an -OH group. To do this, we have compared the dissociation energy of three water molecules with the adsorption energy of three undissociated water molecules. As reported in **Table 5-4**, the dissociative adsorption mode is preferred compared to the undissociated one, with an energy gain from 0.19 eV to 0.60 eV.

Table 5-4 Comparison between the binding energies (ΔE, in eV) for three water molecules on a specific tri-site of the NP model with the DFT(B3LYP-D*) method. Both molecular and dissociated adsorption modes are considered. The tri-site and the atom label are clarified in **Figure 5-6**.

		ΔE(eV)	
tri-site	atom label	molecular	dissociated
A	12 16 1	-3.65	-4.07
B	10 3 8	-2.78	-2.94
C	11 2 3	-2.93	-3.12
D	1 1 3	-3.08	-3.12
E	12 16 18	-2.59	-3.19
F	7 7 14	-2.92	-4.03

Therefore, without considering the possible distortion introduced during the adsorption, we conclude that it is possible to condensate the TETT in the tridentate mode.

5.4.2 TETT adsorption modes

This section is dedicated to the study of the different adsorption modes of the TETT molecule at low coverage. The chemically active sites on the NP surface are the unsaturated acidic cationic (Ti_{4c} and Ti_{5c}) and the basic anionic sites (O_{2c}).

The silane coupling agents (TETT) can be hydrolyzed to silanol derivates. In the TETT molecule, the propyl chain has been functionalized with an ethylenediamine group, which has three substitutional carboxylic groups (**Figure 5-5**).

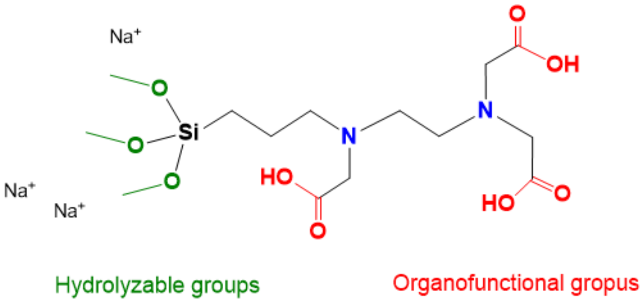

Figure 5-5 The structure of TETT [N-(trimethoxysilylpropyl) ethylene diamine triacetic acid, trisodium salt], with the hydrolyzable group in green and the carboxylic groups in red.

Depending on the hydrolyzation degree of the TETT linker, different adsorption modes on the TiO_2 nanoparticle can be considered. Toledo et al. have observed three different signals in the ^{29}Si and ^{13}C NMR spectra of the functionalized TiO_2 nanoparticles, which were ascribed to the condensation reaction products, and indicate whether each silanol is attached through one ($-OSi(OH)_2R$), two ($-O_2Si(OH)R$) or three ($-O_3SiR$) chemical bonds, respectively.[271]

Even though there are many undercoordinated Ti atoms due to the higher curvature of the NP,[118] the tridentate adsorption is not always feasible because it requires three not sterically hindered and closed Ti atoms. On the flat surface, the tridentate adsorption mode is not observed because the distance to a third unsaturated Ti atom is too long.

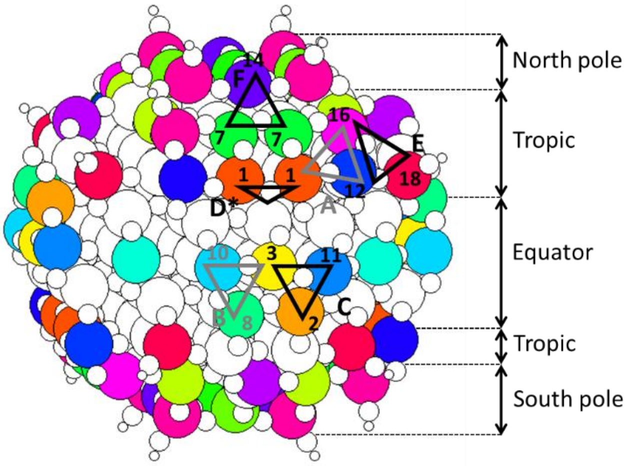

Figure 5-6 Map of the Ti atoms of the spherical anatase TiO_2 nanoparticle with different coordination environments visually shown by the colour coding and numbering. The triangle defines the possible tri-site (triad) in the nanoparticle model.

We have succeeded in binding TETT to four different tri-atomic Ti sites among the selected ones reported in **Table 5-5**. The adsorption energies are similar for the tri-sites E and F and amount to about −3.8 eV since the adsorption takes place on the pole of the NP (**Figure 5-6**). Differently, if the TETT is adsorbed at the equator on the tri-site B and C (**Figure 5-6**), the energy gain drops to -2.48/-2.61 eV.

Table 5-5 Calculated binding energies (ΔE, in eV) for the tridentate adsorption mode of the TETT linker on a specific tri-site (triad) in the NP model with the DFTB method. The name of the triad and the corresponding atom label are given (see **Figure 5-6**). The bidentate adsorption mode is considered if the tridentate adsorption was not successful.

Localization	Triad	Atom label	ΔE(eV) tri-	ΔE(eV) bi-
Tropic	A	12 16 1	-	-2.68
Equator	B	10 3 8	-2.48	
Equator	C	11 2 3	-2.61	
Tropic	D	1 1 3	-	-2.56
Tropic	E	12 16 18	-3.84	
North pole	F	7 7 14	-3.82	

The energy difference between the adsorption at the equator and the pole of the NP (see **Figure 5-6**) is due to the different degree of rearrangement in the NP. We have observed that the O_{2c} at the equator is pushed back inside the NP by 1.3 Å because of the Si repulsion, as shown in **Figure 5-7**.

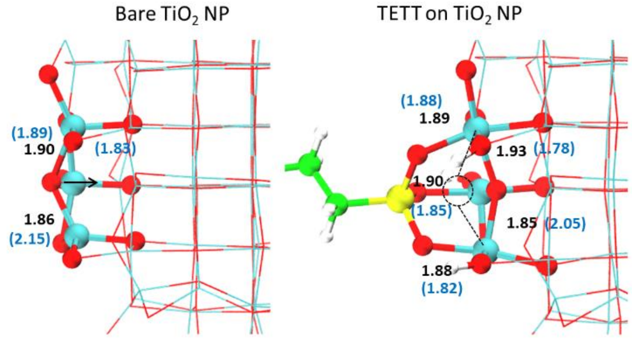

Figure 5-7 Top views of one TETT linker adsorbed on the tri-site C of the spherical NP as obtained by DFTB and DFT calculations. Ti atoms are shown in cyan, O atoms in red, H atoms are shown in white, Si atom in yellow, C atoms in green, and N atoms in blue. Relevant distances, for both methods, are reported Å. The DFT(B3LYP-D*) distances are detailed in parenthesis.

Due to the stereochemical conformation of the Ti atoms on the tri-site A and D, we did not succeed in the adsorption of the linker in the tridentate mode. During the relaxation of the TETT at tri-site-site A and D we have observed an eruption of one of the Ti-O bonds, and the conversion of the tridentate mode to the bidentate one.

The energy gain for the bidentate adsorption at the sites A and D is comparable to the adsorption energy at the tri-sites B and C due to distortions introduced in the tridentate structured on the NP surface.

To clarify the balance between the energy gain and the cost of the distortions, we have studied the energy gain for each Ti-O bond at the tri-site C. We have verified whether the energy per bond in the bidentate or tridentate mode is two or three times the energy bond of the monodentate adsorption or not. The estimation of the binding energies per bond for mono-, bi- and tridentate adsorption of the linker, using DFT and DFTB methods, are reported in **Table 5-3**. Even though the Ti-O bonds are not additive, the energy gain per ligand on the tridentate mode yields more energy than bi- or monodentate ones (see **Table 5-3**). Consequently, despite the distortion introduced in the NP, the tri-dentate mode is still feasible.

The ratio reported in **Table 5-3** is defined as the energy deviation of the tridentate and bidentate mode with respect to the monodentate (monodentate/monodentate, bidentate/monodentate, and tridentate/monodentate). The values obtained with the DFTB methods are in agreement with the DFT ones. The ratios are in qualitative agreement, which justifies the abovementioned scaling (section 5.3.1). Moreover, the DFT geometries are well reproduced by DFTB methods (**Table 5-6** and **Figure 5-8**) and the geometrical details are summarized in **Table 5-6**.

We may conclude this part of the work with the consideration that it is possible to dissociatively adsorb the TETT linker in the tridentate mode, as observed experimentally.[271] The most stable configuration is the adsorption at tri-sites E and F, followed by tri-sites B and C.

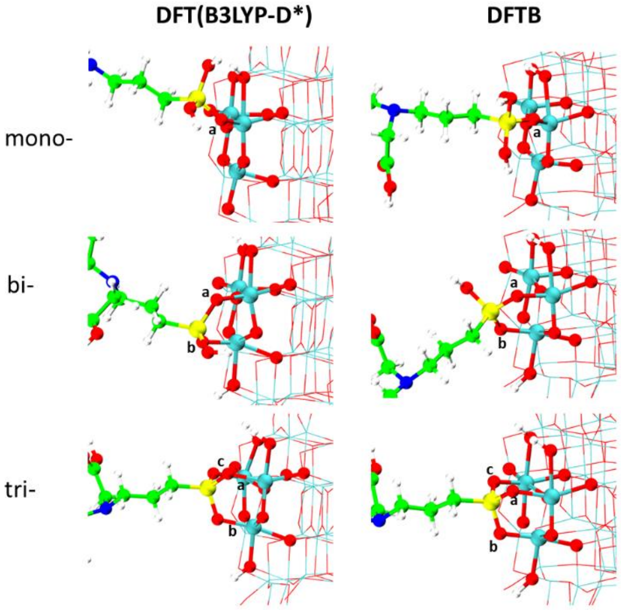

Figure 5-8 Adsorption configurations (side views) for one TETT linker on the tri-site C of the spherical NP as obtained by the DFT(B3LYP-D*) and the DFTB calculations. Ti atoms are shown in cyan, O atoms in red, H

atoms in white, Si atom in yellow, C atoms in green, and N atoms in blue. Relevant covalent bonds are identified with the letters a, b, c, and the corresponding values are reported in **Table 5-6**.

Table 5-6 Calculated bond distances for the mono-, bi- and tri-dentate TETT adsorption mode at the tri-site C. The DFTB value are reported in parenthesis. The letter a, c, and c identify the O atoms involved in the adsorption process (**Figure 5-8**).

		Distance (Å)	
Adsorption mode	O	Si-O	O-Ti
Mono-	a	1.64 (1.58)	1.84 (1.86)
Bi-	a	1.70 (1.63)	1.84 (1.88)
	b	1.67 (1.59)	1.84 (1.91)
Tri-	a	1.65 (1.62)	1.89 (1.88)
	b	1.66 (1.64)	1.85 (1.91)
	c	1.68 (1.61)	1.81 1.89)

5.4.2.1 Electronic properties

As explained in section 4.3.2, DFTB is generally not accurate enough to describe the electronic properties of such delicate functionalized metal oxide systems. However, we have established that performing DFT single point calculations on DFTB optimized geometries effectively improves the description of the electronic structure, providing results in close agreement with DFT. As shown in **Figure 5-9**, the electronic structure calculations were performed at three different levels of theory: DFTB (upper panel **Figure 5-9**), single-point DFT calculation on the DFTB optimized geometry (DFT/DFTB) (middle panel **Figure 5-9**), and DFT (lower panel **Figure 5-9**).

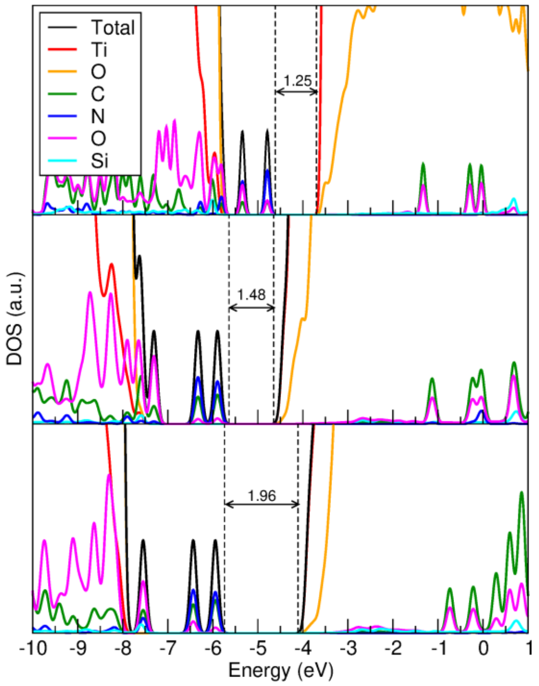

Figure 5-9 Total (DOS) and projected (PDOS) density of states for the tridentate configuration at site C (see **Figure 5-8**) of single TETT molecule adsorption by DFTB (upper panel), DFT/DFTB (middle panel), and DFT (lower panel). The HOMO−LUMO gap is reported for each plot by dashed lines. The zero energy is set to the vacuum level.

The DOS obtained by DFTB is characterized by the presence of two mid-gap states, while those by DFT/DFTB and DFT calculations present three mid-gap states. HOMO and HOMO-1 are mainly related to the C and N atoms of the TETT, and the HOMO-2 peak is ascribed to the O atoms of the molecule. In the DFTB calculations, the HOMO-2 state is inside the valence band due to the underestimated band gap value. The band gap values for the bare NP in DFTB and DFT are 3.11 and 4.13 eV, respectively.[118]

5.4.3 Molecular dynamics at different coverage

In the previous section, we have investigated the adoption mode of the TETT linker on the TiO_2 NP at 0 K. Once we have obtained the equilibrium geometry, we have sampled the configurational space by means of molecular dynamics. The kinetic energy introduced in the simulation, through temperature, allows the system to overcome the barriers in the order of k_BT and to reach the global minimum.

Through MD, we have verified the stability of the investigated adsorption modes and how they evolve with time. For each adsorption site we have done some statistics to analyse the possible transitions tri-dentate to bi-dentate etc... during the simulation. We could expect that the tri-dentate adsorption mode induces some strain that could be released during the molecular dynamics runs. Furthermore, we have explored the possible conformations of the flexible ligand in order to find the most stable interactions with the NP.

5.4.3.1 Analysis of molecular dynamics through structural and electronic indicators

Structural modifications of the TETT linker adsorbed on the nanoparticle during the MD runs have been characterized by angles, distances, and linker orientation. The average dipole moment has also been monitored.

We have considered the evolution of the Si-O-Ti angles and the Ti-O distances (as geometrical parameters) to characterize the trajectories in which the tridentate absorption mode is preserved even at high temperatures. Another relevant aspect is the orientation of the linker during the dynamics. For this, we have plotted the absolute value of the angle (α) (**Figure 5-10**) between the plane, in which the Ti atoms involved in the adsorption lie, and the vector passing through the Si and the farthest N atom in the TETT linker.

Regarding the dipole moment, bulk anatase TiO_2 has not a dipole moment, whereas the nanoparticle may have one due to the asymmetric distribution of Ti and O atoms at the surface of the nanoparticle. We have studied the magnitude of the dipole moment ($\vec{\mu}$) as a function of the time, separating the contribution of the linker from that of the nanoparticle. We are interested in the estimation of how much the dipole moment in the linker and the NP change as a consequence of surface functionalization.

The dipole moment can be approximated as the Mulliken charge (q_i) multiplied by the coordinate vector ($\vec{r_i}$), as reported in the following formula, where the index *i* run over all the N atoms:

$$\vec{\mu} = \sum_{i}^{N} q_i \cdot \vec{r_i} \tag{5.4}$$

The Mulliken charge q_i is express as the atomic number (Z_i) minus the Mulliken population (P_i):

$$q_i = Z_i - P_i \tag{5.5}$$

Considering the component of the coordinate vector $(\vec{r_i})$ for each atom, the final expression of the dipole moment is:

$$\vec{\mu} = \sqrt{(\sum_i x_i \cdot q_i)^2 + (\sum_i y_i \cdot q_i)^2 + (\sum_i z_i \cdot q_i)^2} \tag{5.6}$$

5.4.3.2 Molecular dynamics at low coverage

In this section, we present the analysis of the MD simulations based on the indicators introduced in the previous paragraph. We have sampled the conformational space of the functionalized NP by conducting some statistics to elucidate the adsorption mode of the TETT molecule. Different simulations for the same tri-sites are distinguished by labelling them with an incremental number (md1, md2, etc.).

Tri-site B

Starting from the TETT linker optimized at the tri site B we carried out two molecular dynamics simulations. The statistic is rather small since tri-site B presents one Ti atom that is the is the same as in tri-site C (**Figure 5-6**). Consequently, when considering the adsorption at the tri-site B we exclude the adsorption at the tri-site C and vice versa.

The Si-O-Ti angles and Ti-O distances fluctuate around the equilibrium value during the dynamics md 1 (**Figure 5-11**), because no interactions between the linker and the NP are established. We only observed one intramolecular H-bond between the carboxyl groups. Even the standard deviation for the angle (α), defined in **Figure 5-10**, fluctuated around the mean value (61.4°). On the contrary, in the evolution of the md 2 (**Figure 5-11**) we observed the transition to bidentate adsorption. One proton went back to the oxygen of the TETT molecule, and the reformed -OH group establishes a coordinative bond with the underlying Ti atom.

Moreover, the linker bents and folds the NP surface to form two H-bonds. Accordingly, after the MD run, the optimized md 1 configuration is stabilized by only -0.30 eV, whereas after md 2 it is stabilized by -0.67 eV, given the favorable linker folding and the interactions with the surface (**Figure 5-11**).

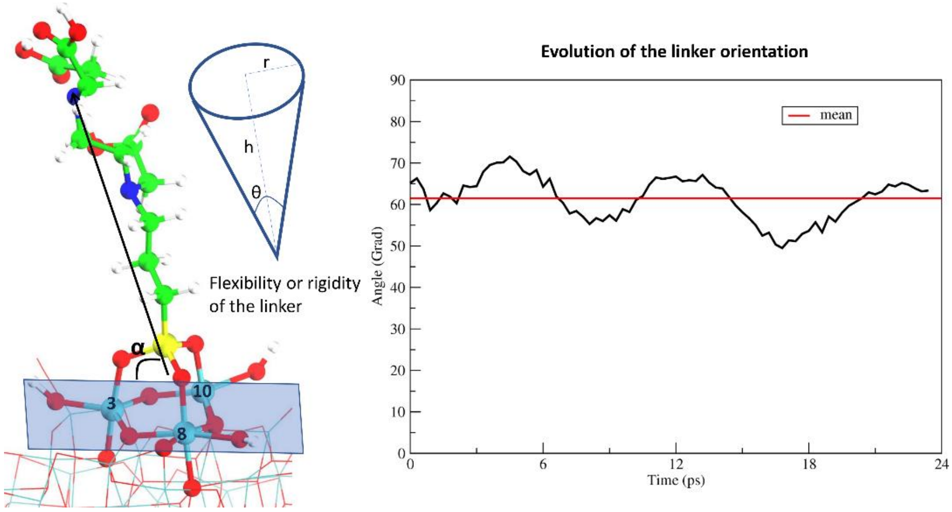

Figure 5-10 On the left, the linker orientation defined as the angle α between the plane (in light blu) that contains the Ti atoms of the tri-site and the vector that join the Si atom (in yellow) and the farthest N atom (in blu) in the linker. On the right, the evolution of the angle α for the md1 related to the tri-site B.

Table 5-7 Calculated adsorption energies (ΔE in eV) for the optimized last snapshot of the molecular dynamics

	ΔE (eV)
md 1	-2.78
md 2	-3.15

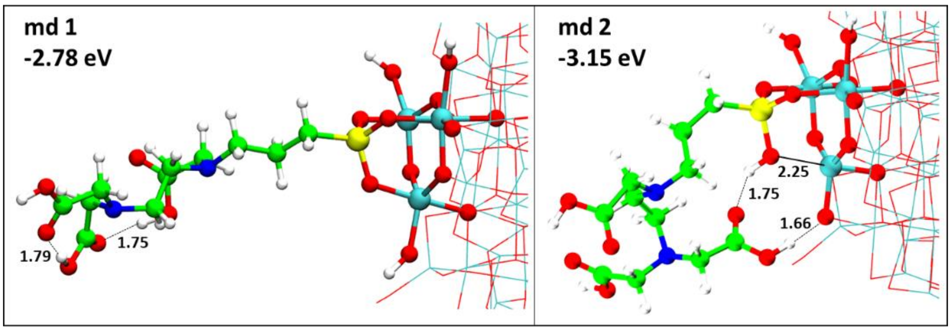

Figure 5-11 Adsorption configurations (side views) and energies per molecule in eV for one TETT linker on the tri-site B of the spherical NP as obtained by DFTB calculations. Ti atoms are shown in cyan, O atoms in red, H atoms in white, Si atom in yellow, C atoms in green, and N atoms in blue. Relevant hydrogen-bonds and coordinative bond are represented by dashed lines and solid lines, respectively. Distances are reported in Å.

Tri-site C

Among the various tri-sites in **Table 5-5**, we have conducted some statistics only for one of them. In particular, we have selected tri-site C to validate the tridentate adsorption mode. Considering six molecular dynamics runs, only in one case we observed the evolution in a bidentate mode (md 4 in **Figure 5-12**). Therefore the covalent adsorption in a tridentate fashion is rather stable.

The calculated adsorption energies of the optimized structure after the thermal treatments (**Table 5-8**) are more stable compared to those obtained at 0 K (-2.61 eV, see **Table 5-5**). The energy gain is related to the number and the strength of the interactions between the linker and the NP.

Table 5-8 Calculates adsorption energy (ΔE in eV) for the optimize last snapshot of the molecular dynamics runs.

	ΔE (eV)
md 1	-3.07
md 2	-4.65
md 3	-3.01
md 4	-3.38
md 5	-4.86
md 6	-4.91

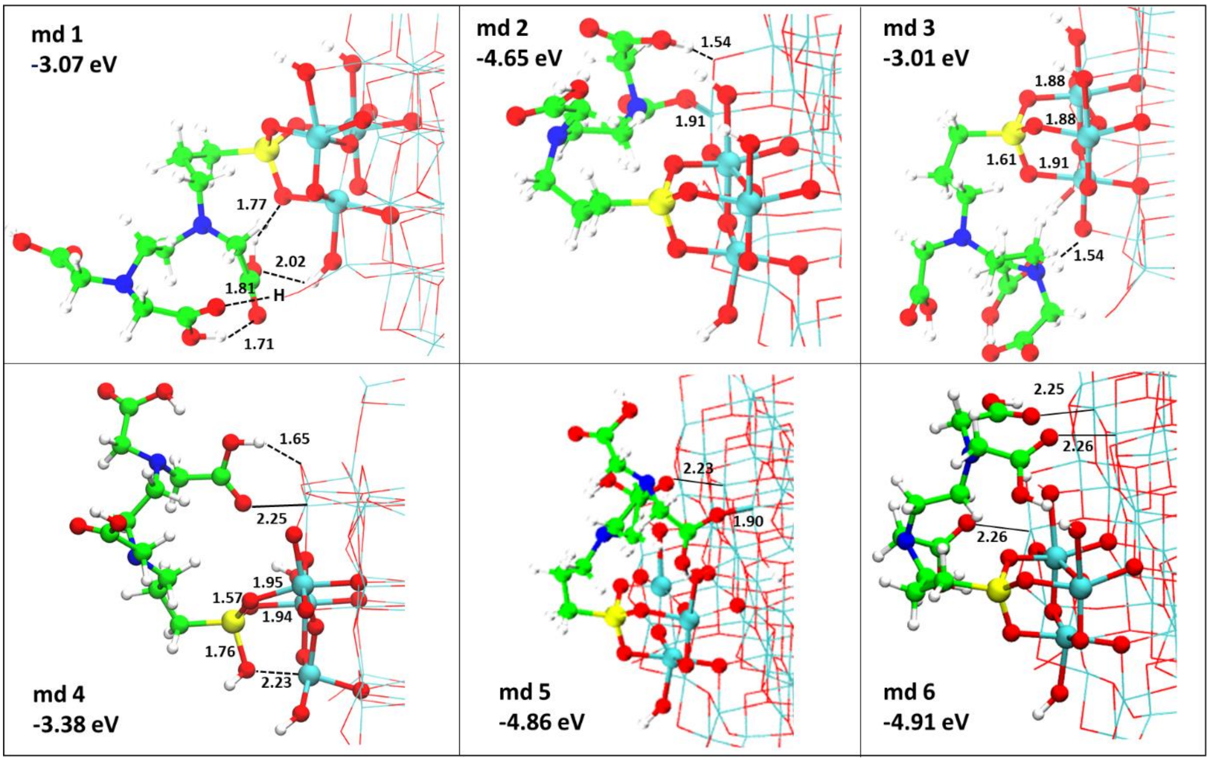

Figure 5-12 Adsorption configurations (side views) and energies per molecule in eV for one TETT linker on the tri-site C of the spherical NP as obtained by DFTB calculations. Ti atoms are shown in cyan, O atoms in red, H atoms in white, Si atom in yellow, C atoms in green, and N atoms in blue. Relevant hydrogen-bonds and coordinative bonds are represented by dashed lines and solid lines, respectively. Distances are reported in Å.

After the evolution of the functionalized nanoparticle model at 300 K, we have optimized the final structure of the trajectory back at 0 K. The configuration obtained after md 6 (**Figure**

5-12) is the most stable (-4.91 eV) for the tri-site C, due to the formation of three coordinative bonds. Also, the weak dispersion interactions within the TETT chain and the nanoparticle surface further stabilize the configuration from md 6.

The energy gain becomes slightly smaller in the configurations where one carboxyl group dissociates, as shown in **Figure 5-12** for md 2 and md 5, i.e. -4.65 eV and -4.86 eV, respectively. On the contrary, in md 1, md 3 and md 4 only H-bonds are formed (**Figure 5-12**), therefore the energy gain is lowered and it is approximately around -3.0 eV (**Table 5-8**).

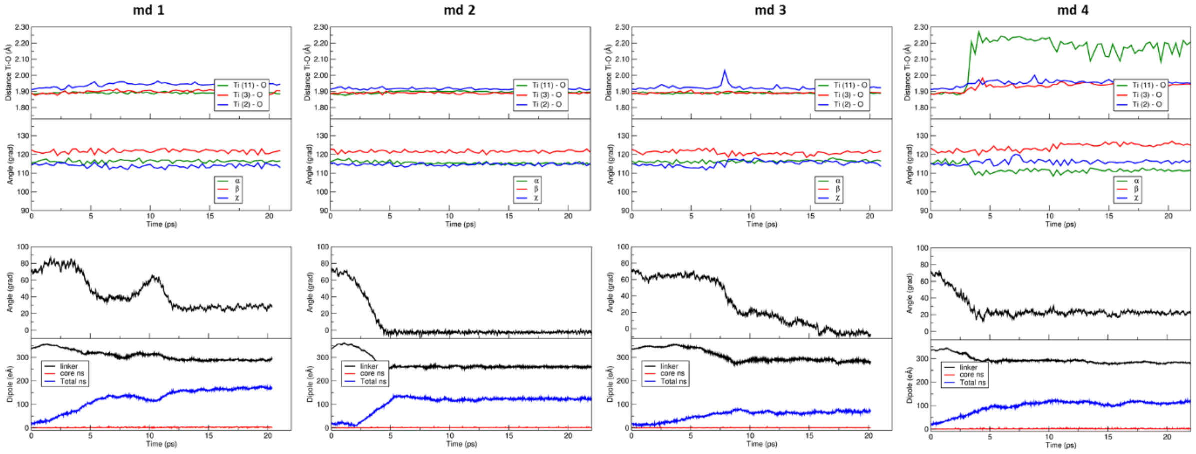

Figure 5-13 Evolution of the md 1, md 2, md 3, and md 4 for the tri-site C. In the upper graphs, the geometrical parameters: the Ti-O distances in Å, and the Ti-O-Si angles in grad. In the lower graphs, the evolution of the angle, in grad, with the dipole moment in eÅ for the linker, the NP, and the core of the NP. The detailed description of the angle and dipole moment are reported in section 5a.

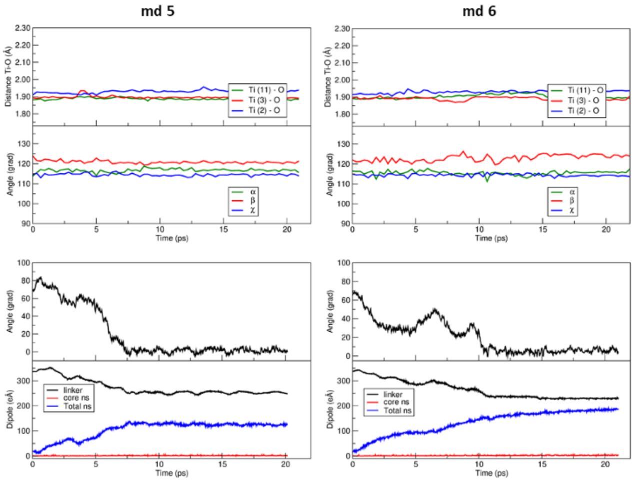

Figure 5-14 Evolution of the md 5 and md 6 for the tri-site C. In the upper graphs, the geometrical parameters: the Ti-O distances in Å, and the Ti-O-Si angles in grad. In the lower graphs, the evolution of the angle, in grad, with the dipole moment in eÅ for the linker, the NP, and the core of the NP. The detailed description of the angle and dipole moment are reported in section 5a.

The evaluation of the dipole moment for the nanoparticle (blue line in **Figure 5-13** and **Figure 5-14**) and the linker (black line in **Figure 5-13** and **Figure 5-14**) describes the interactions between them. As a general statement, the dipole difference between the NP and the linker decrease due to the thermal treatment, and the balance between them can be correlated with the type of interactions.

For the tri-site C, we can identify two extreme situations: on one side the md 3 and on the other the md 6. In md 3, the chain of the linker forms only one H-bond with the NP, whereas in md 6 the linker establishes three dative bonds. We observe that in the md 3 the difference between the linker and the NP is the largest, while in md 6 is the smallest because increasing the number of interaction between them decrease the dipole moment difference.

It is noteworthy that the dipole of the atoms in the core of the NP (red line in **Figure 5-13** and **Figure 5-14**) is constant during the evolution of the MD, because the atoms in the core of the NP are not influenced by the presence of the linker.

As a reference value we have calculated the dipole of the bare NP 10 eÅ (48 D), which is in agreement with other work.[272] However, we have noticed that the NP becomes more polar 200 eÅ (960 D) due to the surface functionalization.

Tri-site E

During all the simulations for the linker adsorbed on the tri-site E (**Figure 5-15**), the Ti-O distances fluctuate around the mean value (dev. St. ± 0.007), which means that the tridentate mode is kept. Accordingly, also the angles do not deviate during the MD runs. The average value for α and γ is 120° and 130°, respectively, whereas the β angle is larger (150°) due to the arrangement of the Ti atoms on the NP surface that make the Ti-O-Si angles not totally symmetric.

Table 5-9 Calculates adsorption energy (ΔE in eV) for the optimize last snapshot of the molecular dynamics.

	ΔE (eV)
md 1	-5.55
md 2	-4.77
md 3	-4.17
md 4	-4.71

The linker bends toward the NP surface during the md 1 and forms two coordinative bonds through the carbonyl (2.24 Å, 1.96 Å) groups, while during md 3 one H-bond and one coordinative bond are formed (**Figure 5-15**).

Ideally the TETT chain, due to the thermal treatment, can form at least two H-bonds for each carboxyl group. However, a considerable distortion in the linker should be introduced to find the orientation which maximize H-bonds with the NP. The TETT chain folds into a conformation such that 4 H-bonds are formed in md 2 and three H-bonds are formed in md 4.

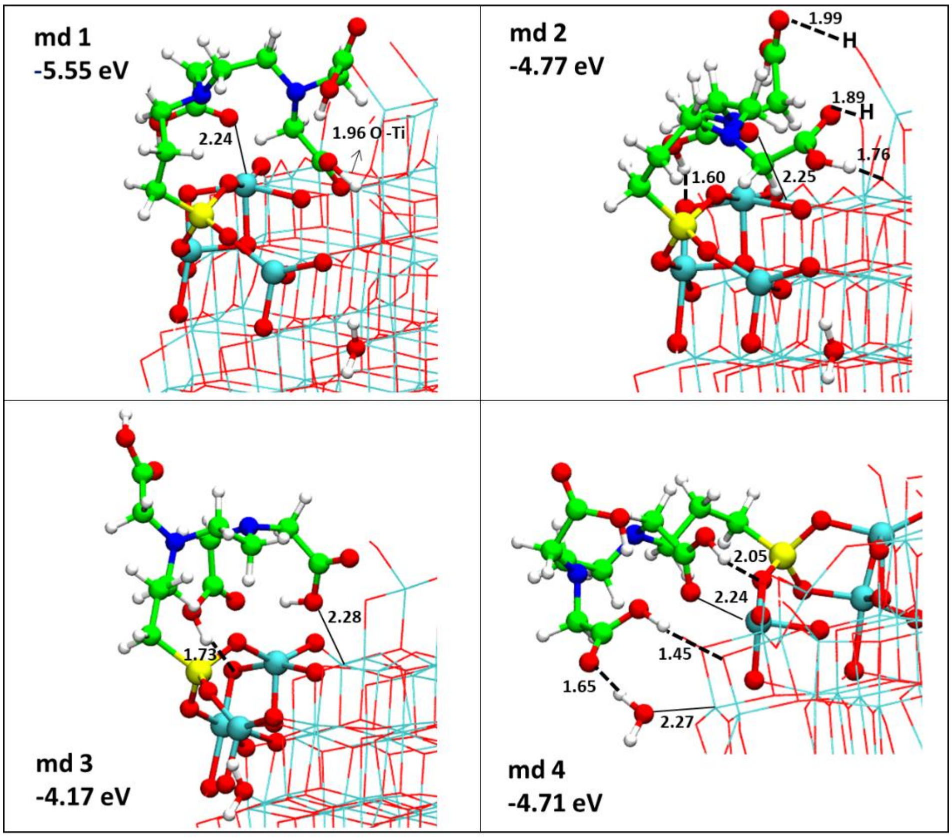

Figure 5-15 Adsorption configurations (side views) and energies per molecule in eV for one TETT linker on the tri-site E of the spherical NP as obtained by DFTB calculations. Ti atoms are shown in cyan, O atoms in red, H atoms in white, Si atom in yellow, C atoms in green, and N atoms in blue. Relevant hydrogen-bonds and coordinative bonds are represented by dashed lines and solid lines, respectively. Distances are reported in Å.

At 0 K before the MD, the tridentate adsorption at the tri-site E (-3.84 eV) is the most stable with respect to the tri-site C (-2.61 eV) and tri-site B (-2.48), see **Table 5-5**. In addition, the configurations obtained after the dynamics starting from the tri-site E are even more stable up to -5.55 eV (**Table 5-9**). The high stability is due to the stable anchoring of the linker in this specify tri-site of the nanoparticle surface.

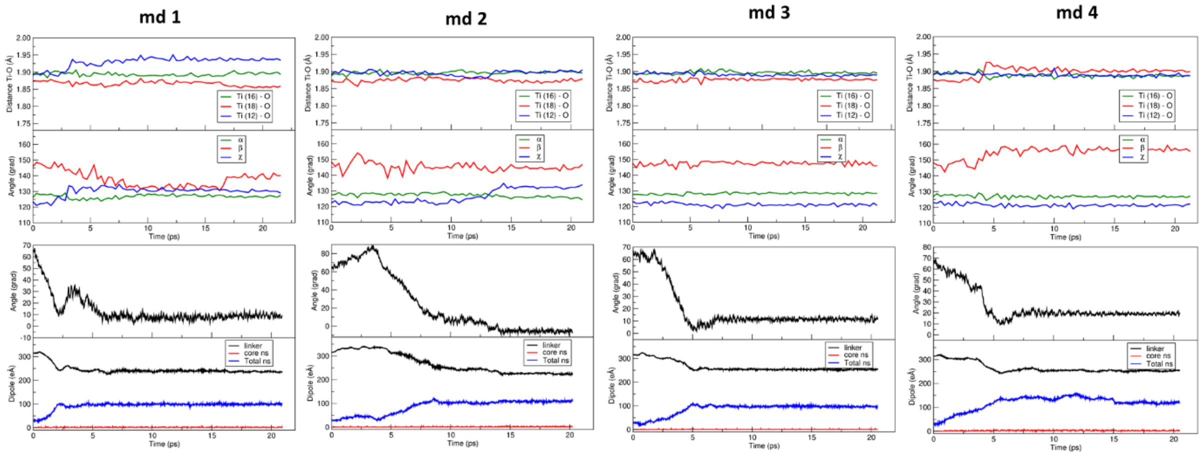

Figure 5-16 Evolution of the md 1, md 2, md 3, and md 4 for the tri-site E. In the upper graphs, the geometrical parameters: the Ti-O distances in Å, and the Ti-O-Si angles in grad. In the lower graphs, the evolution of the angle, in grad, with the dipole moment in eÅ for the linker, the NP, and the core of the NP. The detailed description of the angle and dipole moment are reported in section 5a.

The difference of the dipole moment, between the linker and the NP, in md 3 (**Figure 5-16**), is the highest because the linker establishes one H-bond (1.76 Å) and one coordinative bond (2.28 Å) that are the weakest bonds compared to the same type of interactions in the other dynamics. On the contrary, in md 1, md 2, and md 4 the difference is slightly smaller compare with the md 3 because all the three carboxyl groups are closer to the surface. Therefore, if the linker is closer to the NP surface, the numbers of interactions are higher, and consequently, the smaller is the dipole difference between the dipole of linker and the nanoparticle.

Tri-site F

Also, for the tri-site F the tridentate mode is kept along all the trajectories. The angles Ti-O-Si and Ti-O distances oscillate around the equilibrium value.

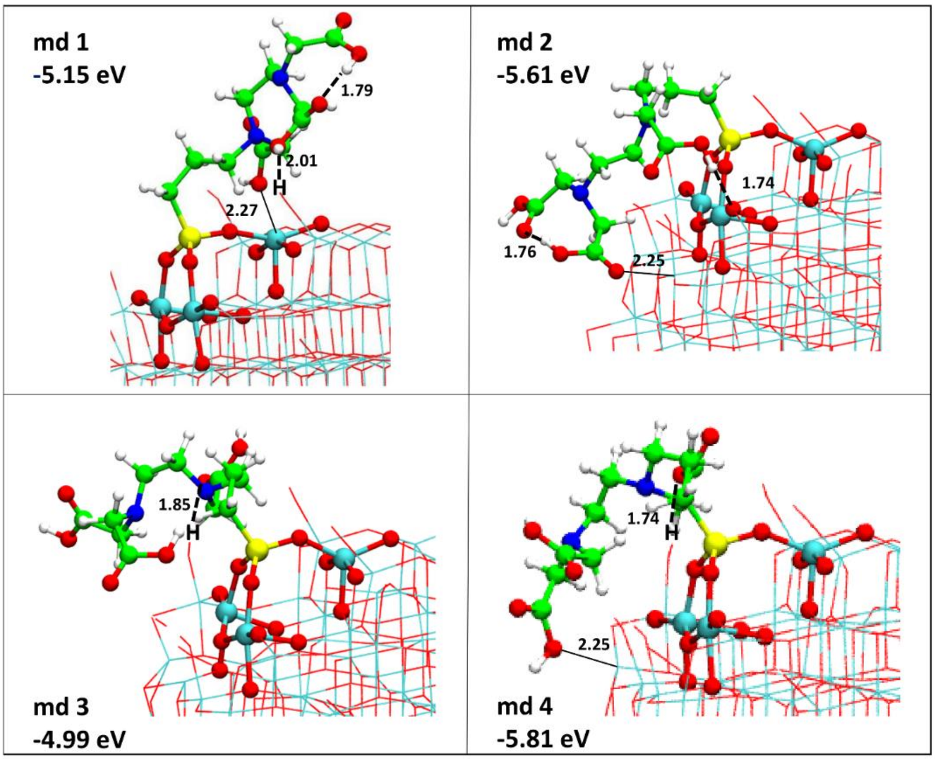

Figure 5-17 Adsorption configurations (side views) and energies per molecule in eV for one TETT linker on the tri-site F of the spherical NP as obtained by DFTB calculations. Ti atoms are shown in cyan, O atoms in red, H atoms in white, Si atom in yellow, C atoms in green, and N atoms in blue. Relevant hydrogen-bonds and coordinative bonds are represented by dashed lines and solid lines, respectively. Distances are reported in Å.

Table 5-10 Calculates adsorption energy (ΔE in eV) for the optimize last snapshot of the molecular dynamics.

	ΔE (eV)
md 1	-5.15
md 2	-5.61
md 3	-4.99
md 4	-5.81

The calculated adsorption energy before the molecular dynamics at the tri-site F (-3.82 eV) is similar to the adsorption at the tri-site E (-3.84 eV), which is consistent since both tri-sites are at the pole of the NP (see **Figure 5-6**). However, after the MD the obtained configurations for the tri-site F are more stable compared to the configurations obtained for the tri-site E after the MD, since the energy gain is larger than -1.2 eV. The TETT linker adsorbed at the tri-site F forms three stable covalent bonds with the undercoordinated Ti atoms without stereochemical tension in the Si-O-Ti angles.

As shown in **Figure 5-18**, the evolution of the dipole moment in md 1 and md 2 is analogous, due to the similar interactions of the linker with the NP. Such interactions are one intramolecular H-bond in the molecule, and one H-bond and one coordinative bond concerning the surface. In md 4 the evolution of the dipole moment has a similar trend, but with respect to the md 1 and md 2 the intramolecular H-bond in the molecule was not observed. Regarding the md 3 the dipole difference between the linker and the NP is most significant due to the minor interactions among the TETT and the NP.

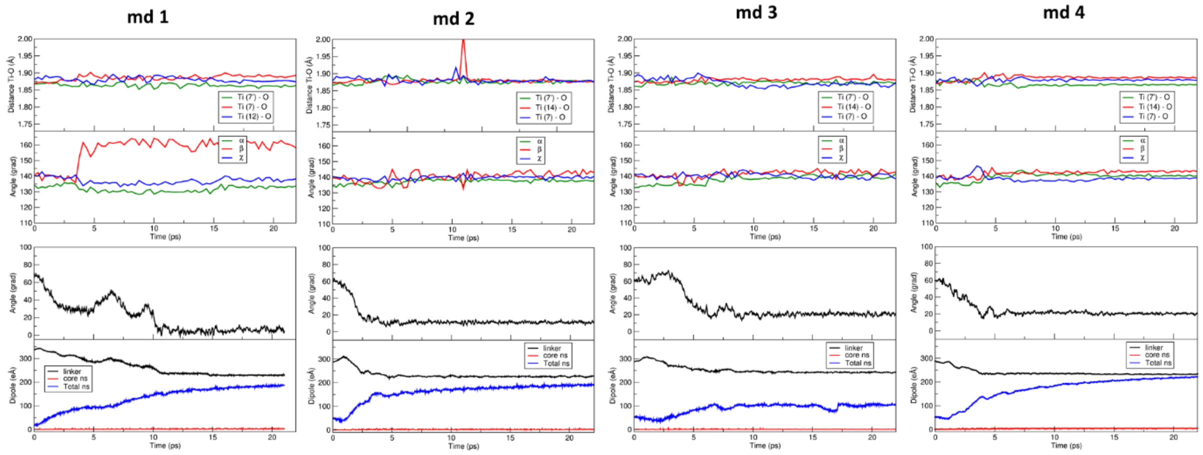

Figure 5-18 Evolution of the md 1, md 2, md 3, and md 4 for the tri-site F. In the upper graphs, the geometrical parameters: the Ti-O distances in Å, and the Ti-O-Si angles in grad. In the lower graphs, the evolution of the angle, in grad, with the dipole moment in eÅ for the linker, the NP and the core of the NP. The detailed description of the angle and dipole moment are reported in section 5a.

To summarize, except for the simulation on the tri site C, the tridentate adsorption mode is kept in all the molecular dynamics runs. The configurations obtained from the evolution of the functionalized nanoparticle are always stabilized compared to the optimized configurations before the molecular dynamics. The temperature allows the TETT linker to overcome the rotational barrier needed to modifying the linker conformation so that the molecule can bend and interact with the nanoparticle surface. The strong covalent bonds of the silanol functionality and the non-covalent interactions of the chain stabilize the linker adsorption on the TiO_2 NP surface at low coverage.

The molecular dynamics simulations reveal that the tri-site F is the most stable among the investigated tridentate configurations.

5.4.3.3 Molecular dynamics at medium coverage and high coverage

In this section, we discuss how the TETT molecules interact among them when the NP surface is decorated with a considerable amount of molecules. We are interested in exploring the packing of the molecules in the monolayer, and in characterizing the interactions involved in the monolayer. In particular, we want to quantify the number of functional groups available for further conjugation, and the number of functional groups involved in the network of the densely packed monolayer.

We have built two models that differ in the number of deposited molecules. The medium coverage has 22 molecules, while the full coverage 40 molecules. In both of them the TETT molecules were added to the NP surface simultaneously, with the carboxylic functionalities point up into the vacuum. Regarding the medium coverage, starting from the tridentate site that we have identified in **Table 5-5**, the TETT was adsorbed in equivalent symmetric sites. Then, the remaining Ti sites have been functionalized in a bidentate fashion.

For the full coverage model, together with the tridentate and bidentate adsorption mode, the remained under coordinated Ti sites have been decorated in a monodentate mode. The tridentate mode is the less abundant (12 tri-sites) compared to the monodentate (18 mono-dentate sites) and bidentate (10 bi-dentate sites) since the multidentate mode requires undercoordinated Ti atoms close to each other.

Both models were subjected to thermal treatment by means of molecular dynamics at 300 K. The medium coverage evolved for 15 ps, while the full coverage for 5 ps, due to the number of atoms 1689 and 2499, respectively.

As a result of the thermal treatment, the chains of the molecules rearrange in the monolayer in order to establish weak interactions among them or with the surface. The temperature effects only the linkers orientation, since the multidentate adsorption modes of the TETT molecule are maintained even at high temperature. We have observed only one transition from tridentate to bidentate in the evolution of the full coverage model.

The hydrogen bonds play a crucial role in determining the conformations and aggregations of TETT molecules in the monolayer. Based on the conventional definition of H-bond[273] (**Figure 5-19**), we have selected a criterion to calculate the number of H-bond in our models. Considering the O···O distance in the interval of $2.1 \text{ Å} < D < 3 \text{ Å}$, and the O—H···O angle (θ) larger than 130° we have counted 82 and 168 H-bonds in the medium (**Figure 5-20**) and in the full coverage (**Figure 5-21**), respectively.

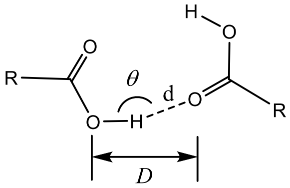

Figure 5-19 Schematic representation of the H-bond between two carboxylic groups in TETT molecules (R). Definition of the H-bond parameters: d = H···O distance, D = O···O distance, and θ = O—H···O angle.

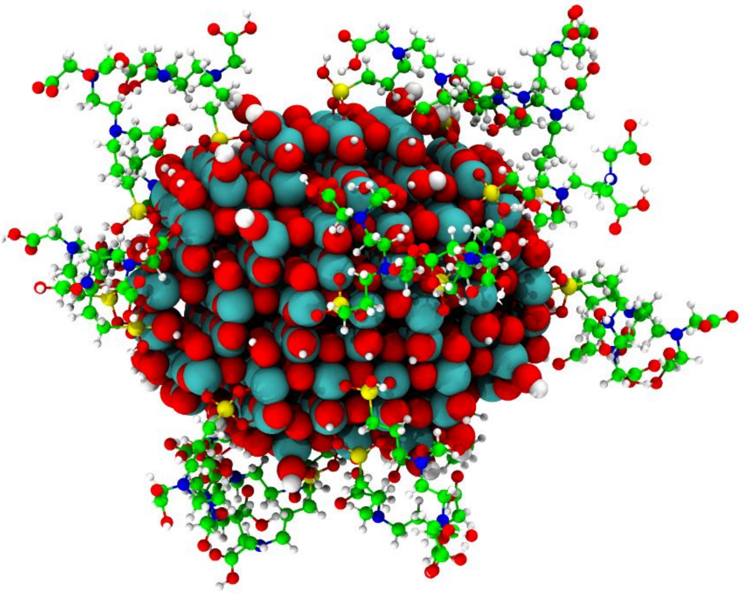

Figure 5-20 TiO_2 nanoparticle decorated with 22 TETT molecules adsorbed in a mixture of tridentate and bidentate fashion. The structure has been optimized after 15 ps of thermal treatment.

Table 5-11 Classification of the H-bonds in the medium and full coverage models.

H-bonds		**Medium coverage**	**High coverage**
With the surface		38	59
In the monoleyer	Intramolecular	18	34
	Intermolecular	13	31
	Dimer	4	16
	Others	9	28
Total in the monolayer		44	109
Total		82	169

During the dynamics, the molecules rearrange and try to get closer to the surface or interact with the neighbouring molecules. As reported in **Table 5-11**, in the medium coverage the number of H-bonds with the surface (38) is comparable to the number of H-bond among the molecule in the monolayer (44). On the contrary, in the full coverage due to the higher density of the molecules, the number of H-bonds in monolayer (109) is almost two times the number of H-bond with the surface (59). The inner H-bonds in the monolayer, such are intermolecular, intramolecular and the H-bonded carboxylic group dimers are not available to further functionalization, but they make the TiO_2 surface biocompatible and water dispersable. However, the intra- and intermolecular H-bond in the outer part of the monolayer have at least a carbonyl or hydroxyl group available for carrying bioactive molecules or drugs.

As one could expect, the average adsorption energy per molecules decreases by 0.40 eV form the medium to high coverage.

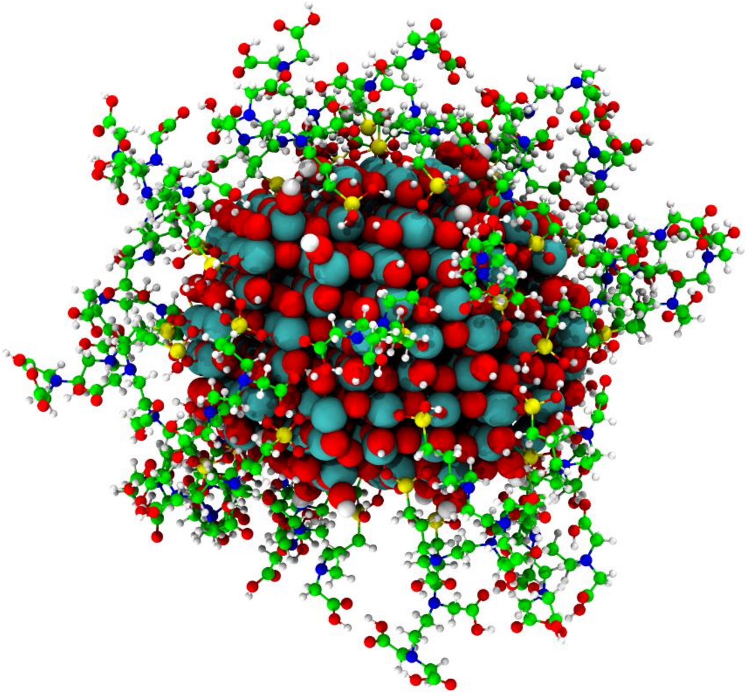

Figure 5-21 TiO_2 nanoparticle decorated with 40 TETT molecules adsorbed in a mixture of tridentate, bidentate, and monodentate fashion. The structure has been optimized after 5 ps of thermal treatment.

5.5 Conclusions

In the present chapter, we have elucidated the nature of the interactions between the bifunctional linker TETT and the curved titanium dioxide nanoparticle.

An extensive set of adsorption modes have been studied. At low coverage and 0 K, the TETT linker preferentially binds in a tridentate fashion on a tri-site E, F, and C with an energy gain of -3.84 eV, -3.82 eV and -2.61 eV, respectively (see **Figure 5-6**).

The TETT molecule has a large number of degrees of freedom, due to the long chain with three laterals −COOH functional groups. Since the geometric configuration and the orientation of the TETT linkers affect the binding strength on the surface of the nanoparticle, we have employed density functional tight binding (DFTB) molecular dynamics to sample the configurational space of the combined TETT/TiO_2 nanoparticle system. After the thermal treatment, all the tridentate configurations taken into consideration are stabilized since the linker has overcome the rotational barriers on the potential energy surface and a lower energy minimum has been reached. Based on the conformational analysis, the most stable configuration (on tri-site F) besides the three Si-O covalent bonds anchoring the molecule at the nanoparticle surface, establishes one coordinative bond ($HO_{TETT}\cdots Ti$), and one H-bond ($C=O_{TETT}\cdots HO_s$) (see **Figure 5-17**), with an energy gain of -1.99 eV.

We have reached a high coverage model by decorating all the reactive sites in the NP. A densely packed monolayer of organic molecules is formed. The TETT molecules are interconnected by some H-bonds.

Not all the carboxylic groups of the TETT linker in the monolayer participate in this H-bond network, therefore such functional groups are still available for tethering other molecules such as solvent or bioactive molecules.

This means that the TETT-modified TiO_2 nanoparticles could be used to build up effective bioconjugates for a wide range of applications such as drug delivery, targeting and imaging. Moreover, the full coating monolayer prevents the uncontrolled interaction of the nanoparticle with biological media, making the system more biocompatible. Finally, the carboxyl end-groups improve NP water dispersibility.

Chapter 6 Summary and Conclusions

Titanium dioxide composite materials have attracted the attention of the scientific community due to their outstanding properties and promising applications. Materials interfaces based on TiO_2 play a crucial role in many of these applications.

In the present work of thesis, different types of titanium dioxide/C-based layer composite materials have been considered. The titanium dioxide surface has been interfaced with both inorganic bidimensional (graphene) and densely packed organic (enediols and silanes) C-based monolayers.

In the first part of the work, the atomic structure of the interface between defective graphene and anatase TiO_2 surface, together with its electronic properties and chemical reactivity with water molecules, were systematically investigated by dispersion corrected hybrid density functional calculations. The magnetism observed for the carbon monovacancy model in graphene (VG) is found to quench when VG is put on TiO_2 (101) surface. The interaction at the VG/TiO_2 interface is based on van der Waals or dispersion forces. However, after overcoming some energy barrier, a C‒O bond may be formed at the interface. Water molecules can dissociate either on top or at the VG/TiO_2 interface. Our study allowed the definition of the possible reaction paths and of the most stable dissociation products. Full dissociation into O + H + H is found to be largely preferred. Very importantly, if the underlying TiO_2 substrate is partially reduced, with oxygen vacancies, water splitting is fully achieved because the two H atoms are left on the graphene layer, whereas the O atom is deep in the TiO_2 surface. Overall, this comprehensive study provides important information on the details of the atomic structure and electronic properties of titania/graphene composites, even when the conditions are not as ideal as one would wish (i.e. carbon vacancy or reduced TiO_2).

In the second part of the work, two studies on a realistic spherical TiO_2 nanoparticle (NP) decorated with densely packed organic monolayers based on the enediol DOPAC and the organosilane TETT were presented, respectively.

For the low coverage model of the TiO_2/DOPAC, we have determined the favorable molecular adsorption modes and analyzed the electronic charge-transfer effects, identifying the new molecular states in the band gap introduced by the adsorbed linker species. On top of that, we have investigated the processes following vis-light photoexcitation of the charge transfer complex: exciton formation, trapping, charge carriers diffusion or recombination. We have learnt that the photoexcited hole is trapped in the π-states of the aromatic ring, whereas the photoexcited electron can hope on different Ti sites, leading to an effective charge transfer separation. Interestingly, the one that provides the strongest binding is the surface Ti atom involved in the bonding with the –COOH functional group in DOPAC. The hole trapping has a beneficial effect of lowering the oxidative power of TiO_2 NP under light irradiation. As a further step, we then consider the molecular layer of enediolic molecules on the NP surface. For the high coverage model, it was necessary to recourse to the approximated-DFT, namely density-functional tight-binding (DFTB), and then calculating the electronic properties at the DFT level. We have observed that molecular states in the gap form a continuous band modifying the absorption of the nanoconjugated. We have also considered the effect of the temperature by means of molecular dynamics, which it showed the high affinity of the –COOH functional group toward the nanoparticle surface. The involvement of the -COOH group of DOPAC in interactions with the NP surface limits the use of this functionalized system (TiO_2/DOPAC) for further bio-conjugation. Nevertheless TiO_2/DOPAC is certainly more biocompatible and photo-sensible to the visible light than bare TiO_2 NPs.

We have built a high coverage model also in the case of the silane (TETT) molecule by decorating all the reactive sites in the NP with 40 molecules. A densely packed monolayer is formed and, after thermal treatment, the TETT molecules are interconnected by some H-bonds. However, since for each linker TETT molecules there are three COOH groups, not all of them participate in this H-bond network, therefore they are still available for tethering other species, such as solvent or bioactive molecules. This means that the TETT-modified TiO_2 nanoparticles could be more effective than DOPAC-modified ones for building up bioconjugates to be used in a wide range of applications, such as drug delivery, targeting and imaging.

To conclude, in the present work of thesis, we have investigated the functionalization of TiO_2 surface with C-based materials. On one hand, we have defined the mechanism how TiO_2/defective graphene interface can promote water dissociation, and, on the other, we have defined the nature of interaction between TiO_2 NP and organic linkers to build potentially efficient carriers for bioconjugation.

References

[1] Wang, L.; Sasaki, T. Titanium Oxide Nanosheets: Graphene Analogues with Versatile Functionalities. *Chem. Rev.* **2014**, *114*, 9455−9486.

[2] Zhang, H.; Banfield, J. F. Thermodynamic Analysis of Phase Stability of Nanocrystalline Titania. *J. Mater. Chem.* **1998**, *8*, 2073−2076.

[3] Ranade, M. R.; Navrotsky, A.; Zhang, H. Z.; Banfield, J. F.; Elder, S. H.; Zaban, A.; Borse, P. H.; Kulkarni, S. K.; Doran, G. S.; Whitfield, H. Energetics of Nanocrystalline TiO_2. J. *Proc. Natl. Acad. Sci. U.S.A.* **2002**, *99*, 6476.

[4] Diebold, U. The surface science of titanium dioxide. *Surf. Sci. Rep.* **2003**, *48*, 53–229.

[5] Xu, H.; Reunchan, P.; Ouyang, S.; Tong, H.; Umezawa, N.; Kako, T.;Ye, J. Anatase TiO_2 Single Crystals Exposed with High-Reactive {111} Facets Toward Efficient H_2 Evolution. *Chem. Mater.* **2013**, *25*, 405–411

[6] Haggerty, J. E. S.; Schelhas, L. T.; Kitchaev, D. A.; Mangum, J. S.; Garten, L. M.; Sun, W.; Stone, K. H.; Perkins, J. D.; Toney, M. F.; Ceder, G.;Ginley, D. S.; Gorman, B. P.; Tate, J. High-Fraction Brookite Films from Amorphous Precursors. *Sci. Rep.* **2017**, *7*, 15232.

[7] Schneider, J.; Matsuoka, M.; Takeuchi, M.; Zhang, J.; Horiuchi, Y.; Anpo, M.; Bahnemann, D. W. Understanding TiO_2 Photocatalysis: Mechanisms and Materials. *Chem. Rev.* **2014**, *114*, 9919–9986.

[8] Hisatomi, T.; Kubota, J.; Domen, K. Recent Advances in Semiconductors for Photocatalytic and Photoelectrochemical Water Splitting. *Chem. Soc. Rev.* **2014**, *43*,7520–7535.

[9] O'Regan, B.; Grätzel, M. A Low-Cost, High-Efficiency Solar Cell Based on Dye-Sensitized Colloidal TiO_2 Films. *Nature* **1991**, *353*, 737–740.

[10] Yang, L. X.; Luo, S. L.; Cai, Q. Y.; Yao, S. Z. A Review on TiO_2 Nanotube Arrays: Fabrication, Properties, and Sensing Applications. *Sci. Bull.* **2010**, *55*, 331–338.

[11] Rajh, T.; Dimitrijevic, N. M.; Bissonnette, M.; Koritarov, T.; Konda, V. Titanium Dioxide in the Service of the Biomedical Revolution. *Chem. Rev.* **2014**, *114*, 10177–10216.

[12] Lee, J. S.; You, K. H.;Park, C. B. Highly Photoactive, Low Bandgap TiO_2 Nanoparticles Wrapped by Graphene. *Adv. Mater.* **2012**, *24*, 1084–1088.

[13] Choi, W.; Termin, A.; Hoffmann, M. R. The Role of Metal Ion Dopants in Quantum-Sized TiO_2: Correlation between Photocreactivity and Charge Carrier Recombination Dynamics. *J. Phys. Chem.* **1994**, *98*, 13669–13679.

[14] Nagaveni, K.; Hegde, M. S.; Madras, G. Photocatalytic Activity of $Ti_{1-x}M_xO_{2\pm\delta}$ (M = W, V, Ce, Zr, Fe, and Cu) Synthesized by Solution Combustion Method. *J. Phys. Chem. B* **2004**, *108*, 20204–20212.

[15] Khan, S. U. M.; Al-Shahry, M.; Ingler, W. B., Jr. Efficient Photochemical Water Splitting by a Chemically Modified n-TiO_2. *Science* **2002**, *297*, 2243–2245.

[16] Barborini, E.; Conti, A. M.; Kholmanov, I. N.; Miseri, P.; Podestà, A.; Milani, P.; Cepek, C.; Sakho, O.; Macovez, R.; Sancrotti, M. Nanostructured TiO_2 Films with 2 eV Optical Gap. *Adv. Mater.* **2005**, *17,* 1842–1846.

[17] Asahi, R.; Morikawa, T.; Ohwaki, T.; Aoki, K.; Taga, Y. Science 2001, 293, 269. Visible-Light Photocatalysis in Nitrogen-Doped Titanium Oxides. *Science* **2001**, *293*, 269–271

[18] Li, Y.; Hwang, D-S.; Lee, N. H.; Kim, S-J. Synthesis and Characterization of Carbon-Coped Titania as an Artificial Solar Light Sensitive Photocatalyst. *Chem. Phys. Lett.* **2005**, *404*, 25–29.

[19] Nakano, Y.; Morikawa, T.; Ohwaki, T.; Taga, Y. Deep-level Optical Spectroscopy Investigation of N-doped TiO_2 Films. *Appl. Phys. Lett.* **2005**, *86*, 132104.

[20] Sant, P. A.; Kamat, P. V. Interparticle Electron Transfer Between Size-Quantized CdS and TiO_2 Semiconductor Nanoclusters. *Phys. Chem. Chem. Phys.* **2002**, *4*, 198–203.

[21] Hoyer, P.; Koenenkamp, R. Photoconduction in Porous TiO_2 Sensitized by PbS Quantum Dots. Appl. Phys. Lett. **1995**, *66*, 349–351.

[22] Tian, Y.; Tatsuma, T. Plasmon-Induced Photoelectrochemistry at Metal Nanoparticles Supported on Nanoporous TiO_2. *Chem. Commun.* **2004**, 1810–1811.

[23] Nazeeruddin, M. K.; De Angelis, F.; Fantacci, S.; Selloni, A.; Viscardi, G.; Liska, P.; Ito, S.; Takeru, B.; Grätzel, M. Combined Experimental and DFT-TDDFT Computational Study of Photoelectrochemical Cell Ruthenium Sensitizers. *J. Am. Chem. Soc.* **2005**, *127*, 16835–16847.

[24] Meyer, G. J. Molecular Approaches to Solar Energy Conversion with Coordination Compounds Anchored to Semiconductor Surfaces. *J. Inorg. Chem.* **2005**, *44*, 6852–6864.

[25] Mak, K. F.; Sfeir, M. Y.; Wu, Y.; Lui, C. H.; Misewich, J. A.; Heinz, T. F. Measurement of the Optical Conductivity of Graphene. *Phys. Rev. Lett.* **2008**, *101*, 196405.

[26] Zhang, Y.; Zhang, N.; Tang, Z.-R.; Xu, Y.-J. Graphene Transforms Wide Band Gap ZnS to a Visible Light Photocatalyst. The New Role of Graphene as a Macromolecular Photosensitizer. *ACS Nano* **2012**, *6*, 9777–9789.

[27] Williams, K. J.; Nelson, C. A.; Yan, X.; Li, L-S.; Zhu, X. Hot Electron Injection from Graphene Quantum Dots to TiO_2. *ACS Nano* **2013**, *4*, 1388–1394.

[28] Hamzeh, M.; Sunahara G.I. In Vitro Cytotoxicity and Genotoxicity Studies of Titanium Dioxide (TiO_2) Nanoparticles in Chinese Hamster Lung Fibroblast Cells. *Toxicol. In Vitro* **2013**, *27*, 864−873.

[29] Shakeel, M.; Jabeen, F.; Shabbir, S.; Asghar, M. S.; Khan, M. S.: Chaudhry, A. S. Toxicity of Nano-Titanium Dioxide (TiO_2-NP) Through Various Routes of Exposure: a Review. *Biol. Trace Elem. Res.* **2016**, *172*,1−36.

[30] Sapsford, K. E.; Algar W. R.; Berti, L.; Gemmill, K. B.; Casey, B. J.; Oh, E.; M.; Stewart, H. M.; Medintz, I. L. Functionalizing Nanoparticles with Biological Molecules: Developing Chemistries that Facilitate Nanotechnology. *Chem. Rev.* **2013**, *113*, 1904−2074.

[31] Neouze, M.-A.; Schubert, U. Surface Modification and Functionalization of Metal and Metal Oxide Nanoparticles by Organic Ligands. *Monatsh Chem* **2009**, *139*, 183–195.

[32] T. Kondo, R. Yamada, K. Uosaki, Organized Organic Ultrathin Films, Fundamentals and Applications, Wiley-VCH, Weinheim, 2013, 7–42.

[33] Heuer-Jungemann, A.; Feliu, N.; Bakaimi, I.; Hamaly, M.; Alkilany, A.; Chakraborty, I.; Masood, A.; Casula, M. F.; Kostopoulou, A.; Eunkeu, Oh.; Susumu, K.; Stewart, M. H.; Medintz, I. G.; Stratakis, E.; Parak, W. J.; and Kanaras, G. A. The role of Ligands in the Chemical Synthesis and Applications of Inorganic Nanoparticles. *Chem. Rev.* **2019**, *119*, 4819–4880.

[34] Moyano, D. F.; Rotello, V. M. Nano Meets Biology: Structure and Function at the Nanoparticle Interface. *Langmuir* **2011**, *27*, 10376–10385.

[35] Jamieson, T., Bakhshi, R.; Petrova, D.; Pocock, R.; Imani, M.; Seifalian, A. M. Biological Applications of quantum dots. *Biomaterials* **2007**, *28*, 4717–4732.

[36] Pujari, S. P.; Scheres, L.; Marcelis, A. T. M.; Zuilhof, H. Covalent Surface Modification of Oxide Surfaces. *Angew. Chem. Int. Ed.* **2014**, *53*, 6322 – 6356.

[37] Linga, D.; Hacketta, M. J.; Hyeona, T. Surface Ligand Synthesis, Modification, Assembly and Biomedical Applications of Nanoparticles. *Nano Today* **2014**, *9*, 457–477. http://dx.doi.org/10.1016/j.nantod.2014.06.005

[38] Hoecker, J.; R. Liffert, R.; Burch, P.; Wehlauch, R.; Gademann, K. Caged Retinoids as Photoinducible Activators: Implications for Cell Differentiation and Neurite Outgrowth. *Org. Biomol. Chem.* **2013**, 11, 3314–3321

[39] Rodenstein, M.; Zürcher, S.; Tosatti, S. G.; Spencer, N. D. Fabricating Chemical Gradients on Oxide Surfaces by Means of Fluorinated, Catechol-Based, Self-Assembled Monolayers. *Langmuir* **2010**, *26*, 16211–6220.

[40] Wehlauch, R.; Hoecker, J.; Gademann, K. Nitrocatechols as Tractable Surface Release Systems *ChemPlusChem* **2012**, *77*, 1071–1074.

[41] Liu, Y.; Khabashesku, V. N.; Halas, N. J. Fluorinated Nanodiamond as a Wet Chemistry Precursor for Diamond Coatings Covalently Bonded to Glass Surface. *J. Am. Chem. Soc.* **2005**, *127*, 3712–3713

[42] Shircliff, R. A.; Stradins, P.; Moutinho, H.; Fennell, J.; Ghirardi, M. L.; Cowley, S. W.; Branz, H. M.; Martin, I. T.; Angle-Resolved XPS Analysis and Characterization of Monolayer and Multilayer Silane Films for DNA Coupling to Silica. *Langmuir* **2013**, *29*, 4057–4067.

[43] Griep-Raming, N.; Karger, M.; Menzel, H. Using Benzophenone-Functionalized Phosphonic Acid To Attach Thin Polymer Films to Titanium Surfaces. *Langmuir* **2004**, *20*, 11811–11814.

[44] Mutin, P. H.; Guerrero, G.; Vioux, A. Hybrid materials from organophosphorus coupling molecules. *J. Mater. Chem.* **2005**, *15*, 3761–3768.

[45] Marcinko, S.; Fadeev, A. Y. Hydrolytic Stability of Organic Monolayers Supported on TiO_2 and ZrO_2. *Langmuir* **2004**, *20*, 2270–2273.

[46] Brodard-Severac, F.; Guerrero, G.; Maquet, J.; Florian, P.; Gervais, C.; Mutin, P. H. High-Field ^{17}O MAS NMR Investigation of Phosphonic Acid Monolayers on Titania. *Chem. Mater.* **2008**, *20*, 5191–5196.

[47] Vittadini, A.; Selloni, A.; Rotzinger, F. P.; Gratzel, M. Investigation of Sensitizer Adsorption and the Influence of Protons on Current and Voltage of a Dye-Sensitized Nanocrystalline TiO_2 Solar Cell. *J. Phys. Chem. B* **2000**,*104*, 1300–1306.

[48] Li, B.; Franking, R.; Landis, E. C.; Kim, H.; Hamers, R. J. Highly Stable Molecular Layers on Nanocrystalline Anatase TiO_2 through Photochemical Grafting. *ACS Appl. Mater. Interfaces* **2009**, *1*, 1013–1022.

[49] Franking, R.; Landis, E. C.; Hamers, R. J. Photochemical Grafting and Patterning ofBiomolecular Layers onto TiO_2 Thin Films. *Langmuir* **2009**, *25*, 10676–10684.

[50] Dahl, M.; Liu, Y.; Yin, Y. Composite Titanium Dioxide Nanomaterials. *Chem. Rev.* **2014**, *114*, 9853−9889.

[51] Zhang, Z.; Wang, C.-C.; Zakaria, R.; Ying, J. Y. Role of Particle Size in Nanocrystalline TiO_2-Based Photocatalysts. *J. Phys. Chem. B* **1998**, *102*, 10871−10878.

[52] Qu, Y.; Duan, X. Progress, Challenge and Perspective of Heterogeneous Photocatalyst. *Chem. Soc. Rev.* **2013**, *42*, 2568−2580.

[53] Xiang, Q.; Yu, J. Jaroniec, M. Graphene-Based Semiconductor Photocatalysts. *Chem. Soc. Rev.* **2012**, *41*, 782–796.

[54] Zhang, H.; Lv, X.; Li, Y.; Wang, Y.; Li, J. P25-Graphene Composite as a High Performance Photocatalyst. *ACS Nano* **2010**, *4*, 380–386.

[55] Woan, K.; Pyrgiotakis, G.; Sigmund, W. Photocatalytic Carbon-Nanotube–TiO_2 Composites. *Adv. Mater.* **2009**, *21*, 2233–2239.

[56] Fujishima, A.; Honda, K. Electrochemical Photolysis of Water at a Semiconductor Electrode. *Nature* **1972**, 238, 37−38.

[57] Fujishima, A.; Rao, T. N.; Tryk, D. A. Titanium dioxide photocatalysis. *J. Photochem. Photobiol. C* **2000**, 1, 1–21.

[58] Borgarello, E.; Kiwi, J.; Gràtzel, M.; Pelizzetti, E.; Visca, M. Visible Light Induced Water Cleavage in Colloidal Solutions of Chromium-Doped Titanium Dioxide Particles. *J. Am. Chem. Soc.* **1982**, *104*, 2996–3002.

[59] Fu, Q.; Bao, X.; Surface Chemistry and Catalysis Confined Under Two-Dimensional Materials. *Chem.Soc.Rev*. **2017**, *46*, 1842–1874.

[60] Yao, Y.; Fu, Q.; Zhang, Y. Y.; Weng, X.; Li, H.; Chen, M.; Jin, L.;Dong, A.; Mu, R.; Jiang, P.; Liu, L.; Bluhm, H.; Liu, Z.; Zhang, S. B.; Bao, X Graphene Cover-Promoted Metal-Catalyzed Reactions. *Proc. Natl. Acad. Sci. U. S. A.* **2014**, *111*, 17023−17028.

[61] Ferrighi, L.; Perilli, D.; Selli, S.; Di Valentin, C. Water at the Interface Between Defective Graphene and Cu or Pt (111) Surfaces. *ACS Appl. Mater. Interfaces* **2017**, *9*, 29932−29941

[62] Deng, J.; Deng, D.; Bao, X. Robust Catalysis on 2D Materials Encapsulating Metals: Concept, Application, and Perspective. *Adv. Mater.* **2017**, *29*, 1606967.

[63] Ferrighi, L.; Datteo, M.; Fazio, G.; Di Valentin. C. Catalysis under Cover: Enhanced Reactivity at the Interface between (Doped) Graphene and Anatase TiO_2. *J. Am. Chem. Soc.***2016,** *138*, 7365−7376.

[64] He, Z.; Guai, G.; Liu, J.; Guo, C.; Chye, J. S. C.; Li, C. M.; Tan, T. T. Y. Nanostructure control of graphene-composited TiO_2 by a one-step solvothermal approach for high performance dye-sensitized solar cells. *Nanoscale* **2011**, 3, 4613−4616.

[65] Lee, T. Y.; Alegaonkar, P. S.; Yoo, J.-B. Fabrication of dye sensitized solar cell using TiO_2 coated carbon nanotubes. *Thin Solid Films* **2007**, *515*, 5131−5135.

[66] Muduli, S.; Lee, W.; Dhas, V.; Mujawar, S.; Dubey, M.; Vijayamohanan, K.; Han, S.-H.; Ogale, S. Enhanced Conversion Efficiency in Dye-Sensitized Solar Cells Based on Hydrothermally Synthesized TiO_2-MWCNT Nanocomposites. *ACS. Appl. Mater. Interfaces* **2009**, *1*, 2030−2035.

[67] Tang, Y.-B.; Lee, C.-S.; Xu, J.; Liu, Z.-T.; Chen, Z.-H.; He, Z.; Cao, Y.-L.; Yuan, G.; Song, H.; Chen, L.; Luo, L.; Cheng, H.-M.; Zhang, W.-J.; Bello, I.; Lee, S.-T. Incorporation of Graphenes in Nanostructured TiO_2 Films via Molecular Grafting for Dye-Sensitized Solar Cell Application. *ACS Nano* **2010**, *4*, 3482−3488.

[68] Hagfeldt, A.; Boschloo, G.; Sun, L.; Kloo, L.; Pettersson, H. Dye-Sensitized Solar Cells. *Chem. Rev.* **2010**, *110*, 6595−6663.

[69] Batmunkh, M.; Biggs, M. J.; Shapter, J. G. Carbonaceous Dye-Sensitized Solar Cell Photoelectrodes. *Adv. Sci.* **2015**, *2*, 1400025.

[70] Ackroyd, R., Kelty, C., Brown, N. & Reed, M. The History of Photodetection and Photodynamic Therapy. *Photochem. Photobiol.* **2001**, *74*, 656–669.

[71] Spikes, J. D. in Primary Photoprocesses in Biology and Medicine (eds Berghausen, R. V., Jori, G., Land, E. J. & Truscott, T. H.) 209–227 (Plenum Press, New York,1985).

[72] Dolmans, D. E.; Fukumura, D.; Jain. R. K. Photodynamic Therapy for Cancer. *Nat. Rev. Cancer* **2003**, *3*, 380–387.

[73] Scholkmann, F.; Kleiser, S.; Metz, A. J.; Zimmermann, R.; Mata Pavia, J.; Wolf, U.; Wolf, M. A Review on Continuous Wave Functional Near-Infrared Spectroscopy and Imaging Instrumentation and Methodology. Neuroimage **2014**, *85*, 6−27.

[74] Jańczyk, A. Wolnicka-Głubisz, A.; Urbanska, K.; Kisch, H.; Stochel G.; Macyk W. Photodynamic Activity of Platinum (IV) Chloride Surface-Modified TiO_2 Irradiated with Visible Light. *Free Radical Biol. Med.* **2008**, *44*, 1120−1130.

[75] George, S.; Pokhrel, S.; Ji, Z.; Henderson, B. L.; Xia, T.; Li, L.; Zink, J. I.; Nel A. E.; Mädler, L. Role of Fe Doping in Tuning the Band Gap of TiO_2 for the Photo-Oxidation-Induced Cytotoxicity Paradigm. *J. Am. Chem. Soc*. **2011**, *133*, 11270−11278.

[76] Li, Z.; Mi, L.; Wang, P. N.; Chen, J. K. Study on the Visible-Light-Induced Photokilling Effect of Nitrogen-Doped TiO_2 Nanoparticles on Cancer Cells. *Nanoscale Res. Lett.* **2011**, *6*, 356.

[77] Xu, S.; Shen, J.; Chen, S.; Zhang, M.; Shen, T. Active Oxygen Species (${}^1O_2$, $O_2^{\cdot -}$) Generation in the System of TiO_2 Colloid Sensitized by Hypocrellin B. *J. Photochem. Photobiol. B* **2002**, 67, 64−70.

[78] Tokuoka, Y.; Yamada, M.; Kawashima, N.; Miyasaka, T. Anticancer Effect of Dye-sensitized TiO_2 Nanocrystals by Polychromatic Visible Light Irradiation. *Chem. Lett.* **2006**, *35*, 496−497.

[79] Lopez, T., Ortiz, E.; Alvarez,M.; Navarrete, J.;. Odriozola, J. A.; Martinez-Ortega, F.; Páez-Mozo, E. A. Escobar, P.; Espinoza, K. A.; Rivero, I. A. Study of the Stabilization of Zinc Phthalocyanine in Sol-Gel TiO_2 for Photodynamic Therapy Applications. *Nanomed.* **2010**, 6, 777−785.

[80] Rajh, T.; Nedeljkovic, J. M.; Chen, L. X.; Poluektov, O.; Thurnauer, M. C. Improving Optical and Charge Separation Properties of Nanocrystalline TiO_2 by Surface Modification with Vitamin C. *J. Phys. Chem. B* **1999**, *103*, 3515−3519.

[81] Rajh, T.; Chen, L. X.; Lukas, K.; Liu, T.; Thurnauer, M. C.; Tiede, D. M. Surface Restructuring of Nanoparticles: An Efficient Route for Ligand−Metal Oxide Crosstalk. *J. Phys. Chem. B* **2002**, *106*, 10543−11168.

[82] Xu, J.; Sun, Y.; Huang, J.; Chen, C.; Liu, G.; Jiang, Y.; Zhao, Y.; Jiang, Z. Photokilling Cancer Cells Using Highly Cell-Specific Antibody–TiO_2 Bioconjugates and Electroporation. *Bioelectrochemistry* **2007**, *71*, 217−222.

[83] Ogino, C.; Shibata, N.; Sasai, R.;Takaki, K.; Miyachi, Y.; Kuroda, S.; Ninomiya, K.; Shimizu, N. Construction of Protein-Modified TiO_2 Nanoparticles for use with Ultrasound Irradiation in a Novel Cell Injuring Method. *Bioorg. Med. Chem. Lett.* **2010**, *20*, 5320−5320.

[84] Rozhkova, E. A.; Ulasov, I.; Lai, B.; Dimitrijevic, N. M.; Lesniak M. S.; Rajh, T. A High-Performance Nanobio Photocatalyst for Targeted Brain Cancer Therapy. *Nano Lett.* **2009**, *9*, 3337-3342.

[85] Sortino, S.; Photoactivated Nanomaterials for Biomedical Release Applications. *J. Mater. Chem*. **2012**, *22*, 301−318.

[86] Uddin, M. J.; Mondal, D.; Morris, C. A.; Lopez, T.; Diebold, U.; Gonzalez, R. D. An in Vitro Controlled Release Study of Valproic Acid Encapsulated in a Titania Ceramic Matrix. *Appl. Surf. Sci.* **2011**, 257, 7920−7927.

[87] Wu, K. C.; Yamauchi, T.; Hong, C. Y.; Yang, Y. H.; Liang, Y. H.; Funatsu, T.; Tsunoda, M. Biocompatible, Surface Functionalized Mesoporous Titania Nanoparticles for Intracellular Imaging and Anticancer Drug Delivery. *Chem. Commun.* **2011**, *47*, 5232−5232.

[88] Li, Q.; Wang, W.; Lu, X.; Tian, H.; Jiang, H.; Lv, G.; Guo, D.; Wu, C.; Chen, B. The incorporation of Daunorubicin in Cancer Cells Through the Use of Titanium Dioxide Whiskers. *Biomaterials* **2009**, *30*, 4708−4715.

[89] Qin, Y.; Sun, L.; Li, X.; Cao, Q.; Wang, H.; Tang, H.; Ye, L. Highly Water-Dispersible TiO_2 Nanoparticles for Doxorubicin Delivery: Dffect of Loading Mode on Therapeutic Efficacy. *J. Mater. Chem.* **2011**, *21*, 18003−18010.

[90] Lin, C. C.; Chu, Y. M.; Chang, H.-C. In Situ Encapsulation of Antibody on TiO_2 Nanowire Immunosensor via Electro-Polymerization of Polypyrrole Propylic Acid. *Sens. Actuators B* **2013**, *187*, 533−539.

[91] Thurn, K. T.; Paunesku, T.; Wu, A.; Brown, E. M. B.; Lai, B.; Vogt, S.; Maser, J.; Aslam, M.; Dravid, V.; Bergan, R.; Woloschak, G. E. Labeling TiO_2 Nanoparticles with Dyes for Optical Fluorescence Microscopy and Determination of TiO_2–DNA Nanoconjugate Stability. *Small* **2009**, *5*, 1318−1325.

[92] Yin, Z.-F.; Long Wu, L.; Yang, H. G.; Su, Y. H. Recent Progress in Biomedical Applications of Titanium Dioxide. *Phys. Chem. Chem. Phys.* **2013**, *15*, 4844−4858.

[93] Conde, J.; Jorge T. Dias, J. T.; Grazú, V.; Moros, M.; Baptista, P. V.; de la Fuente, J. M. Revisiting 30 Years of Biofunctionalization and Surface Chemistry of Inorganic Nanoparticles for Nanomedicine. *Front. Chem.* **2014**, *2*, *https://doi.org/10.3389/fchem.2014.00048*.

[94] De Angelis, F.; Di Valentin, C.; Fantacci, S.; Vittadini, A.; Selloni, Theoretical Studies on Anatase and Less Common TiO_2 Phases: Bulk, Surfaces, and Nanomaterials. *A. Chem. Rev.* **2014**, *114*, 9708−9753.

[95] Burdett, J. K.; Hughbanks, T.; Miller, G. J.; Richardson, J. W.; Jr., Smith, J. V. Structural-Electronic Relationships in Inorganic Solids: Powder Neutron Diffraction Studies of the Rutile and Anatase Polymorphs of Titanium Dioxide at 15 and 295 K. *J. Am. Chem. Soc.* **1987**, *109*, 3639−1987.

[96] Lazzeri, M.; Vittadini, A.; Selloni, Structure and Energetics of Stoichiometric TiO_2 Anatase Surfaces. *A. Phys. Rev. B* **2001**, *63*, 155409.

[97] Asahi, R.; Taga, Y.; Mannstadt, W.; Freeman, A. Electronic and Optical Properties of Anatase TiO_2. *J. Phys. Rev. B* **2000**, *61*, 7459−7565.

[98] Kavan, L.; Grätzel, M.; Gilbert, S. E.; Klemenz, C.; Scheel, H. J. Electrochemical and Photoelectrochemical Investigation of Single-Crystal Anatase. *J. Am. Chem. Soc.* **1996**, *118*, 6716−6723.

[99] Zhang, Y. F.; Lin, W.; Li, Y.; Ding, K. N.; Li, J. Q. A Theoretical Study on the Electronic Structures of TiO_2: Effect of Hartree−Fock Exchange. *J. Phys. Chem. B* **2005**, *109*, 19270−19277.

[100] Di Valentin, C.; Selloni, A. Bulk and Surface Polarons in Photoexcited Anatase TiO_2. *J. Phys. Chem. Lett.* **2011**, *2*, 2223−2228.

[101] Deskins, N. A.; Dupuis, M. Electron Transport Via Polaron Hopping in Bulk TiO_2: A Density Functional Theory Characterization. *Phys. Rev. B* **2007**, *75*, 195212.

[102] Micic, O. I.; Zhang, Y.; Cromack, K. R.; Trifunac, A. D.; Thurnauer, M. C Trapped Holes on Titania Colloids Studied by Electron Paramagnetic Resonance. *J. Phys. Chem.* **1993**, *97*, 7277−7283

[103] Deskins, N. A.; Dupuis, M. Intrinsic Hole Migration Rates in TiO_2 from Density Functional Theory. *J. Phys. Chem. C* **2009**, *113*, 346−358.

[104] Arrouvel, C.; Digne, M.; Breysse, M.; Toulhoat, H.; Raybaud, P. Effects of Morphology on Surface Hydroxyl Concentration: a DFT Comparison of Anatase–TiO_2 and γ-Alumina Catalytic Support. *J. Catal.* **2004**, *222*, 152−166

[105] Barnard, A. S.; Zapol, P. Effects of Particle Morphology and Surface Hydrogenation on the Phase Stability of TiO_2. *P. Phys. Rev. B* **2004**, *70*, 235403.

[106] Labat, F.; Baranek, P.; Adamo, C. Structural and Electronic Properties of Selected Rutile and Anatase TiO_2 Surfaces: An ab Initio Investigation. *J. Chem. Th. Comput.* **2008**, *4*, 341−352.

[107] Zhao, Z.; Li, Z.; Zou, Z. Surface Properties and Electronic Structure of Low-Index Stoichiometric Anatase TiO_2 Surfaces. *J. Phys. Condensed Matter* **2010**, *22*, 175008.

[108] Esch, T. R.; Gadaczek, I.; Bredow, T. Surface Structures and Thermodynamics of Low-Index of Rutile, Brookite and Anatase – A comparative DFT study. *Appl. Surf. Sci.* **2014**, *288*, 275−287

[109] Chen, W.; Kuang, Q.; Wang, Q.; Xie, Z. Engineering a High Energy Surface of Anatase TiO_2 Crystals Towards Enhanced Performance for Energy Conversion and Environmental Application. *RSC Adv.* **2015**, *5*, 20396−20409.

[110] Hengerer, R.; Kavan, L.; Bolliger, B.; Erbudak, M.; Grätzel, M. Surface Investigations on Single Crystal Anatase TiO_2. *Mater. Res. Soc. Symp. Proc.* **2000**, *623*.

[111] Burda, C.; Chen, X.; Narayanan, R.; El-Sayed, M. A. Chemistry and Properties of Nanocrystals of Different Shapes. *Chem. Rev.* **2005**, *105*, 1025−1102.

[112] Hummer, D. R.; Kubicki, J. K.; Kent, P. R. C.; Post, J. E.; Heaney, P. J. Origin of Nanoscale Phase Stability Reversals in Titanium Oxide Polymorphs. *J. Phys. Chem. C* **2009**, *113*, 4240–4245.

[113] Li, Y-F.; Liu, Z-P. Particle Size, Shape and Activity for Photocatalysis on Titania Anatase Nanoparticles in Aqueous Surroundings. *J. Am. Chem. Soc.* **2011**, *133*, 15743–15752.

[114] Nunzi, F.; Mosconi, E.; Storchi, L.; Ronca, E.; Selloni, A.; Gratzel, M.; De Angelis, F. Inherent Electronic Trap States in TiO_2 Nanocrystals: Effect of saturation and sintering. *Energy Environ. Sci.* **2013**, *6*, 1221–1229.

[115] Nunzi, F.; Storchi, L.; Manca, M.; Giannuzzi, R.; Gigli, G.; De Angelis, F. Shape and Morphology Effects on the Electronic Structure of TiO_2Nanostructures: From Nanocrystals to Nanorods. *ACS Appl. Mater. Interfaces* **2014**, *6*, 2471−2478.

[116] Pavan K. Naicker, P. K.; Cummings, P. T.; Zhang, H.; Banfield, J. F. Characterization of Titanium Dioxide Nanoparticles Using Molecular Dynamics Simulations. *J. Phys. Chem. B* **2005**, *109*, 15243−15249.

[117] Morales-García, Á.; Escatllar, A. M.; Illas, F.; Bromley, S. T. Understanding the Interplay Between Size, Morphology and Energy Gap in Photoactive TiO_2 Nanoparticles. *Nanoscale*, **2019**,*11*, 9032−9041.

[118] Selli, D.; Fazio, F.; Di Valentin. C. Modelling Realistic TiO_2 Nanospheres: A Benchmark Study of SCC-DFTB Against Hybrid DFT. *J. Chem. Phys. 147*, **2017**, 164701.

[119] Ceperley, D. M.; Alder, B. J. Ground State of the Electron Gas by a Stochastic Method. *Alder Phys. Rev. Lett.* **1980**, *45*, 566−569.

[120] Koch, W.; Holthausen, M.C. A Chemist's Guide to Density Functional Theory, 2nd Ed., Willey-VCH, Weinheim, 2001.

[121] Tang, H.; Lévy, F.; Berger, H.; Schmid, P. Urbach Tail of Anatase TiO_2. *Phys. Rev. B* **1995**, *52*, 7771−7774.

[122] Labat, F.; Baranek, P.; Domain, C.; Minot, C.; Adamo, C. Density Functional Theory Analysis of the Structural and Electronic Properties of TiO_2 Rutile and Anatase Polytypes: Performances of Different Exchange-Correlation Functionals. *J. Chem. Phys.* **2007,** *126*, 154703.

[123] Chiodo, L.; García-Lastra, J. M.; Iacomino, A.; Ossicini, S.; Zhao J.; Petek, H.; Rubio, A. Self-energy and Excitonic Effects in the Electronic and Optical Properties of TiO_2 Crystalline Phases. *Phys. Rev. B* **2010**, *82*, 045207.

[124] Lee, C.; Yang, W.; Parr, R. G. Development of the Colle-Salvetti Correlation-Energy Formula into a Functional of the Electron Density. *Phys. Rev. B* **1988**, *37*, 785

[125] Becke, A. D. A New Mixing of Hartree–Fock and Local Density-Functional Theories. *J. Chem. Phys.* **1993**, *98*, 1372–1377.

[126] F. Jensen, Introduction to Computational Chemistry (JohnWiley & Sons, West Sussex, 2006.

[127] Sildos, I.; Kiisk, V.; Lange, S.; Aarik, J. Time-Resolved Exciton-Emission Spectrosopy of Anatase. *Proc. SPIE* **2003**, 5122, 56–60.

[128] Matthew, W.; Foulkes C.; Haydock, R. Tight-Binding Models and Density-Functional Theory. *Phys. Rev. B* **1989**, *39*, 520–536.

[129] Eschrig, H.; Bergert, I. Optimized LCAO Version for Band-Structure Calculations–Application to Copper. *Phys Status Solidi B* **1978**, *90*, 621–628.

[130] Eschrig, H. Optimized LCAO Method and the Electronic Structure of Extended Systems. Springer-Verlag Berlin Heidelberg; **1988**.

[131] Frauenheim, T.; Seifert, G.; Elstner, M.; Hajnal, Z.; Jungnickel, G.; Porezag, D.; Suhai, S.; Scholz, R. A Self-Consistent Charge Density-Functional Based Tight Binding Method for Predictive Materials Simulations in Physics, Chemistry and Biology. *Phys Status Solidi B* **2000**, *217*, 41–62.

[132] Feynman, R. P. Forces in Molecules. *Phys. Rev.* **1939**, *56*, 340–343.

[133] D. Frenkel, B. Smith, Understanding Molecular Simulations, 2nd edition, Academic Press, 2002.

[134] Bloch, F. Über die Quantenmechanik der Elektronen in Kristallgittern. *Zeitschrift fur Physik* **1929**, *52*, 555–600.

[135] Monkhorst, H. J.; Pack, J. D. Special Points for Brillouin-Zone Integrations. *Phys. Rev. B* **1976**, *13*, 5188–5192.

[136] Shirai, K.; Sugimoto, T.; Watanabe, K.; Haruta, M.; Kurata, H.; Matsumoto, Y. Effect of Water Adsorption on Carrier Trapping Dynamics at the Surface of Anatase TiO_2 Nanoparticles. *Nano Lett.* **2016**, *16*, 1323–1327.

[137] Novoselov, K. S.; Geim, A. K.; Morozov, S. V.; Jiang, D.; Zhang, Y.; Dubonos, S. V.; Grigorieva, I. V.; Firsov, A. A. Electric Field Effect in Atomically Thin Carbon Films. *Science* **2004**, *306*, 666–669.

[138] Geim, A. K.; Novoselov, K. S. The Rise of Graphene. *Nat. Mater.* **2007**, *6*, 183–191.

[139] Castro Neto, A. H.; Guinea, F.; Peres, N. M. R.; Novoselov, K. S.; Geim, A. K. The Electronic Properties of Graphene. *Rev. Mod. Phys.* **2009**, *81*, 109–162.

[140] Deng, D.; Novoselov, K. S.; Fu, Q.; Zheng, N.; Tian, Z.; Bao, X. Catalysis with Two-dimensional Materials and Their Heterostructures. *Nat. Nano* **2016**, *11*, 218–230.

[141] Yao, Y.; Fu, Q.; Zhang, Y. Y.; Weng, X.; Li, H.; Chen, M.; Jin, L.; Dong, A.; Mu, R.; Jiang, P.; Liu, L.; Bluhm, H.; Liu, Z.; Zhang, S. B.; Bao, X. Graphene Cover-promoted Metal-catalyzed Reactions. *Proc. Natl. Acad. Sci. U.S.A.* **2014**, *111*, 17023–17028.

[142] Deng, J.; Deng, D.; Bao, X. Robust Catalysis on 2D Materials Encapsulating Metals: Concept, Application, and Perspective. *Adv. Mater.* **2017**, *29*, 1606967.

[143] Han, L.; Wang, P.; Dong, S. Progress in Graphene-based Photoactive Nanocomposites as a Promising Class of Photocatalyst. *Nanoscale* **2012**, *4*, 5814.

[144] Xiang, Q.; Yu, J.; Jaroniec, M. Graphene-based Semiconductor Photocatalysts. *Chem. Soc. Rev.* **2012**, *41*, 782–96.

[145] Yang, M.-Q.; Zhang, N.; Pagliaro, M.; Xu, Y.-J. Artificial Photosynthesis over Graphene-semiconductor Composites. Are We Getting Better? *Chem. Soc. Rev.* **2014**, *43*, 8240–8254.

[146] Roy-Mayhew, J. D.; Aksay, I. A. Graphene Materials and Their Use in Dye-sensitized Solar Cells. *Chem. Rev* **2014**, *114*, 6323–6348.

[147] Lee, J. S.; You, K. H.; Park, C. B. Highly Photoactive, Low Band Gap TiO_2 Nanoparticles Wrapped by Graphene. *Adv. Mater.* **2012**, *24*, 1084–1088.

[148] Liu, H.; Lv, T.; Zhu, Z. Template-assisted Synthesis of Hollow TiO_2@rGO Core–shell Structural Nanospheres with Enhanced Photocatalytic Activity. *J. Mol. Catal. A: Chem.* **2015**, *404-405*, 178–185

[149] Xu, C.; Zhu, J.; Yuan, R.; Fu, X. More Effective Use of Graphene in Photocatalysis by Conformal Attachment of Small Sheets to TiO_2 Spheres. *Carbon* **2016**, *96*, 394–402.

[150] Liu, H.; Liu, S.; Zhang, Z.; Dong, X.; Liu, T. Hydrothermal Etching Fabrication of TiO_2@graphene Hollow Structures: Mutually Independent Exposed {001} and {101} Facets Nanocrystals and Its Synergistic Photocaltalytic Effects. *Sci. Rep.* **2016**, *6*, 33839.

[151] Huang, Q.; Tian, S.; Zeng, D.; Wang, X.; Song, W.; Li, Y.; Xiao, W.; Xie, C. Enhanced Photocatalytic Activity of Chemically Bonded TiO_2/Graphene Composites Based on the Effective Interfacial Charge Transfer through the C–Ti Bond. *ACS Catal.* **2013**, *3*, 1477–1485.

[152] Low, J.; Yu, J.; Ho, W. Graphene-Based Photocatalysts for CO_2 Reduction to Solar Fuel. *J. Phys. Chem. Lett.* **2015**, *6*, 4244–4251.

[153] Tan, L. L.; Chai, S. P.; Mohamed, A. R. Synthesis and Applications of Graphene-based TiO_2 Photocatalysts. *ChemSusChem* **2012**, *5*, 1868–1882.

[154] Zhou, K.; Zhu, Y.; Yang, X.; Jiang, X.; Li, C. Preparation of Graphene–TiO_2 Composites with Enhanced Photocatalytic Activity. *New J. Chem.* **2011**, *35*, 353–359.

[155] Ferrighi, L.; Fazio, G.; Di Valentin, C. Charge Carriers Separation at the Graphene/(101) Anatase TiO_2 Interface. *Adv. Mater. Interfaces* **2016**, *3*, 1500624.

[156] Williams, K. J.; Nelson, C. A.; Yan, X.; Li, L.-S.; Zhu, X. Hot Electron Injection from Graphene Quantum Dots to TiO_2. *ACS Nano* **2013**, *7*, 1388–1394.

[157] Bachmatiuk, A.; Mendes, R. G.; Hirsch, C.; Jähne, C.; Lohe, M. R.; Grothe, J.; Kaskel S.; Fu, L.; Klingeler R.; Eckert, J.; Wick P.; Rümmeli M. H. Few-Layer Graphene Shells and Nonmagnetic Encapsulates: A Versatile and Nontoxic Carbon Nanomaterial. *ACS Nano* **2013**, *12*, 10552–10562.

[158] Wu, R.; Shen, S.;Xia, G.; Zhu, F.; Lastoskie C.; Zhang J. Soft-Templated Self-Assembly of Mesoporous Anatase TiO_2/Carbon Composite Nanospheres for High-Performance Lithium Ion Batteries. *ACS Appl. Mater. Interfaces* **2016**, *8*, 19968−19978

[159] Tong, X.; Zeng, M.; Li, J.; Li, F. UV-assisted Synthesis of Surface Modified Mesoporous TiO_2/G Microspheres and Its Electro Chemical Performances in Lithium Ion Batteries. *Appl. Surf. Sci.* **2017**, *392*, 897–903.

[160] Liu, H.; Guo, K.; Duan, C.; Dong, X.; Gao, J. Hollow TiO_2 Modified Reduced Graphene Oxide Microspheres Encapsulating Hemoglobin for a Mediator-free Biosensor. *Biosens. Bioelectron.* **2017**, *87*, 473–479

[161] Zhao, H.; Ding, R.; Zhao, X.; Li, Y.; Qu, L.; Pei, H.; Yildirimer, L.; Wu, Z.; Zhang, W. Graphene-based Nanomaterials for Drug and/or Gene Delivery, Bioimaging, and Tissue Engineering. *Drug Discov. Today* **2017**, *22*, 1302–1317.

[162] Rajh, T.; Dimitrijevic, N. M.; Bissonnette, M.; Koritarov, T.; Konda, V. Titanium Dioxide in the Service of the Biomedical Revolution. *Chem. Rev.* **2014**, *114*, 10177−10216.

[163] Banhart, F.; Kotakoski, J.; Krasheninnikov, A. V. Structural Defects in Graphene. *ACS Nano* **2011**, *5*, 26–41.

[164] Terrones, H.; Lv, R.; Terrones, M.; Dresselhaus, M. S. The Role of Defects and Doping in 2D Graphene Sheets and 1D Nanoribbons. *Rep. Prog. Phys.* **2012**, *75*, 062501.

[165] Zhang N.; Yang M.; Liu S.; Sun Y.; Xu Y. Waltzing with the Versatile Platform of Graphene to Synthesize Composite Photocatalysts. Chem. Rev. **2015**, *115*, 10307−10377.

[166] Liang, Y. T.; Vijayan, B. K.; Gray K. A.; Hersam, M. C. Minimizing Graphene Defects Enhances Titania Nanocomposite-Based Photocatalytic Reduction of CO_2 for Improved Solar Fuel Production. Nano Lett. **2011**, *11*, 2865−2870.

[167] Zhang, Y.; Zhang N.; Tang Z.; Xu, Y. Improving the Photocatalytic Performance of Graphene–TiO_2 Nanocomposites via a Combined Strategy of Decreasing Defects of Graphene and Increasing Interfacial Contact. *Phys. Chem. Chem. Phys.*, **2012**, *14*, 9167–9175.

[168] Gass M. H.; Bangert, U.; Bleloch A. L.; Wang, P.; Nair, R. R.; Geim, A. K. Free-standing Graphene at Atomic Resolution. *Nat. Nanotechnol.* **2008**, *3*, 676–681.

[169] Meyer, J. C.; Kisielowski C.; Erni R.; Rossell M. D.; Crommie M. F.; Zettl A. Direct Imaging of Lattice Atoms and Topological Defects in Graphene Membranes. *Nano Lett.* **2008**, *8*, 3582–3586.

[170] Rodríguez-Manzo, J. A.; Cretu, O.; Banhart, F. Trapping of Metal Atoms in Vacancies of Carbon Nanotubes and Graphene. *ACS Nano* **2010**, *4*, 3422–3428.

[171] Zoberbier, T.; Chamberlain, T. W.; Biskupek, J.; Suyetin, M.; Majouga, A. G.; Besley, E.; Kaiser, U.; Khlobystov, A. N. Investigation of the Interactions and Bonding between Carbon and Group VIII Metals at the Atomic Scale. *Small* **2016**, *12*, 1649–1657.

[172] Fampiou, I.; Ramasubramaniam, A. Influence of Support Effects on CO Oxidation Kinetics on CO-Saturated Graphene-Supported Pt_{13} Nanoclusters. *J. Phys. Chem. C* **2015**, *119*, 8703–8710.

[173] Lim, D.-H.; Wilcox, J. Mechanisms of the Oxygen Reduction Reaction on Defective Graphene-Supported Pt Nanoparticles from First-Principles. *J. Phys. Chem. C* **2012**, *116*, 3653−3660.

[174] Kim, K.; Lee, H. B.; Johnson, R. W.; Tanskanen, J. T.; Liu, N.; Kim, M. G.; Pang, C.; Ahn, C.; Bent, S. F.; Bao, Z. Selective Metal Deposition at Graphene Line Defects by Atomic Layer Deposition. *Nat. Commun.* **2014**, *5*, 4781.

[175] Kim, G.; Jhi, S. H.; Lim, S.; Park, N. Effect of Vacancy Defects in Graphene on Metal Anchoring and Hydrogen Adsorption. *Appl. Phys. Lett.* **2009**, *94*, 173102.

[176] Ramos-Castillo, C. M.; Reveles, J. U.; Zope, R. R.; de Coss, R. Palladium Clusters Supported on Graphene Monovacancies for Hydrogen Storage. *J. Phys. Chem. C* **2015**, *119*, 8402–8409.

[177] Junkaew, A.; Rungnim, C.; Kunaseth, M.; Arroyave, R.; Promarak, V.; Kungwan, N.; Namuangruk, S. Metal Cluster-deposited Graphene as an Adsorptive Material for m-xylene. *New J. Chem.* **2015**, *39*, 9650–9658.

[178] Ferrighi, L.; Perilli, D.; Selli, D.; Di Valentin, C. Water at the Interface Between Defective Graphene and Cu or Pt (111) Surfaces. *ACS Appl. Mater. Interfaces* **2017**, *9*, 29932–29941.

[179] Mu, R.; Fu, Q.; Jin, L.; Yu, L.; Fang, G.; Tan, D.; Bao, X. Visualizing Chemical Reactions Confined under Graphene. *Angew. Chem. Int. Ed.* **2012**, *51*, 4856–4859.

[180] Zhang, Y.; Fu, Q.; Cui, Y.; Mu, R.; Jin, L.; Bao, X. Enhanced Reactivity of Graphene Wrinkles and Their Function as Nanosized Gas Inlets for Reactions Under Graphene. *Phys. Chem. Chem. Phys.* **2013**, *15*, 19042–19048.

[181] Zhang, Y.; Weng, X.; Li, H.; Li, H.; Wei, M.; Xiao, J.; Liu, Z.; Chen, M.; Fu, Q.; Bao, X. Hexagonal Boron Nitride Cover on Pt(111): A New Route to Tune Molecule–Metal Interaction and Metal-Catalyzed Reactions. *Nano Lett.* **2015**, *15*, 3616–3623.

[182] Wei, M.; Fu, Q.; Wu, H.; Dong, A.; Bao, X. Hydrogen Intercalation of Graphene and Boron Nitride Monolayers Grown on Pt(111). *Top. Catal.* **2016**, *59*, 543–549.

[183] Kidambi, P. R.; Bayer, B. C.; Blume, R.; Wang, Z. J.; Baehtz, C.; Weatherup, R. S.; Willinger, M. G.; Schloegl, R.; Hofmann, S. Observing Graphene Grow: Catalyst-graphene Interactions During Scalable Graphene Growth on Polycrystalline Copper. *Nano Lett.* **2013**, *13*, 4769–4778.

[184] Reckinger, N.; Van Hooijdonk, E.; Joucken, F.; Tyurnina, A. V.; Lucas, S.; Colomer, J. F. Anomalous Moiré Pattern of Graphene Investigated by Scanning Tunneling Microscopy: Evidence of Graphene Growth on Oxidized Cu(111). *Nano Res.* **2013**, *7*, 154–162.

[185] Ferrighi, L.; Di Valentin, C. Oxygen Reactivity on Pure and B-doped Graphene over Crystalline Cu(111). Effects of the Dopant and of the Metal Support. *Surf. Sci.* **2015**, *634*, 68–75.

[186] Olson, E. J.; Ma, R.; Sun, T.; Ebrish, M. A.; Haratipour, N.; Min, K.; Aluru, N. R.; Koester, S. J. Capacitive Sensing of Intercalated H_2O Molecules Using Graphene. *ACS Appl. Mater. Interfaces* **2015**, *7*, 25804–25812.

[187] Lee, D.; Ahn, G.; Ryu, S. Two-dimensional Water Diffusion at a Graphene-silica Interface. *J. Am. Chem. Soc.* **2014**, *136*, 6634–6642.

[188] Lu, H.; Lipatov, A.; Ryu, S.; Kim, D. J.; Lee, H.; Zhuravlev, M. Y.; Eom, C. B.; Tsymbal, E. Y.; Sinitskii, A.; Gruverman, A. Ferroelectric Tunnel Junctions with Graphene Electrodes. *Nat. Commun.* **2014**, *5*, 5518.

[189] Politano, A.; Cattelan, M.; Boukhvalov, D. W.; Campi, D.; Cupolillo, A.; Agnoli, S.; Apostol, N. G.; Lacovig, P.; Lizzit, S.; Farías, D.; Chiarello, G.; Granozzi, G.; Larciprete R. Unveiling the Mechanisms Leading to H_2 Production Promoted by Water Decomposition on Epitaxial Graphene at Room Temperature. *ACS Nano* **2016**, *10*, 4543−4549.

[190] Feng, X.; Maier, S.; Salmeron, M. Water Splits Epitaxial Graphene and Intercalates. *J. Am. Chem. Soc.* **2012**, *134*, 5662–5668.

[191] Boukhvalov, D. W.; Son, Y. W.; Ruoff R. S. Water Splitting over Graphene-Based Catalysts: Ab Initio Calculations. *ACS Catal.* **2014**, *4*, 2016−2021.

[192] Böttcher, S.; Vita, H.; Weser, M.; Bisti, F.; Dedkov, Yuriy S.; Horn, K. Adsorption of Water and Ammonia on Graphene: Evidence for Chemisorption from X-ray Absorption Spectra. *J. Phys. Chem. Lett.* **2017**, *8*, 3668−3672.

[193] Voloshina, E.; Usvyat, D.; Schütz, M.; Dedkovcd, Y.; Paulusa, B. On the physisorption of water on graphene: a CCSD(T) study. *Phys. Chem. Chem. Phys.* **2011**, *13*, 12041–12047.

[194] Böttcher, S.; Weser , M.; Dedkov1, Y.; Horn, K.; Voloshina, E. N.; Paulus, B. Graphene on Ferromagnetic Surfaces and Its Functionalization with Water and Ammonia. *Nanoscale Res. Lett.* **2011**, *6*, 214

[195] Ferrighi, L.; Datteo, M.; Fazio, G.; Di Valentin, C. Enhanced Reactivity at the Interface between (Doped) Graphene and Anatase TiO_2. *J. Am. Chem. Soc.* **2016**, *138*, 7365–7376.

[196] Ronchi, C.; Datteo, M.; Perilli, D.; Ferrighi, L.; Fazio, G.; Selli, D.; Di Valentin, C. π Magnetism of Carbon Monovacancy in Graphene by Hybrid Density Functional Calculations. *J. Phys. Chem. C* **2017**, *121*, 8653–8661.

[197] Dovesi, R.; Orlando, R.; Erba, A.; Zicovich-Wilson, C. M.; Civalleri, B.; Casassa, S.; Maschio, L.; Ferrabone, M.; Pierre, M. D. L.; D'Arco, P.; Noël, Y.; Causà, M.; Rérat, M.; Kirtman, B. CRYSTAL14: A Program for the Ab Initio Investigation of Crystalline Solids. *Int. J. Quantum Chem.* **2014**, *114*, 1287–1317.

[198] Lee, C.; Yang, W.; Parr, R. G. Development of the Colle-Salvetti Correlation-energy Formula into a Functional of the Electron Density. *Phys. Rev. B* **1988**, *37*, 785–789.

[199] Becke, A. D. Density-functional Thermochemistry. III. The Role of Exact Exchange. *J. Chem. Phys.* **1993**, *98*, 5648-5652.

[200] Grimme, S. Semiempirical GGA-type Density Functional Constructed with a Long-range Dispersion Correction. *J. Comput. Chem.* **2006**, *27*, 1787-1799.

[201] Civalleri, B.; Zicovich-Wilson, C. M.; Valenzano, L.; Ugliengo, P. B3LYP Augmented with an Empirical Dispersion Term (B3LYP-D*) as Applied to Molecular Crystals. *CrystEngComm* **2008**, *10*, 405–410.

[202] Padmanabhan, H.; Nanda, B. R. K. Interwined Lattice Deformation and Magnetism in Monovacancy Graphene. *Phys. Rev. B* **2016**, *93*, 165403

[203] Rodrigo, L.; Pou, P.; Pérez, R. Graphene Monovacancies: Electronic and Mechanical Properties From Large Scale Ab Initio Simulations. *Carbon* **2016**, *103*, 200−208.

[204] Zhang, Y.; Li, S. Y.; Huang, H.; Li, W. T.; Qiao, J. B.; Wang, W. X.; Yin, L. J.; Bai, K. K.; Duan, W.; He, L. Scanning Tunneling Microscopy of the π Magnetism of a Single Carbon Vacancy in Graphene. *Phys. Rev. Lett.* **2016**, *117,* 166801.

[205] Cohen A. J.; Mori-Sánchez P.; Yang W. Insights into Current Limitations of Density Functional Theory. *Science* **2008**, *321*, 792−794.

[206] Polo, V.; Kraka, E.; Cremer, D. Electron Correlation and the Self-Interaction Error of Density Functional Theory. *Mol. Phys* **2002**, *100*, 1771−1790.

[207] Heyd J.; Scuseria G. E.; Ernzerhof M. Hybrid Functionals Based on a Screened Coulomb Potential. *J. Chem. Phys.* **2003,** *118*, 8207−8215.

[208] Perdew, J. P. Electronic Structure of Solids' 91, Akademie Verlag, Berlin, **1991**.

[209] Adamo, C.; Barone, V.; Toward Reliable Density Functional Methods without Adjustable Parameters: The PBE0 Model. *J. Chem. Phys*. **1999**, *110*, 6158−6170.

[210] Ferrari, A. M.; Pisani, C. Reactivity of the Non Stoichiometric Ni_3O_4 Phase Supported at the Pd (100) Surface: Interaction with Au and Other Transition Metal Atoms. *Phys. Chem. Chem. Phys.* **2008**, *10*, 1463−1470.

[211] Liu L.; Liu Z.; Liu A.; Gu X.; Ge C.; Gao F.; Dong L. Engineering the TiO_2–Graphene Interface to Enhance Photocatalytic H_2 Production. *ChemSusChem* **2014**, *7*, 618–626.

[212] Wang, P.; Zhan, S.; Xia, Y.; Ma S.; Zhou Q.; Li, Y. The Fundamental Role and Mechanism of Reduced Graphene Oxide in rGO/Pt-TiO_2 Nanocomposite for High-performance Photocatalytic Water Splitting. *Appl. Catal. B-Environ.* **2017**, *207*, 335–346.

[213] Zhang H.; Lv X.; Li Y.; Wang Y.; Li J. P25-Graphene Composite as a High Performance Photocatalyst. *ACS Nano* **2010**, *4*, 380–386

[214] Vijayan B. K.; Dimitrijevic N. M.; Finkelstein-Shapiro D.; Wu J.; Gray K. A. Coupling Titania Nanotubes and Carbon Nanotubes To Create Photocatalytic Nanocomposites. *ACS Catal.* **2012**, *2*, 223–229.

[215] Ayissi, S.; Charpentier, P. A.; Farhangi, N.; Wood, J. A.; Palotás, K.; Hofer, W. A. Interaction of Titanium Oxide Nanostructures with Graphene and Functionalized Graphene Nanoribbons: A DFT Study. *J. Phys. Chem. C* **2013**, *117*, 25424–25432.

[216] Bukowski, B.; Deskins, N. A. The Interactions between TiO_2 and Graphene with Surface Inhomogeneity Determined Using Density Functional Theory. *Phys. Chem. Chem. Phys.* **2015**, *17*, 29734–29746.

[217] Xiang Q.; Yu J.; Jaroniec M. Enhanced Photocatalytic H_2-production Activity of Graphene-modified Titania Nanosheets. *Nanoscale*, **2011**, *3*, 3670.

[218] Setvín, M.; Aschauer, U.; Scheiber, P.; Li, Y.; Hou, W.; Schmid, M.; Selloni A.; Diebold, U. Reaction of O_2 with Subsurface Oxygen Vacancies on TiO_2 Anatase (101). *Science* **2013**, *341*, 988–991.

[219] Erathodiyil, N.; Ying, J. Y. Functionalization of Inorganic Nanoparticles for Bioimaging Application. *Acc. Chem. Res*. **2011**, *44*, 925–935.

[220] Dimitrijevic, N. M.; De la Garza, L; Rajh, T. Light-Induced Charge Separation across Bio-Inorganic Interface. *Int. J. Mod. Phys. B* **2009**, *23*, 473 473–491.

[221] Geiselera, B.; Fruk, L. Bifunctional Catechol Based Linkers for Modification of TiO_2 Surfaces. *J. Mater. Chem.* **2012**, *22*, 735–741.

[222] Bülbül, G.; Hayat, A.; Liua, X.; Andreescu, A. Reactivity of Nanoceria Particles Exposed to Biologically Relevant Catechol-Containing Molecules. *RSC adv.* **2016**, *6*, 60007–60014.

[223] Duncan, W.; Prezhdo, O.V. Theoretical Studies of Photoinduced Electron Transfer in Dye-Sensitized TiO_2. *Annu. Rev. Phys. Chem.* **2007**, *58*, 143–184.

[224] Huang, D.; Zhou, H.; Gao, J. Nanoparticles Modulate Autophagic Effect in a Dispersity-Dependent Manner. *Sci. Rep.* **2015**, *5*, 14361.

[225] Yun, J.; Sonabend, A. M.; Ulasov, I. V.; Kim, D. H.; Rozhkova, E. A.; Novosad, V.; Dashnaw, S.; Brown, T.; Canoll, P.; Bruce, J. N.; Lesniak, M. S. A Novel Adenoviral Vector Labeled with Superparamagnetic Iron Oxide Nanoparticles for Real-Time Tracking of Viral Delivery. *J. Clin. Neurosci.* **2012**, *19*, 875–880.

[226] Shi, H.; Magaye, R.; Castranova, V.; Zhao, J. Titanium Dioxide Nanoparticles: a Review of Current Toxicological Data. *Part Fibre Toxicol*. **2013**, *10*, 1–33.

[227] Duan, D.; Liu, H.; Xu, Y.; Han, Y.; Xu, M.; Zhang, Z.; Liu, Z. Activating TiO_2 Nanoparticles: Gallium-68 Serves as a High-Yield Photon Emitter for Cerenkov-Induced Photodynamic Therapy. *ACS Appl. Mater. Interfaces* **2018**, *10*, 5278–5286.

[228] Rozhkova, E. A.; Ulasov, I. V.; Kim, D. H.; Dimitrijevic, N. M.; Bader, S. D.; Lesniak, M. S.; Rajh, T. Multifunctional Nano-Bio Materials within Cellular Machinery. *Int. J. Nanosci.* **2011**, *10*, 899–908.

[229] Shrestha, N.K.; Macak, J. M.; Schmidt-Stein, F.; Hahn, R.; Mierke, C. T.; Fabry, B.; Schmuki, P. Magnetically Guided Titania Nanotubes for Site-Selective Photocatalysis and Drug Release. *Angew. Chem. Int. Ed.* **2009**, *48*, 969–972.

[230] Thurn, K. T; Paunesku, T.; Wu. A.; Brown, E. M.; Lai, B.; Vogt, S.; Maser, J.; Aslam, M.; Dravid, V.; Bergan, R.; Woloschak, G. E. Labeling TiO_2 Nanoparticles with Dyes for Optical Fluorescence Microscopy and Determination of TiO_2-DNA Nanoconjugate Stability. *Small* **2009**, *5*, 1318–1325.

[231] Endres, P. J.; Paunesku, T.; Vogt, S.; Meade, T. J.; Woloschak, G. E. DNA−TiO_2 Nanoconjugates Labeled with Magnetic Resonance Contrast Agents. *J. Am. Chem. Soc.* **2007**, *129*, 15760–15761.

[232] Brown, T.; Thurn, T.; Xin, L.; Liu, W.; Bazak, R.; Chen, S.; Lai, B.; Vogt, S.; Jacobsen, C.; Tatjana Paunesku, T.; Woloschak, G. E. Intracellular in Situ Labeling of TiO_2 Nanoparticles for Fluorescence Microscopy Detection. *Nano Res.* **2018**, *11*, 464–476.

[233] Yin, Z. F.; Wu, L.; Yang, H. G.; Su, Y. H. Recent Progress in Biomedical Applications of Titanium Dioxide. *Phys. Chem. Chem. Phys.* **2013**, *15*, 4844–4858.

[234] Fazio, G.; Ferrighi, L; Di Valentin, C. Spherical versus Faceted Anatase TiO_2 Nanoparticles: A Model Study of Structural and Electronic Properties. *J. Phys. Chem. C* **2015**, *119*, 20735–20746.

[235] Finkelstein-Shapiro, D.; Davidowski, S. K.; Lee, B. P.; Guo, C.; Holland, G. P.; Rajh, T.; Gray, K. A.; Yarger, J. L.; Calatayud, M. Direct Evidence of Chelated Geometry of Catechol on TiO_2 by a Combined Solid-State NMR and DFT Study. *J. Phys. Chem. C* **2016**, *120*, 23625–23630.

[236] Liu, L.-M.; Li, S.-C.; Cheng, H.; Diebold, U.; Selloni, A. Growth and Organization of an Organic Molecular Monolayer on TiO_2: Catechol on Anatase (101). *J. Am. Chem. Soc.* **2011**, *133*, 7816–7823.

[237] Li, S. C.; Chu, L. N.; Gong, X. Q.; Diebold, U. Hydrogen Bonding Controls the Dynamics of Catechol Adsorbed on a TiO_2(110) Surface. *Science* **2010**, *328*, 882–884.

[238] Hurst, J. S.; Fry, H. C.; Gosztola, D. J.; Rajh, T. Utilizing Chemical Raman Enhancement: A Route for Metal Oxide Support-Based Biodetection. *J. Phys. Chem. C* **2011**, *115*, 620–630.

[239] Yuan, Y.; Chen, S.; Paunesku, T.; Gleber, S. C.; Liu, W. C.; Doty, B. C.; Mak, R.; Deng, J.; Jin, Q.; Lai., B.; Brister, K.; Flachenecker, C.; Jacobsen, C.; Vogt, S.; Woloschak, G. E. Epidermal Growth Factor Receptor Targeted Nuclear Delivery and High-Resolution Whole Cell X-ray Imaging of Fe_3O_4@TiO_2 Nanoparticles in Cancer Cells. *ACS Nano* **2013**, *7*, 10502–10517.

[240] Yeung K. L.; Maira, A. J.; Stolz, J.; Hung, E; Ho, N. K-C.; Wei, A. C.; Soria, J.; Chao, K-J.; Yue, P. L. Ensemble Effects in Nanostructured TiO_2 Used in the Gas-Phase Photooxidation of Trichloroethylene. *J. Phys. Chem. B* **2002**, *106*, 4608–4616.

[241] Chen, L. X.; Rajh, T.; Wang, Z.; Thurnauer, M. C. XAFS Studies of Surface Structures of TiO_2 Nanoparticles and Photocatalytic Reduction of Metal Ions. *J. Phys. Chem. B* **1997**, *101*, 10668–10697.

[242] Radoičić, M. B.; Janković, I. A.; Despotović, V. N.; Šojić, D. V.; Savić, T. D.; Šaponjića Z. V.; Abramović, B. F.; Čomora, M. I. The role of surface defect sites of titania nanoparticles in the photocatalysis: Aging and modification. *Appl. Catal. B: Environ.* **2013**, *138*, 122–127.

[243] de la Garza, L.; Saponjic, Z. V.; Dimitrijevic, N. M.; Thurnauer, M. C.; Rajh, T. Surface States of Titanium Dioxide Nanoparticles Modified with Enediol Ligands. *J. Phys. Chem. B* **2006**, *110*, 680–686.

[244] Hurst, S. J.; Christopher Fry, H. C.; Gosztola, D. J.; Finkelstein-Shapiro, D.; Vladimiro Mujica, V.; Rajh, T. Mechanistic studies into the Raman enhancement of enediol-semiconducting nanoparticle conjugates and their use in biological applications. *Proc. SPIE* 7758, Physical Chemistry of Interfaces and Nanomaterials IX, **2010**, *77580E*, doi:10.1117/12.862931

[245] Elstner, M.; Porezag, D.; Jungnickel, G.; Elsner, J.; Haugk, M.; Frauenheim, T.; Suhai, S.; Seifert, G. Self-Consistent-Charge Density Functional Tight-Binding Method for Simulations of Complex Materials Properties. *Phys. Rev. B* **1998**, *58*, 7260–7268.

[246] Elstner, M.; Seifert, G. Density Functional Tight Binding. *Phil. Trans. R. Soc. A* **2014**, *372*, 1–12.

[247] Civalleri, B.; D’Arco, Ph.; Orlando, R.; Saunders, V. R.; Dovesi, R. Hartree–Fock Geometry Optimisation of Periodic Systems with the Crystal code. *Chem. Phys. Lett.* **2001**, *348*, 131−138.

[248] Aradi, B.; Hourahine, B.; Frauenheim, T. DFTB+, a Sparse Matrix-Based Implementation of the DFTB Method. *J. Phys. Chem. A* **2007**, *111*, 5678–5684.

[249] Selli, D.; Fazio, G.; Seifert, G.; Di Valentin, C. Water multilayers on TiO_2 (101) Anatase Surface: Assessment of a DFTB-Based Method. *J. Chem. Theory Comput.* **2017**, *13*, 3862–3873.

[250] Hu, H.; Lu, Z.; Elstner, M.; Hermans, J.; Yang, W. Simulating Water with the Self-Consistent-Charge Density Functional Tight Binding Method: From Molecular Clusters to the Liquid State. J. Phys. Chem. A, **2007**, *111*, 5685–5691.

[251] Elstner, M. The SCC-DFTB method and Its Application to Biological Systems. *Theor Chem Acc* **2006**, *116*, 316–325.

[252] Sodeyama, K.; Sumita, M.; O'Rourke, C.; Terranova, U.; Islam, U.; Han, L.; Bowler, D. R.; Tateyama, Y. Protonated Carboxyl Anchor for Stable Adsorption of Ru N749 Dye (Black Dye) on a TiO_2 Anatase (101) Surface. *J. Phys. Chem. Lett.* **2012**, *3*, 472–477.

[253] Deskins, N. A.; Dupuis, M. Electron Transport Via Polaron Hopping in Bulk TiO_2: A Density Functional Theory Characterization. *Phys. Rev. B* **2007**, *45*, 195212–10.

[254] Fazio, G.; Ferrighi, L.; Di Valentin, C. Photoexcited Carriers Recombination and Trapping in Spherical vs Faceted TiO_2 Nanoparticles. *Nano Energy* **2016**, *27*, 673–689.

[255] Atkins, P.; Overton, T.; Rourke, J.; Weller, M.; Armstrong. F. Inorganic chemistry. 6th edition. W. H. Freeman and Company, **2014**

[256] Beutner, R.; Michael, J.; Schwenzer, B.; Scharnweber, D. Biological Nano-Functionalization of Titanium-Based Biomaterial Surfaces: a Flexible Toolbox. *J. R. Soc. Interface*, **2010**, *7*, S93–S105.

[257] Ye, L.; Pelton, R.; Brook, M. A. Biotinylation of TiO_2 Nanoparticles and Their Conjugation with Streptavidin. *Langmuir*, **2007**, *23*, 5630–5637.

[258] Plueddemann, E. P.Silane Coupling Agents,2nd ed.; Plenum Press: NewYork, ***1991***.

[259] Ahmed, A.; Bonner, C.; Desai, A. D. *Biomed. Microdevices* **2001**, *3*, 89–96.

[260] Gu, W.; Song, G.; Li, S.; Shao, C.; Yan, C.; Ye, L. Chlorotoxin-Conjugated, PEGylated Gd_2O_3 Nanoparticles as a Glioma-Specific Magnetic Resonance Imaging contrast agent. *RSC Adv.*, **2014**, *4*, 50254–50260.

[261] Qin, Y.; Sun, L.; Li, X.; Cao, Q.; Wang, H.; Tang, X.; Ye, L. Highly Water-Dispersible TiO_2 Nanoparticles for Doxorubicin Delivery: Effect of Loading Mode on Therapeutic Efficacy. *J. Mater. Chem.* **2011**, *21*, 18003–18010.

[262] Liu, S.; Meng, X. Y.; Perez-Aguilar, J. M.; Zhou, R. An In Silico Study of TiO_2 Nanoparticles Interaction with Twenty Standard Amino Acids in Aqueous Solution. *Sci. Rep.* **2016**, *6*, 37761.

[263] Luan, B.; Huynh, T.; Zhou, R. Simplified TiO_2 Force Fields for Studies of its Interaction with Biomolecules. *J. Chem. Phys.* **2015**, *142*, 234102.

[264] Carravetta, V.; Monti, S. Peptide−TiO_2 Surface Interaction in Solution by Ab Initio and Molecular Dynamics Simulations. *J. Phys. Chem. B* **2006**, *110*, 6160−6169.

[265] Monti, S.; Carravetta, V.; Battocchio, C.; Iucci, G.; Polzonetti, G. Peptide/TiO_2 Surface Interaction: A Theoretical and Experimental Study on the Structure of Adsorbed ALA-GLU and ALA-LYS. *Langmuir* **2008**, *24*, 3205−3214.

[266] Monti, S. Molecular Dynamics Simulations of Collagen-Like Peptide Adsorption on Titanium-Based Material Surfaces. *J. Phys. Chem. C* **2007**, *111*, 6086−6094.

[267] Livage, J.; Henry, M.; Sanchez, C. Sol-Gel Chemistry of Transition Metal Oxides. *Prog. Solid St. Chem.***1988**, *18*, 250−341.

[268] Cargnello, M.; Gordon, T. R.; Murray. C. B. Solution-Phase Synthesis of Titanium Dioxide Nanoparticles and Nanocrystals. *Chem. Rev.* **2014**, *114*, 9319−9345.

[269] Schlechta, C. A.; Maurer, J. A. Functionalization of Glass Substrates: Mechanistic Onsights into the Surface Reaction of Trialkoxysilanes. *RSC Adv.* **2011**, *1*, 1446–1448.

[270] Fazio, G.; Selli, D.; Ferraro, L.; Seifert, G.; Di Valentin, C. Curved TiO_2 Nanoparticles in Water: Short (Chemical) and Long (Physical) Range Interfacial Effects. *ACS Appl. Mater. Interfaces* **2018**, *10*, 29943–29953.

[271] Toledo, L.; Racine, L.; Pérez, V.; Henríquez, J. P.; Auzely-Velty, R.; Urbano, B. F. Physical Nanocomposite Hydrogels Filled with Low Concentrations of TiO_2 Nanoparticles: Swelling, Networks Parameters and Cell Retention Studies. *Mater. Sci. Eng. C* **2018**, *92*, 769–778.

[272] Yan, W.; Li, S.; Zhang, Y.; Yao, Q.; Tse. S. D. Effects of Dipole Moment and Temperature on the Interaction Dynamics of Titania Nanoparticles during Agglomeration. *J. Phys. Chem. C* **2010**, *114*, 10755–10760.

[273] Steiner, T. The Hydrogen Bond in the Solid State. *Angew. Chem. Int*. **2002**, *41*, 48–76.

List of Figures

List of Tables

List of Publications

- Ronchi, C.; Datteo, M.; Kaviani, M.; Selli, D.; Di Valentin, C. Unraveling Dynamical and Light Effects on Functionalized Titanium Dioxide Nanoparticles for Bioconjugation. *Journal of Physical Chemistry C* **2019**, *123*, 10130-10144.

- Datteo, M.; Liu, H.; Di Valentin, C. Water on Graphene-Coated TiO_2: Role of Atomic Vacancies. *ACS Appl. Mater. Interfaces* **2018**, *10*, 5793-5804.

- Ronchi, C.; Datteo, M.; Perilli, D.; Ferrighi, L.; Fazio, G.; Selli, D.; Di Valentin, C. π Magnetism of Carbon Monovacancy in Graphene by Hybrid Density Functional Calculations. *Journal of Physical Chemistry C* **2017**, *121*, 8653-8661.

- Ferrighi, L.; Datteo, M.; Fazio, G.; Di Valentin, C. Catalysis under Cover: Enhanced Reactivity at the Interface between (Doped) Graphene and Anatase TiO_2. *Journal of the American Chemical Society* **2016**, *138*, 7365-7376.

- Ferrighi, L.; Datteo, M.; Di Valentin, C. Boosting Graphene Reactivity with Oxygen by Boron Doping: Density Functional Theory Modeling of the Reaction Path. *Journal of Physical Chemistry C* **2014**, *118*, 223-230.